ISBN 978-82-471-2297-6 (printed ver.)
ISBN 978-82-471-2298-3 (electronic ver.)
ISSN 1503-8181

Doctoral theses at NTNU, 2010:163

Knut Erik Teigen

Development and use of interface-capturing methods for investigation of surfactant-covered drops in electric fields

NTNU
Norwegian University of
Science and Technology

Thesis for the degree of
philosophiae doctor

Faculty of Engineering Science and Technology
Department of Energy and Process Engineering

NTNU
Norwegian University of
Science and Technology

Doctoral theses at NTNU, 2010:163

NTNU

Knut Erik Teigen

Development and use of interface-capturing methods for investigation of surfactant-covered drops in electric fields

Thesis for the degree of philosophiae doctor

Trondheim, October 2010

Norwegian University of
Science and Technology
Faculty of Engineering Science and Technology
Department of Energy and Process Engineering

NTNU
Norwegian University of
Science and Technology

NTNU
Norwegian University of Science and Technology

Thesis for the degree of philosophiae doctor

Faculty of Engineering Science and Technology
Department of Energy and Process Engineering

ISBN 978-82-471-2297-6 (printed ver.)
ISBN 978-82-471-2298-3 (electronic ver.)
ISSN 1503-8181

Doctoral Theses at NTNU, 2010:163

Printed by Tapir Uttrykk

Abstract

THIS THESIS investigates the development and use of interface-capturing methods for detailed simulations of surfactant-covered drops in electric fields.

A mathematical model is established for the full hydrodynamic behavior of the drops, including both electric forces caused by an applied electric field and forces due to the non-uniform surface tension caused by the presence of surfactants. Equations for the electric field and for the coupled evolution of surfactant on the interface and in the bulk are also considered.

Numerical methods suitable for the solution of the mathematical model are investigated. Both the level-set method and the phase-field method are used. For the level-set method, the ghost-fluid method which treats discontinuities across the interface in a sharp manner is considered and compared to the conceptually simpler continuous surface-force method. For the phase-field method, sophisticated numerical approaches including nonlinear multigrid methods on block-structured adaptive grids are used to enable simulations in full 3D.

Several physical configurations are examined. It is shown how an electric field can suppress the partial coalescence phenomenon occurring when a drop coalesces with an interface. Is is demonstrated that the presence of a surfactant can considerably slow down a sedimenting drop due to inhibition of internal circulation. Conversely, an electric field speeds up the sedimentation due to stretching which leads to reduced drag. The deformation of a surfactant-covered leaky dielectric drop in an electric field is studied, and rich deformation behavior due to the complex interaction between the electric field and the surfactant is demonstrated. Finally, full 3D simulations of a drop in shear flow are performed, with particular emphasis on the influence of a soluble surfactant. It is shown that the deformation of a drop with soluble surfactant in general lies between that of a clean drop and that of a drop covered with insoluble surfactant. However, for the breakup of a drop, it is shown that for the insoluble case, the drop can break up at a earlier time compared to a clean drop, while for the soluble case, the drop can break up at a later time.

Preface

The present work was initiated as part of the research project "Electrocoalescence – Criteria for an efficient process in real crude oil systems"; coordinated by SINTEF Energy Research. The project is supported by The Research Council of Norway, under the contract no: 169466/S30, and by the following industrial partners: Aker Solutions AS, BP Exploration Operating Company Ltd, Hamworthy Technology & Products AS, Petrobras, Saudi Aramco, Shell Technology Norway AS and Statoil ASA.

I would like to thank my supervisor, Professor Inge R. Gran, for trusting me to pursue my own ideas and thoughts. Thanks are also due to my co-supervisor, Dr. Svend Tollak Munkejord, for always having an open door, an open ear and an open mind. Many thanks to the rest of the electrocoalescence project members and partners for interesting discussions.

I am indebted to Professor John Lowengrub for inviting me to University of California, Irvine. My stay at UC Irvine was enlightening and enjoyable both from a personal and a professional perspective. I also extend thanks to all the people at Lowengrub's lab who contributed to the work, Fang Jin, Fan Wang, Peng Song, Steven Wise, Xiangrong Li, Zhengzheng Hu and to the rest of the people there for welcoming me.

The financial support received from the Leiv Eiriksson mobility programme is gratefully acknowledged. I am also grateful from the support from the Fulbright Foundation, in particular for their invaluable aid in all the practical matters of going abroad and for the inspiring Philadelphia Fulbright Seminar.

Finally, I extend my deepest gratitude to my wife and daughter for helping me keep a healthy work-life balance and getting my mind off of partial differential equations.

Trondheim, July 2010
Knut Erik Teigen

Contents

1 Introduction

> I really cannot see why so many of our compatriots should find the scientific approach dull and dissapointing. It is a common mistake to think that all that matters in science is logic and the understanding and appliction of fixed laws. In fact, imagination plays a decisive role in science, and especially in natural science.
>
> Werner Heisenberg (1901–1976)

> Science is not formal logic – it needs the free play of the mind in as great a degree as any other creative art.
>
> Max Born (1882–1970), winner of the Nobel Prize in Physics

1.1 Background

Oil extracted from offshore oil wells typically contains a significant amount of water. As a result of the oil-water mixture passing through valves and pumps, this water takes the form of small drops, see Figure 1.1 for an example. Since the density of water is larger than that of the oil, it is common to remove the water by sedimentation, where the oil-water mixture is placed in large separation tanks and the water drops eventually fall to the bottom of the tank and is extracted. There is a trend towards moving oil production to floating vessels, called floating production, storing and offloading (FPSO) units. These units have restricted space, so the large separation tanks are problematic. Also, due to uncertainties in future oil production, there is a push towards developing heavier, more viscous oils. These issues create a need for more efficient, and more compact separation units.

In order to understand the separation process, it is instructive to consider a single, small water drop falling through a viscous oil. An approximation of the terminal velocity of such a drop is given by Stokes' law,

$$V_t = \frac{\Delta\rho g D^2}{18\mu}. \tag{1.1}$$

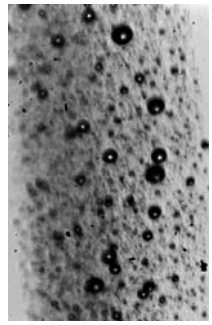

Figure 1.1: Picture of a water-in-oil emulsion reproduced from Chiesa (2004). The water drops appear black due to the image-capturing technique.

Here, $\Delta\rho$ is the density difference between water and oil, g is the gravitational acceleration, D is the diameter of the drop and μ is the viscosity of the oil. This formula makes it clear that for heavy, viscous oils and small water drops, the sedimentation process can be very time consuming. It is also evident that to speed up the process, the parameter that has the most significant impact on the falling velocity is the drop diameter. Hence, the most efficient way to speed up the sedimentation process is to obtain larger drops by drop coalescence. This simple observation is utilized in electrostatic coalescers. Due to the large difference in electrical conductivity between salt water and oil, the water behaves as a conductor and the oil as an insulator. When an electric field is applied to a water-in-oil mixture, the water drops are polarized as illustrated in Figure 1.2. This leads to attractive forces between the water drops, which again lead to coalescence.

A drop coalescence event can typically be divided into three stages. The first is drop approach, where the drops are brought into contact. The second is film-thinning, where the thin oil film between the drops is squeezed out by the approaching interfaces. The third and final stage is film rupture and coalescence. To see at which of stage the electric field has greatest influence, it is elucidating to approximate the two drops as dipoles. This leads to a simple expression for the force between them (see e.g. Klingenberg *et al.* (1991)),

$$F = \frac{24\pi\varepsilon E_0^2 R^6}{h^4}, \tag{1.2}$$

where ε is the permittivity of the oil, E_0 is the electric field magnitude, R is the drop radius and h is the distance between the drops. Due to the h^{-4} term, we understand that the drops need to be very close in order for the electric forces to have a significant impact. Therefore, the electric field mainly speeds up

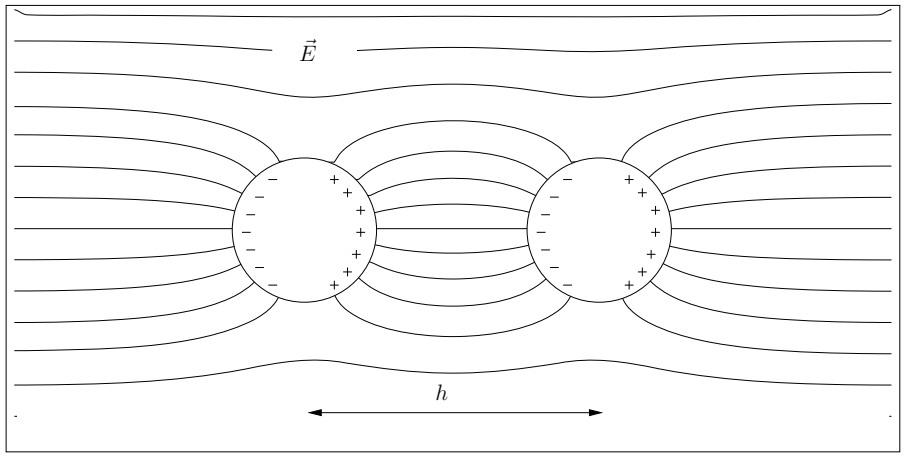

Figure 1.2: Illustration of the polarization of two conducting water drops in an insulating oil when subjected to an electric field. The lines represent electric field lines (taken from a numerical simulation).

the film-thinning process, and other forces are needed to bring the drops into contact. In modern commercial electrocoalescers, the electrodes are typically placed where the flow is turbulent. The turbulent forces increase the collision frequency, and the electric forces increase the probability of coalescence during a collision event.

Another factor that is important during the film-thinning process, is the prescence of surface-active agents (surfactants). Surfactants are amphiphilic organic compounds which are naturally present in the crude oil, and can be adsorbed at the oil-water interface. The presence of surfactants reduce the surface tension of the interface, and this can in turn significantly impact the film-thinning process. When two drops approach each other, as illustrated in Figure 1.3, surfactant molecules will be swept from the tip of the drop. This will create a surface-tension gradient, which gives rise to tangential stresses along the interface. These stresses will reduce the internal circulation in the drop and inhibit the drainage of the intermediate oil film. It has been observed (see e.g. Yang and Maa (1984); Leal (2004)) that the presence of surfactants may significantly increase the coalescence time. The combined effect of surfactants and electric fields on the coalescence process has received little attention in the literature. However, the deformation of a single drop was studied experimentally in Ha and Yang (1998) and it was found that the presence of surfactants affected both the amount of deformation and the mode of breakup.

In order to obtain a deeper understanding of the electrocoalescence process,

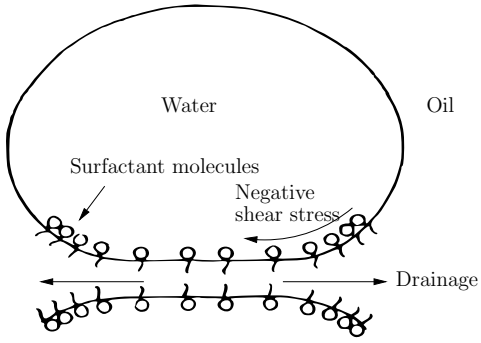

Figure 1.3: Illustration of the reduced drainage of the oil film between two approaching water drops in the presence of surface active molecules.

this work sets out to establish mathematical models for describing the above processes. It is also necessary to develop the numerical methods needed to solve the mathematical models in an accurate and efficient manner.

1.2 Relevance to other areas

It is important to emphasize that the present work has relevance reaching beyond just the problem of electrocoalescence. The models and methods developed here can easily be applied to a multitude of other interesting areas.

Electric fields are used to control or modify two-phase flows in several different areas. These include enhanced heat transfer in heat exchangers (e.g. Laohalertdecha *et al.* (2007)), drop generation in inkjet printers (e.g. Yu *et al.* (2005); Shin *et al.* (2004)) and drop manipulation on lab-on-a-chip devices (e.g. Link *et al.* (2006); Cristini and Tan (2004)),

The topic of surfactants is also important in other areas. Besides their impact on drop break-up and coalescence (e.g. Hu *et al.* (2000); Hudson *et al.* (2003); Leal (2004); Hameed *et al.* (2008)), surfactants play important roles in vortex pair interaction (e.g., Tryggvason *et al.* (1992); Hirsa and Willmarth (1994)), fingering (e.g. Troian *et al.* (1990); Matar and Troian (1999)) and are also important in biomedical applications (e.g. Singh and Cameotra (2004) and in the food industry (e.g. Nitschke and Costa (2007).

Solving the surfactant dynamics can be generalized to the problem of solving an equation along a general, moving interface and where the bulk dynamics and interface dynamics are coupled. Problems where this is important include biomembranes where transmembrane proteins play an important role in intra- and extra- cellular dynamics (e.g. Kockelkoren *et al.* (2003); Allain and Amar

(2008); Levine and Rappel (2005); Gomez-Marin *et al.* (2007)), epitaxially grown thin films where adsorbing/desorbing adatoms affect the dynamics and coarsening of the thin film (e.g. Fried and Gurtin (2004); Stocker and Voigt (2008); Li *et al.* (2009a)), and electrochemical dissolution of binary alloys where one component is removed selectively and dissolved in an electrolyte solution (e.g. Erlebacher *et al.* (2001); Eilks and Elliott (2008)).

2 Mathematical modelling and numerical methods

> Essentially, all models are wrong, but some are useful.
>
> George E. P. Box

> Today you are in an entirely different situation. You don't have to put the problem on a Procrustean bed and mutilate it before you attack it numerically.
>
> Peter Lax - winner of the Abel Price 2005

In this chapter, a brief overview of the mathematical models and numerical methods employed in this work are given. The flow dynamics in a many industrial processes covers a wide range of scales, and it is impossible to include all scales in a single model. Therefore, a multiscale approach to modelling is envisioned, where different models suitable for each scale are used together. Figure 2.1 shows an illustration of such a modelling hierarchy for the electrocoalescence process. At the microscale, interface-tracking/capturing methods are employed. These methods are capable of accurately resolving the movement of the drops and the deformation of the interfaces. As demonstrated in Cristini and Tan (2004), these methods are ideal for studying breakup and coalescence phenomena. The level of detail of interface-capturing techniques can in many cases provide information that is not immediately available from experiments. However, they also require high grid resolutions, so the number of drops that can be simulated is limited to small systems. Typically, only one or two drops can be simulated within reasonable times on a single workstation.

In discrete particle methods, each drop is modelled as a spherical particle, and force relationships between these particles are used to advance the solution in time. This simplified arrangement allows for more drops to be simulated. In Melheim (2007), electrocoalescence was simulated using 1×10^6 drops. The quality of such a simulation is obviously highly dependent on the accuracy of the models used to represent the forces between the particles.

Even larger systems may be taken into consideration using multi-fluid methods. Here, only the averaged effect of drops are taken into account. This gives rise to unknown terms in the flow models, which need to be modelled to obtain

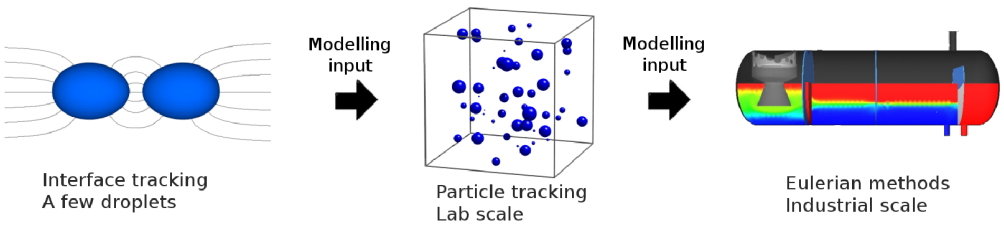

Figure 2.1: An illustration of the multiscale approach.

a closed system. Again, the quality of such a simulation is dependent on the accuracy of the models used.

To derive the models needed for discrete-particle methods and multi-fluid methods a combination of theory and experiments are needed. Theoretical considerations and insight into the physical phenomena can provide a good starting point, and experiments can be used to find unknown constants or to tweak the model parameters. There is a two-way interaction between experiments and numerical simulations. Simulations can provide insight that can assist in designing useful experiments, and results from experiments can aid in developing more accurate simulation tools. The purpose of this work is to develop representative mathematical models and accurate interface-capturing methods for simulating the electrocoalescence process on the microlevel. In particular, models and methods suitable for studying the combined effect of an electric field and surface-active agents are considered.

2.1 Mathematical formulation

Consider a domain $\Omega \subset \mathbb{R}^{2,3}$, which contains a closed interface, Γ. The interior of the interface is $\Omega_0 \subset \Omega$, and the exterior is $\Omega_1 \subset \Omega$. See Figure 2.2 for an illustration. The interface is allowed to move, deform, and even change topology. A complete mathematical model for this problem includes equations governing the flow and appropriate interface relations accounting for discontinuities at the interface. These are considered next.

2.1.1 Flow equations

We assume that the flow is governed by the Navier–Stokes equations in each phase, with additional terms accounting for interfacial-tension forces and

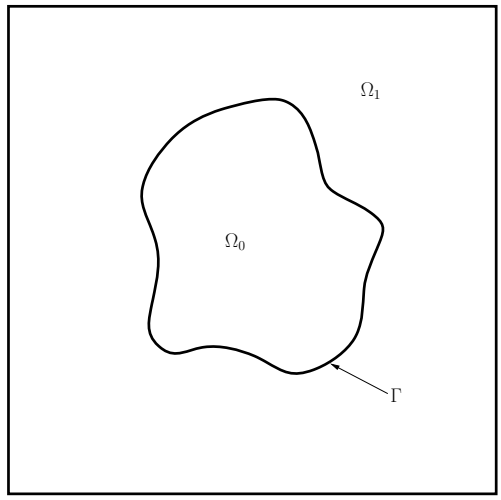

Figure 2.2: Illustration of the mathematical domain.

electric forces. The Navier–Stokes equations are

$$\begin{aligned} \rho\left(\frac{\partial \boldsymbol{u}}{\partial t} + (\boldsymbol{u}\cdot\nabla)\boldsymbol{u}\right) &= -\nabla p + \nabla\cdot[\mu(\nabla\boldsymbol{u} + \nabla\boldsymbol{u}^T)] \\ &\quad + \boldsymbol{f}_c + \boldsymbol{f}_e, \\ \nabla\cdot\boldsymbol{u} &= 0, \end{aligned} \tag{2.1}$$

where ρ is the density, $\boldsymbol{u}$ is the velocity, p is the pressure and μ is the dynamic viscosity. The effect of an interface, Γ, in the domain results in a singular surface force which can be expressed by

$$\boldsymbol{f_c}(\boldsymbol{x},t) = \int_{\Gamma(t)} \boldsymbol{F}(s,t)\delta(\boldsymbol{x} - \boldsymbol{X}(s,t))\mathrm{d}s, \tag{2.2}$$

where s is the arc-length, $\boldsymbol{X}(s,t)$ is the parametrization of the interface, $\boldsymbol{x}$ is the spatial position and δ is the Dirac delta function. $\boldsymbol{F}$ is given by

$$\boldsymbol{F} = \gamma\kappa\boldsymbol{n} + \nabla_\Gamma\gamma. \tag{2.3}$$

Here, γ is the interfacial tension, κ the curvature and $\boldsymbol{n}$ is the inward pointing unit normal vector. The surface gradient operator, ∇_Γ can be written as

$$\nabla_\Gamma = (\boldsymbol{I} - \boldsymbol{n}\otimes\boldsymbol{n})\nabla. \tag{2.4}$$

The first term on the right-hand side of Equation (2.3) accounts for the capillary force which acts perpendicularly to the drop interface. This force is present at

all liquid interfaces. The second term is an additional force due to gradients in the interfacial tension, which can occur if surfactants are present on the interface. This force acts tangentially to the interface.

The electric force is given by the divergence of the Maxwell stress tensor, $\boldsymbol{f}_e = \nabla \cdot \boldsymbol{M}$, where

$$\boldsymbol{M} = \varepsilon \left[\boldsymbol{E}\boldsymbol{E} - \frac{1}{2}(\boldsymbol{E} \cdot \boldsymbol{E})\boldsymbol{I} \right]. \tag{2.5}$$

Here, $\boldsymbol{E}$ is the electric field and $\boldsymbol{I}$ is the identity tensor. We assume perfect dielectric materials with no free charges. A conducting drop in an insulating medium, which is the case for a water drop in oil, can then be approximated by setting $\varepsilon_{\text{water}} \gg \varepsilon_{\text{oil}}$.

With these assumptions, the electric potential, Ψ, can be calculated from the following Laplace equation:

$$\nabla \cdot (\varepsilon \varepsilon_0 \nabla \Psi) = 0, \tag{2.6}$$

The electric field can then be calculated as

$$\boldsymbol{E} = -\nabla \Psi, \tag{2.7}$$

With the above assumptions, $\nabla \cdot \boldsymbol{M} = \boldsymbol{0}$ everywhere except at the interface.

Next, we assume that the interface is covered by surfactants, and we let f denote the surfactant concentration defined on Γ. The presence of a surfactant will decrease the interfacial tension of the interface. We assume that the dependence of the interfacial tension is governed by a Langmuir equation of state,

$$\gamma(f) = \gamma_0 \left[1 + \frac{\mathcal{R}T f_\infty}{\gamma_0} \ln\left(1 - \frac{f}{f_\infty} \right) \right], \tag{2.8}$$

where $\mathcal{R}$ is the ideal gas constant, T is the absolute temperature, γ_0 is the interfacial tension of a clean interface and f_∞ is the maximum interfacial surfactant concentration. The dimensionless factor $\beta = \mathcal{R}T f_\infty / \gamma_0$ is often denoted the surface elasticity parameter and expresses the sensitivity of the interfacial tension to changes in the surfactant concentration. For a dilute surfactant concentration, the above expression can be simplified to give a linear equation,

$$\gamma(f) = \gamma_0 - \mathcal{R}T f. \tag{2.9}$$

This expression is often used in the literature. A comparison between these two expressions is given in Figure 2.3. It is evident that the linear equation of state is a good match at low concentrations, but fails to reproduce the steep gradient at higher concentrations. The non-linear equation of state is used for all simulations in this work.

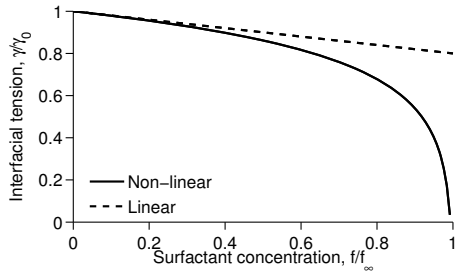

Figure 2.3: Dependence of surface tension on surfactant concentration. Comparison of a linear and non-linear equation of state. $\beta = 0.2$.

Assuming that f may be extended off Γ, the sharp-interface representation of the evolution of the surface surfactant is given by (see e.g. Xu and Zhao (2003))

$$\frac{\partial f}{\partial t} + \boldsymbol{u} \cdot \boldsymbol{\nabla} f - \boldsymbol{n} \cdot \boldsymbol{\nabla} \boldsymbol{u} \cdot \boldsymbol{n} f = D_f (\boldsymbol{\nabla}^2 - \boldsymbol{n} \cdot \boldsymbol{\nabla} \boldsymbol{\nabla} \cdot \boldsymbol{n} - \kappa \boldsymbol{n} \cdot \boldsymbol{\nabla}) f + j, \quad (2.10)$$

where D_f is the diffusion coefficient. The source term, j, accounts for adsorption and desorption of surfactant and is given by

$$j(f, F) = r_a F_s (f_\infty - f) - r_d f. \quad (2.11)$$

Here, r_a and r_d are adsorption and desorption coefficients, respectively, and F_s is the surfactant concentration immediately adjacent to the surface.

Now, assume that f is soluble in Ω_1, but not in Ω_0. Let there be a bulk concentration, F, in Ω_1, which is governed by

$$\frac{\partial F}{\partial t} + \boldsymbol{\nabla} \cdot (F \boldsymbol{u}) = D_F \boldsymbol{\nabla}^2 F \text{ in } \Omega_1, \quad (2.12)$$

with the boundary condition at Γ

$$D_F \boldsymbol{\nabla} F \cdot \boldsymbol{n} = -j \text{ on } \Gamma. \quad (2.13)$$

Here, D_F is the diffusion coefficient in the bulk.

The equations for the surfactant on the interface and in the bulk are coupled through the source term, j. In order to simplify the mathematical representation, let δ be the surface delta function such that

$$\int_\Gamma f \, \mathrm{d}\Gamma = \int_\Omega f \delta \, \mathrm{d}\Omega. \quad (2.14)$$

Also, let H be the Heaviside function,

$$H = \begin{cases} 1 & \text{in } \Omega_1, \\ 0 & \text{in } \Omega_0. \end{cases} \tag{2.15}$$

The equation for the interfacial surfactant, Equation (2.10), can now be extended to the general domain Ω (see e.g. Rätz and Voigt (2006)),

$$\frac{\partial}{\partial t}(f\,\delta) + \boldsymbol{\nabla}\cdot(f\,\delta\,\boldsymbol{u}) = D_f\boldsymbol{\nabla}\cdot(\delta\boldsymbol{\nabla}f) + \delta j, \tag{2.16}$$

The formulation given by Equation (2.16) is considerably simpler than the sharp-interface formulation.

Similarly, the bulk concentration can be generalized to the general domain by

$$\frac{\partial}{\partial t}(H\,F) + \boldsymbol{\nabla}\cdot(H\,F\,\boldsymbol{u}) = D_F\boldsymbol{\nabla}\cdot(H\boldsymbol{\nabla}F) - \delta j, \tag{2.17}$$

where the boundary condition has been included using the approach from Li *et al.* (2009b). By introducing numerical regularizations of the delta function and Heaviside function, the much simpler mathematical expressions can be used to evolve the surfactant concentrations.

2.1.2 Interface relations

The variation in physical properties in the two domains gives rise to discontinuities across the interface which need to be considered to complete the model. The jump conditions for the two-phase problem without electric fields can be found in e.g. Kang *et al.* (2000). In Hansen (2005); Bjørklund (2009) these are extended to include electric fields, and in Lervåg (2008) the Marangoni stresses are included. Here, we summarize the jump conditions as

$$[\boldsymbol{u}] = 0, \tag{2.18}$$

$$[p] = 2[\mu]\boldsymbol{n}\cdot\boldsymbol{\nabla}\boldsymbol{u}\cdot\boldsymbol{n} + \boldsymbol{n}\cdot[\boldsymbol{M}]\cdot\boldsymbol{n} + \sigma\kappa, \tag{2.19}$$

$$[\Psi] = 0, \tag{2.20}$$

$$\begin{aligned}[\mu\boldsymbol{\nabla}\boldsymbol{u}] = [\mu]\big(&(\boldsymbol{n}\cdot\boldsymbol{\nabla}\boldsymbol{u}\cdot\boldsymbol{n})\boldsymbol{n}\boldsymbol{n} + (\boldsymbol{n}\cdot\boldsymbol{\nabla}\boldsymbol{u}\cdot\boldsymbol{t})\boldsymbol{n}\boldsymbol{t} \\ &- (\boldsymbol{n}\cdot\boldsymbol{\nabla}\boldsymbol{u}\cdot\boldsymbol{t})\boldsymbol{t}\boldsymbol{n} + (\boldsymbol{t}\cdot\boldsymbol{\nabla}\boldsymbol{u}\cdot\boldsymbol{t})\boldsymbol{t}\boldsymbol{t}\big) \\ &- (\boldsymbol{t}\cdot[\boldsymbol{M}]\cdot\boldsymbol{n})\boldsymbol{t}\boldsymbol{n} - (\boldsymbol{t}\cdot\boldsymbol{\nabla}_\Gamma\sigma)\boldsymbol{t}\boldsymbol{n},\end{aligned} \tag{2.21}$$

$$[\boldsymbol{\nabla}p] = 0, \tag{2.22}$$

$$[\varepsilon\boldsymbol{n}\cdot\boldsymbol{\nabla}\Psi] = 0. \tag{2.23}$$

With the complete models in place, the question remains how to tackle them numerically. In particular, how to address the interface is the major challenge, and this will be considered in the next section.

2.2 Numerical methods

In this work, the equations from the previous sections are solved using the finite-difference method on Cartesian grids. Standard discretization methods from the literature are employed, and more details can be found in the individual papers. This chapter will focus on how the interface is represented and how the boundary conditions between the two phases are captured. Two approaches are considered, the level-set method and the phase-field method. Both are interface-capturing methods, which means that instead of tracking the interface explicitly using a surface mesh, it is captured implicitly by an auxiliary function defined in the entire domain. This leads to a significantly simpler implementation, since Cartesian grids can be used and topological changes are handled automatically.

2.2.1 The level-set method

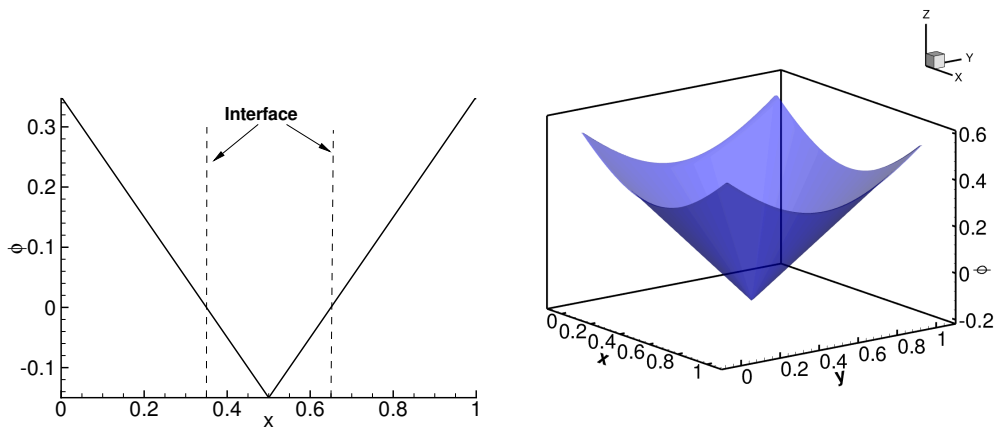

(a) 1D level-set function (b) 2D level-set function

Figure 2.4: Illustration of the level-set function representing a drop with radius 0.15.

In the level-set method (see e.g. Sussman *et al.* (1994); Osher and Fedkiw

(2003)), the interface is defined implicitly by the zero level set

$$\Gamma = \{\boldsymbol{x} | \phi(\boldsymbol{x}, t) = 0\}, \tag{2.24}$$

where ϕ is the level-set function, which denotes the signed distance to the interface. An example of how the level-set function looks for a drop is given in Figure 2.4. The level-set function moves with the interface velocity $\boldsymbol{u}_{\text{int}}$ according to

$$\frac{\partial \phi}{\partial t} + \boldsymbol{u}_{\text{int}} \cdot \nabla \phi = 0. \tag{2.25}$$

Note that this equation is a pure advection equation, and hence accurate numerical schemes must be used to solve this equation. Additionally, to discretize this equation numerically, the interface velocity must be extended off the interface. Adalsteinsson and Sethian (1999) showed that the velocity could be extrapolated orthogonally from the interface by solving

$$\frac{\partial \boldsymbol{u}}{\partial \tau} + S(\phi_0)\boldsymbol{n} \cdot \nabla \boldsymbol{u} = \boldsymbol{0}, \tag{2.26}$$

where S is a sign function given by

$$S(\phi) = \frac{\phi}{\sqrt{\phi^2 + 2\Delta x^2}}. \tag{2.27}$$

As the level-set function is advected, it will not remain an exact distance function due to numerical errors. This can be alleviated using reinitialization procedures, that attempt to keep the interface position intact while resetting the level-set function to a distance function. The standard level-set reinitialization procedure is used here, that is we solve the additional equation

$$\begin{aligned} \frac{\partial \phi}{\partial \tau} + S(\phi_0)(|\nabla \phi| - 1) &= 0, \\ \phi(\boldsymbol{x}, 0) &= \phi_0(\boldsymbol{x}). \end{aligned} \tag{2.28}$$

An attractive feature of the level-set method is the simple access to geometrical properties, in particular the normal vector and the curvature. With the level-set function as a signed distance function, the normal vector can be calculated as

$$\boldsymbol{n} = \frac{\nabla \phi}{|\nabla \phi|}, \tag{2.29}$$

and the curvature as

$$\kappa = -\nabla \cdot \left(\frac{\nabla \phi}{|\nabla \phi|} \right). \tag{2.30}$$

The density, viscosity and permittivity are discontinuous across the interface. These are handled in two different ways in this work. The simplest and most common method is the continuous surface force (CSF) method, introduced by Brackbill *et al.* (1992), where the singular surface force is smoothed across a narrow region,

$$\boldsymbol{f}_c = \gamma\kappa\nabla H_\Gamma - (\nabla_\Gamma\gamma)\delta_\Gamma. \tag{2.31}$$

where H_Γ is the regularized Heaviside function, defined as

$$H_\Gamma(\phi) = \begin{cases} 0 & \phi < -\epsilon \\ \frac{1}{2} + \frac{\phi}{2\epsilon} + \frac{1}{2\pi}\sin\left(\frac{\pi\phi}{\epsilon}\right) & |\phi| \le \epsilon \\ 1 & \phi > \epsilon. \end{cases} \tag{2.32}$$

Here, ϵ is the smearing width. In this work, the interface is smeared across three grid cells, i.e. $\epsilon = 1.5h$, where h is the grid spacing. The regularized surface delta function, δ_Γ, is defined as

$$\delta_\Gamma(\phi) = \begin{cases} 0 & |\phi| < \epsilon \\ \frac{1}{2\epsilon}\left(1 + \cos\frac{\pi\phi}{\epsilon}\right) & |\phi| \ge \epsilon. \end{cases} \tag{2.33}$$

The physical properties are also smoothed according to

$$\rho(H_\Gamma) = \rho_1 H_\Gamma + (1 - H_\Gamma)\rho_2, \tag{2.34}$$

$$\mu(H_\Gamma) = \mu_1 H_\Gamma + (1 - H_\Gamma)\mu_2, \tag{2.35}$$

$$\frac{1}{\varepsilon} = \frac{H_\Gamma}{\varepsilon_1} + \frac{1 - H_\Gamma}{\varepsilon_2}. \tag{2.36}$$

It was shown by Tomar *et al.* (2007) that using a harmonic mean for the electrical properties was beneficial over an arithmetic mean. Note that in principle, the above regularizations of the delta function and Heaviside function could be used to solve the surfactant equations from the previous section. However, this was found not to work very well, which is believed to be because these regularizations are not accurate enough. Recently, there has been a lot of work on finding more accurate representations, for instance Smereka (2006); Towers (2007); Min and Gibou (2008), which may lead to better results. In this work, only an insouble, interfacial surfactant was considered together with the level-set method, and the sharp-interface representation given by Equation (2.10) was solved directly. This is also the approach taken in Xu and Zhao (2003); Xu *et al.* (2006).

The second method of handling the discontinuities is the ghost-fluid method (GFM) (see e.g. Fedkiw (1999)). Here, instead of smearing out the discontinuities,

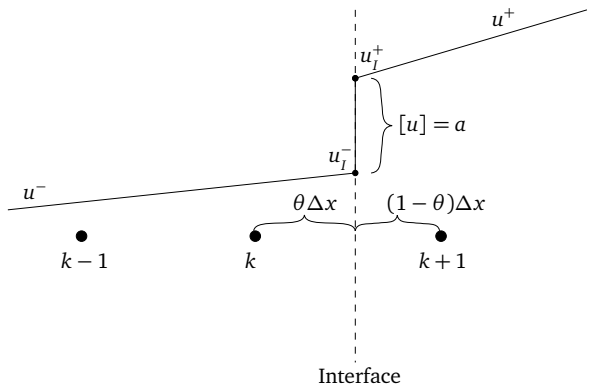

Figure 2.5: Illustration of the discretization of a discontinuous variable across an interface.

they are handled in a sharp manner by employing the interface relations. This gives a more accurate numerical method, at the expense of a more complex implementation. The basic principle of the method will be illustrated by considering the discretization of the following 1D Poisson equation:

$$\frac{\mathrm{d}u}{\mathrm{d}x}\left(\beta\frac{\mathrm{d}u}{\mathrm{d}x}\right) = f. \tag{2.37}$$

The GFM requires jump conditions, which are relations between the physical quantities on each side of the interface. In the following, the interfacial jump is denoted by $[x] = x^+ - x^-$, where superscript + denotes the side of the interface where ϕ is positive, and superscript $-$ denotes the side of the interface where ϕ is negative. For the purpose of this section, we assume that the interface conditions are given by

$$[u] = a \tag{2.38}$$

$$\left[\beta\frac{\mathrm{d}u}{\mathrm{d}x}\right] = b. \tag{2.39}$$

We also assume that β is constant in each phase. Suppose that we have the condition given in Figure 2.5, where an interface is located between k and $k+1$. The standard, second-order discretization of Equation (2.37) is

$$\frac{\beta_{k+1/2}\frac{u_{k+1}-u_k}{\Delta x} - \beta_{k-1/2}\frac{u_k-u_{k-1}}{\Delta x}}{\Delta x} = f_k. \tag{2.40}$$

This discretization gives second-order accuracy if f and u are smooth functions. But here, because of the discontinuity between points k and $k+1$, there will be

an error at the interface, which will smear the discontinuity. Instead, we would like to use the value at the interface, i.e.

$$\frac{\beta^- \frac{u_I^- - u_k}{\theta \Delta x} - \beta^- \frac{u_k - u_{k-1}}{\Delta x}}{\Delta x} = f_k. \tag{2.41}$$

Here, θ is the normalized distance to the interface,

$$\theta = \frac{x_I - x_k}{\Delta x}. \tag{2.42}$$

The main idea of the GFM is to use the jump conditions to find an approximation of the interfacial value. Discretizing the second jump condition, Equation (2.39), gives

$$\beta^+ \frac{u_{k+1} - u_I^+}{(1-\theta)\Delta x} - \beta^- \frac{u_I^- - u_k}{\theta \Delta x} = b. \tag{2.43}$$

We can now find the approximated value at the interface by using the first jump condition, Equation (2.38):

$$u_I^- = \frac{1}{\theta\beta^+ + (1-\theta)\beta^-} \left[\theta\beta^+ u_{k+1} + (1-\theta)\beta^- u_k - \theta\beta^+ a - \theta(1-\theta)\Delta x b\right]. \tag{2.44}$$

Finally, this can be inserted into Equation (2.41) to give the following symmetric discretization:

$$\frac{\hat{\beta}(u_{k+1} - u_k) - \beta^-(u_k - u_{k-1})}{\Delta x^2} = f_k + \frac{\hat{\beta} a}{\Delta x^2} + \frac{(1-\theta)\hat{\beta} b}{\beta^+ \Delta x}, \tag{2.45}$$

where $\hat{\beta}$ is defined as

$$\hat{\beta} = \frac{\beta^+ \beta^-}{\theta\beta^+ + (1-\theta)\beta^-}. \tag{2.46}$$

This method can be applied in a dimension-by-dimension fashion, so an extension to two or three dimensions is straightforward.

2.2.2 The phase-field method

The phase-field method is used in a lot of different areas. For an overview of its use in fluid mechanics, see e.g. Anderson *et al.* (1998); Jacqmin (1999). In the phase-field method, the interface is defined implicitly through a phase-field function, c, which is 1 in Ω_0, and varies rapidly but smoothly to 0 in Ω_1. More precisely, the phase-field function is taken as

$$c(\boldsymbol{x}, t) = \frac{1}{2}\left[1 - \tanh\left(\frac{r(\boldsymbol{x}, t)}{2\sqrt{2}\epsilon}\right)\right], \tag{2.47}$$

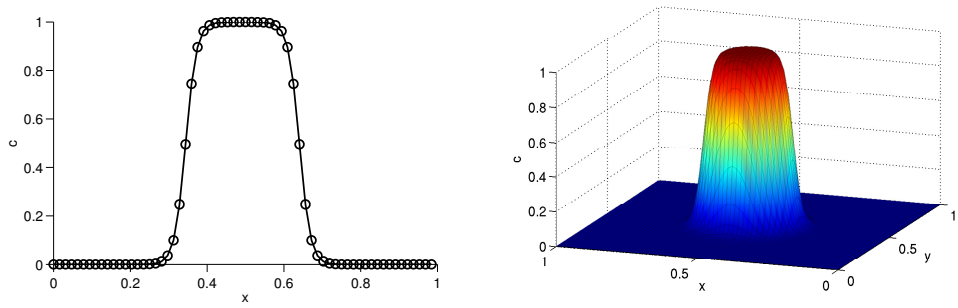

(a) 1D phase-field function (b) 2D phase-field function

Figure 2.6: Illustration of the phase-field function representing a drop.

where ϵ is a small parameter related to the interface thickness. An example of how the phase-field function looks for a drop is given in Figure 2.6. Here, the radius of the drop is 0.15, and the interface thickness parameter is 0.01. As is evident from the figure, the phase-field function can in the context of two-phase flow be interpreted as a concentration.

To advect the phase-field function, a Cahn-Hilliard equation is solved,

$$\frac{\partial c}{\partial t} + \nabla \cdot (c\boldsymbol{u}) = \nabla \cdot (M(c)\nabla \mu_c), \tag{2.48}$$

$$\mu_c = g'(c) - \epsilon^2 \nabla^2 c, \tag{2.49}$$

where $M = \sqrt{c^2(1-c)^2}$ is a mobility function and $g = c^2(1-c)^2/4$ is a double well potential. μ_c is called the chemical potential and ϵ is a small parameter related to the interface thickness. Note that the above equation system is fourth-order and non-linear, which requires specialized numerical methods to solve in an efficient manner.

Since the phase-field method uses a diffuse interface similar to the CSF method, regularizations of the surface delta function and Heaviside function are needed. In the phase-field context, several definitions of the delta function are available from the literature. In this work, the approximation from Rätz and Voigt (2006),

$$\delta_\Gamma \approx B(c) = \frac{3\sqrt{2}}{\epsilon} c^2(1-c)^2, \tag{2.50}$$

is used for the surface equation. For the surface-tension term and the boundary condition in the bulk equation, the approximation

$$\delta_\Gamma \approx |\nabla c| \tag{2.51}$$

is used. This is to avoid any scaling of the equations. In the surface equation, the constants in Equation (2.50) cancel out in the discretized equations. The regularized Heaviside function, is simply taken as

$$H(c) \approx 1 - c. \tag{2.52}$$

2.2.3 Discussion

The level-set method and the phase-field method share many similarities, in particular when the level-set method is used in conjunction with the CSF method for handling the interface discontinuities. In fact, some works exist that borrow from both methods. For instance, in Olsson and Kreiss (2005), a level-set method is designed that uses an interface profile similar to the phase-field function. Artificial compression is then used to keep the shape and width of the profile constant which leads to a conservative scheme with respect to mass conservation. In Kronbichler and Kreiss (2008), a hybrid method was studied where the level-set method was used for external flow, while the phase-field method was used to capture contact-line dynamics near solid boundaries.

One of the key advantages of the phase-field method is that no artificial compression or reinitialization is needed, these effects are already incorporated in the Cahn-Hilliard equation. Another advantage is that the phase-field method is more flexible with respect to complex physical effects. The diffuse interface in the phase-field method can be viewed as a layer that stores a mixing energy that gives rise to interfacial tension. The use of this energy formulation makes it easy to include more complex physical effects. For instance, the phase-field method was used to include viscoelasticity in Yu *et al.* (2005), contact-line dynamics in Kronbichler and Kreiss (2008) and bending energy in the context of vesicle membranes in Lowengrub *et al.* (2009). Another attractive feature of the phase-field method is that it is possible to derive thermodynamically consistent models, see e.g. Anderson *et al.* (1998); Penrose and Fife (1990). In this work, the method is used to handle the problem of coupling the bulk surfactant to the interfacial surfactant. This does not require any energy considerations, but the approach takes advantage of the phase-field method's ability to incorporate complex boundary conditions on the interface in a simple manner.

However, the complexity of the Cahn-Hilliard equation makes it difficult to handle numerically. The use of a diffuse interface layer also makes the method less accurate and robust for certain problems compared to the ghost-fluid method. In other words, both numerical approaches used in this work are useful, but their advantages and disadvantages should be taken into account when deciding which method to use for a particular problem.

3 Present contribution

> You need the willingness to fail all the time. You have to generate many ideas and then you have to work very hard only to discover that they don't work. And you keep doing that over and over until you find one that does work.
>
> John Backus (1924–2007)

> If little labour, little are our gains:
> Man's fortunes are according to his pains.
>
> Robert Herrick (1591–1674)

The main contribution of this work is six articles published in peer-reviewed journals and conferences. In this section, a brief summary of each paper is given.

Paper A – Sharp interface simulations of drop deformation in electric fields
Co-author: Svend Tollak Munkejord

In this paper, a thorough evaluation of the accuracy of the ghost-fluid method in the context of electric fields is given. The method is compared both against theoretical results and the simpler continuous surface-force method. Such an evaluation was found lacking from Hansen (2005), where the use of the ghost-fluid method for problems involving electric fields was first introduced. The paper also extends the 2D method presented in Hansen (2005) to a more physically relevant axisymmetrical geometry. Figure 3.1 demonstrates the sharp-interface behavior of the GFM and the higher accuracy compared to the CSF method.

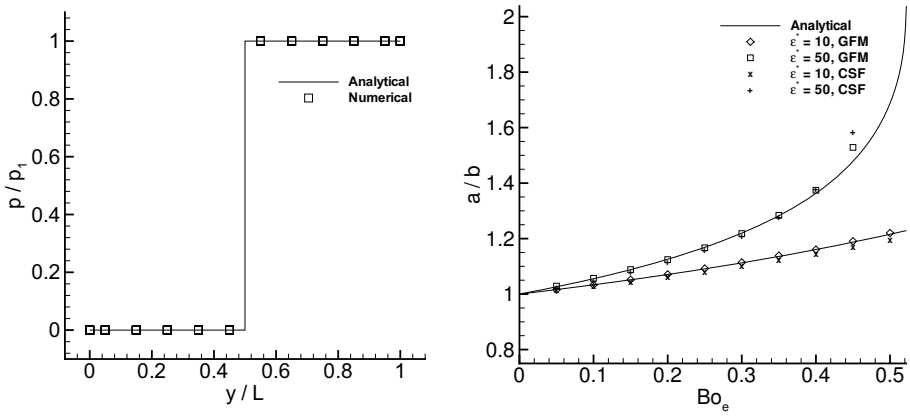

(a) Horizontal interface test case.

(b) Deformation of spherical drop test case.

Figure 3.1: (a) shows the ghost-fluid method applied to a horizontal interface test case. The pressure in the y-direction for a calculation with 10 grid points is compared to the exact solution. Note that the discontinuity in pressure is sharply resolved. (b) shows a comparison of the deformation of a drop in an electric field between theoretical values and the CSF method and the GFM. Note that the GFM is closer to the theoretical values.

Paper B – A computational study of the coalescence process between a drop and an interface in an electric field
Co-authors: Svend Tollak Munkejord and Erik Bjørklund

This paper considers the coalescence between a drop and a planar interface. When no electric field is applied, partial coalescence may occur, where a small portion of the drop does not coalesce but remain dispersed in the continuous phase. It has been shown experimentally in e.g. Allan and Mason (1962) that when an electric field is applied, this partial coalescence is suppressed. This paper investigates the problem numerically using the previously validated method. First, excellent agreement with experiments for a case without electric fields is demonstrated. Then, it is shown that the results with an applied electric field is in qualitative agreement with the experimental observations, and a physical explanation of the process is suggested. A figure from the paper demonstrating the difference with and without an electric field is shown in Figure 3.2.

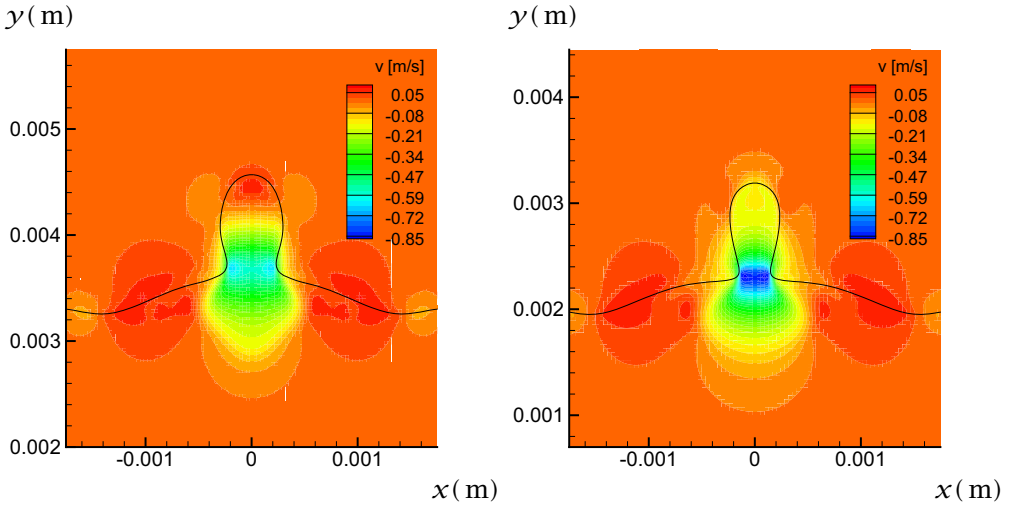

(a) No electric field (b) Applied electric field, $Bo_e = 0.1$

Figure 3.2: Comparison of the neck thickness and drainage rate with and without an electric field. The electric field gives a thicker neck and increased emptying rate, which suppresses the pinching off of a daughter drop.

Paper C – Sharp interface simulations of surfactant-covered drops in electric fields
Co-authors: Karl Ynge Lervåg and Svend Tollak Munkejord

In this paper, a model for surfactants is introduced. To the authors' knowledge, this is the first time the ghost-fluid method has been applied to the surfactant problem. The model is validated and used to study a falling drop. It is shown that the surfactant generally reduces the deformation and the terminal velocity of the drop. The reduction is most pronounced in the nearly spherical regime where the drop behavior is similar to a solid sphere due to the interface immobilization caused by the presence of a surfactant. This is shown in Figure 3.3. The electric field increases the terminal velocity by stretching the drop in the direction of the electric field which reduces the drag on the drop. This effect is largest for the surfactant-covered drop, which is deformed more due to the lower average interfacial tension.

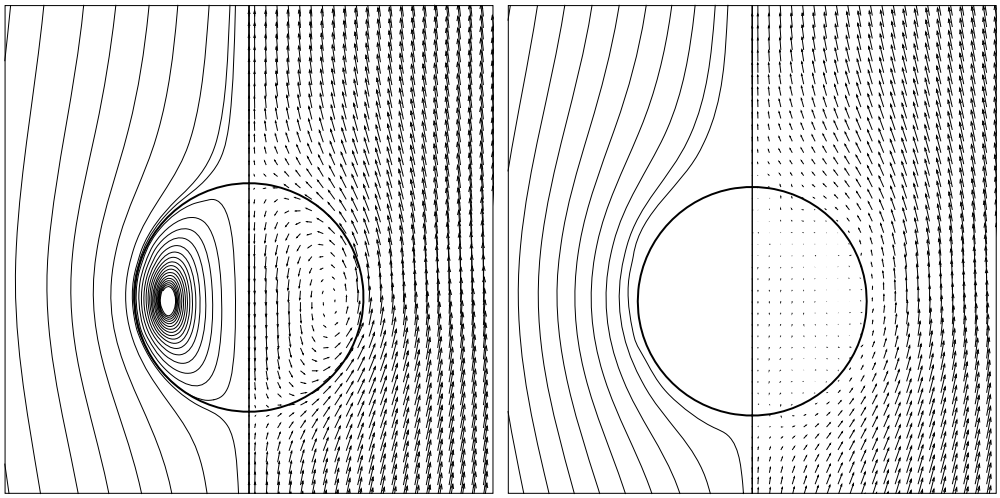

(a) Clean (b) Contaminated

Figure 3.3: Low Re drop. Streamlines and velocity vectors in a coordinate system moving with the drop centroid. Note how the internal circulation is completely stopped in the contaminated case, making the drop behave like a solid particle.

Paper D – Influence of surfactant on drop deformation in an electric field
Co-author: Svend Tollak Munkejord

This paper investigates the influence of surfactants on the deformation of a drop in an electric field. Instead of assuming a conducting drop and an insulating continuous phase, we extend the model to support a finite conductivity in both phases. This gives a much wider range of deformation behaviors and correspondingly interesting surfactant influence. The deformation can be both prolate and oblate, depending on the ratio of conductivities and permittivities. Additionally, the direction of the induced circulation can be both clockwise and counter-clockwise for the prolate shapes. It was found that for prolate deformation and counter-clockwise circulation, the presence of surfactant leads to greater deformation at low surfactant concentrations. At high surfactant concentrations and high electric capillary numbers, however, the effect of surfactant dilution becomes stronger than the effect of reduced interfacial tension at the tips, and the deformation decreases. For prolate deformation and clockwise flow, the surfactants are swept in the opposite direction, and cause a reduction in deformation. For oblate deformation, which always gives clockwise flow, the results are similar to that of prolate deformation and counter-clockwise flow, deformation is increased until dilatational effects start to dominate. However, this occurs earlier here, since the surfactant is not concentrated at the tips, but instead spread out over the equator of the drop. Finally, it was shown that for smaller viscosity ratios, the influence of surfactant is stronger, since the relative importance of the Marangoni stresses becomes higher. Figure 3.4 shows the deformation as a function of electric capillary number for various surfactant coverages at a low viscosity ratio.

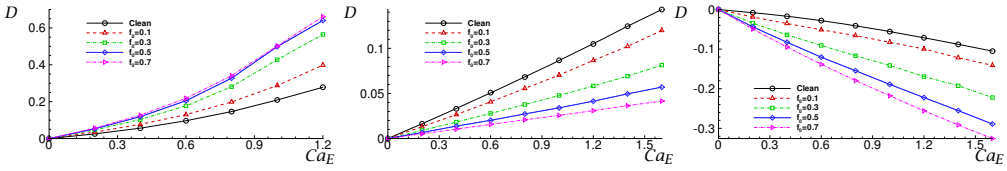

(a) Case A (b) Case B (c) Case C

Figure 3.4: Deformation as a function of electric capillary number for various surfactant coverages at viscosity ratio $\mu_r = 0.1$. Note that for case A, surfactant leads to more deformation, for case B surfactant leads to less deformation while for case C, the deformation is negative (oblate deformation instead of prolate) and surfactant leads to more deformation.

Paper E – A diffuse-interface approach for modeling transport, diffusion and adsorption/desorption of material quantities on a deformable interface

Co-authors: Xiangrong Li, John Lowengrub, Fan Wang and Axel Voigt

This paper introduces changes in both mathematical modelling and numerical methods. Instead of restricting the surfactant to the interface, we couple the interfacial surfactant concentration to a concentration in the bulk. This is a more physically realistic model. Instead of using the level-set method to capture the interface, the phase-field method is employed. These share many similarities, but the phase-field method makes it easier to handle the complexity of the coupled bulk/interface problem. The model is solved using semi-implicit time discretization and block-structured adaptive grids for the spatial discretization. The semi-implicit time discretization allows longer time steps to be taken, and the adaptive grids limit high resolution grids to regions of interest. Additionally, a non-linear multigrid method is used to solve the equation systems arising at every time step. All these improvements lead to a much more efficient numerical method, suitable for full 3D simulations. The paper introduces the numerical method, proves the convergence of the method and demonstrates the accuracy and efficiency of the method on multiple test cases. Figure 3.5 shows one of these test cases, the deformation of a 3D drop in a deformation field.

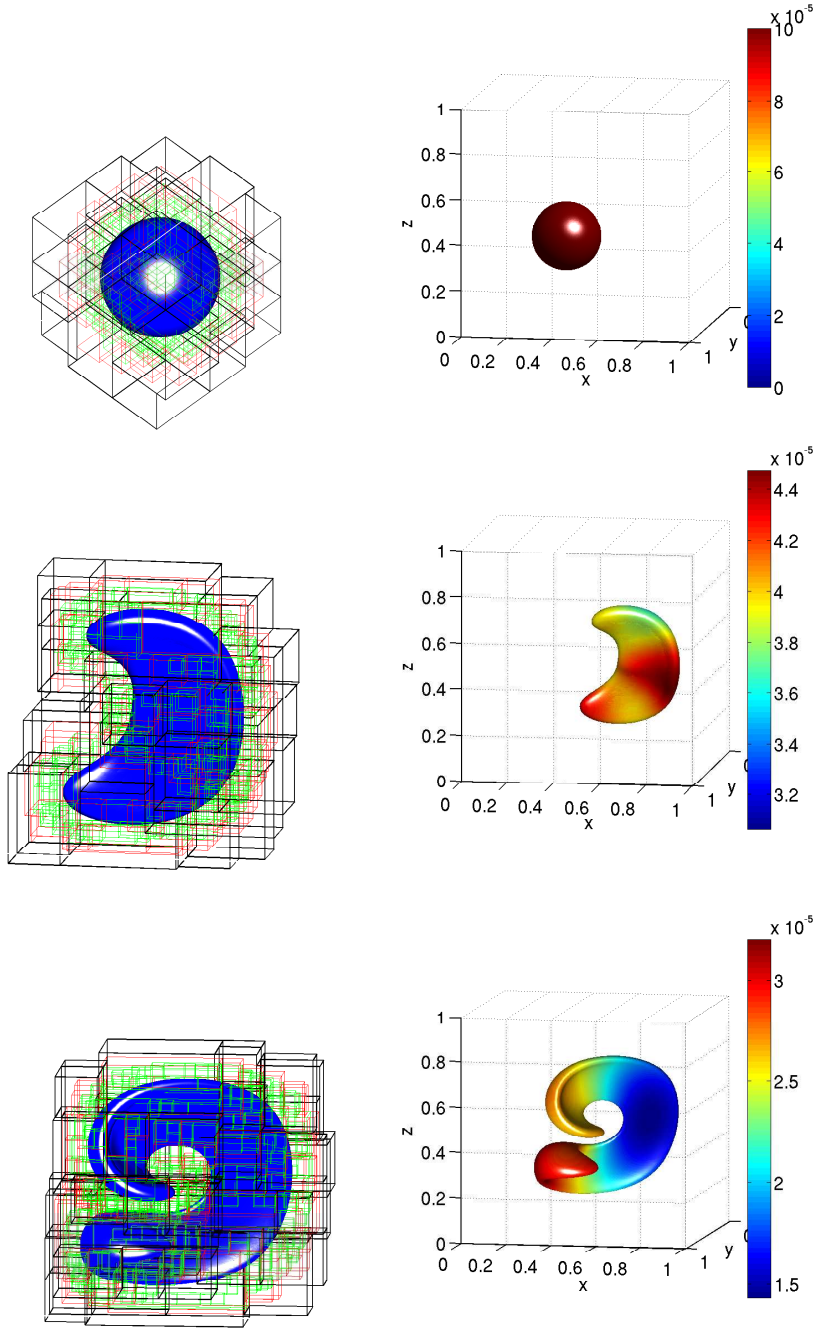

(a) Adaptive grid (b) Interfacial surfactant concentration

Figure 3.5: Sphere in 3D deformation field. Illustration of the adaptive grids and interfacial surfactant concentration. Inside the black boxes, the grid spacing is $h = 1/64$, inside the red boxes $h = 1/128$ and inside the green boxes $h = h_{\min} = 1/256$.

Paper F – A diffuse-interface method for two-phase flows with soluble surfactants

Co-authors: John Lowengrub, Peng Song and Axel Voigt

In this paper, the phase-field method introduced in the previous paper is coupled to a flow solver. The method is validated, and used to study the influence of surfactant solubility on a drop in shear flow in both 2D and 3D. It is shown that the deformation of a drop with soluble surfactant in general lies between that of a clean drop and that of a drop covered with insoluble surfactant. However, for the breakup of a drop, it is shown that for the insoluble case, the drop can break up at a earlier time compared to a clean drop, while for the soluble case, the drop can break up at a later time. Figure 3.6 shows the breakup of the drop with soluble surfactant.

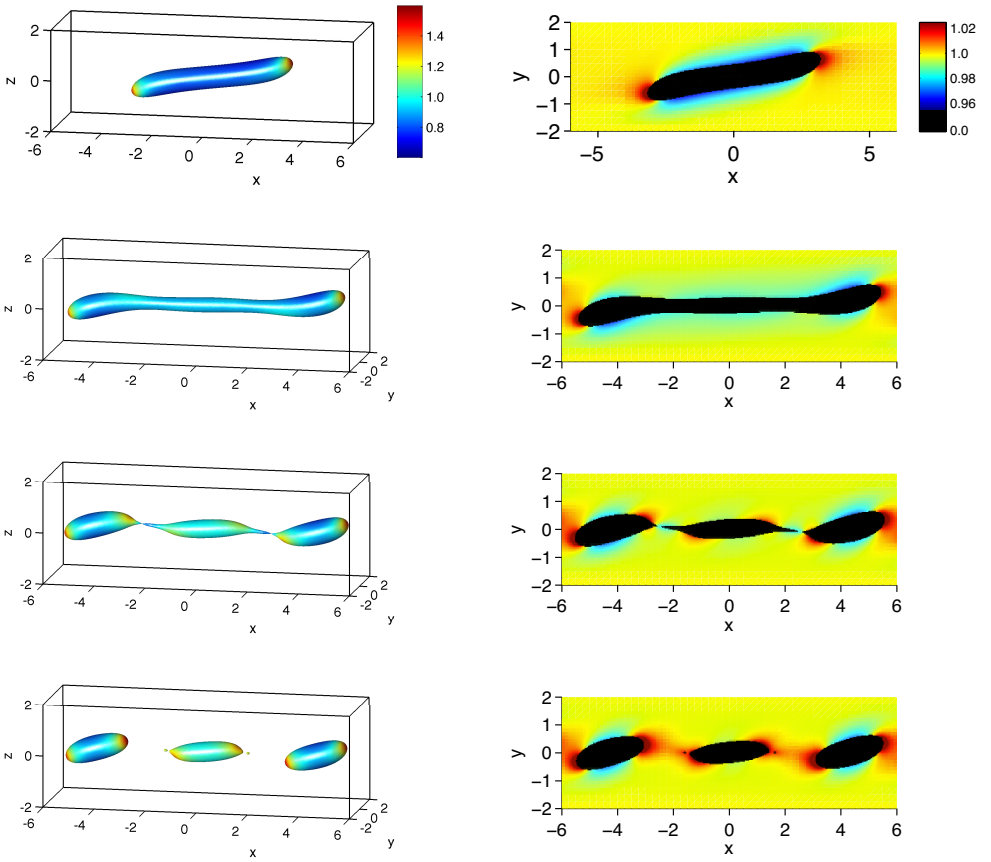

Figure 3.6: Three-dimensional simulation of a drop in shear flow with soluble surfactant. The left column shows the drop shape with the surface colored according to the interface surfactant concentration. The right column shows a slice of the bulk surfactant concentration along the x-axis.

4 Conclusions and recommendations for further work

> The more I learn, the more I learn how little I know.
>
> Socrates (469 BC–399 BC)

> The more you know, the less you understand.
>
> Laozi

In addition to the conclusions given in each separate paper, some general conclusions can be drawn. The contributions made in this work can be divided in to three parts, mathematical modelling, numerical methods and investigation of physics.

First, consider the mathematical models. The models include the full Navier–Stokes equations in each phase, with additional terms accounting for the effect of an electric field and the effect of non-uniform surface tension. Equations for the electric field and the coupled evolution of surfactant on the interface and in the bulk were also considered. Several extensions to the model are possible. In particular, for high concentrations of surfactant, an aggregate may form on the interface. This film can be expected to behave in a viscoelastic manner. Models for drops with viscoelastic membranes have been developed for the study of biological flows and could also be considered for the present problem. Another issue not discussed in this work is the presence of close-range forces when two interfaces get close together, for instance the attractive van der Waals force. In particular, steric repulsion forces may become important when aggregates form causing a physical barrier against coalescence. In general, although such forces have in some cases been considered in conjunction with interface-capturing methods, the usefulness of this could be questioned since these forces become important at length scales below what can typically be resolved with the current numerical methods. This suggests a study at a lower level than the interface tracking/capturing level, perhaps using molecular dynamics methods.

Next, consider the numerical methods. This work has investigated the use of interface-capturing methods for multiphysics problems. Both the level-set method and the phase-field method were used, and both were found capable of handling the complex mathematical models considered. Although not tested explicitly in this work, it is expected that the accuracy of the phase-field method

performs relatively similar to the CSF level-set method. As shown in papers A and C, the GFM is more accurate than the CSF method. This comes at the expense of a more complex implementation. In particular, implementing a semi-implicit solver for the GFM, as was done with the phase-field method, would be very difficult. It could be interesting to investigate a compromise where the simpler terms are treated using GFM and the more complex with CSF. The advantage of a semi-implicit scheme is the removal of a particularly stringent restriction on the time step where the time step is inversely proportional to the square of the grid spacing. This restriction makes accurate simulations of small, viscous drops very time consuming. Another issue is the need for very high resolution during a coalescence or breakup event. The block-structured, adaptive grid used here with the phase-field method helps alleviate this problem. In particular, it was shown that full 3D simulations were feasible using this method. However, only a serial implementation was developed for this work. A parallelization of the code would allow the study of more complex arrangements of drops.

Finally, consider the investigation of physics. It was shown how an electric field can suppress the partial coalescence phenomenon occurring when a drop coalesces with an interface. Next, it was demonstrated that the presence of a surfactant can considerably slow down a sedimenting drop due to inhibition of internal circulation. Conversely, an electric field speeds up the sedimentation due to stretching which leads to reduced drag. Next, the deformation of a surfactant-covered leaky dielectric drop was studied. This is not immediately useful with respect to a water-in-oil emulsion, since the conductivity of water is always several orders of magnitude higher than crude oil, but is interesting for other applications. It was shown that the presence of surfactant could lead to both more deformation and less deformation depending on the fluid properties due to the complex interaction between the electric field and the surfactant. Finally, the deformation of a drop in shear flow was studied, with particular emphasis on the influence of a soluble surfactant. It was shown that the deformation of a drop with soluble surfactant in general lies between that of a clean drop and that of a drop covered with insoluble surfactant. However, for the breakup of a drop, it was shown that for the insoluble case, the drop can break up at a earlier time compared to a clean drop, while for the soluble case, the drop can break up at a later time. In general, the usefulness of the presented methods for studying drop dynamics in great detail was demonstrated. Opportunities for future work are plentiful. Only a small parameter set was considered in this work, so more in-depth studies of the same setups would be interesting. Further, simulations of drops colliding in external flows would be particularly elucidating. This would be an important step

towards developing models higher up in the multiscale modelling hierarchy. There has been a lot of work in the literature on drop collisions in compressional flows and shear flows. However, little work has been done for an applied electric field, so this would be a natural starting point for further investigations.

Bibliography

Adalsteinsson, D. and Sethian, J. A. The fast construction of extension velocities in level set methods. *J. Comput. Phys.*, volume 148: pages 2–22, 1999.

Allain, J.-M. and Amar, M. B. Biphasic vesicle: Instability induced by adsorption of proteins. *Physica A*, volume 337: pages 531–545, 2008.

Allan, R. S. and Mason, S. G. Particle behavior in shear and electric fields. I. Deformation and burst of fluid drops. *Proc. R. Soc. A*, volume 267: pages 45–61, 1962.

Anderson, D. M., McFadden, G. B. and Wheeler, A. A. Diffuse-interface methods in fluid mechanics. *Ann. Rev. Fluid Mech.*, volume 30, no. 1: pages 139–165, 1998.

Bjørklund, E. The level-set method applied to droplet dynamics in the presence of an electric field. *Comput. Fluids*, volume 38, no. 2: pages 358 – 369, 2009.

Brackbill, J. U., Kothe, D. B. and Zemach, C. A continuum method for modeling surface tension. *J. Comput. Phys.*, volume 100: pages 335–354, 1992.

Chiesa, M. Electrocoalescence modeling: an engineering approach. In: *Proceedings of the 15th Australasian Fluid Mechanics Conference*. 2004.

Cristini, V. and Tan, Y. Theory and numerical simulation of droplet dynamics in complex flows-a review. *Lab Chip*, volume 4: pages 257–264, 2004.

Eilks, C. and Elliott, C. Numerical simulation of dealloying by surface dissolution by the evolving surface finite element method. *J. Comput. Phys.*, volume 227: pages 9727–9741, 2008.

Erlebacher, J., Aziz, M., Karma, A., Dimitrov, N. and Sieradzki, K. Evolution of nanoporosity in dealloying. *Nature*, volume 410: pages 450–453, 2001.

Fedkiw, R. P. A non-oscillatory Eulerian approach to interfaces in multimaterial flows. *J. Comput. Phys.*, volume 152: pages 457–492, 1999.

Fried, E. and Gurtin, M. A unified treatment of evolving interfaces accounting for small deformations and atomic transport with emphasis on grain-boundaries and epitaxy. *Adv. Appl. Mech.*, volume 40: pages 1–177, 2004.

Gomez-Marin, A., Garcia-Ojalvo, J. and Sancho, J. Self-sustained spatiotemporal oscillations induced by membrane-bulk coupling. *Phys. Rev. Lett.*, volume 98: page 168303, 2007.

Ha, J. and Yang, S. Effect of nonionic surfactant on the deformation and breakup of a drop in an electric field. *J. Colloid and Interface Sci.*, volume 206, no. 1: pages 195 – 204, 1998.

Hameed, M., Siegel, M., Young, Y.-N., Li, J., Booty, M. R. and Papageorgiou, D. T. Influence of insoluble surfactant on the deformation and breakup of a bubble or thread in a viscous fluid. *J. of Fluid Mech.*, volume 594: pages 307–340, 2008.

Hansen, E. B. *Numerical simulation of droplet dynamics in the presence of an electric field*. Ph.D. thesis, NTNU, 2005.

Hirsa, A. and Willmarth, W. W. Measurements of vortex pair interaction with a clean or contaminated free surface. *J. Fluid Mech.*, volume 259: pages 25–45, 1994.

Hu, Y. T., Pine, D. J. and Leal, L. G. Drop deformation, breakup, and coalescence with compatibilizer. *Phys. Fluids*, volume 12: pages 484–489, 2000.

Hudson, S. D., Jamieson, A. M. and Burkhart, B. E. The effect of surfactant on the efficiency of shear-induced drop coalescence. *J. Colloid and Interface Sci.*, volume 265: pages 409 – 421, 2003.

Jacqmin, D. Calculation of two-phase Navier-Stokes flows using phase-field modeling. *J. Comput. Phys.*, volume 155: pages 96–127, 1999.

Kang, M., Fedkiw, R. and Liu, X. A boundary condition capturing method for multiphase incompressible flow. *J. Sci. Comput.*, volume 15: pages 323–360, 2000.

Klingenberg, D. J., van Swol, F. and Zukoski, C. F. The small shear rate response of electrorheological suspensions. i. simulation in the point–dipole limit. *J. Chem. Phys.*, volume 94, no. 9: pages 6160–6169, 1991.

Kockelkoren, J., Levine, H. and Rappel, W.-J. Computational approach for modeling intra- and extracellular dynamics. *Phys. Rev. E*, volume 68, no. 3: page 037702, Sep 2003.

Kronbichler, M. and Kreiss, G. A hybrid level-set-Cahn-Hilliard model for two-phase flow. In: *Proceedings of the 1st European Conference on Microfluidics*. 2008.

Laohalertdecha, S., Naphon, P. and Wongwises, S. A review of electrohydrodynamic enhancement of heat transfer. *Renew. Sustain. Energy Rev.*, volume 11, no. 5: pages 858 – 876, 2007.

Leal, L. G. Flow induced coalescence of drops in a viscous fluid. *Phys. of Fluids*, volume 16, no. 6: pages 1833–1851, 2004.

Lervåg, K. Y. *Simulation of two-phase flows with varying surface tension*. Master's thesis, NTNU, 2008.

Levine, H. and Rappel, W.-J. Membrane-bound turing patterns. *Phys. Rev. E*, volume 72, no. 6: page 061912, Dec 2005.

Li, B., Lowengrub, J., Rätz, A. and Voigt, A. Geometric evolution laws for thin crystalline films: Modeling and numerics. *Commun. Comput. Phys.*, volume 6: pages 433–482, 2009a.

Li, X., Lowengrub, J., Rätz, A. and Voigt, A. Solving PDEs in complex geometries: A diffuse domain approach. *Comm. Math. Sci.*, volume 7: pages 81–107, 2009b.

Link, D. R., Grasland-Mongrain, E., Duri, A., Sarrazin, F., Cheng, Z., Cristobal, G., Marquez, M. and Weitz, D. A. Electric control of droplets in microfluidic devices. *Angew. Chem., Int. Ed. Engl.*, volume 45, no. 16: pages 2556–2560, 2006.

Lowengrub, J. S., Rätz, A. and Voigt, A. Phase-field modeling of the dynamics of multicomponent vesicles: Spinodal decomposition, coarsening, budding, and fission. *Phys. Rev. E*, volume 79, no. 3: page 031926, Mar 2009.

Matar, O. K. and Troian, S. M. The development of transient fingering patterns during the spreading of surfactant coated films. *Phys. Fluids*, volume 11: pages 3232–3246, 1999.

Melheim, J. A. *Computer simulation of turbulent electrocoalescence*. Ph.D. thesis, Norwegian University of Science and Technology, Trondheim, 2007.

Min, C. and Gibou, F. Robust second-order accurate discretizations of the multi-dimensional Heaviside and Dirac delta functions. *J. Comput. Phys.*, volume 227: pages 9686–9695, 2008.

Nitschke, M. and Costa, S. Biosurfactants in food industry. *Trends in Food Sci. and Technol.*, volume 18, no. 5: pages 252 – 259, 2007.

Olsson, E. and Kreiss, G. A conservative level set method for two phase flow. *J. Comput. Phys.*, volume 210, no. 1: pages 225–246, 2005.

Osher, S. and Fedkiw, R. *Level set methods and dynamic implicit surfaces*. Springer, 2003.

Penrose, O. and Fife, P. C. Thermodynamically consistent models of phase-field type for the kinetic of phase transitions. *Physica D: Nonlinear Phenomena*, volume 43, no. 1: pages 44 – 62, 1990.

Rätz, A. and Voigt, A. PDEs on surfaces—a diffuse interface approach. *Commun. Math. Sci.*, volume 4: pages 575–590, 2006.

Shin, D.-Y.-Y., Grassia, P. and Derby, B. Numerical and experimental comparisons of mass transport rate in a piezoelectric drop-on-demand inkjet print head. *Int. J. Mech. Sci.*, volume 46, no. 2: pages 181 – 199, 2004.

Singh, P. and Cameotra, S. S. Potential applications of microbial surfactants in biomedical sciences. *Trends in Biotechnology*, volume 22, no. 3: pages 142 – 146, 2004.

Smereka, P. The numerical approximation of a delta function with application to level set methods. *J. Comput. Phys.*, volume 211: pages 77–90, 2006.

Stocker, C. and Voigt, A. A level set approach to anisotropic surface evolution with free adatoms. *SIAM J. Appl. Math*, volume 69: pages 64–80, 2008.

Sussman, M., Smereka, P. and Osher, S. A level set approach for computing solutions to incompressible two-phase flow. *J. Comput. Phys.*, volume 114: pages 146–159, 1994.

Teigen, K. E., Lervåg, K. Y. and Munkejord, S. T. Sharp interface simulations of surfactant-covered drops in electric fields. In: *Proceedings of Fifth European Conference on Computational Fluid Dynamics*. 2010a.

Teigen, K. E., Li, X., Lowengrub, J., Wang, F. and Voigt, A. A diffuse-interface approach for modelling transport, diffusion and adsorption/desorption of material quantities on a deformable interface. *Comm. Math. Sci*, volume 7: pages 1009–1037, 2009.

Teigen, K. E. and Munkejord, S. T. Sharp interface simulations of drop deformation in electric fields. *IEEE Trans. on Diel. and Elect. Ins.*, volume 16: pages 475–482, 2009.

Teigen, K. E. and Munkejord, S. T. Influence of surfactant on drop deformation in an electric field. *Phys. Fluids*, 2010. Submitted.

Teigen, K. E., Munkejord, S. T. and Bjørklund, E. A computational study of the coalescence process between a drop and an interface in an electric field. In: *Proceedings of 6th International Conference on CFD in the Oil & Gas, Metallurgical and Process Industries*. 2008.

Teigen, K. E., Song, P., Lowengrub, J. and A.Voigt. A diffuse-interface method for two-phase flows with soluble surfactants. *J. Comput. Phys.*, 2010b. Submitted.

Tomar, G., Gerlach, D., Biswas, G., Alleborn, N., Sharma, A., Durst, F., Welch, S. W. J. and Delgado, A. Two-phase electrohydrodynamic simulations using a volume-of-fluid approach. *J. Comput. Phys.*, volume 227: pages 1267–1285, 2007.

Towers, J. D. Two methods for discretizing a delta function supported on a level set. *J. Comput. Phys*, volume 220: pages 915–931, 2007.

Troian, S. M., Herbolzheimer, E. and Safran, S. A. Model for the fingering instability of spreading surfactant drops. *Phys. Rev. Lett.*, volume 65: pages 333–336, Jul 1990.

Tryggvason, G., Abdollahi-Alibeik, J., Willmarth, W. W. and Hirsa, A. Collision of a vortex pair with a contaminated free surface. *Phys. Fluids A*, volume 4: pages 1215–1229, 1992.

Xu, J. J., Li, Z., Lowengrub, J. and Zhao, H. A level set method for interfacial flows with surfactant. *J. Comput. Phys*, volume 212: pages 590–616, 2006.

Xu, J. J. and Zhao, H. An Eulerian formulation for solving partial differential equations along a moving interface. *J. Sci. Comp.*, volume 19: pages 573–594, 2003.

Yang, Y. M. and Maa, J. R. Bubble coalescence in dilute surfactant solutions. *J. Colloid and Interface Sci.*, volume 98: pages 120–125, 1984.

Yu, J.-D., Sakai, S. and Sethian, J. A coupled quadrilateral grid level set projection method applied to ink jet simulation. *J. Comput Phys.*, volume 206, no. 1: pages 227 – 251, 2005.

A Sharp interface simulations of drop deformation in electric fields

Teigen, K.E, Munkejord, S.T.,
IEEE Transactions on Dielectrics and Electrical Insulation. Volume 16, Number 2 (2009), 475-482

Sharp-interface simulations of drop deformation in electric fields

Knut Erik Teigen
Norwegian University of Science and Technology (NTNU)
Department of Energy and Process Engineering
Kolbjørn Hejes v 1B, NO-7491 Trondheim, Norway

and **Svend Tollak Munkejord**
SINTEF Energy Research
Energy Processes
NO-7465 Trondheim, Norway

ABSTRACT

This paper describes numerical simulations of two-phase electrohydrodynamics using a sharp-interface method. Simulations are performed on typical test cases from the literature, and the results are compared to methods that use a smeared interface. The results show that the sharp-interface method gives significant improvements in accuracy.

Index Terms — **Numerical analysis, electrohydraulics, dielectric materials, finite difference methods, hydrodynamics, interface phenomena.**

1 INTRODUCTION

ELECTROHYDRODYNAMIC flows are in general very complex due to the interactions between electric forces and flow dynamics, and analytical results are limited to simplified setups. The addition of more than one phase to the system further complicates the analysis. This inherent complexity encourages the use of numerical methods to gain additional insight into the physical phenomena.

Early numerical simulations of electrohydrodynamics typically assume either Stokes flow or inviscid flow, which makes it possible to formulate the problem using integral equations. These equations can then be efficiently solved using the boundary-element method (BEM). In [1], the deformation of a drop was studied using this approach, and in [2], the interaction between drop pairs was investigated.

In [3] and [4], a finite-element method which allowed a solution at finite Reynolds numbers was employed to study drop deformation in electric fields. It concluded that while the creeping-flow assumption was valid for low drop deformations, it was not able to predict phenomena occurring for higher deformations.

The methods mentioned so far do not take into account topological changes, e.g. the merging and breakup of drops. Recently, numerical methods have been developed that allow such topological changes. In the seminal paper [5], a front-tracking method was presented that uses a set of connected marker points to represent the interface. The handling of topological changes is fairly complex. First, a search has to be made among the front elements to identify situations where a topology change is needed. Then, the elements have to be updated to account for the change. Additionally, when the interface is stretched, restructuring of the interface is necessary to maintain sufficient accuracy. This is a complicated process, especially in three dimensions. The jumps in physical properties across the interface is handled using smoothing. In [6], the front-tracking method was extended to account for electric fields, and the distribution of drops in a channel was investigated. This study, however, did not take the merging of colliding drops into account.

In [7], the Lattice-Boltzmann method (LBM) was used to study drop deformation in electric fields. The most attractive feature of the LBM for multiphase flow is that no explicit treatment of the interface is needed. Briefly, the main idea of the LBM is to model the flow on a mesoscopic scale. A particle distribution function is introduced whose evolution is governed by the collisions and propagation of the particles moving on a lattice. In order to simulate multiphase flows, a particle interaction force is introduced between the two components, which mimics the effect of a repulsive force.

However, the resulting interface is diffusive, i.e. it is a transitional region where the jumps in physical properties

Manuscript received on 28 May 2008, in final form 18 December 2008.

across the interface are smeared out. Unfortunately, in [7], the accuracy of this approach was not evaluated directly, but some discrepancies in the induced flow field compared to theory for a drop in an electric field were found, and these were attributed to the use of a diffuse interface.

A third method that has recently been used for simulating electrohydrodynamic flows is the coupled level-set and volume-of-fluid (CLSVOF) method [8]. In the level-set method [9, 10], the surface is described via an implicit function defined as the signed distance to the interface. This allows automatic handling of topological changes, along with simple calculation of normal vectors and curvature. A disadvantage with the method is that it does not inherently conserve mass. The VOF method uses a volume-fraction function to describe the interface. This approach ensures good mass conservation, but it is complicated to calculate the curvature accurately. In addition, the position of the interface is not known exactly, but is constructed using splines. The CLSVOF method combines the advantages of the two methods, and eliminates some of the disadvantages. The method was used in [11] to investigate electrohydrodynamic effects on film boiling in perfect dielectrics and in [12], the method was used on the leaky dielectric model and some accuracy tests were performed. In both papers, the continuous-surface-force (CSF) approach was used to handle surface-tension forces and electric forces. In this approach, a Heaviside function is used to smear the properties in a region around the interface. In [12], it was shown that by using a modified approach to the smearing of electrical properties, the accuracy was improved considerably.

The method used in the present work was proposed in [13, 14]. It also uses the level-set method to capture the interface, but instead of using a Heaviside function to treat the discontinuities, the ghost-fluid method (GFM) [15,16] is used. The ghost-fluid method modifies the numerical stencils near the interface to directly take the discontinuities into account. This gives improved accuracy in the computation of surface forces. The high accuracy also significantly reduces the errors in mass conservation.

In [14], the ability of the method to simulate drop oscillations, drop breakup, and drop-drop coalescence due to electric fields were presented. However, no test cases were performed that quantitatively measured the accuracy of the method. This work attempts to give a thorough evaluation of the method, comparing it to the test cases used in [12] and also to theoretical results for drop deformation. The discussion is limited to perfect dielectric fluids. It is possible to employ the method on the leaky-dielectric model as well, but that is more complex due to jumps in tangential stresses across the interface, and hence beyond the scope of this work.

2 GOVERNING EQUATIONS AND NUMERICAL METHODS

The numerical method used for the calculations is described in detail in [13, 14], and will only be briefly reviewed here. The full Navier-Stokes equations are solved in each phase, and the interface between the two phases is captured using the level-set method. The ghost-fluid method is used to treat discontinuities across the interface in a sharp manner. To account for electric forces, a Poisson equation is solved for the electric potential, which is then used to calculate the jump in the Maxwell stress tensor across the interface.

2.1 FLOW EQUATIONS

The flow is governed by the incompressible Navier-Stokes equations, with additional terms accounting for surface-tension forces and electric forces:

$$\rho\left(\frac{\partial \mathbf{u}}{\partial t}+(\mathbf{u}\cdot\nabla)\mathbf{u}\right)=-\nabla p+\nabla\cdot[\mu(\nabla\mathbf{u}+\nabla\mathbf{u}^T)] +\mathbf{F}+\nabla\cdot\boldsymbol{M}, \qquad \nabla\cdot\mathbf{u}=0. \tag{2.1}$$

Here, ρ is the density, $\mathbf{u}$ is the velocity vector, p is the pressure, μ is the viscosity, $\mathbf{F}$ is the surface-tension force and $\boldsymbol{M}$ is the Maxwell stress tensor.

The surface tension force, due to the presence of an interface, Γ, can be expressed by

$$\mathbf{F}(\mathbf{x},t)=\int_{\Gamma(t)}\mathbf{f}(s,t)\delta(\mathbf{x}-\mathbf{X}(s,t))\boldsymbol{d}s, \tag{2.2}$$

where s is the arc-length, $\mathbf{X}(s,t)$ is the parameterization of the interface, $\mathbf{x}$ is the spatial position and δ is the Dirac delta function. $\mathbf{f}$ is given by

$$\mathbf{f}=\sigma\kappa\mathbf{n}. \tag{2.3}$$

Here, σ denotes the surface-tension coefficient, κ is the curvature of the interface, and $\mathbf{n}$ is the unit normal vector.

In this work, all equations are solved in an axisymmetric geometry, so that the divergence operator and Laplacian operator become

$$\nabla\cdot\mathbf{f}=\frac{\partial f_x}{\partial x}+\frac{\partial f_y}{\partial y}+\frac{f_x}{x} \tag{2.4}$$

and

$$\nabla\cdot(\nabla\mathbf{f})=\frac{\partial^2\mathbf{f}}{\partial x^2}+\frac{\partial^2\mathbf{f}}{\partial y^2}+\frac{1}{x}\frac{\partial\mathbf{f}}{\partial x}, \tag{2.5}$$

respectively. Note that the subscripts indicate the vector component, and not the partial derivative of the vector. In addition to the above Laplace operator, one has to add $-f_x/x^2$ to the viscous term in the x-momentum equation.

2.2 ELECTRIC FORCES

We assume perfect dielectric materials with no free charges. With these assumptions, the electric potential, Ψ, can be calculated from the following Laplace equation:

$$\nabla\cdot(\varepsilon\varepsilon_0\nabla\Psi)=0, \tag{2.6}$$

where $\varepsilon_0=8.8542$ pF/m is the vacuum permittivity and ε is

the relative permittivity of the fluid. The electric field can then be calculated as

$$\mathbf{E} = -\nabla\Psi, \tag{2.7}$$

and the Maxwell stress tensor as

$$\boldsymbol{M} = \varepsilon\varepsilon_0\left(\mathbf{E}\mathbf{E} - \frac{1}{2}(\mathbf{E}\cdot\mathbf{E})\boldsymbol{I}\right). \tag{2.8}$$

Here, $\boldsymbol{I}$ is the identity tensor. With the above assumptions, $\boldsymbol{M} = \boldsymbol{0}$ everywhere except at the interface.

2.3 INTERFACE CAPTURING

The interface is captured using the level-set method [9,10]. This method allows accurate computation of the evolution of an interface, along with automatic handling of topological changes. The ghost-fluid method [15, 16] is used to take discontinuities across the interface into account. This method handles the jumps in physical properties directly in the numerical stencils, without the need for any smearing of properties.

The interface is defined by the zero level set

$$\Gamma = \{\mathbf{x} \mid \phi(\mathbf{x}, t) = 0\}, \tag{2.9}$$

and is evolved by

$$\frac{\partial\phi}{\partial t} + \mathbf{u}_\Gamma\cdot\nabla\phi = 0. \tag{2.10}$$

Here, ϕ denotes the signed distance to the interface. $\mathbf{u}_\Gamma$ is the velocity on the interface. This velocity is not readily available, but in [17] it was shown that this velocity could be obtained by extrapolating the velocity orthogonally from the interface. This is achieved by solving

$$\frac{\partial\mathbf{u}}{\partial\tau} + S(\phi_0)\mathbf{n}\cdot\nabla\mathbf{u} = 0, \tag{2.11}$$

where τ is a pseudo-time and S is a sign function. Here,

$$S(\phi) = \frac{\phi}{\sqrt{\phi^2 + 2\Delta x^2}} \tag{2.12}$$

is used. Note that equation (2.11) is hyperbolic, so it is not necessary to solve it to steady state, since only the information a few grid points away from the interface is relevant to the evolution of the interface.

The standard level-set reinitialization procedure presented in [9] is used to keep the level-set function as a signed distance function throughout the computation. This is accomplished by solving

$$\begin{aligned} &\frac{\partial\phi}{\partial\tau} + S(\phi_0)(|\nabla\phi| - 1) = 0 \\ &\phi(\mathbf{x}, 0) = \phi_0(\mathbf{x}). \end{aligned} \tag{2.13}$$

Reinitialization is performed every second time step.

One of the advantages with the level-set method is the easy calculation of normal vectors and curvatures. The unit normal vector can be found as

$$\mathbf{n} = \frac{\nabla\phi}{|\nabla\phi|}, \tag{2.14}$$

and the curvature as

$$\kappa = -\nabla\cdot\mathbf{n}. \tag{2.15}$$

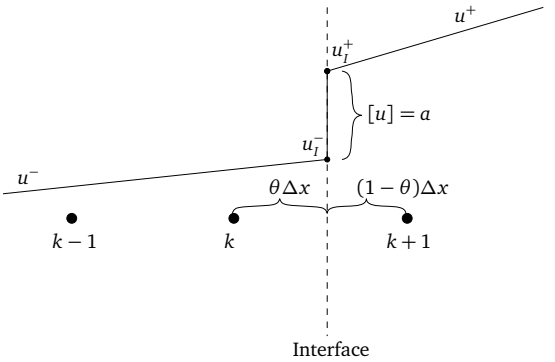

Figure 1. Illustration of the discretization of a discontinuous variable across an interface.

The ghost-fluid method will be illustrated here by considering the discretization of the following 1D Poisson equation:

$$\frac{du}{dx}\left(\beta\frac{du}{dx}\right) = f. \tag{2.16}$$

The ghost-fluid method requires jump conditions, which are relations between the physical quantities on each side of the interface. In the following, the interfacial jump is denoted by $[x] = x^+ - x^-$, where x^+ is the interfacial value on the side of the interface where ϕ is positive, and x^- is on the other side. For the purpose of this section, we assume that the interface conditions are given by

$$[u] = a \tag{2.17}$$

and

$$\left[\beta\frac{du}{dx}\right] = b. \tag{2.18}$$

Suppose that we have the condition given in Figure 1, where an interface is located between k and $k+1$. Instead of using the standard, second-order discretization

$$\frac{\beta_{k+1/2}\dfrac{u_{k+1} - u_k}{\Delta x} - \beta_{k-1/2}\dfrac{u_k - u_{k-1}}{\Delta x}}{\Delta x} = f_k \tag{2.19}$$

we would like to use the value at the interface,

$$\frac{\hat{\beta}\dfrac{u_I^- - u_k}{\theta\Delta x} - \beta_{k-1/2}\dfrac{u_k - u_{k-1}}{\Delta x}}{\Delta x} = f_k \tag{2.20}$$

where θ is the normalized distance to the interface,

$$\theta = \frac{x_I - x_k}{\Delta x} \tag{2.21}$$

An approximation of the interfacial value can be found by using the jump conditions. Discretizing equation (2.18) gives

$$\beta^+\frac{u_{k+1} - u_I^+}{(1-\theta)\Delta x} - \beta^-\frac{u_{k+1} - u_I^-}{\theta\Delta x} = b. \tag{2.22}$$

We can now find the approximated value at the interface by using equation (2.17):

$$u_I^- = \frac{1}{\theta\beta^+ + (1-\theta)\beta^-}[\theta\beta^+ u_{k+1} + (1-\theta)\beta^- u_k - \theta\beta^+ a - \theta(1-\theta)\Delta x b]. \quad (2.23)$$

Finally, this can be inserted into (2.20) to give the following symmetric discretization:

$$\frac{\hat{\beta}(u_{k+1} - u_k) - \beta^-(u_k - u_{k-1})}{\Delta x^2} = f_k + \frac{\hat{\beta}a}{\Delta x^2} + \frac{(1-\theta)\hat{\beta}b}{\beta^+ \Delta x} \quad (2.24)$$

where $\hat{\beta}$ denotes the extrapolated value of the coefficient,

$$\hat{\beta} = \frac{\beta^+\beta^-}{\theta\beta^+ + (1-\theta)\beta^-}. \quad (2.25)$$

This method can be applied in a dimension-by-dimension fashion, so an extension to two and three dimensions is trivial.

The jump conditions for viscous, incompressible flow is given in [16] and for dielectric fluids in [13]. The jump in pressure is

$$[p] = 2[\mu]\mathbf{n}\cdot\nabla\mathbf{u}\cdot\mathbf{n} + \mathbf{n}\cdot[\boldsymbol{M}]\cdot\mathbf{n} + \sigma\kappa\mathbf{n}\cdot\mathbf{n}. \quad (2.26)$$

The jumps in velocities are

$$[\mathbf{u}] = 0,$$
$$[\mu\nabla\mathbf{u}] = [\mu]\mathbf{n}\cdot\nabla(\mathbf{u}\cdot\mathbf{n})\mathbf{n}\mathbf{n} + [\mu]\mathbf{t}\cdot\nabla(\mathbf{u}\cdot\mathbf{n})\mathbf{n}\mathbf{t} - [\mu]\mathbf{t}\cdot\nabla(\mathbf{u}\cdot\mathbf{n})\mathbf{t}\mathbf{n} + [\mu]\mathbf{t}\cdot\nabla(\mathbf{u}\cdot\mathbf{t})\mathbf{t}\mathbf{t}. \quad (2.27)$$

For the electric potential, the jump conditions for perfect dielectrics are

$$[\Psi] = 0,$$
$$[\varepsilon\varepsilon_0\nabla\Psi\cdot\mathbf{n}] = 0. \quad (2.28)$$

2.4 NUMERICS

A second-order projection scheme is used to solve the Navier-Stokes equations. First, a temporary vector field, $\mathbf{a}$, is calculated:

$$\mathbf{a} = -(\mathbf{u}\cdot\nabla)\mathbf{u} + \nabla\cdot[\mu(\nabla\mathbf{u} + \nabla\mathbf{u}^T)]. \quad (2.29)$$

Then the pressure is found by solving

$$\nabla\cdot\left(\frac{\nabla p}{\rho}\right) = \nabla\cdot\mathbf{a}. \quad (2.30)$$

Finally, the velocity field is calculated with

$$\frac{\partial\mathbf{u}}{\partial t} = \mathbf{a} - \frac{\nabla p}{\rho}. \quad (2.31)$$

The evolution in time for the Navier-Stokes equations, the level-set equation and the velocity extrapolation is performed using a four-step, third-order, strong stability preserving (SSP) Runge-Kutta (RK) method (see e.g. [18]), while a four-step, second order SSP RK method is employed for the reinitialization of the level-set equation. The equations are spatially discretized on a staggered grid, with scalar values stored in cell centers and vector values stored at cell boundaries. The convective terms are discretized using the fifth order Weighted Essentially Non-Oscillatory (WENO) scheme [19], and viscous terms are discretized using standard second-order central differences.

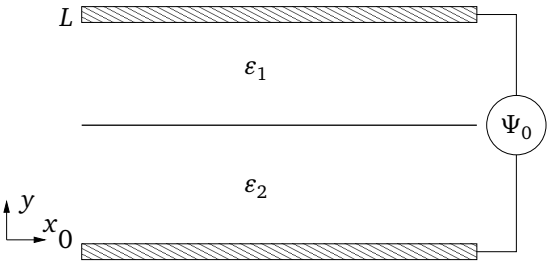

Figure 2. Configuration of the horizontal-interface test case.

3 METHOD EVALUATION

This section compares results from the CSF approach used in [12] and [11] with results from the sharp-interface method used here. The first test case is a horizontal interface in an electric field. This test case tests the ability of the numerical method to accurately predict the jumps across an interface. Then, results for the deformation of a dielectric drop subject to an electric field are presented.

3.1 A HORIZONTAL INTERFACE IN AN ELECTRIC FIELD

An interface is placed between two parallel plates, the upper medium has permittivity ε_1 and the lower medium has permittivity ε_2. The upper parallel plate is given a potential Ψ_0 while the lower plate is grounded. This configuration is illustrated in Figure 2. This test case is excellent for evaluating the handling of the discontinuity in electrical properties, and was considered in both [12] and [11]. In [11], an arithmetic mean is used to find the smoothed electric permittivities, while in [12], it was shown that using a harmonic mean gives significantly better results. In this section, these results are compared to the results obtained with the ghost-fluid method.

The equation for the electric potential is a Laplace equation with constant coefficients in each phase. This equation can be solved by noting that the potential is continuous across the interface (equation (2.28)). The solution is

$$\Psi_1 = 2\Psi_0 \frac{1}{\varepsilon_1/\varepsilon_2 + 1}\frac{y - L}{L} + \Psi_0$$
$$\Psi_2 = 2\Psi_0 \frac{1}{1 + \varepsilon_2/\varepsilon_1}\frac{y}{L}. \quad (3.1)$$

The electric field in each phase can then be found by using equation (2.7):

$$E_1 = -\frac{2\Psi_0}{L}\frac{1}{\varepsilon_1/\varepsilon_2 + 1}$$
$$E_2 = -\frac{2\Psi_0}{L}\frac{1}{1 + \varepsilon_2/\varepsilon_1}. \quad (3.2)$$

The pressure jump is given by equation (2.26), which for this case is

Table 1. Physical properties and analytical values for the horizontal-interface test case.

Quantity	Value
Plate distance, L	0.01
Permittivity 1, ε_1	70
Permittivity 2, ε_2	1
Potential difference, Ψ_0	100
Electric field 1, E_1	-2.8169×10^{2}
Electric field 2, E_2	-1.9718×10^{4}
Pressure jump, $[p]$	-1.6959×10^{-3}

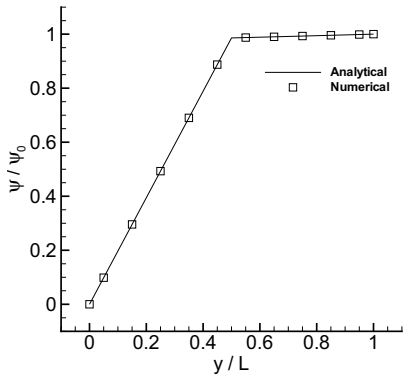

Figure 3. The horizontal-interface test case. The electric potential in the *y*-direction, scaled by the potential difference, for a calculation with 10 grid points.

$$[p] = \mathbf{n}\cdot[\boldsymbol{M}]\cdot\mathbf{n} = \frac{1}{2}\varepsilon_0(\varepsilon_1 E_1^2 - \varepsilon_2 E_2^2). \qquad (3.3)$$

We now analyze the accuracy of the ghost-fluid method for this test case. The chosen physical parameters along with the computed analytical solutions are given in Table 1, and are equivalent to those used in [12].

The ghost-fluid method uses an extrapolated value for the value at the interface in the discretization. Because the solution is linear in this particular case, this should give an exact solution for all grid sizes. Figure 3 shows the solution for the potential for a grid with 10 grid points, compared with the analytical solution. The 2-norm of the relative error is 5.29×10^{-16}, which means that the electric potential is accurately solved to machine precision, as expected. In [11] and [12], data is not provided for the accuracy of the CSF method when applied to the horizontal-interface test case. We found that for 10 grid points, the 2-norm of the relative error was 0.85% when using a harmonic mean to smear the permittivities, and 65.9% when using an arithmetic mean.

For the error of the electric field of phase 1, together with the error in the pressure jump, [12] report 4.8×10^{-3} % and 9.7×10^{-3} %, respectively, for a 40-point grid. We use the ghost-fluid method for calculating the gradient of the potential and for the discretization of the pressure equation, so again we expect an exact solution for all grid sizes for this particular test case. Figure 4 and Figure 5 show the computed solutions of the electric field and the pressure, respectively, together with the analytical solutions, for a grid with 10 points. The relative error for the value of the electric field was 2.21×10^{-15} and the error for the pressure jump was 7.64×10^{-15}. Clearly, the ghost-fluid method is significantly better than the CSF method for this test case.

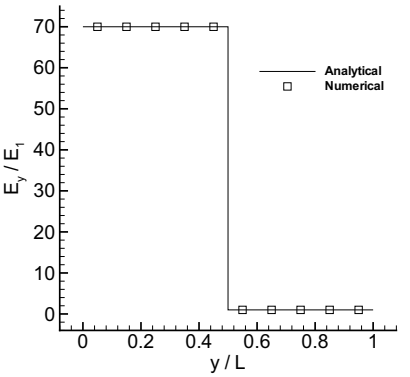

Figure 4. The horizontal-interface test case. The electric field in the *y*-direction, scaled by the exact solution for phase 1, for a calculation with 10 grid points.

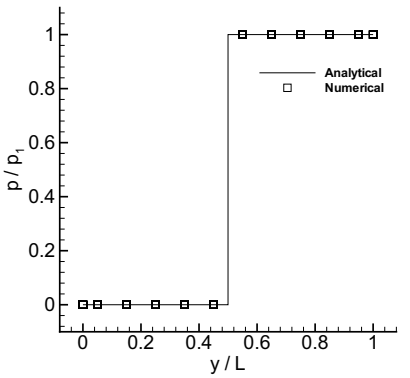

Figure 5. The horizontal-interface test case. The pressure in the *y*-direction, scaled by the exact solution for phase 1, for a calculation with 10 grid points.

3.2 A SPHERICAL DROP SUBJECT TO AN ELECTRIC FIELD

This test case serves to assess the accuracy of the ghost-fluid method for an axisymmetric problem. Finding the potential around a dielectric sphere in an electric field is a classical problem in electrodynamics (see e.g. [20]), with the following solution in spherical coordinates:

$$\Psi_{\text{an}}(r,\theta)=\begin{cases} -\dfrac{3}{\bar{\varepsilon}+2}E_0 r\cos\theta & \text{if } r\le R; \\ \left(\dfrac{\bar{\varepsilon}-1}{\bar{\varepsilon}+2}\dfrac{R^3}{r^3}-1\right)E_0 r\cos\theta & \text{if } r>R. \end{cases} \tag{3.4}$$

Here, $\bar{\varepsilon}$ is the permittivity ratio between the drop and the surrounding medium. The electric field is then

$$E_x(r,\theta)=\begin{cases} 0 & \text{if } r\le R; \\ -\dfrac{3}{2}\dfrac{\bar{\varepsilon}-1}{\bar{\varepsilon}+2}\dfrac{R^3}{r^3}E_0\sin 2\theta & \text{if } r>R. \end{cases}$$

$$E_y(r,\theta)=\begin{cases} \dfrac{3}{\bar{\varepsilon}+2}E_0 & \text{if } r\le R; \\ \left[\dfrac{\bar{\varepsilon}-1}{\bar{\varepsilon}+2}\dfrac{R^2}{r^3}\left(3\sin^2\theta-1\right)+1\right]E_0 & \text{if } r>R. \end{cases} \tag{3.5}$$

Note that this is the electric field in the *x*-direction and *y*-direction, but defined using r and θ for the purpose of a more compact presentation. These values can be compared to those found by the present algorithm by taking only one time step, so that there is no deformation of the sphere. The physical properties used for the test case is given in Table 2. A domain size of $3R\times 6R$ was used. The error in the potential, together with the convergence behavior, is given in Table 3. The order of convergence is defined as

$$\mathcal{O}=\frac{\ln(E_2/E_1)}{\ln(N_2/N_1)}, \tag{3.6}$$

Where E_i is the error on a grid with N_i grid points. The error is low even for small grid sizes, and the convergence is that expected of the ghost-fluid method.

Figure 6 shows a comparison of the potential contour lines for the analytical and numerical result. Figure 7, which shows stream-traces of the electric field, further demonstrates the accuracy of the ghost-fluid method.

Table 2. Physical properties and analytical values for the spherical-drop test case.

Quantity	Value
Drop radius, R	1×10^{-3}
Surface tension, σ	32×10^{-4}
Permittivity 1, ε_1	10
Permittivity 2, ε_2	1
Initial electric field, E_0	3.4543×10^{5}

Table 3. The 2-norm of the error in the potential for the spherical-drop test case, along with the order of convergence.

R/h	$\lvert\Psi-\Psi_{\text{an}}\rvert$ ($\times10^{-6}$ V)	Order
5	23.1	-
10	12.3	0.91
20	7.59	0.70
40	3.69	1.04

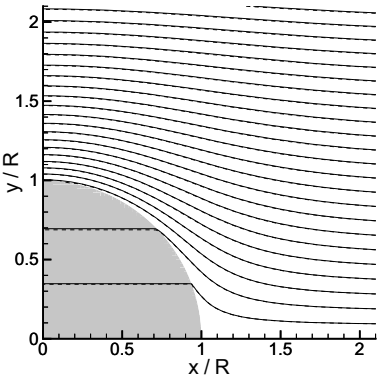

Figure 6. The spherical-drop test case. Comparison of analytical (solid) and numerical (dashed) potential around a dielectric drop for $R/h=40$.

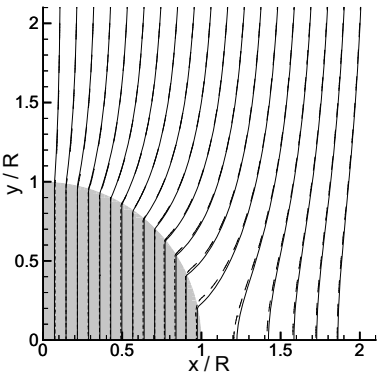

Figure 7. The spherical-drop test case. Comparison of analytical (solid) and numerical (dashed) electric field around a dielectric drop for $R/h=40$.

In [12], they compared the pressure jump across the interface along the *x*-axis, where the jump in pressure is the highest, to the theoretical result. The pressure jump is given by equation (2.26), which for this particular problem becomes

$$[p]=\frac{2\sigma}{R}-\frac{9}{2}\frac{\bar{\varepsilon}-1}{(\bar{\varepsilon}+2)^2}\varepsilon_0 E_0^2 \tag{3.7}$$

The error for the maximum pressure jump when using the ghost-fluid method is given in Table 4. For $R/h=10$, the

Table 4. The relative error for the maximum pressure jump across the interface of a spherical drop.

R/h	Relative error, $[p]$ ($\times10^{-3}$ Pa)	Order
5	8.74	-
10	3.38	1.37
20	1.63	1.05
40	0.482	1.76

error is nearly equal to that reported in [12] for $R/h = 160$. This shows the superiority of the sharp-interface approach compared to the smeared-interface approach. The convergence behavior is similar for the two methods.

3.3 DEFORMATION OF A SPHERICAL DROP SUBJECT TO AN ELECTRIC FIELD

If an electric field is applied to an initially spherical drop in a matrix fluid of different permittivity, the drop will deform. As explained in [2], a perfect dielectric drop will always stretch in the direction of the electric field. The amount of stretching depends on the permittivity ratio, $\bar{\varepsilon}$, and the ratio between electric forces and capillary forces, expressed by the dielectric Bond number,

$$\mathrm{Bo_e} = \frac{\varepsilon_2 \varepsilon_0 D}{\sigma} E_0^2. \tag{3.8}$$

An expression for the steady-state deformation was found in [21], by an energetic approach. Good agreement with finite-element computations was reported. The expression can be written as

$$\mathrm{Bo_e} = \frac{4a^2 e - 2a^{7/2}\sin^{-1} e + 6a^{1/2}e^{-2}\sin^{-1} e - 6a^2 e^{-1}}{\left(\frac{\bar{\varepsilon}-1}{1+n(\bar{\varepsilon}-1)}\right)^2 \left(\frac{-2ne}{1-e^2} - 3ne^{-1} + e^{-1}\right)}$$

$$n = \frac{1-e^{-2}}{e^3}\left(\ln\sqrt{\frac{1+e}{1-e}} - e\right) \tag{3.9}$$

$$e^2 = 1 - b^2/a^2$$

$$b^2 = R_0^3/a$$

For permittivity ratios above approximately 20, the elongation is no longer single-valued, and hysteresis may occur. The parameter range that allows hysteresis is very narrow, $20 \le \bar{\varepsilon} \le 25$. For other values, the drop shape is unstable, and the drop will begin to emit small drops from its tips to lower its radius and thereby reattain a stable value. A series of numerical calculations were performed to compare the numerical method to the above theoretical result. To avoid having to run the simulations to steady state, the simulations were run for one oscillation period with viscosities equal to zero, and the average between the maximum and the minimum value was used as the steady state value. This will not be entirely correct due to numerical diffusion, but is considered sufficient for the present purpose. The computational domain was $3R_0 \times 9R_0$, and a grid size of 160×481 was used. For this grid size, the relative error in using the values for an inviscid computation compared to running to steady state was found to be 1.3×10^{-3} for $\mathrm{Bo_e} = 0.05$ when using the ghost-fluid method.

A comparison between the theoretical values and the computational values for the ratio of the semi-major and the semi-minor axes are given in Figure 8. The CSF results are computed using the approach from [11], with permittivities approximated using harmonic mean. The results for the ghost-fluid method are significantly closer to the theoretical predictions than the results for the CSF approach.

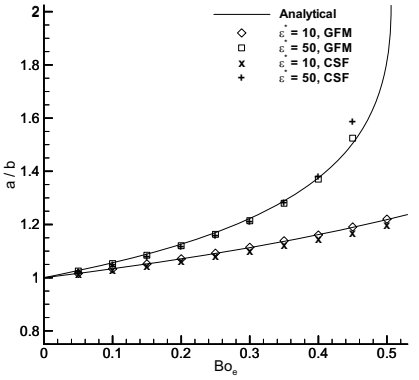

Figure 8. Deformation of spherical-drop test case. Comparison of the deformation between the theoretical values given by equation (3.9) and the numerical results for varying dielectric Bond number and permittivity ratios.

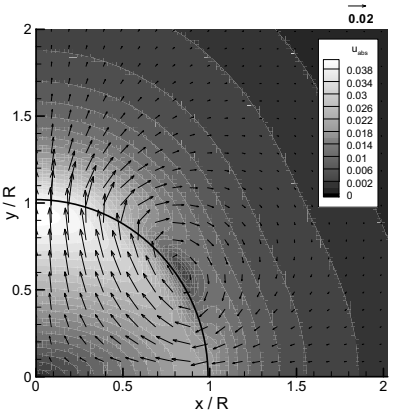

Figure 9. The prolate shape and induced flow field for $\mathrm{Bo_e} = 0.05$ and $\bar{\varepsilon} = 10$ when velocities are at a maximum. The contours show velocity magnitude. $\rho_1 = \rho_2 = 100\ \mathrm{kg/m^3}$, $\sigma = 1$ N/m, $\mu_1 = \mu_2 = 0.01$ Pa s.

An example of the induced flow field is given in Figure 9. This is when the flow field reaches a maximum, just before the surface-tension forces begin reversing the flow. Note that the velocity is highest towards the pole of the drop. For high field strengths, this can lead to conical ends, as shown in [22]. The flow tends to zero as the droplet reaches its equilibrium shape.

Since the electric field is abruptly applied at $t = 0$, inertia will cause the drop to overshoot the asymptotic value for the deformation, and then oscillate about this value until the viscous effects have damped out the motion. This overshoot may cause the drop to become unstable at values lower than those predicted by equation (3.9). For the values used here, the theoretical expression predicts breakup at $\mathrm{Bo_e} \approx 0.522$. However, at $\mathrm{Bo_e} \approx 0.5$, the numerical calculations no longer reach a steady-state value. Predicting when breakup occurs

will then no longer be a function of just Bo_e and $\bar{\varepsilon}$, but will also depend on the viscosities and densities of the two media. Investigating such a criterion is beyond the scope of this work.

4 CONCLUSION

This work presented an evaluation of a sharp-interface approach to simulating two-phase, electrohydrodynamic flows. The sharp-interface method was shown to give significant improvements in accuracy compared to smeared-interface approaches.

The generality of the method allows it to be used in a wide range of problems involving two-phase flows and electric fields. The inherent handling of topological changes makes the method attractive for studying problems involving breakup or coalescence, for instance film boiling and emulsion stability.

Only perfect dielectric fluids were considered in this work. A natural extension is to apply the method to the leaky dielectric model. This will be presented in a future work.

ACKNOWLEDGMENT

This work is funded by the project "Electrocoalescence -- Criteria for an efficient process in real crude oil systems"; coordinated by SINTEF Energy Research. The project is supported by The Research Council of Norway, under the contract no: 169466/S30, and by the following industrial partners: Aibel AS, Aker Solutions AS, BP Exploration Operating Company Ltd, Saudi Aramco, Shell Technology Norway AS, StatoilHydro ASA and Petrobras.

The authors thank Joris Verschaeve for interesting discussions regarding the Lattice-Boltzmann method. Further, the constructive comments of the referees have improved the article.

REFERENCES

[1] J. Sherwood, "Breakup of fluid droplets in electric and magnetic fields", J. Fluid Mech, Vol. 188, pp. 133–146, 1988.

[2] J. Baygents, N. Rivette, and H. Stone, "Electrohydrodynamic deformation and interaction of drop pairs", J. Fluid Mech., Vol. 368, pp. 359–375, 1998.

[3] T. Tsudaka, Y. Yamamoto, T. Katayama and M. Hozawa, "Theoretical and experimental studies of circulations inside and outside a deformed drop moving in a quiescent liquid", J. Chem. Engng. Japan, Vol. 27, pp. 662-666, 1994.

[4] J. Q. Feng, and T. C. Scott, "A computational analysis of electrohydrodynamics of a leaky dielectric drop in an electric field", J. Fluid Mech., Vol. 311, pp. 289-326, 1996.

[5] S.O. Unverdi, and G. Tryggvason, "A front-tracking method for viscous, incompressible, multi-fluid flows", J. Comp. Phys., Vol. 100, pp. 25–37, 1992.

[6] A. Fernandez, G. Tryggvason, J. Che, and S. Ceccio, "The effects of electrostatic forces on the distribution of drops in a channel flow: two-dimensional oblate drops", Phys. Fluids, vol. 17, No. 093302. 2005.

[7] J. Zhang and D.Y. Kwok, "A 2D lattice Boltzmann study on electrohydrodynamic drop deformation with the leaky dielectric theory", J. Comput. Phys., Vol. 206, pp. 150–161, 2005.

[8] M. Sussman and E.G. Puckett, "A coupled level set and volume-of-fluid method for computing 3D and axisymmetric incompressible two/phase flows", J. Comput. Phys., Vol. 162 , pp. 301–337, 2000.

[9] M. Sussman, P. Smereka, and S. Osher, "A level set approach for computing solutions to incompressible two-phase flow", J. Comput. Phys., Vol. 114, pp. 146–159, 1994.

[10] S. Osher and R. Fedkiw, *Level Set Methods and Dynamic Implicit Surfaces*. Springer, 2003.

[11] S. Welch and G. Biswas, "Direct simulation of film boiling including electrohydrodynamic forces", Phys. Fluids, Vol. 19, No. 012106, 2007.

[12] G. Tomar, D. Gerlach, G. Biswas, N. Alleborn, A. Sharma, D. Durst, S. Welch, and A. Delgado, "Two-phase electrohydrodynamic simulations using a volume-of-fluid approach", J. Comput. Phys., Vol. 227, pp. 1267–1285, 2007.

[13] E. B. Hansen, "*Numerical Simulation of Droplet Dynamics in the Presence of an Electric Field*", Ph.D. dissertation, Norwegian University of Science and Technology (NTNU), 2005.

[14] E. Bjørklund, "The level-set method applied to droplet dynamics in the presence of an electric field", Comput. Fluids, Vol. 38, pp. 358-369, 2009.

[15] R. Fedkiw, "A non-oscillatory Eulerian approach to interfaces in multimaterial flows", J. Comput. Phys., Vol. 152, pp. 457–492, 1999.

[16] M. Kang, R. Fedkiw, and X. Liu, "A boundary condition capturing method for multiphase incompressible flow", J. Sci. Comput., Vol. 15, pp. 323–360, 2000.

[17] H. K. Zhao, T. Chan, B. Merriman, and S. Osher, "A variational level set approach to multi-phase motion", J. Comput. Phys., Vol. 127, pp. 179-195, 1996.

[18] J. F. B. M. Kraaijevanger, "Contractivity of Runge-Kutta methods", BIT (Nordisk tidskrift for informationsbehandling) Num. Math., Vol. 31, pp. 482-528, 1991.

[19] G. Jiang and D. Peng, "Weighted ENO schemes for Hamilton-Jacobi equations", Society for Industrial and Applied Mathematics (SIAM) J. Sci. Comp., Vol. 21, pp. 2126–2143, 2000.

[20] D. Griffiths, *Introduction to electrodynamics*. Prentice-Hall, Inc, 1999.

[21] A. Ramos and A. Castellanos, "Equilibrium shapes and bifurcation of captive dielectric drops subjected to electric fields", J. Electrostatics, Vol. 33, pp. 61-86, 1994.

[22] G. Taylor, "Disintegration of Water Drops in an Electric Field", Proc. R. Soc. London Ser. A, Vol. 280, pp. 383-397, 1964.

Knut Erik Teigen was born in Norway in 1983. He received the M.S. degree in mechanical engineering from the Norwegian University of Science and Technology (NTNU) in 2007. Presently, he is a Ph.D. candidate at the Department of Energy and Process Engineering at NTNU. His research interests are computational fluid dynamics, in particular the numerical simulation of two-phase flows.

Svend Tollak Munkejord was born in Norway in 1974. He received the M.S. degree in mechanical engineering from NTNU in 1997, and the Ph.D. degree from the same university in 2006. Presently, he is a research scientist at SINTEF Energy Research. His research interests include the mathematical modeling and numerical analysis of two-phase flows.

B A computational study of the coalescence process between a drop and an interface in an electric field

Teigen, K.E, Munkejord, S.T., Bjørklund, E.,
In 6th International Conference on CFD in the Oil & Gas, Metallurgical and Process Industries
SINTEF/NTNU , Trondheim, Norway, June 10–12 2008

6th International Conference on CFD in the Oil & Gas, Metallurgical and Process Industries *CFD2008-078*
SINTEF / NTNU, Trondheim, Norway
10–12 June 2008

A COMPUTATIONAL STUDY OF THE COALESCENCE PROCESS BETWEEN A DROP AND AN INTERFACE IN AN ELECTRIC FIELD

Knut Erik TEIGEN,[1*] **Svend Tollak MUNKEJORD**,[2] **Erik BJØRKLUND**[3]

[1] NTNU, Department of Energy and Process Engineering, 7491 Trondheim, Norway
[2] SINTEF Energy Research, Energy Processes, 7465 Trondheim, Norway
[3] Aibel AS, 1375 Billingstad, Norway
[*]E-mail: knutert@gmail.com

ABSTRACT

The coalescence process between a drop and an interface may not be instantaneous, but result in the creation of a smaller secondary drop. This process may be repeated several times before the coalescence is complete. Experiments have shown that an electric field can suppress this phenomenon and give coalescence in a single stage. In this paper, the influence of an electric field on the partial coalescence process is studied using numerical simulations. The results show that higher electric Bond numbers reduce the time from pinch-off of a secondary drop to recoalescence, and eventually give single-staged coalescence. A single-stage coalescence event is presented in detail, and the mechanism producing it discussed. The results support arguments from the literature that single-staged coalescence is caused by an increased downward momentum due to electrostatic attraction.

Keywords: Coalescence, electrocoalescence, electrohydrodynamics, level-set method, ghost-fluid method

NOMENCLATURE

δ	Dirac delta function
Ψ	Electric potential [V]
Γ	Interface
κ	Curvature [m^{-1}]
ϕ	Level-set function
μ	Dynamic viscosity [$\mathrm{Pa}\cdot\mathrm{s}$]
$\mu^\star$	Viscosity ratio
ε	Relative permittivity
ε_0	Vacuum permittivity ($=8.85\times10^{-12}\,\mathrm{F/m}$)
$\varepsilon^\star$	Permittivity ratio
ρ	Density [$\mathrm{kg/m}^3$]
$\rho^\star$	Density ratio
σ	Interfacial tension [$\mathrm{N/m}^2$]
τ	Pseudo-time
τ_2	Time from pinch-off to recoalescence
$\boldsymbol{M}$	Maxwell stress tensor [$\mathrm{N/m}^2$]
$\boldsymbol{a}$	Temporary vector field [$\mathrm{m/s}^2$]
$\boldsymbol{e}$	Electric field [V/m]
$\boldsymbol{F}$	Strength of surface force [$\mathrm{N/m}^2$]
$\boldsymbol{f}$	Arbitrary vector field
$\boldsymbol{g}$	Gravitational acceleration [$\mathrm{m/s}^2$]
$\boldsymbol{n}$	Unit normal vector
$\boldsymbol{t}$	Unit tangential vector
$\boldsymbol{u}$	Velocity [m/s]
$\boldsymbol{X}$	Interface parametrization [m]
$\boldsymbol{x}$	Spatial position [m]
$\hat{\boldsymbol{F}}$	Surface force [$\mathrm{N/m}^3$]
a	x-aligned semi-axis of ellipse [m]
b	y-aligned semi-axis of ellipse [m]
D	Diameter [m]
e	Ellipse eccentricity
p	Pressure [Pa]
S	Sign function
t	Time [s]
t_{ic}	Inertio-capillary time
Be	Electric Bond number ($=\varepsilon_1\varepsilon_0 D E_0^2/\sigma$)
Bo	Bond number ($=\lvert\rho_1-\rho_2\rvert g D^2/\sigma$)
Oh	Ohnesorge number ($=\mu_1/\sqrt{\rho_1\sigma D}$)

INTRODUCTION

Electric fields are currently being employed to speed up the separation of water from oil during oil production from offshore wells. An electric field increases the coalescence rate between water drops which again enhances the settling process. Numerical calculations may give additional insight into the fundamental processes occurring in an electrocoalescer, and thereby help to optimize the separation process.

The partial coalescence phenomenon was made widely known by Charles and Mason (1960a) and Charles and Mason (1960b). They attributed the phenomenon to a static Rayleigh-Plateau instability, and gave a criterion for partial coalescence based on the viscosity ratio. However, in Blanchette and Bigioni (2006), it was demonstrated that the Rayleigh-Plateau instability could not be the cause of the instability, and instead proposed the convergence of capillary waves on the tip of the droplet as the dominating mechanism. A detailed study of the propagation of these capillary waves was made in Gilet *et al.* (2007), and it was concluded that other viscous mechanisms also play an important role in the process.

In Thoroddsen and Takehara (2000), partial coalescence was observed in a system with a viscosity ratio much higher than the criterion stated in Charles and Mason (1960b). Blanchette and Bigioni tried to give a criterion based on the Ohnesorge number and the Bond number, and found that for low Bond numbers, i.e. for drops with negligible gravitational effects, the critical Ohnesorge number was approximately 0.026. Yue *et al.* (2006) made an extensive parameter study using numerical simulations, and found an expression for the critical Ohnesorge number based on the viscosity ratio. However, they did not consider larger Bond numbers, so a universal criterion for the occurrence of partial coalescence remains elusive.

The influence of electric fields on the partial coalescence phenomenon was discussed briefly in Charles and Mason (1960b). It was observed that the rest time of the drop decreased when an electric field was applied. Also, above a critical field strength, the drop was found to coalesce with the interface in a single stage. In Allan and Mason (1961), the influence of electric fields was studied in more detail. They proposed that single-stage coalescence was a result of an additional downward momentum of the water column due to electrostatic attraction, leading to a faster emptying of the drop.

The present work investigates the influence of an electric field on the partial coalescence process using numerical simulations. First, the governing equations and numerical methods are presented. These are then validated by comparison with experimental and theoretical results. Finally, calculations of the partial coalescence process with applied electric fields are presented and discussed.

GOVERNING EQUATIONS AND NUMERICAL METHODS

The numerical method used for the calculations is described in detail in Bjørklund (2008) and Hansen (2005), and will only be briefly reviewed here. The full Navier–Stokes equations are solved in each phase, and the interface between the two phases is captured using the level-set method. The ghost-fluid method is used to treat discontinuities across the interface in a sharp manner. To account for electric forces, a Poisson equation is solved for the electric potential, which is then used to calculate the Maxwell stress tensor.

Flow equations

The flow is governed by the incompressible Navier–Stokes equations, with added terms for surface tension forces and electric forces:

$$\begin{aligned}\rho\left(\frac{\partial \boldsymbol{u}}{\partial t}+(\boldsymbol{u}\cdot\nabla)\boldsymbol{u}\right) &= -\nabla p+\nabla\cdot[\mu(\nabla\boldsymbol{u}+\nabla\boldsymbol{u}^T)]+\rho\boldsymbol{g}\\ &\quad +\hat{\boldsymbol{F}}+\nabla\cdot\boldsymbol{M},\\ \nabla\cdot\boldsymbol{u} &= 0.\end{aligned} \tag{1}$$

The effect of an interface, Γ, in the domain results in a singular surface force which can be expressed by

$$\hat{\boldsymbol{F}}(\boldsymbol{x},t)=\int_{\Gamma(t)}\boldsymbol{F}(s,t)\delta(\boldsymbol{x}-\boldsymbol{X}(s,t))\mathrm{d}s, \tag{2}$$

where s is the arc-length, $\boldsymbol{X}(s,t)$ is the parametrization of the interface, $\boldsymbol{x}$ is the spatial position and δ is the Dirac delta function. $\boldsymbol{F}$ is given by

$$\boldsymbol{F}=\sigma\kappa\boldsymbol{n}. \tag{3}$$

Here, σ is the interfacial tension, κ the curvature and $\boldsymbol{n}$ is the outward pointing unit normal vector.

In this work, all equations are solved in an axisymmetric geometry, so that the divergence operator and Laplacian operator become

$$\nabla\cdot\boldsymbol{f}=\frac{1}{x}\frac{\partial}{\partial x}(xf_x)+\frac{\partial f_y}{\partial x}=\frac{\partial f_x}{\partial x}+\frac{\partial f_y}{\partial y}+\frac{f_x}{x}, \tag{4}$$

$$\nabla\cdot(\nabla\boldsymbol{f})=\frac{1}{x}\frac{\partial}{\partial x}\left(x\frac{\partial\boldsymbol{f}}{\partial x}\right)+\frac{\partial^2\boldsymbol{f}}{\partial y^2}=\frac{\partial^2\boldsymbol{f}}{\partial x^2}+\frac{\partial^2\boldsymbol{f}}{\partial y^2}+\frac{1}{x}\frac{\partial\boldsymbol{f}}{\partial x} \tag{5}$$

where the subscripts indicate the component, and not the partial derivative of the vector $\boldsymbol{f}$. In addition to the above Laplace operator, one has to add $-f_x/x^2$ to the viscous term in the x–momentum equation.

Electric forces

We assume perfect dielectric materials with no free charges. In Allan and Mason (1961), it was concluded

that the ionic strength of the aqueous solution had little influence on the coalescence process. Furthermore, Brown and Hanson (1965) found that it is the electric field at the interface, rather than the charge it carries, that is dominating the process.

With these assumptions, the electric potential, Ψ, can be calculated from the following Laplace equation:

$$\nabla\cdot(\varepsilon\varepsilon_0\nabla\Psi) = 0, \tag{6}$$

The electric field can then be calculated as

$$\boldsymbol{e} = -\nabla\Psi, \tag{7}$$

and the Maxwell stress tensor as

$$\boldsymbol{M} = \varepsilon\varepsilon_0\left[\boldsymbol{ee} - \frac{1}{2}(\boldsymbol{e}\cdot\boldsymbol{e})\boldsymbol{I}\right], \tag{8}$$

where $\boldsymbol{I}$ is the identity tensor. With the above assumptions, $\nabla\cdot\boldsymbol{M} = \boldsymbol{0}$ everywhere except at the interface.

Interface capturing

The interface is captured using the level-set method (Sussman *et al.* (1994); Osher and Fedkiw (2003)). This method allows accurate computation of the evolution of an interface, along with automatic handling of topological changes. The ghost-fluid method (Fedkiw (1999); Kang *et al.* (2000)) is used to take discontinuities across the interface into account. This method handles the jumps in physical properties directly in the numerical stencils, without the need for any smearing of properties.

The interface is defined by the zero level set

$$\Gamma = \{\boldsymbol{x}|\phi(\boldsymbol{x},t) = 0\}, \tag{9}$$

and is evolved by

$$\frac{\partial\phi}{\partial t} + \boldsymbol{u}_{\text{int}}\cdot\nabla\phi = 0. \tag{10}$$

Here, $\boldsymbol{u}_{\text{int}}$ is the velocity on the interface. To be able to solve this equation numerically, the interface velocity is extended off the interface. In Adalsteinsson and Sethian (1999), it was shown that the velocity could be extrapolated orthogonally from the interface by solving

$$\frac{\partial\boldsymbol{u}}{\partial\tau} + S(\phi_0)\boldsymbol{n}\cdot\nabla\boldsymbol{u} = 0, \tag{11}$$

where S is a sign function given by

$$S(\phi) = \frac{\phi}{\sqrt{\phi^2 + 2\Delta x^2}}. \tag{12}$$

Note that this equation is hyperbolic, so it is not necessary to solve it to steady state, since only the information a few grid points away from the interface is relevant.

The standard level-set reinitialization procedure is used to keep the level-set function as a signed distance function throughout the computation. This is accomplished by solving

$$\begin{aligned}\frac{\partial\phi}{\partial\tau} + S(\phi_0)(|\nabla\phi| - 1) = 0,\\ \phi(\boldsymbol{x},0) = \phi_0(\boldsymbol{x}).\end{aligned} \tag{13}$$

Reinitialization is performed every second time step.

The ghost-fluid method is used to handle the discontinuities across the interface in a sharp manner. This method requires jump conditions, which are relations between the physical quantities on each side of the interface. In the following, the interfacial jump is denoted by $[x] = x^+ - x^-$, where x^+ is the interfacial value on the side of the interface where ϕ is positive, and x^- is on the other side.

The jump in the velocity gradient is

$$[\mu\nabla\boldsymbol{u}] = [\mu]\boldsymbol{n}\cdot\nabla(\boldsymbol{u}\cdot\boldsymbol{n})\boldsymbol{nn} + [\mu]\boldsymbol{t}\cdot\nabla(\boldsymbol{u}\cdot\boldsymbol{n})\boldsymbol{nt} \tag{14}$$

$$- [\mu]\boldsymbol{t}\cdot\nabla(\boldsymbol{u}\cdot\boldsymbol{n})\boldsymbol{tn} \tag{15}$$

$$+ [\mu]\boldsymbol{t}\cdot\nabla(\boldsymbol{u}\cdot\boldsymbol{t})\boldsymbol{tt}, \tag{16}$$

where $\boldsymbol{t}$ the tangential vector. The jump in the pressure is

$$[p] = 2[\mu]\boldsymbol{n}\cdot\nabla\boldsymbol{u}\cdot\boldsymbol{n} + \boldsymbol{n}\cdot[\boldsymbol{M}]\cdot\boldsymbol{n} + \sigma\kappa\boldsymbol{n}\cdot\boldsymbol{n}, \tag{17}$$

The jump conditions for the electric potential and its gradient are

$$[\Psi] = 0, \tag{18}$$

$$[\varepsilon\varepsilon_0\nabla\Psi\cdot\boldsymbol{n}] = 0. \tag{19}$$

The latter is zero since we assume no free charges.

Numerics

A second-order projection scheme is used to solve the Navier–Stokes equations. First, a temporary vector field, $\boldsymbol{a}$, is calculated:

$$\boldsymbol{a} = -(\boldsymbol{u}\cdot\nabla)\boldsymbol{u} + \nabla\cdot[\mu(\nabla\boldsymbol{u} + \nabla\boldsymbol{u}^T)]. \tag{20}$$

Then the pressure is found by solving

$$\nabla\cdot\left(\frac{\nabla p}{\rho}\right) = \nabla\cdot\boldsymbol{a}. \tag{21}$$

Finally, the velocity field is calculated with

$$\frac{\partial\boldsymbol{u}}{\partial t} = \boldsymbol{a} - \frac{\nabla p}{\rho} \tag{22}$$

The evolution in time is performed using a third order, strong stability preserving (SSP) Runge-Kutta (RK) method (Gottlieb *et al.* (2001)), while a second order SSP RK method is employed for the evolution of the level-set equation, the reinitialization of the level-set equation and extrapolation of the velocity field.

The equations are spatially discretized on a staggered grid, with scalar values stored in cell centers and vector values stored at cell boundaries. The convective terms are discretized using the fifth order Weighted Essentially Non-Oscillatory (WENO) scheme (Jiang and Peng (2000)), and viscous terms are discretized using standard second order central differences.

One substep in the RK solver can be summarized as follows:

1. Solve Equation (6) for the electric potential
2. Calculate electric field and electric forces using Equations (7)-(8)
3. Calculate a temporary vector field with Equation (20)
4. Solve Equation (21) to find the pressure
5. Calculate the final velocity field using Equation (22)
6. Extrapolate the velocity from the previous time step by solving Equation (11)
7. Update the level-set function with Equation (10), using the extrapolated velocities
8. Reinitialize the level-set function by solving Equation (13)

Dimensionless groups

In Yue *et al.* (2006) the following four dimensionless groups were used to describe the partial coalescence phenomena:
The Ohnesorge number, relating viscous forces to interfacial tension forces

$$Oh = \frac{\mu_1}{\sqrt{\rho_1 \sigma D}}, \tag{23}$$

the Bond number, relating gravitational forces to interfacial tension forces

$$Bo = \frac{|\rho_1 - \rho_2| g D^2}{\sigma}, \tag{24}$$

the density ratio

$$\rho^\star = \frac{\rho_1}{\rho_2} \tag{25}$$

and the viscosity ratio

$$\mu^\star = \frac{\mu_1}{\mu_2}. \tag{26}$$

Here, the subscripts 1 and 2 denote the drop and the matrix phase, respectively. D is the diameter of the drop and σ is the interfacial tension between the two phases. The addition of an electric field gives three new variables in the system; the initial electric field, E_0, and the permittivities of the two phases, ε_1 and ε_2. This calls for two new dimensionless variables to properly describe the system. Here, we choose the electric Bond number, relating electric forces to interfacial-tension forces

$$Be = \frac{\varepsilon_1 \varepsilon_0 D}{\sigma} E_0^2, \tag{27}$$

and the permittivity ratio

$$\varepsilon^\star = \frac{\varepsilon_1}{\varepsilon_2}. \tag{28}$$

Any other dimensionless quantity can now ideally be represented as a function of these dimensionless parameters.

We use the same time scale as Yue *et al.* (2006),

$$t_{\text{ic}} = \sqrt{\frac{\rho_1 D^3}{\sigma}}. \tag{29}$$

Quantity	Value
Initial drop diameter, D_0	1/3
Drop density, ρ_1	1.0
Drop viscosity, μ_1	1.0×10^{-2}
Drop permittivity, ε_1	180
Matrix density, ρ_2	1.0
Matrix viscosity, μ_2	1.0×10^{-2}
Matrix permittivity, ε_2	3
Interfacial tension, σ	1.0
Electric field, E_0	6.42×10^{4}

Table 1: Numerical parameters for the oscillating drop calculation.

CODE VALIDATION

Oscillating drop driven by an electric field

This test case aims at demonstrating the validity of the model for the electric forces. An initially spherical drop is exposed to an electric field. This will induce surface forces on the interface between the two fluids, set up by the permittivity difference, and result in a stretching of the drop in the direction of the electric field. This process is illustrated in Figure 1.

An expression for the steady-state elongation of the droplet can be found by balancing the hydrodynamic pressure with the electrostatic pressure (Garton and Krasucki (1964); Taylor (1964)). For drops with finite permittivities, this expression can be written as

$$E_0\sqrt{\frac{D_0\varepsilon_0\varepsilon_2}{\sigma}} = 2\left(\frac{a}{b}\right)^{2/3}\sqrt{2-\frac{b}{a}-\left(\frac{b}{a}\right)^3} \tag{30}$$

$$\cdot\left|\frac{1}{1-\varepsilon_1/\varepsilon_2}-\frac{b^2}{a^2}I_2\right| \tag{31}$$

$$I_2 = \frac{1}{2}e^{-3}\ln\left(\frac{1+e}{1-e}\right)-e^{-2} \tag{32}$$

$$e^2 = 1-\frac{b^2}{a^2} \tag{33}$$

$$\tag{34}$$

A series of calculations on varying grid sizes was performed and compared with the analytic expression above. The numerical parameters for the numerical calculations are given in Table 1. For these values, the asymptotic expression gives $a = 0.3290$ and $b = 0.3422$.

Figure 2 compares calculations with the axisymmetric code to the asymptotic value. As expected, the calculations converge toward oscillating around the asymptotic value.

Partial coalescence without electric field: Comparison with experiment

In Chen *et al.* (2006), an experiment was performed of a water droplet merging with an interface between 20 %

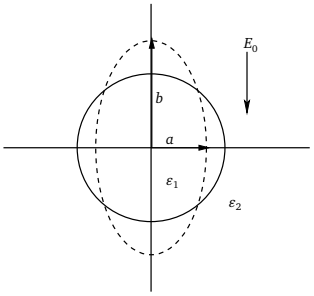

Figure 1: Illustration of the stretching of an initially spherical drop when an electric field is applied.

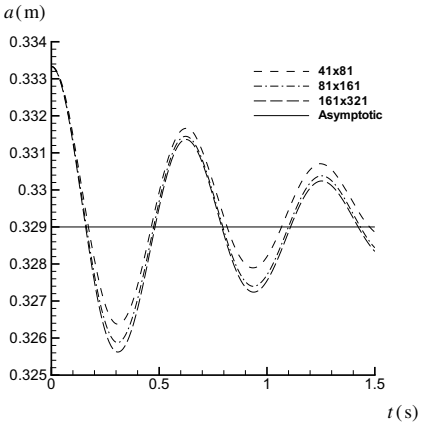

Figure 2: The evolution of the x-aligned semi-axis of an initially spherical drop subjected to an electric field. The dashed line indicates the theoretical steady state.

polybutene in decane and water, with no electric field applied. They presented a particularly clear image sequence of a partial coalescence event, which is used here for comparison with the numerical results. The physical properties of the system used are given in Table 2. Note that Chen *et al.* (2006) use a different definition of the Ohnesorge number than this work.

A numerical calculation with the same properties was performed to verify that the numerical method was capable of calculating the partial coalescence process. The numerical setup is illustrated in Figure 3. The computational domain is given by $R = 3D$ and $H = 6D$, the height of the water interface is $H_1 = 2D$ and the initial distance from the interface to the drop is $H_2 = 0.02D$. The grid size used was 100×200.

Figure 4 shows snapshots from the experiment performed in Chen *et al.* (2006), and Figure 5 shows the comparable snapshots from the numerical calculation. The simulation is capable of reproducing the partial coalescence of the experiment, and also captures the evolution of the interface with quantitative precision. In particular, the numerical method is capable of predicting the evolution of the capillary wave, indicated by arrows in Figure 4.

Quantity	Value
Drop diameter, D	1.1×10^{-3}
Drop density, ρ_1	1000
Drop viscosity, μ_1	1.0×10^{-3}
Matrix density, ρ_2	760
Matrix viscosity, μ_2	2.0×10^{-3}
Interfacial tension, σ	2.97×10^{-2}
Ohnesorge number, Oh	5.53×10^{-3}
Bond number, Bo	9.59×10^{-2}

Table 2: Physical properties of the partial coalescence experiment performed by Chen *et al.* (2006).

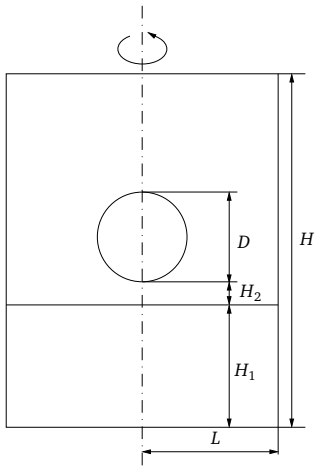

Figure 3: A schematic of the geometry for the numerical simulation. Axisymmetry is imposed across the centerline, so only the right half is actually part of the computational domain.

RESULTS AND DISCUSSIONS

In this section, the effect of an electric field on the partial coalescence process is discussed. Calculations are performed using the same numerical setup and physical properties as in the previous section, but now a potential difference is applied between the upper and lower boundary. Additionally, the height of the numerical domain is increased to $H = 7.5D$, to ensure that the drop is not affected by the upper boundary. The grid size used for these simulations was 90×225.

It should be noted that the initial conditions used here does not take into account the approach of the drop and the resting of the drop on the interface. Several authors (Charles and Mason (1960b); Allan and Mason (1961); Brown and Hanson (1965); Eow and Ghadiri (2003)) have found that an important effect of adding an electric field is a reduction in rest time due to additional attractive forces during the approach of the drop. However, the purpose of this study is to examine the actual coalescence process, and not the reduction in rest time.

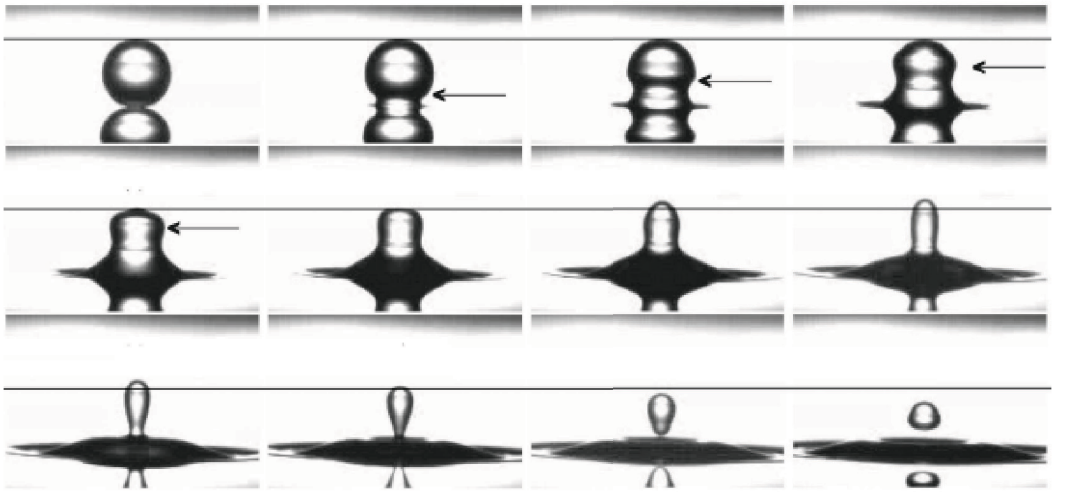

Figure 4: Snapshots of a water droplet merging with an interface between 20 % polybutene in decane and water. The initial drop diameter $D = 1.1\,\mathrm{mm}$, $Bo = 0.0959$, $Oh = 0.00417$, and the pictures are $542\,\mu\mathrm{s}$ apart in time. The location of the capillary wave is shown by the arrows. The horizontal lines, which are at the same height in all three rows, help in tracking the motion of the top of the drop. Reprinted with permission from X. Chen, S. Mandre and J. J. Feng, Partial coalescence between a drop and a liquid-liquid interface. *Phys. Fluids*, volume 18, 2006. Article 051705. Copyright 2006, American Institute of Physics.

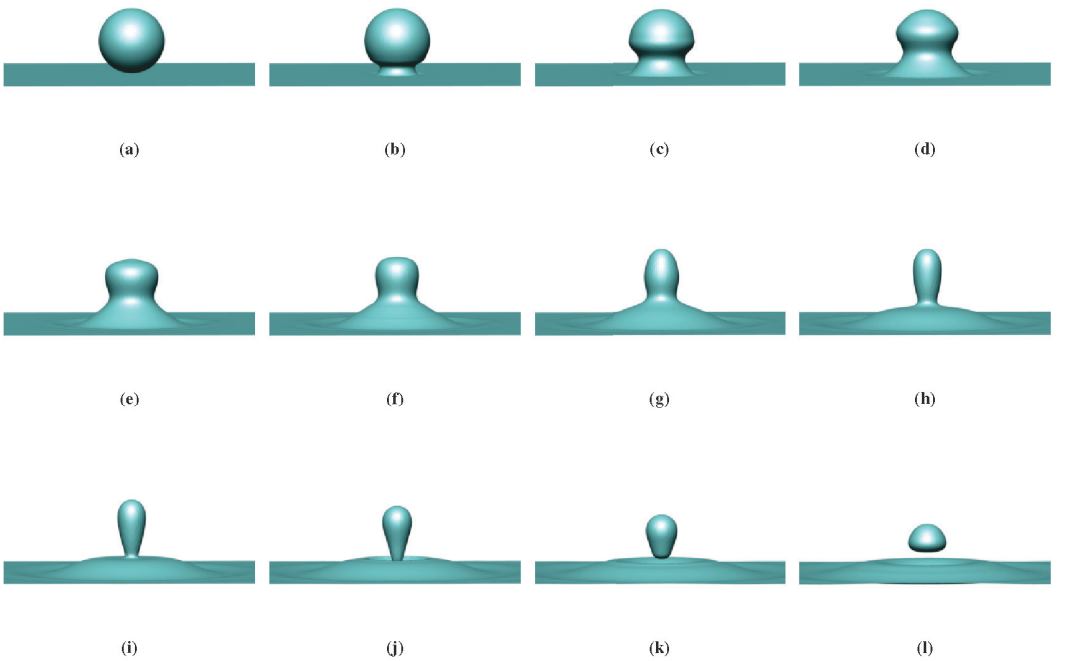

Figure 5: Snapshots from numerical simulation corresponding to the above figure. The numerical simulation is in good agreement with the experiment. In particular, the evolution of the capillary wave, indicated with arrows in the above figure, is accurately predicted.

Effect of the electric Bond number

Figure 6 shows the time interval from pinch-off to coalescence of the secondary drop, denoted τ_2, for different electric Bond numbers. The interval decreases until single stage coalescence is obtained at $Be = 0.075$. This trend is equivalent to that observed in Allan and Mason (1961). Single-staged coalescence is then observed at a range of electric Bond numbers, until pinch-off occurs again at $Be = 0.15$. The reappearance of multi-staged coalescence at higher field strengths was not observed by Allan and Mason (1961) and Eow and Ghadiri (2003). However, recent experiments (Hellesø (2008)) confirm that this behaviour may occur.

Snapshots from the entire calculation for $Be = 0.1$ are given in Figure 7. The potential drop across the drop and the aqueous phase is nearly zero, which was also observed in Allan and Mason (1961) and Brown and Hanson (1965). In Figure 4 it is clearly shown that without an electric field, the height of the liquid column increases during the emptying. With an electric field applied, the height decreases steadily throughout the entire event. The actual pinch-off in Figure 5, (k), corresponds to (h) in Figure 7. The liquid bridge for the simulation with an applied electric field is thicker, and the capillary forces are not large enough for pinch-off to occur.

Allan and Mason attributed single-stage coalescence to enhanced drainage of the drop due to electrostatic attraction. Figure 8 shows a comparison of the relative pressure distribution with and without an applied electric field at $t = 4.0 \times 10^{-4}$ s. The electric forces at the interface gives a higher pressure inside the drop, and hence a higher downward momentum. This is further illustrated in Figure 9, which shows the magnitude of the velocity in the y-direction. Without an electric field, the upper part of the liquid column has a positive velocity. Only the lower part of the column is emptied, which produces a thin filament which eventually pinches off. With an electric field, the entire column has a negative velocity, which additionally is everywhere larger than without an electric field. This increased emptying rate prevents the liquid bridge from pinching off. This also explains why the liquid bridge gets thinner from (b) to (h) in Figure 7, while it thickens thereafter. Initially, the capillary forces dominate, which causes a thinning of the liquid bridge. The capillary forces depend on the curvature, so they will get lower as the drop turns into a liquid column. Meanwhile, the pressure due to electric forces builds up inside the drop and accelerates the fluid inside. This is what causes the thickening and prevents pinch-off.

Effect of the permittivity ratio

Three simulations were performed at different permittivity ratios. The time from pinch-off to recoalescence is plotted in Figure 10. It is evident that for values much lower or higher than that used in the previous section, the coalescence becomes multi-staged again.

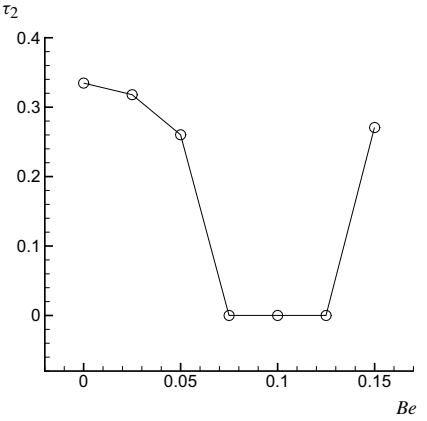

Figure 6: Time from pinch-off to recoalescence of secondary drop for varying electric Bond number. For an intermediate range of electric Bond numbers, the coalescence is single-staged.

For a low permittivity ratio, this is because the electric forces are too small to give the necessary downward momentum to prevent pinch-off.

For a high permittivity ratio, the increased stretching of the drop outweighs the effect of the downward momentum, which causes pinch-off to occur.

CONCLUSIONS

This article presented a computational investigation of the partial coalescence phenomenon, with and without electric fields applied.

It was shown that the numerical model is capable of reproducing a partial coalescence event with near quantitative precision in the absence of electric fields.

For the calculations with an applied electric field, the numerical model was able to reproduce trends reported in the literature. In particular, suppression of the partial coalescence process for higher electric fields observed in experiments was reproduced.

Detailed information from a single-staged coalescence event was presented that provides insight that is not immediately available from experiments. These results showed that the pressure inside the drop is higher when an electric field is applied. This increases the emptying rate of the drop, and thereby supports the argument that single-stage coalescence is caused by an increased downward momentum caused by the electric forces at the interface.

The present results do, however, not give a complete picture of partial coalescence under the influence of electric fields. More simulations should be performed using a wider range of the dimensionless parameters. In particular, only one Ohnesorge number and Bond number was investigated here. An investigation of higher Bond

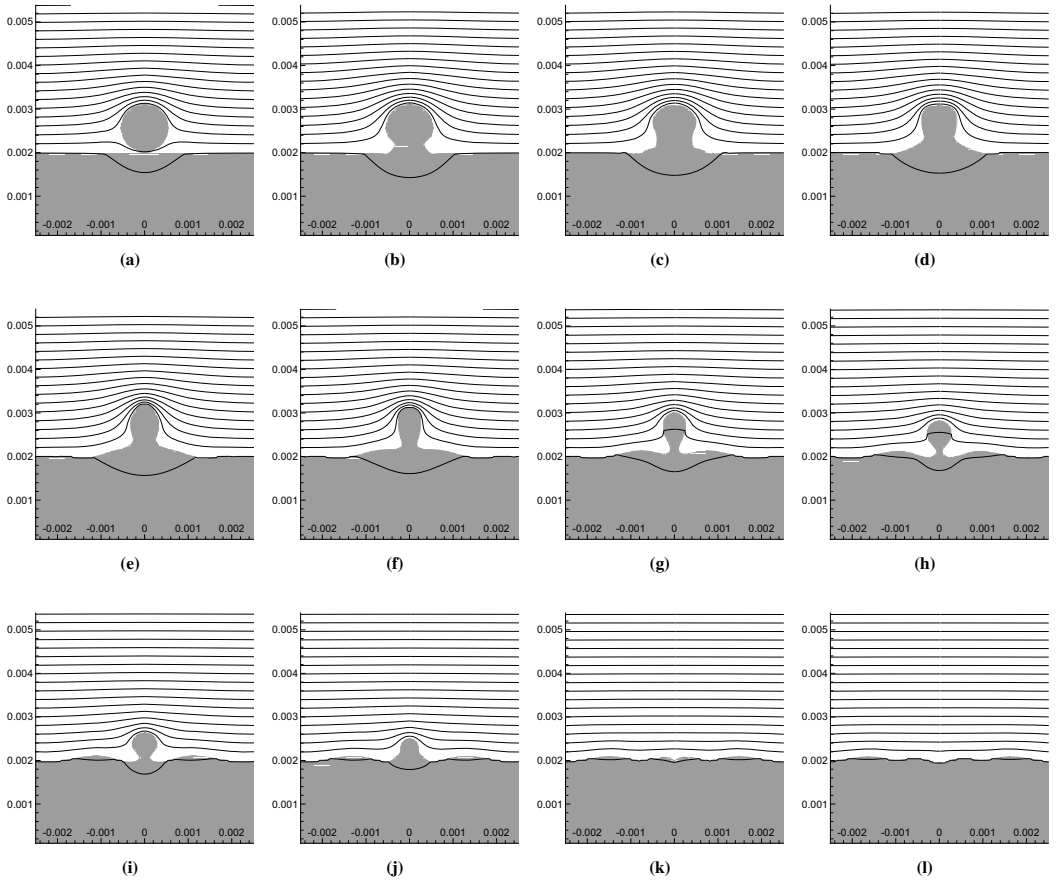

Figure 7: Snapshots from numerical simulation with $D = 1.1\,\text{mm}$, $Bo = 0.0959$, $Oh = 0.00417$, and $Be = 0.1$, demonstrating single stage coalescence. The time interval is $\Delta t = 7.75 \times 10^{-4}\,\text{s}$, and the contour lines show the electric potential with a 10 V interval. The potential in the aqueous phase is close to uniform, due to the high relative permittivity.

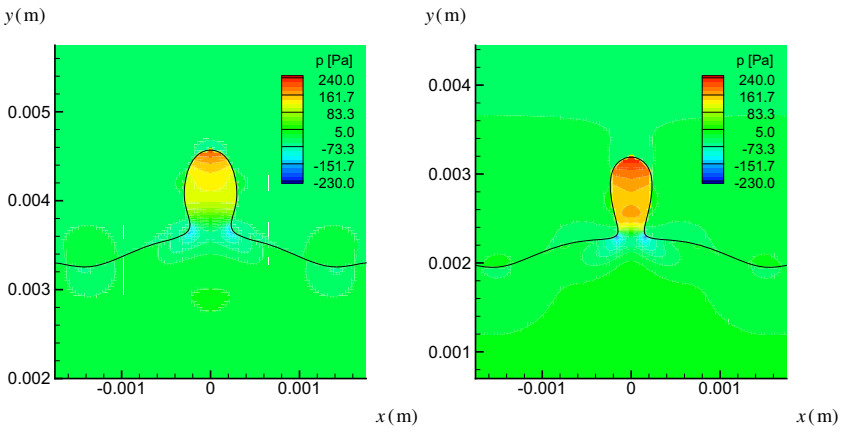

(a) No electric field

(b) Applied electric field, $Be = 0.1$

Figure 8: Contour plot of relative pressure at $t = 4.0 \times 10^{-4}\,\text{s}$, with and without an electric field. The electric field gives a higher pressure inside the drop, due to the additional electric forces at the interface.

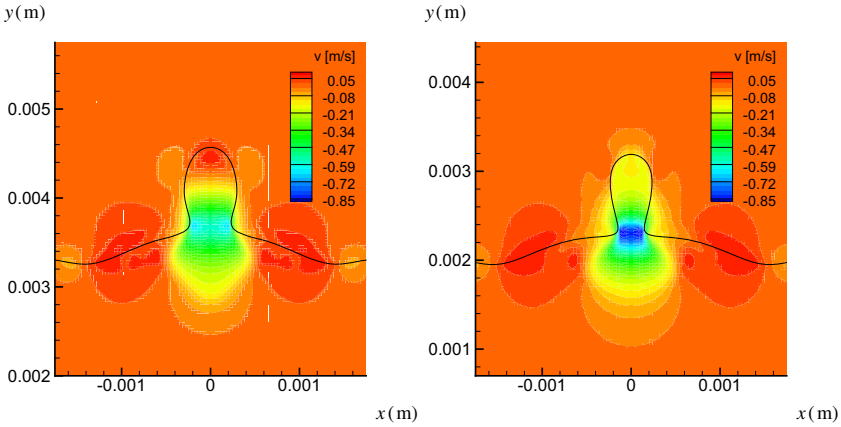

(a) No electric field

(b) Applied electric field, $Be = 0.1$

Figure 9: Contour plot of vertical velocity at $t = 4.0 \times 10^{-4}$ s, with and without an electric field. The electric field gives an increased emptying rate of the drop.

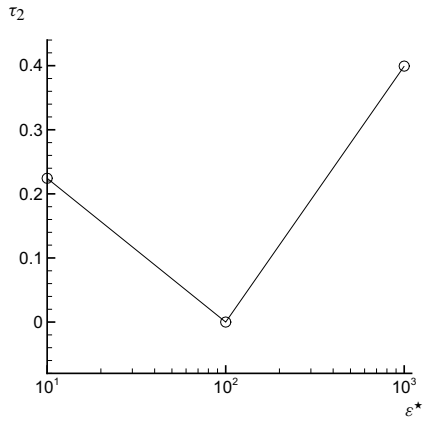

Figure 10: Time from pinch-off to recoalescence of secondary drop for varying permittivity ratio.

numbers, electric Bond numbers and permittivity ratios requires a full simulation of the approach of the drop.

Finally, the influence of impurities on the interface has not been taken into account in the numerical modeling. Such impurities may cause surface tension gradients which give rise to additional forces that may modify the coalescence behaviour. However, recent experiments (Hellesø (2008)) performed with water drops in real crude oils show the same qualitative behaviour as the results presented here.

ACKNOWLEDGEMENTS

This work is funded by the project "Electrocoalescence – Criteria for an efficient process in real crude oil systems"; co-ordinated by SINTEF Energy Research. The project is supported by The Research Council of Norway, under the contract no: 169466/S30, and by the following industrial partners: Aibel AS, Aker Kvaerner Process Systems AS, StatoilHydro ASA, BP Exploration Operating Company Ltd, Shell Technology Norway AS, Petrobras.

REFERENCES

Adalsteinsson, D. and Sethian, J. A. The fast construction of extension velocities in level set methods. *J. Comput. Phys.*, volume 148: pages 2–22, 1999.

Allan, R. S. and Mason, S. G. Effects of electric ifelds on coalescence in liquid+liquid systems. *Trans. Faraday Soc.*, volume 57: pages 2027–2040, 1961.

Bjørklund, E. The level-set method applied to droplet dynamics in the presence of an electric field. *Comput. Fluids*, 2008. Accepted.

Blanchette, F. and Bigioni, T. P. Partial coalescence of drops at liquid interfaces. *Nat. Phys*, volume 2, no. 254, 2006.

Brown, A. H. and Hanson, C. Effect of oscillating electric fields on coalescence in liquid+liquid systems. *Trans. Faraday Soc.*, volume 61: pages 1754–1760, 1965.

Charles, G. E. and Mason, S. G. The coalescence of liquid drops with flat liquid/liquid interfaces. *J. Colloid Sci.*, volume 15: pages 236–267, 1960a.

Charles, G. E. and Mason, S. G. The mechanism of partial coalescence of liquid drops at liquid/liquid interfaces. *J. Colloid Sci.*, volume 15: pages 105–122, 1960b.

Chen, X., Mandre, S. and Feng, J. J. Partial coalescence between a drop and a liquid-liquid interface. *Phys. Fluids*, volume 18, no. 051705, 2006.

Eow, J. S. and Ghadiri, M. The behaviour of a liquid-liquid interface and drop-interface coalescence under the influence of an electric field. *Colloids and Surfaces*

A: Physiochem. Eng. Aspects, volume 215: pages 101–123, 2003.

Fedkiw, R. P. A non-oscillatory eulerian approach to interfaces in multimaterial flows. *J. Comput. Phys.*, volume 152: pages 457–492, 1999.

Garton, C. G. and Krasucki, Z. Bubbles in insulating liquids: Stability in an electric field. *Proc. R. Soc. London*, volume 280: pages 221–226, 1964.

Gilet, T., Mulleners, K., Lecomte, J. P., Vandewalle, N. and Dorbolo, S. Critical parameters for the partial coalescence of a droplet. *Phys. Rev. E*, volume 75, no. 036303, 2007.

Gottlieb, S., Shu, C. W. and Tadmor, E. Strong stability-preserving high-order time discretization methods. *SIAM Review*, volume 43: pages 89–112, 2001.

Hansen, E. B. *Numerical simulation of droplet dynamics in the presence of an electric field*. Ph.D. thesis, NTNU, 2005.

Hellesø, S. M. Personal communication, 2008.

Jiang, G. S. and Peng, D. Weighted eno schemes for hamilton-jacobi equations. *SIAM J. Sci. Comp.*, volume 21: pages 2126–2143, 2000.

Kang, M., Fedkiw, R. and Liu, X. A boundary condition capturing method for multiphase incompressible flow. *J. Sci. Comput.*, volume 15: pages 323–360, 2000.

Osher, S. and Fedkiw, R. *Level set methods and dynamic implicit surfaces*. Springer, 2003.

Sussman, M., Smereka, P. and Osher, S. A level set approach for computing solutions to incompressible two-phase flow. *J. Comput. Phys.*, volume 114: pages 146–159, 1994.

Taylor, G. Disintegration of water droplets in an electric field. *Proc. R. Soc. London*, volume 280: pages 383–397, 1964.

Thoroddsen, S. T. and Takehara, K. The coalescence cascade of a drop. *Phys. Fluids*, volume 12, no. 1265, 2000.

Yue, P., Zhou, C. and Feng, J. J. A computational study of the boalescence between a drop and an interface in newtonian and viscoelastic fluids. *Phys. Fluids*, volume 18, no. 102102, 2006.

C Sharp interface simulations of surfactant-covered drops in electric fields

Teigen, K.E, Lervåg, K.Y., Munkejord, S.T.,
In Fifth European Conference on Computational Fluid Dynamics,
ECCOMAS CFD 2010,
Lisbon, Portugal, June 14–17 2010

V European Conference on Computational Fluid Dynamics
ECCOMAS CFD 2010
J. C. F. Pereira and A. Sequeira (Eds)
Lisbon, Portugal,14-17 June 2010

SHARP INTERFACE SIMULATIONS OF SURFACTANT-COVERED DROPS IN ELECTRIC FIELDS

Knut Erik Teigen*, Karl Yngve Lervåg† and Svend Tollak Munkejord†

*Norwegian University of Science and Technology,
Department of Energy and Process Engineering
NO-7491 Trondheim, Norway
e-mail: knut.erik.teigen@ntnu.no, knutert@gmail.com

†SINTEF Energy Research, Energy Processes
NO-7465 Trondheim, Norway
e-mail: {karl.lervag,svend.t.munkejord}@sintef.no

Key words: fluid dynamics, multiphase flow, surfactant, level-set method, sharp interface, ghost-fluid method

Abstract. *A level-set method for computations of interfacial flows with insoluble surfactants with electric fields is presented. The discontinuities at the interface are captured in a sharp manner using the ghost-fluid method. The accuracy of the method is tested and compared to the standard level-set method. The method is then used to study the combined effect of insoluble surfactants and electric fields on the motion and deformation of a falling drop. It is found that the surfactant generally reduces the deformation and the terminal velocity of the drop. This reduction is most pronounced in the nearly spherical regime where the drop behavior is similar to a solid sphere due to the interface immobilization caused by the presence of a surfactant. The electric field increases the terminal velocity by stretching the drop in the direction of the electric field. This effect is largest for the surfactant-covered drop, which is deformed more due to the lower average interfacial tension.*

1 INTRODUCTION

The presence of surface-active agents (surfactants) at fluid interfaces can have a considerable effect on flow dynamics. Surfactants are amphiphilic organic compounds, which can be adsorbed at liquid-gas or liquid-liquid interfaces. The presence of surfactants typically alters the interface dynamics by a reduction in the interfacial tension. An inhomogeneous distribution of surfactants produces gradients in interfacial tension, which again gives rise to tangential forces along the interface. Through this so-called Marangoni effect, surfactants can play an important role in several physical phenomena, for instance vortex pair interaction[50,14], fingering[49,29] and drop break-up and coalescence[15,17,25,12].

The authors' interest is the influence of surfactants on the breaking of water-in-oil emulsions. In some oil fields, heavy oils with high viscosity combined with surface-active

components like asphaltenes and resins make it hard to extract the water using traditional sedimentation processes. In order to accelerate the sedimentation process, an electric field can be applied to the emulsion[8]. This will introduce attractive forces between the water drops, which increase the coalescence rate and thereby also the sedimentation rate.

Both the influence of surfactants and electric fields on drops have been studied numerically. However, to the authors' knowledge, this is the first numerical study of the combined effect of surfactant and electric fields. The available numerical methods for detailed simulations of two-phase flows can roughly be divided into two categories: interface-tracking and interface-capturing methods. Interface-tracking methods use either a separate grid for the interface, or a set of interconnected points to mark the interface. Examples of methods which have been applied to both surfactants and electric fields include the boundary-integral method[41,32,31,40,24] and the front-tracking method[19,56,34,16]. In general, interface-tracking approaches can be made very accurate, but can be relatively complicated to implement, especially in three dimensions and for problems involving topological changes.

In interface-capturing methods, the interface is not tracked explicitly, but instead is implicitly defined through a regularization of the interface. This means that the evolution of the interface is handled independently of the underlying grid, which greatly simplifies gridding, discretization and handling of topological changes. Well known methods in this category include the volume-of-fluid method[39,18], the phase-field method[46,47] and the level-set method[54,53,52,48,3]. Other novel methods are the lattice-Boltzmann method with electric fields[57] and the smoothed particle hydrodynamics method with soluble surfactants[2].

In this paper, we build upon the previous work of Xu et al. (2006)[53], and use the level-set method to represent the interface. However, instead of using the immersed-interface method[26] (IIM) to handle discontinuities across the interface, we employ the ghost-fluid method[9] (GFM). For the case of constant coefficients in the jump conditions, the GFM is a lower order version of the IIM. The main disadvantage of the IIM is that discontinuity relations for higher-order derivatives must be developed and implemented. For more complex physical systems, these may not be available *a priori*, in which case an iterative method has to be used to calculate the discontinuites, leading to a more complex implementation and a more expensive computation. The GFM has the advantages that it is more accurate than the standard level-set method based on a diffuse interface, the so-called continuous surface force (CSF) method, while remaining computationally efficient and relatively easy to implement for both two- and three-dimensional problems. A ghost-fluid method for electric fields was presented in Hansen (2008)[3], and we use the same methodology here.

The paper is organized as follows: In Section 2, we state the governing equations and briefly discuss the numerical method. In Section 3 we present simulations demonstrating the capabilities of the method. We first compare the accuracy to a diffuse-interface method using a test case with an available analytical solution, then we present simulations of a

falling drop and discuss the influence of surfactants and electric fields. Section 4 concludes the work.

2 GOVERNING EQUATIONS AND NUMERICAL METHODS

The full Navier–Stokes equations are solved in each phase, and the interface between the two phases is captured using the level-set method. The ghost-fluid method is used to treat discontinuities across the interface in a sharp manner.

2.1 Flow equations

The flow is governed by the incompressible Navier–Stokes equations, with added terms for interfacial-tension forces and electric forces:

$$\begin{aligned} \rho\left(\frac{\partial \boldsymbol{u}}{\partial t} + (\boldsymbol{u}\cdot\boldsymbol{\nabla})\boldsymbol{u}\right) &= -\boldsymbol{\nabla}p + \boldsymbol{\nabla}\cdot[\mu(\boldsymbol{\nabla}\boldsymbol{u} + \boldsymbol{\nabla}\boldsymbol{u}^T)] + \rho\boldsymbol{g} + \boldsymbol{F_e} + \boldsymbol{F_s}, \\ \boldsymbol{\nabla}\cdot\boldsymbol{u} &= 0. \end{aligned} \tag{1}$$

Here, ρ is the density, $\boldsymbol{u}$ is the velocity, p is the pressure, μ is the dynamic viscosity and $\boldsymbol{g}$ is the gravitational acceleration. F_e is the force due to the presence of an electric field. The effect of an interface, Γ, in the domain results in a singular interfacial force which can be expressed by

$$\boldsymbol{F_s}(\boldsymbol{x}, t) = \int_{\Gamma(t)} \hat{\boldsymbol{F}}_{\boldsymbol{s}}(s, t)\delta(\boldsymbol{x} - \boldsymbol{X}(s, t))\mathrm{d}s, \tag{2}$$

where s is the arc-length, $\boldsymbol{X}(s, t)$ is the parametrization of the interface, $\boldsymbol{x}$ is the spatial position and δ is the Dirac delta function. For the present problem, $\hat{\boldsymbol{F}}_{\boldsymbol{s}}$ is given by

$$\hat{\boldsymbol{F}}_{\boldsymbol{s}} = \sigma\kappa\boldsymbol{n} - \boldsymbol{\nabla}_\Gamma\sigma \tag{3}$$

The first term accounts for the normal capillary force due to interfacial tension. Here, σ is the coefficient of interfacial tension, κ the curvature and $\boldsymbol{n}$ is the outward pointing unit normal vector. The second term is the Marangoni force, which is caused by gradients in the interfacial tension and acts tangentially to the interface. The interfacial gradient, $\boldsymbol{\nabla}_\Gamma$, is given by

$$\boldsymbol{\nabla}_\Gamma = (\boldsymbol{I} - \boldsymbol{n}\boldsymbol{n})\boldsymbol{\nabla}, \tag{4}$$

where $\boldsymbol{I}$ is the identity tensor.

2.2 Surfactants

Gradients in the interfacial tension occur due to the presence of an insoluble surfactant on the interface. The dynamics of the surfactant concentration, f, is governed by[54,53]

$$\begin{aligned} &\frac{\partial f}{\partial t} + \boldsymbol{u}\cdot\boldsymbol{\nabla}f - \boldsymbol{n}\cdot\boldsymbol{\nabla}\boldsymbol{u}\cdot\boldsymbol{n}f \\ &\quad = D_f\left(\boldsymbol{\nabla}^2 f - \boldsymbol{n}\cdot\boldsymbol{\nabla}\boldsymbol{\nabla}\cdot\boldsymbol{n}f + \kappa(\boldsymbol{n}\cdot\boldsymbol{\nabla}f)\right) \end{aligned} \tag{5}$$

where D_f is the surfactant diffusion coefficient. We employ the Langmuir equation of state to relate the interfacial tension and surfactant concentration,

$$\sigma(f) = \sigma_0 \left[1 + \beta \ln\left(1 - \frac{f}{f_\infty}\right)\right]. \tag{6}$$

Here, $\beta = \bar{R}T f_\infty/\sigma_0$ is the interface elasticity number, which is a measure of the sensitivity of interfacial tension to surfactant concentration. f_∞ is the maximum surfactant packing, $\bar{R}$ is the universal gas constant, T the temperature and σ_0 is the interfacial tension of a clean interface.

In this paper, we will assume that the surfactant is restricted to the interface, i.e. it will not be able to dissolve into the surrounding fluid. Surfactants behave as insoluble monolayers in two limits[37]. The first corresponds to dilute bulk concentrations, for which the diffusion flux from the bulk is slow compared to the interface convection flux. The second limit corresponds to slow adsorption-desorption exchange, which can occur in aqueous systems with long-chained surfactants.

Since we assume that the surfactant is insoluble, it is only defined on the interface. In order to solve the evolution equation numerically, we must therefore first extend the surfactant concentration off the interface[58]. This is accomplished by solving[1]

$$\frac{\partial f}{\partial \tau} + S(\phi_0)\boldsymbol{n} \cdot \boldsymbol{\nabla} f = 0. \tag{7}$$

Here, S is a sign function given by

$$S(\phi) = \frac{\phi}{\sqrt{\phi^2 + 2\Delta x^2}}. \tag{8}$$

Note that this equation is hyperbolic, so it is not necessary to solve it to steady state, since only the information a few grid points away from the interface is relevant.

2.3 Electric forces

We want to model a conductive drop in an otherwise dielectric medium, for instance a water drop in oil. This can be achieved by assuming perfect dielectric materials with no free charges, and then choosing a high permittivity ratio between the two phases[30].

With these assumptions, the electric force is given by

$$\boldsymbol{F}_e = \boldsymbol{\nabla} \cdot \boldsymbol{M}, \tag{9}$$

where $\boldsymbol{M}$ is the Maxwell stress tensor,

$$\boldsymbol{M} = \varepsilon\varepsilon_0 \left[\boldsymbol{E}\boldsymbol{E} - \frac{1}{2}(\boldsymbol{E} \cdot \boldsymbol{E})\boldsymbol{I}\right]. \tag{10}$$

Here, $\boldsymbol{E}$ is the electric field. With the above assumptions, $\boldsymbol{\nabla\cdot M} = \boldsymbol{0}$ everywhere except at the interface. The electric field is divergence free, such that

$$\boldsymbol{E} = -\boldsymbol{\nabla}\Psi, \tag{11}$$

where Ψ is the electric potential. The electric potential is found from the following Laplace equation:

$$\boldsymbol{\nabla\cdot}(\varepsilon\varepsilon_0\boldsymbol{\nabla}\Psi) = 0. \tag{12}$$

2.4 Interface capturing

The interface is captured using the level-set method[44,36]. This method allows accurate computation of the evolution of an interface, along with automatic handling of topological changes. The ghost-fluid method[9,21] (GFM) is used to take discontinuities across the interface into account. This method handles the jumps in physical properties directly in the numerical stencils, without the need for any smearing of properties.

The GFM requires jump conditions, which are relations between the physical quantities on each side of the interface. The jump conditions for the present problem are[21,3,13]

$$[\boldsymbol{u}] = 0, \tag{13}$$

$$[p] = 2[\mu]\boldsymbol{n}\cdot\boldsymbol{\nabla u}\cdot\boldsymbol{n} + \boldsymbol{n}\cdot[\boldsymbol{M}]\cdot\boldsymbol{n} + \sigma\kappa, \tag{14}$$

$$[\Psi] = 0, \tag{15}$$

$$\begin{aligned}[\mu\boldsymbol{\nabla u}] = [\mu]\Big(&(\boldsymbol{n}\cdot\boldsymbol{\nabla u}\cdot\boldsymbol{n})\boldsymbol{nn} + (\boldsymbol{n}\cdot\boldsymbol{\nabla u}\cdot\boldsymbol{t})\boldsymbol{nt} \\ &- (\boldsymbol{n}\cdot\boldsymbol{\nabla u}\cdot\boldsymbol{t})\boldsymbol{tn} + (\boldsymbol{t}\cdot\boldsymbol{\nabla u}\cdot\boldsymbol{t})\boldsymbol{tt}\Big) \\ &- (\boldsymbol{t}\cdot[\boldsymbol{M}]\cdot\boldsymbol{n})\boldsymbol{tn} - (\boldsymbol{t}\cdot\boldsymbol{\nabla}_\Gamma\sigma)\boldsymbol{tn},\end{aligned} \tag{16}$$

$$[\boldsymbol{\nabla}p] = 0, \tag{17}$$

$$[\varepsilon\boldsymbol{n}\cdot\boldsymbol{\nabla}\Psi] = 0. \tag{18}$$

A well-known issue with the level-set method is that it does not conserve mass. The more accurate ghost-fluid discretization somewhat alleviates the problem, but for long-running simulations it is still an issue. In particular, since we use an explicit time-integration method in this work, simulations at low Reynolds numbers (i.e. highly viscous fluids) suffer from severe mass loss. We therefore introduce a simple mass correction scheme for these simulations. At each time step, we add a constant, α, to the level-set function, where α is found by solving the equation

$$\int_\Omega H(\phi)(\phi+\alpha)\mathrm{d}\Omega = \int_\Omega H(\phi_0)\phi_0\mathrm{d}\Omega. \tag{19}$$

Here, ϕ_0 is the initial level-set function. The effect of this correction scheme is to add any lost mass back globally over the entire drop. Since mass loss typically occurs in regions of high curvature and low resolution, this scheme works well for low Reynolds number

drops, which tend to remain nearly spherical. We note that more sophisticated approaches for dealing with the mass loss exist. These include coupling with Lagrangian particles[7], coupling with the VOF method[43,51] and using modified advection procedures[35,38,28].

2.5 Numerics

A second-order projection scheme is used to solve the Navier–Stokes equations. The evolution in time is performed using a four-step third-order, strong stability-preserving (SSP) Runge-Kutta (RK) method[23,22], while a second-order SSP RK method is employed for the evolution of the level-set equation, the reinitialization of the level-set equation and extrapolation of the velocity field and surfactant concentration.

The equations are spatially discretized on an equidistant staggered grid with cell spacing h, where scalar values are stored in cell centers and vector values are stored at cell boundaries. The convective terms are discretized using the fifth order Weighted Essentially Non-Oscillatory (WENO) scheme[20], and Laplacian and gradient terms are discretized using the ghost-fluid version of standard, second-order central differences. The Poisson equations for pressure and electric potential are solved using a multigrid algorithm.

To reduce the computational costs, we use a simple scheme to move the domain along with the falling drop. If the mass center of the drop moves to a neighboring grid cell, the grid is shifted one cell in the opposite direction to account for this, and data is extrapolated to the new grid cells.

3 RESULTS

In this Section, we present some numerical results on drop dynamics using the above method. We begin by validating the implementation of the Marangoni stresses by simulating a bubble rising due to thermocapillary effects. Here, we also compare the results to the CSF method. The implementation of electric forces has been validated and compared against the CSF method elsewhere[46]. Next, we investigate the influence of surfactants and electric fields on a viscous drop falling through a viscous medium, e.g. a water drop falling through oil. Two representative systems are studied, one at a low Reynolds number where the drop remains spherical, and one at a high Reynolds number where the drop deforms significantly.

3.1 Bubble rising due to thermocapillary effects

As a test case for the implementation of the interfacial-tension force, we will simulate the thermocapillary migration of a bubble. It is well known that due to the dependence of interfacial tension on temperature, there will be a discontinuity in the tangential stresses across the interface for a bubble in a temperature gradient[55]. The result is a motion of the drop in a direction that will reduce its interfacial free energy. The flow at the interface will be from the warmer to the cooler pole of the bubble, and therefore, the bubble will move

in the direction of the warmer pole. This motion is known as thermocapillary migration.

We assume that the temperature varies as

$$\frac{T(z)}{T_\infty} = \frac{z}{L}, \tag{20}$$

where L is the domain height, and the relationship between temperature and interfacial tension is

$$\sigma(z) = \sigma_0 \left(1 - \beta \frac{T(z)}{T_\infty}\right). \tag{21}$$

We assume that the pressure in the surrounding fluid is zero. Then the pressure inside the bubble is given by

$$p(z) = \frac{2\sigma(z)}{R}, \tag{22}$$

where R is the bubble radius. For a viscous bubble in a linear temperature gradient, an approximation for the terminal rise velocity is[55]

$$V_{YBG} = \frac{2\Big(\sigma_0 \beta R/L - \Delta\rho g R^2 (\mu_1 + \mu_2)/\mu_2\Big)}{(6\mu_1 + 9\mu_2)}. \tag{23}$$

Here, we choose a domain size $5R \times 15R$, and parameters $\mu_1 = \mu_2 = 0.2\,\mathrm{Pa,s}$, $R = 0.5\,\mathrm{m}$, $\sigma_0 = 1.0\,\mathrm{N/m}$ and $\beta = 1.0$. Gravity effects are neglected. According to Eq. (23), this should give a Reynolds number of $\mathrm{Re} = 0.0444$, which is well within the creeping flow regime for which the equation is valid.

We first compare the GFM and the CSF method with respect to Eq. (22) for the pressure. Fig. 1a shows a close-up of pressure contours inside the bubble. In Fig. 1b, the pressure along the vertical center line is compared to the analytical result for both the GFM and the CSF method for $R/h = 10$. We see that with the GFM, the jump in pressure at the interface is treated in a sharp manner, and that the pressure inside the bubble is accurately captured. For the CSF, however, the discontinuity is smeared out, and the jump in pressure is over-predicted. In Table 1, the relative error of the pressure in the bubble center is given together with convergence rates for the GFM. The error decreases in a first-order fashion, which is consistent with other results obtained with the GFM[3].

Next, we compare the simulated rise velocity to Eq. (23). The computational rise velocity was calculated with

$$V(t) = \frac{\int_\Omega H(\boldsymbol{x}, t)\boldsymbol{u}(\boldsymbol{x}, t) \cdot \boldsymbol{e}_z \mathrm{d}\Omega}{\int_\Omega H(\boldsymbol{x}, t)\mathrm{d}\Omega}, \tag{24}$$

where $H(\boldsymbol{x}, t)$ is the smeared out Heaviside function and $\boldsymbol{e}_z$ is the unit vector in the z-direction. This integral was evaluated using the midpoint rule.

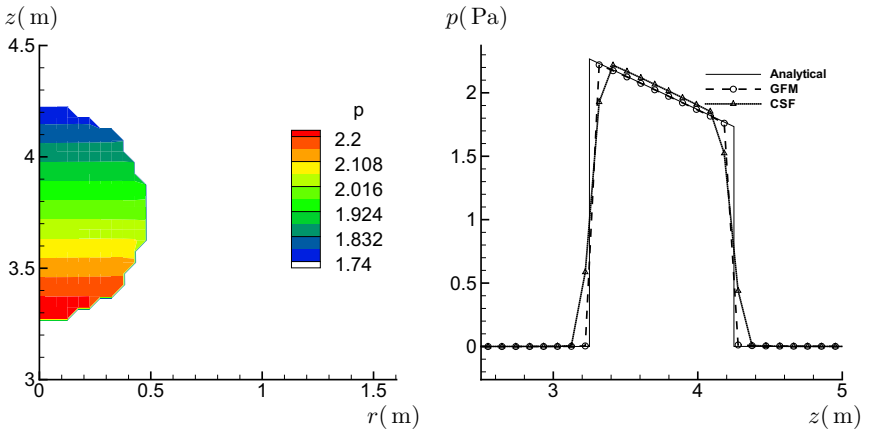

(a) Pressure contours after one time step.

(b) Pressure along vertical centerline compared to analytical result, Eq. (22).

Figure 1: Pressure after one time step for a bubble rising in a linear surfactant gradient.

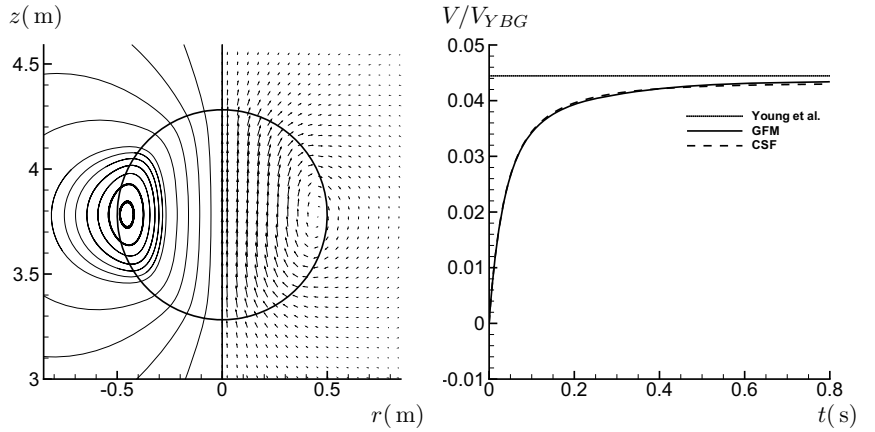

(a) Velocity vectors at steady state.

(b) Rise velocity compared to theoretical result.

Figure 2: Velocity field at steady state and rise velocity versus time for the thermocapillary migration test case.

Table 1: Thermocapillary migration test case. Error and convergence for the pressure inside the bubble after one time step.

R/h	Relative error ($\times 10^{-2}$)	Order
10	1.28	–
20	0.655	0.97
30	0.330	0.99
40	0.168	0.98

Table 2: Parameters for falling drop at low Reynolds number

Parameter	Symbol	Value
Drop radius	R	$1.03 \times 10^{-3}\,\mathrm{m}$
Drop density	ρ_1	$1.128 \times 10^{3}\,\mathrm{kg/m^3}$
Matrix density	ρ_2	$9.49 \times 10^{2}\,\mathrm{kg/m^3}$
Drop viscosity	μ_1	$6.3 \times 10^{-3}\,\mathrm{Pa\,s}$
Matrix viscosity	μ_2	$3.8 \times 10^{-2}\,\mathrm{Pa\,s}$
Interfacial tension	σ	$2.91 \times 10^{-3}\,\mathrm{N/m}$
Surfactant concentration	f_0	$2.4 \times 10^{-6}\,\mathrm{mol/m^2}$
Maximum surfactant packing	f_∞	$6.0 \times 10^{-6}\,\mathrm{mol/m^2}$
Interface elasticity	β	0.4
Diffusion coefficient	D_f	$1 \times 10^{-6}\,\mathrm{m^2/s}$
Electric field	E_0	$8 \times 10^{5}\,\mathrm{V/m}$
Drop relative permittivity	ε_1	250
Matrix relative permittivity	ε_2	1

The velocity field around the bubble at steady state is shown in Fig. 2a for a grid spacing of $R/h = 10$. The figure is in good agreement with results from the literature[34]. Fig. 2b shows the normalized rise velocity for both the GFM and the CSF method. After an initial acceleration phase, the velocity approaches the theoretical prediction asymptotically. We observe that the results for the GFM is closer to the theoretical value. However, the accuracy is surprisingly good for both methods considering the relatively coarse grid used. For the GFM, the difference between the theoretical rise velocity and the computed at $t = 0.8\,\mathrm{s}$ is 2.38%, while for the CSF method, the difference is 3.31%.

3.2 Falling drop at low Reynolds number

We now consider a drop falling in a gravity field at a low Reynolds number. The parameters chosen are given in Table 2. In terms of dimensionless numbers, these pa-

rameters give an Eötvös number of $\mathrm{Eo} = \Delta\rho g D^2/\sigma = 0.256$ and a Morton number of $\mathrm{Mo} = \Delta\rho g\mu_2^4/\rho_2^2\sigma^3 = 1.65 \times 10^{-4}$. For these low values, the drop moves slowly with a nearly spherical shape[4].

At low Reynolds numbers, we can compare our numerical results to the Hadamard-Rybczynski formula for a viscous drop in creeping flow[11],

$$V_{T,\mathrm{HR}} \frac{2\Delta\rho g R^2(\mu_1 + \mu_2)}{3\mu_2(3\mu_1 + 2\mu_2)}. \tag{25}$$

For the parameters considered here, we get $V_{T,\mathrm{HR}} = 1.53 \times 10^{-2}\,\mathrm{m/s}$, or $\mathrm{Re} = 0.785$.

For the simulations, we choose a domain size of $16R \times 32R$ and a grid spacing of $R/h = 20$. The simulated terminal velocity is $V_T = 1.40 \times 10^{-2}\,\mathrm{m/s}$, which is close to the predicted value. The discrepancy is most likely due to the simulation being performed in a bounded domain, as opposed to the formula which is derived for an infinite domain.

Next, we look at the effect of having a surfactant on the interface. For the contaminated drop, the simulated terminal velocity is reduced to $V_T = 0.96 \times 10^{-2}\,\mathrm{m/s}$. The reason for this becomes evident by looking at the velocity profiles given in Figure 3. For the contaminated drop, the internal circulation nearly disappears, and the drop behaves close to a rigid particle. The Stokes formula for a rigid, spherical particle in creeping flow,

$$V_{T,\mathrm{S}} \frac{2\Delta\rho g R^2}{9\mu_2}, \tag{26}$$

gives $V_{T,\mathrm{S}} = 1.09 \times 10^{-2}\,\mathrm{m/s}$, which is close to the terminal velocity for the contaminated drop. Again, the discrepancy is attributed to the bounded domain.

Figure 4a shows the surfactant concentration as a function of the arc length, s, measured in the counter-clockwise direction. The surfactant concentration takes the shape of an S-curve, and hence the Marangoni stresses are evenly distributed across the drop. The consequence of this is illustrated in Figure 4b, which shows the interface velocity for both the clean and the contaminated drop. The interface velocity of the contaminated drop is greatly reduced across the entire drop interface.

We then consider the effect of an electric field. The drop is allowed to reach a steady state before the electric field is switched on. The strength of the electric field can be characterized by the electric capillary number, $\mathrm{Ca}_E = \varepsilon_0\varepsilon_2 D E_0^2/\sigma$. A conductive drop submitted to an electric field becomes unstable when $\mathrm{Ca}_E \approx 0.41$[45]. However, here the gravitational force will act to stabilize the drop, allowing the use of an even higher Ca_E. We choose $\mathrm{Ca}_E = 0.45$, which gives $E_0 \approx 8 \times 10^5\,\mathrm{V/m}$.

Figure 5a illustrates the drop shape for the clean drop, along with electric field lines and velocity vectors. The drop clearly stretches into a prolate shape. This more streamlined profile gives a reduction in drag and hence a higher terminal velocity. The terminal velocity was calculated to be $V_T = 1.50 \times 10^{-2}\,\mathrm{m/s}$, an increase over the clean drop without an electric field. The aspect ratio of the drop is 0.770, while theory predicts

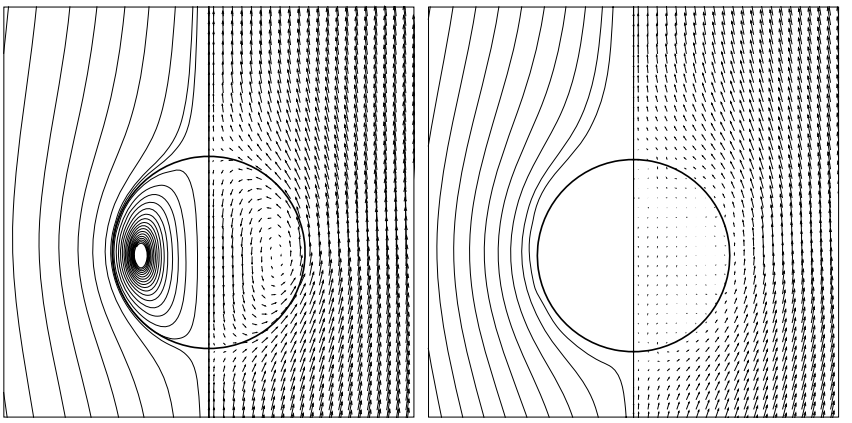

(a) Clean (b) Contaminated

Figure 3: Low Re drop. Streamlines and velocity vectors in a coordinate system moving with the drop centroid. Velocity vectors are plotted at every other grid point.

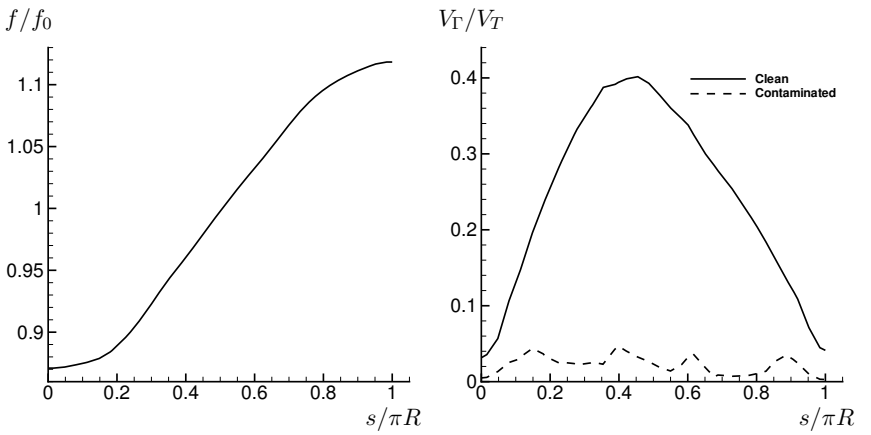

(a) Surfactant concentration (b) Interface velocities

Figure 4: Low Re drop. Surfactant concentration and interface velocities as functions of arc length.

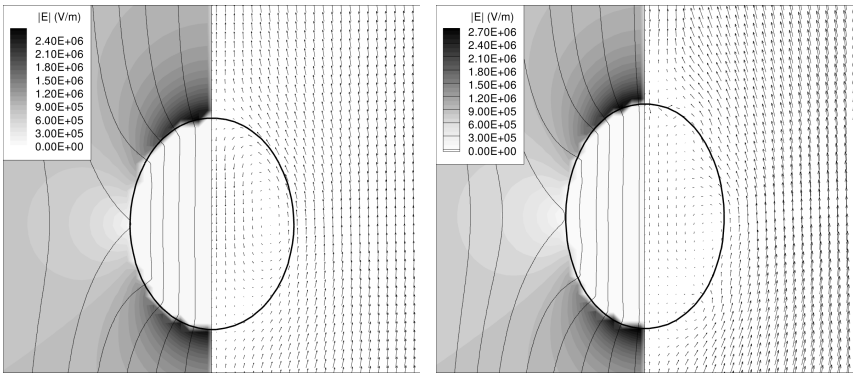

(a) Clean (b) Contaminated

Figure 5: Low Re drop with electric field. The left part of the drop shows streamlines of the electric field and contours colored by the electric field magnitude. The right part of the drop shows velocity vectors in a coordinate system moving with the drop centroid. Velocity vectors are plotted at every other grid point.

a minimum aspect ratio of 0.526[45]. Since we have an electric field stronger than the predicted critical value for a stationary drop, this demonstrates the stabilizing effect of the gravitational force.

The contaminated drop with an electric field is shown in Figure 5b. For this drop, the terminal velocity has increased to $V_T = 1.09 \times 10^{-2}\,\mathrm{m/s}$ compared to the contaminated drop without an electric field. This increase in terminal velocity is much larger than for the clean drop, which is caused by the lower average surface tension yielding a higher degree of stretching. An aspect ratio of 0.700 is calculated for the contaminated drop compared to 0.770 for the clean drop.

Finally, we observe that the electric field lines are close to perpendicular to the interface at the drop interface, and that the electric field magnitude is close to zero inside the drop. This indicates that our method of approximating a conductive drop in a dielectric medium by simulating a dielectric/dielectric system with high permittivity ratio is satisfactory.

3.3 Falling drop at high Reynolds number

We now consider a drop at a relatively high Reynolds number. We use the same parameters as above, with the exception of a higher radius, $R = 5.15 \times 10^{-3}$, and a lower matrix viscosity, $\mu_2 = 0.19$, to achieve a higher Reynolds number. The dimensionless parameters for this case becomes $\mathrm{Eo} = 6.4$ and $\mathrm{Mo} = 1.03 \times 10^{-5}$. For a clean drop, the calculated terminal velocity was $V_T = 0.131\,\mathrm{m/s}$ which gives $\mathrm{Re} = 67.4$. An experiment performed with the same parameters gave $\mathrm{Re} = 67.9$[33], which very close to the simulated value. Since the viscosity of the matrix fluid is lower in this case, we expect the boundaries

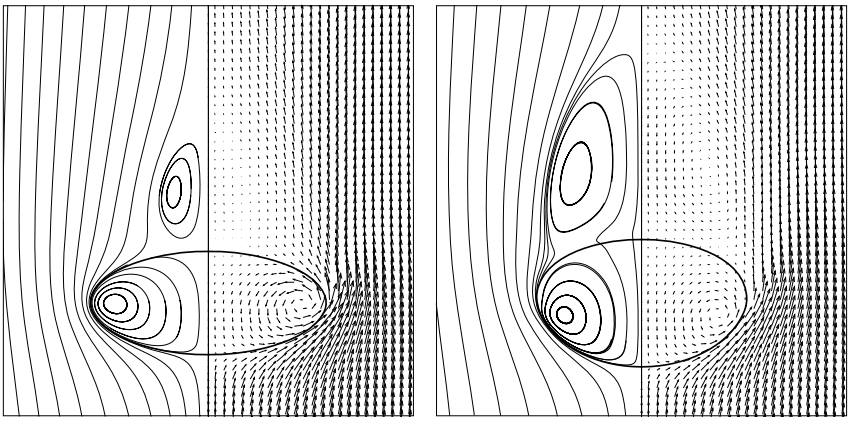

(a) Clean (b) Contaminated

Figure 6: High Re drop. Streamlines and velocity vectors in a coordinate system moving with the drop centroid. Velocity vectors are plotted at every other grid point.

to have less influence for this drop. The excellent agreement with the experiment indicates that this is indeed the case. Figure 6a shows the drop shape and velocity pattern. At this higher Re, the drop deforms into an ellipsoidal shape, and a vortex is formed behind the drop.

We then add surfactants to the system. It is well known that for contaminated drops or bubbles moving at higher Reynolds numbers through an otherwise stagnant fluid, the surfactants will be swept to the rear of the drop. This will create a region where the interface is nearly immobile due to the resulting high Marangoni stresses, while the front of the drop will be surfactant-free and mobile. The immobile region is often denoted the *stagnant cap*. Several models have been developed which relate the cap angle to e.g. the drag coefficient. The numerical method used here requires no assumption of a stagnant cap, and no *a priori* estimate of the cap angle is necessary.

The resulting drop shape and velocity pattern for the contaminated drop is given in Figure 6b. It is evident that the deformation is smaller than for the clean drop. Additionally, we see that the center of the internal vortex has moved closer to the front, and that the trailing vortex is larger for the contaminated drop. This results in a lower terminal velocity of $V_T = 0.119\,\mathrm{m/s}$ compared to $V_T = 0.131\,\mathrm{m/s}$ for the clean drop. This is a much lower difference than for the low Re drop.

The surfactant concentration is shown in Figure 7a. Here, the gradient in the surfactant concentration does not vary smoothly like for the low Re drop. Instead, there is no surfactant at the tip of the drop, followed by a sharp jump in concentration towards the back of the drop. This jump in concentration will effectively immobilize this part of the

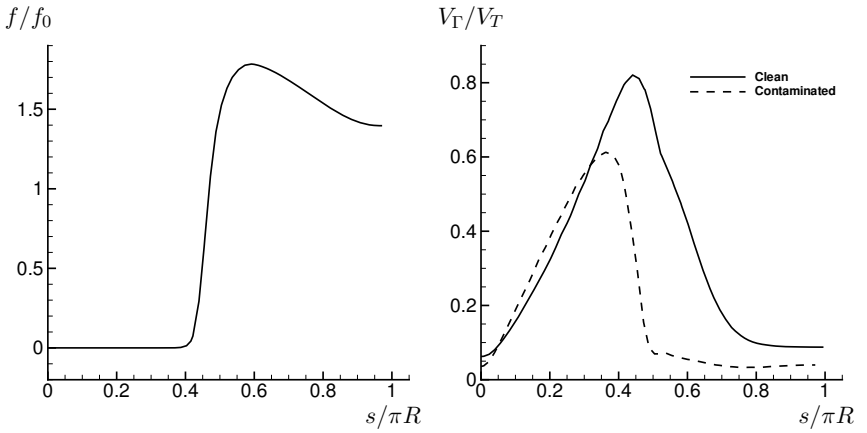

(a) Surfactant concentration (b) Interface velocities

Figure 7: High Re drop. Surfactant concentration and interface velocities as functions of arc length.

drop, due to high Marangoni stresses. This is further illustrated in Figure 7b, which shows the interface velocity for both the clean and contaminated drop. Here we clearly see that for the contaminated drop the interface velocity is greatly reduced in the region of high surfactant concentration.

We then consider the effect of an electric field. The electric capillary number is $\mathrm{Ca}_E = 0.7835$, which gives an electric field of $E_0 = 5 \times 10^5\,\mathrm{V/m}$. We use a higher Ca_E here since the stabilizing convection is stronger. For the clean drop, the terminal velocity increases to $V_T = 0.138\,\mathrm{m/s}$. As can be seen in Figure 8a, there is little change compared to the case without an electric field. For the contaminated drop, shown in Figure 8b, there is a more pronounced change. This is also reflected in the terminal velocity, which increases to the same as the clean drop, $V_T = 0.138\,\mathrm{m/s}$. Again, this is caused by the lower surface tension of the contaminated drop allowing a higher degree of stretching.

If the electric field is increased to $E_0 = 6 \times 10^5\,\mathrm{V/m}$, the clean drop remains stable, while the contaminated drop becomes unstable. This is due to the stagnant cap, which has a very low interfacial tension compared to the clean drop. This makes the drop less resistant to the electric stresses and renders it unstable at a lower electric field strength. The evolution of the drop is shown in Figure 9, with the drop revolved around the z-axis and colored according to the surfactant concentration. When the electric field is switched on, the back of the drop starts to stretch, while the front of the drop remains stable. Eventually, the stretched part develops a pointed tip and we see the formation of a small drop on the tip. It has been shown both experimentally and numerically that conductive drops become pointed and starts emitting small drops from the tips[45,40,27,6,42]. An

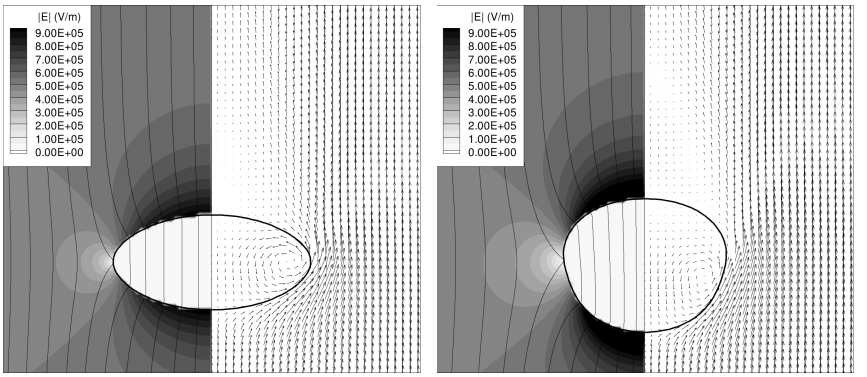

(a) Clean (b) Contaminated

Figure 8: High Re drop with electric field. The left part of the drop shows streamlines of the electric field and contours colored by the electric field magnitude. The right part of the drop shows velocity vectors in a coordinate system moving with the drop centroid. Velocity vectors are plotted at every other grid point.

interesting observation is that as the tip starts to form, surfactant is swept from the tip and towards the middle of the drop. The drop formed at the tip has a very low concentration of surfactants. This is a fundamentally different process from surfactant-covered drops being stretched in extensional flows or shear flows. For these flows, surfactant is swept to the drop tips and contributes to the tip-streaming process[32,5,39,47]. This creates small drops with high surfactant concentrations which consequently are very stable. The present simulations suggest that this is not the case for drops broken due to electric fields.

Another interesting phenomenon suggested by the experimental results of Ha & Yang[10] is that the presence of a surfactant can cause the break-up mode to change from bulbous end formation to tip-streaming. The proposed physical mechanism was the same as for drops in shear flows. Again, our numerical results suggest that this may not be the correct explanation for the observed behavior.

4 CONCLUSIONS

A level-set method for computations of interfacial flows with insoluble surfactants and electric fields was presented. It was shown that the method is more accurate than the standard level-set method at handling the pressure jump at the interface. Currently, the method only handles insoluble surfactants. A natural extension of the method is to include solubility. For instance, the method proposed in Teigen et al.[46] for the phase-field method is also applicable to the level-set method.

The method was used to study an axisymmetric drop falling in an otherwise quiescent fluid. It was found that the surfactant reduced the deformation and the terminal velocity

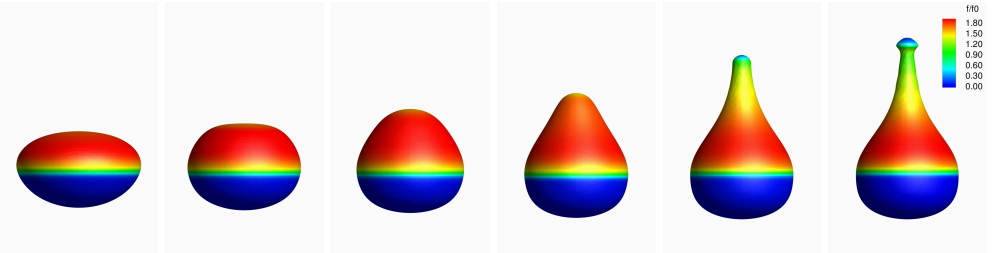

Figure 9: Behavior of contaminated drop above the critical field strength. The drop surface is colored according to surfactant concentration. The first frame shows the drop before the electric field is switched on. The subsequent frames are at times 0.7, 1.0, 1.3, 1.6 and 1.7 seconds after the field has been switched on.

of the drop. The reduction was most pronounced at low Reynolds number, where the drop remains spherical. Here, the surfactant-covered drop behaved similarly to a solid sphere. These results are in agreement with experiments and simulations in the literature. The effect of an electric field was mainly to increase the terminal velocity. This is due to the drop stretching in the direction of the electric field, which gives a lower projected interface area and hence lower drag. This effect was also more evident at lower Reynolds numbers, which was attributed to lower convection forces which allowed the drop to stretch more. The effect of an electric field on the contaminated drop was also to increase the terminal velocity. However, the effect was slightly higher here, due to the overall lower interfacial tension of the contaminated drop which gives a lower resistance to deformation.

Only two different drops were investigated in this study, and the surfactant parameters and electric fields were not varied. It would be instructive to investigate a wider range of drop shapes, and study the influence of the surfactant parameters and electric fields in more detail. In particular, the observed behavior of an unstable drop is fundamentally different from previous results for drops in extensional flows or shear flows, and this warrants further studies.

Acknowledgement

This work forms part of the Electrocoalescence project, supported by The Research Council of Norway (169466/S30), and by the following industrial partners: Aker Solutions AS, BP Exploration Operating Company Ltd, Hamworthy Technology and Products AS, Shell Technology Norway AS, Petrobras, Saudi Aramco and Statoil ASA.

References

[1] D. Adalsteinsson and J.A. Sethian. The fast construction of extension velocities in level set methods. *J. Comput. Phys.*, 148:2–22, 1999.

[2] S. Adami, X.Y. Hu, and N.A. Adams. A conservative SPH method for surfactant dynamics. *J. Comput. Phys.*, 229(5):1909 – 1926, 2010.

[3] E. Bjørklund. The level-set method applied to droplet dynamics in the presence of an electric field. *Comput. Fluids*, 38(2):358–369, 2008.

[4] R. Clift, J. R. Grace, and M. E. Weber. *Bubbles, Drops and Particles*. Dover, Mineola, 2005.

[5] R. A. De Bruijn. Tipstreaming of drops in simple shear flows. *Chem. Eng. Sci.*, 48:277–284, 1993.

[6] N. Dubash and A. J. Mestel. Breakup behavior of a conducting drop suspended in a viscous fluid subject to an electric field. *Phys. Fluids*, 19:072101, 2007.

[7] D. Enright, R. Fedkiw, J. Ferziger, and I. Mitchell. A hybrid particle level set method for improved interface capturing. *J. Comput. Phys.*, 183:83–116, 2002.

[8] J. S. Eow and M. Ghadiri. Electrostatic enhancement of coalescence of water droplets in oil: a review of the technology. *Chem. Eng. J.*, 85:357–368, 2002.

[9] R. P. Fedkiw. A non-oscillatory Eulerian approach to interfaces in multimaterial flows. *J. Comput. Phys.*, 152:457–492, 1999.

[10] J. Ha and S. Yang. Effect of nonionic surfactant on the deformation and breakup of a drop in an electric field. *J. Colloid and Interface Sci.*, 206(1):195 – 204, 1998.

[11] J. S. Hadamard. Mouvement permanent lent d'une sphère liquide et visqueuse dans un liquide visqueux. *CR Acad. Sci.*, 1911.

[12] M. Hameed, M. Siegel, Y.-N. Young, J. Li, M. R. Booty, and D. T. Papageorgiou. Influence of insoluble surfactant on the deformation and breakup of a bubble or thread in a viscous fluid. *J. of Fluid Mech.*, 594:307–340, 2008.

[13] E. B. Hansen. *Numerical simulation of droplet dynamics in the presence of an electric field*. PhD thesis, Norwegian University of Science and Technology, Trondheim, 2005.

[14] A. Hirsa and W. W. Willmarth. Measurements of vortex pair interaction with a clean or contaminated free surface. *J. Fluid Mech.*, 259:25–45, 1994.

[15] Y. T. Hu, D. J. Pine, and L. Gary Leal. Drop deformation, breakup, and coalescence with compatibilizer. *Phys. Fluids*, 12:484–489, 2000.

[16] J. Hua, L. K. Lim, and C. Wang. Numerical simulation of deformation/motion of a drop suspended in viscous liquids under influence of steady electric fields. *Phys. Fluids*, 20(11):113302, 2008.

[17] Steven D. Hudson, Alex M. Jamieson, and Brian E. Burkhart. The effect of surfactant on the efficiency of shear-induced drop coalescence. *J. Colloid Interface Sci.*, 265:409 – 421, 2003.

[18] Ashley J. James and John Lowengrub. A surfactant-conserving volume-of-fluid method for interfacial flows with insoluble surfactant. *J. of Comput. Phys.*, 201:685 – 722, 2004.

[19] Y. J. Jan. *Computational Studies of Bubble Dynamics*. PhD thesis, University of Michigan, 1994.

[20] G. S. Jiang and D. Peng. Weighted ENO schemes for Hamilton-Jacobi equations. *SIAM J. Sci. Comp.*, 21:2126–2143, 2000.

[21] M. Kang, R. Fedkiw, and X. Liu. A boundary condition capturing method for multiphase incompressible flow. *J. Sci. Comput.*, 15:323–360, 2000.

[22] D. I. Ketcheson and A. C. Robinson. On the practical importance of the SSP property for Runge-Kutta time integrators for some common Godunov-type schemes. *Int. J. Numer. Meth. Fluids*, 48(3):271–303, January 2005.

[23] J. F. B. M Kraaijevanger. Contractivity of Runge-Kutta methods. *BIT*, 31(3):482–528, 1991.

[24] E. Lac and G. M. Homsy. Axisymmetric deformation and stability of a viscous drop in a steady electric field. *J. Fluid Mech.*, 590:239–264, 2007.

[25] L. G. Leal. Flow induced coalescence of drops in a viscous fluid. *Phys. of Fluids*, 16(6):1833–1851, 2004.

[26] R. J. LeVeque and Z. L. Li. The immersed interface method for elliptic equations with discontinuous coefficients and singular sources. *SIAM J. Num. Anal.*, 31:1019–1044, 1997.

[27] L. E. Lundgaard, G. Berg, A. Pedersen, and P. J. Nilsen. Electrocoalescence of water drop pairs in oil. In *Proceedings of 14th International Conference on Dielectric Liquids (ICDL 2002)*, 2002.

[28] E. Marchandise, J. F. Remacle, and N. Chevaugeon. A quadrature-free discontinuous galerkin method for the level set equation. *J. Comput. Phys.*, 212:338 – 357, 2006.

[29] O. K. Matar and S. M. Troian. The development of transient fingering patterns during the spreading of surfactant coated films. *Phys. Fluids*, 11:3232–3246, 1999.

[30] J. R. Melcher and G. I. Taylor. Electrohydrodynamics: A review of the role of interfacial shear stresses. *Annu. Rev. Fluid Mech.*, 1:111–146, 1969.

[31] W. J. Milliken and L. G. Leal. The influence of surfactant on the deformation and breakup of a viscous drop - the effect of surfactant solubility. *J. Colloid and Interface Sci.*, 166:275–285, 1994.

[32] W. J. Milliken, H. A. Stone, and L. G. Leal. The effect of surfactant on transient motion of Newtonian drops. *Phys. Fluids A*, 5:69–79, 1993.

[33] Z. Mohamed-Kassim and E. K. Longmire. Drop coalescence through a liquid/liquid interface. *Physics of Fluids*, 16(7):2170–2181, 2004.

[34] M. Muradoglu and G. Tryggvason. A front-tracking method for computation of interfacial flows with soluble surfactants. *J. Comput. Phys.*, 227:2238–2262, 2008.

[35] E. Olsson and G. Kreiss. A conservative level set method for two phase flow. *J. Comput. Phys.*, 210(1):225–246, 2005.

[36] S. Osher and R. Fedkiw. *Level set methods and dynamic implicit surfaces*. Springer, 2003.

[37] Y. Pawar and K. J. Stebe. Marangoni effects on drop deformation in an extensional flow: The role of surfactant physical chemistry. I. insoluble surfactants. *Physics of Fluids*, 8(7):1738–1751, 1996.

[38] D. A. Di Pietro, S. Lo Forte, and N. Parolini. Mass preserving finite element implementations of the level set method. *Appl. Numer. Math.*, 56:1179–1195, 2006.

[39] Y. Y. Renardy, M. Renardy, and V. Cristini. A new volume-of-fluid formulation for surfactants and simulations of drop deformation under shear at a low viscosity ratio. *European Journal of Mechanics - B/Fluids*, 21:49 – 59, 2002.

[40] J. D. Sherwood. Breakup of fluid droplets in electric and magnetic fields. *J. Fluid Mech.*, 188:133 – 146, 1988.

[41] H. A. Stone and L. G. Leal. The effect of surfactants on drop deformation and breakup. *J. Fluid Mech*, 220:161–186, 1990.

[42] G. Supeene, C. R. Koch, and S. Bhattacharjee. Deformation of a droplet in an electric field: Nonlinear transient response in perfect and leaky dielectric media. *J. of Colloid and Interface Sci.*, 318(2):463 – 476, 2008.

[43] M. Sussman and E. Puckett. A coupled level set and volume-of-fluid method for computing 3D and axisymmetric incompressible two-phase flows. *J. Comput. Phys.*, 162:301–337, 2000.

[44] M. Sussman, P. Smereka, and S. Osher. A level set approach for computing solutions to incompressible two-phase flow. *J. Comput. Phys.*, 114:146–159, 1994.

[45] G. Taylor. Disintegration of water droplets in an electric field. *Proc. R. Soc. London*, 280:383–397, 1964.

[46] K. E. Teigen, X. Li, J. Lowengrub, F. Wang, and A. Voigt. A diffuse-interface approach for modelling transport, diffusion and adsorption/desorption of material quantities on a deformable interface. *Comm. Math. Sci.*, 7:1009–1037, 2009.

[47] K. E. Teigen, J. Lowengrub, P. Song, , and A. Voigt. A diffuse-interface method for two-phase flows with soluble surfactants. *J. Comput. Phys.*, 2009. Submitted.

[48] G. Tomar, D. Gerlach, G. Biswas, N. Alleborn, A. Sharma, F. Durst, S. W. J. Welch, and A. Delgado. Two-phase electrohydrodynamic simulations using a volume-of-fluid approach. *J. Comput. Phys.*, 227:1267–1285, 2007.

[49] S. M. Troian, E. Herbolzheimer, and S. A. Safran. Model for the fingering instability of spreading surfactant drops. *Phys. Rev. Lett.*, 65:333–336, Jul 1990.

[50] G. Tryggvason, J. Abdollahi-Alibeik, W. W. Willmarth, and A. Hirsa. Collision of a vortex pair with a contaminated free surface. *Phys. Fluids A*, 4:1215–1229, 1992.

[51] S. P. van der Pijl, A. Segal, C. Vuik, and P. Wesseling. A mass-conserving level-set method for modelling of multi-phase flows. *Int. J. Num. Meth. Fluids*, 47:339–361, 2005.

[52] S. W. J. Welch and G. Biswas. Direct simulation of film boiling including electrohydrodynamic forces. *Phys. Fluids*, 19(012106), 2007.

[53] J. J. Xu, Z. Li, J. Lowengrub, and H. Zhao. A level set method for interfacial flows with surfactant. *J. Comput. Phys.*, 212:590–616, 2006.

[54] J. J. Xu and H. Zhao. An Eulerian formulation for solving partial differential equations along a moving interface. *J. Sci. Comp.*, 19:573–594, 2003.

[55] N. O. Young, J. S. Goldstein, and M. J. Block. The motion of bubbles in a vertical temperature gradient. *J. Fluid Mech.*, 6(03):350–356, 1959.

[56] J. Zhang, D.M. Eckmann, and P.S. Ayyaswamy. A front tracking method for a deformable intravascular bubble in a tube with soluble surfactant transport. *J. Comput. Phys.*, 214:366 – 396, 2006.

[57] J. Zhang and D. Y. Kwok. A 2D lattice Boltzmann study on electrohydrodynamic drop deformation with the leaky dielectric theory. *J. Comput. Phys.*, 206:150–161, 2005.

[58] H. K. Zhao, T. Chan, B. Merriman, and S. Osher. A variational level set approach to multiphase motion. *J. Comput. Phys.*, 127(1):179 – 195, 1996.

D Influence of surfactant on drop deformation in an electric field

Teigen, K.E, Munkejord, S.T.,
Submitted to Physics of Fluids, 2010

Influence of surfactant on drop deformation in an electric field

Knut Erik Teigen[1, a)] and Svend Tollak Munkejord[2, b)]
[1)] *Department of Energy and Process Engineering, Norwegian University of Science and Technology (NTNU), NO-7491 Trondheim, Norway*
[2)] *SINTEF Energy Research, P.O. Box 4761 Sluppen, NO-7465 Trondheim, Norway*

The deformation of a surfactant-covered, viscous drop suspended in a viscous fluid under the influence of an electric field is investigated using numerical simulations. The full Navier–Stokes equations are solved in both fluid phases, and the motion of the interface and the interfacial discontinuities are handled using the level-set method. The leaky-dielectric model is used to take into account the effect of an electric field. The surfactant is assumed to be insoluble, and an evolution equation for the motion of surfactant is solved along the drop surface. The surfactant concentration and the interfacial tension are coupled through a non-linear equation of state.

The numerical results show that the effect of surfactant strongly depends on the relative permittivity and conductivity between the fluids. The presence of surfactant can both increase and reduce the deformation, depending on the shape of the deformation and the direction of the electrically induced circulation.

PACS numbers: 47.65.-d, 47.55.D-, 47.55.dk
Keywords: Drop deformation, two-phase flow, electrohydrodynamics, surfactant

I. INTRODUCTION

Electric fields are used to manipulate drops in several industrial applications. These include taking advantage of induced circulation to promote heat transfer in heat exchangers[16] and increasing the coalescence rate between water drops to enhance demulsification in crude oils[7]. It is common for such fluid systems to contain surface-active agents, either naturally present as impurities or deliberately added to modify the properties of the system. For the case of demulsification of crude oils, crude oils contain natural surfactants such as asphaltenes, resins, waxes and naphthenic acids[24], but surfactants are also added to the system to act as a demulsifier.

The effect of surfactants on the steady-state deformation of a drop has been studied by, among others, Milliken *et al.*[20], Pawar and Stebe[22] and Eggleton *et al.*[5], Eggleton and Stebe[6] for a drop in extensional flow and by Li and Pozrikidis[17] and Lai *et al.*[15] for a drop in shear flow. Due to the external flow, surfactant will be swept to the tips of the drop. This gives rise to gradients in the interfacial tension which causes stresses tangential to the surface, often denoted Marangoni stresses, that try to redistribute the surfactant. The convection of surfactant gives a higher interfacial tension at the middle of the drop and a lower interfacial tension at the tips compared to a clean surface, which promotes a higher deformation. On the other hand, as the drop is stretched, the surfactant concentration is diluted due to the increase in interfacial area. For high Marangoni stresses, the interfacial tension can increase over the entire drop, and this dilatation can reduce deformation compared to a clean drop. For relatively dilute surfactant concentrations, the Marangoni stresses are low, so that the first effect dominates, and the deformation is larger than that of a clean drop. For very high surfactant concentrations, however, a small non-uniformity in surfactant gives rise to large Marangoni stresses, and the effect of dilatation becomes dominant, resulting in lower deformation compared to a clean drop. The influence of surfactants on breakup has been studied among others by Milliken *et al.*[20] and Eggleton *et al.*[4] for a drop in extensional flow and by De Bruijn[3] and Renardy *et al.*[23] for a drop in shear flow. It was observed that for dilute concentrations of surfactants, tip-streaming would occur, where the drop tips would become highly curved and emit small drops.

When the velocity field is induced by an electric field as opposed to externally applied through e.g. a shear flow, we may expect the drop behavior to be different. Of particular interest is the fact that a drop in an electric field may deform into either a prolate shape or an oblate shape depending on the electrical properties of the fluid system[18,26]. For the case of prolate deformation, the induced circulation can in addition run both from pole to equator and vice-versa, which will obviously affect the deformation when a surfactant is present.

To the authors' knowledge, the only study of the combined effect of electric fields and surfactants is Ha and Yang[9]. They demonstrated that for a relatively highly conducting drop, the change in deformation is only due to a uniform lowering of interfacial tension. This is not surprising, since for such a conductive drop, the electric field lines will be close to perpendicular to the drop interface, and the electric field inside the drop will be close to zero. Hence, the drop is unable to support a tangential stress and as the drop reaches a steady state the induced flow will tend to zero. The surfactant will eventually redistribute itself due to diffusion and the deformation will become equal to that of a clean surface (given the proper scaling of the electric field strength). For a leaky-dielectric system in which the drop deformed

[a)] Electronic mail: knut.erik.teigen@ntnu.no
[b)] Electronic mail: svend.t.munkejord@sintef.no

into an oblate shape, however, it was found that the presence of surfactant gave a larger deformation than that of a clean surface.

The aim of this work is to study the deformation of a surfactant-covered drop in an electric field using numerical simulations. In Section II we give the mathematical formulation of the problem and present our numerical method. In Section III we investigate the steady-state deformation for different configurations of electrical properties and the influence of surfactants. Concluding remarks and proposals for future work are given in Section V.

II. MATHEMATICAL MODEL AND NUMERICAL METHOD

A. The level-set method

We consider a system of two immiscible phases separated by an interface, Γ. We use the level-set method[21,25] to capture this interface, which allows handling of the discontinuities at the interface in a simple and accurate manner.

In the level-set method, the interface is defined implicitly by the zero level set

$$\Gamma = \{\boldsymbol{x} | \phi(\boldsymbol{x}, t) = 0\}, \tag{1}$$

where ϕ is the level-set function, which denotes the signed distance to the interface. The level-set function moves with the interface velocity $\boldsymbol{u}_{\text{int}}$ according to

$$\frac{\partial \phi}{\partial t} + \boldsymbol{u}_{\text{int}} \cdot \boldsymbol{\nabla} \phi = 0. \tag{2}$$

To allow this equation to be solved numerically, the interface velocity is extended off the interface. Adalsteinsson and Sethian [1] showed that the velocity could be extrapolated orthogonally from the interface by solving

$$\frac{\partial \boldsymbol{u}}{\partial \tau} + S(\phi_0) \boldsymbol{n} \cdot \boldsymbol{\nabla} \boldsymbol{u} = 0, \tag{3}$$

where S is a sign function given by

$$S(\phi) = \frac{\phi}{\sqrt{\phi^2 + 2\Delta x^2}}. \tag{4}$$

The standard level-set reinitialization procedure is used to keep the level-set function as a signed distance function throughout the computation. This is accomplished by solving

$$\begin{aligned} \frac{\partial \phi}{\partial \tau} + S(\phi_0)(|\boldsymbol{\nabla} \phi| - 1) = 0, \\ \phi(\boldsymbol{x}, 0) = \phi_0(\boldsymbol{x}). \end{aligned} \tag{5}$$

Reinitialization is performed every other time step.

With the level-set function as a signed distance function, the normal vector (inward) can be calculated as

$$\boldsymbol{n} = \frac{\boldsymbol{\nabla} \phi}{|\boldsymbol{\nabla} \phi|}, \tag{6}$$

and the curvature as

$$\kappa = -\boldsymbol{\nabla} \cdot \left(\frac{\boldsymbol{\nabla} \phi}{|\boldsymbol{\nabla} \phi|} \right). \tag{7}$$

The density, viscosity, permittivity and conductivity are discontinuous across the interface. We smooth these properties over a narrow transition region using

$$\rho(H_\Gamma) = \rho_1 H_\Gamma + (1 - H_\Gamma)\rho_2, \tag{8}$$

$$\mu(H_\Gamma) = \mu_1 H_\Gamma + (1 - H_\Gamma)\mu_2, \tag{9}$$

$$\frac{1}{\varepsilon} = \frac{H_\Gamma}{\varepsilon_1} + \frac{1 - H_\Gamma}{\varepsilon_2}, \tag{10}$$

$$\frac{1}{\sigma} = \frac{H_\Gamma}{\sigma_1} + \frac{1 - H_\Gamma}{\sigma_2}, \tag{11}$$

where H_Γ is the regularized Heaviside function, defined as

$$H_\Gamma(\phi) = \begin{cases} 0 & \phi < -\epsilon \\ \frac{1}{2} + \frac{\phi}{2\epsilon} + \frac{1}{2\pi} \sin\left(\frac{\pi \phi}{\epsilon}\right) & |\phi| \leq \epsilon \\ 1 & \phi > \epsilon. \end{cases} \tag{12}$$

Here, ϵ is the smearing width. We employ a smearing width of $\epsilon = 1.5h$, where h is the grid spacing.

It was shown by Tomar *et al.* [27] that using a harmonic mean for the electrical properties was beneficial over an arithmetic mean.

We also define the regularized surface delta function,

$$\delta_\Gamma(\phi) = \begin{cases} 0 & |\phi| < \epsilon \\ \frac{1}{2\epsilon}\left(1 + \cos\frac{\pi \phi}{\epsilon}\right) & |\phi| \geq \epsilon. \end{cases} \tag{13}$$

B. Governing equations for the flow

We assume that the flow is governed by the axisymmetric Navier–Stokes equations in each phase, with additional terms accounting for interfacial-tension forces and electric forces. The Navier–Stokes equations are

$$\begin{aligned} \rho\left(\frac{\partial \boldsymbol{u}}{\partial t} + (\boldsymbol{u} \cdot \boldsymbol{\nabla})\boldsymbol{u}\right) = -\boldsymbol{\nabla} p + \boldsymbol{\nabla} \cdot [\mu(\boldsymbol{\nabla} \boldsymbol{u} + \boldsymbol{\nabla} \boldsymbol{u}^T)] \\ + \boldsymbol{f}_c + \boldsymbol{f}_e, \\ \boldsymbol{\nabla} \cdot \boldsymbol{u} = 0, \end{aligned} \tag{14}$$

where ρ is the density, $\boldsymbol{u}$ is the velocity, p is the pressure, μ is the dynamic viscosity, $\boldsymbol{f}_c$ is the capillary force and $\boldsymbol{f}_e$ is the electric force. The capillary force is given by the divergence of the capillary-pressure tensor, $\mathsf{F_c}$:

$$\boldsymbol{f}_c = \boldsymbol{\nabla} \cdot \mathsf{F_c} = \gamma \kappa \boldsymbol{\nabla} H_\Gamma - (\boldsymbol{\nabla}_\Gamma \gamma)\delta_\Gamma. \tag{15}$$

Here, γ is the interfacial tension, δ_Γ is the regularized delta function, I is the identity tensor, $\boldsymbol{n}$ is the inward-pointing normal vector, κ is the mean curvature and $\boldsymbol{\nabla}_\Gamma = (I - \boldsymbol{n} \otimes \boldsymbol{n})\boldsymbol{\nabla}$ the surface-gradient operator.

The electric force is given by the divergence of the Maxwell stress tensor, $\boldsymbol{f}_e = \boldsymbol{\nabla}\cdot M$, where

$$M = \varepsilon\left[\boldsymbol{E}\boldsymbol{E} - \frac{1}{2}(\boldsymbol{E}\cdot\boldsymbol{E})I\right]. \tag{16}$$

Here, $\boldsymbol{E}$ is the electric field. We assume that the fluids are leaky dielectric. That is, we assume that the volume charges reach steady state in a much shorter time than the fluid. This means that the equation for charge conservation

$$\frac{\mathrm{D}q_v}{\mathrm{D}t} + \boldsymbol{\nabla}\cdot\boldsymbol{J} = 0, \tag{17}$$

where $\boldsymbol{J} = \sigma\boldsymbol{E}$ is the current density, can be simplified to

$$\boldsymbol{\nabla}\cdot\boldsymbol{J} = \boldsymbol{\nabla}\cdot(\sigma\boldsymbol{E}) = 0, \tag{18}$$

where σ is the conductivity. Because the electric field is divergence free, this can be written as

$$\boldsymbol{\nabla}\cdot(\sigma\boldsymbol{\nabla}\Psi) = 0, \tag{19}$$

where Ψ is the electric potential. We do not calculate the Maxwell tensor directly, but instead calculate the electric force using an equivalent volume-force representation given by

$$\boldsymbol{f}_e = -\frac{1}{2}(\boldsymbol{E}\cdot\boldsymbol{E})\boldsymbol{\nabla}\varepsilon + q_v\boldsymbol{E}, \tag{20}$$

where $q_v = \boldsymbol{\nabla}\cdot(\varepsilon\boldsymbol{E})$ is the volume-charge density.

Next, we assume that there is an insoluble surfactant present on the interface, which modifies the interfacial tension. The dynamics of the surfactant concentration, f, is governed by[28,29]

$$\begin{aligned}\frac{\partial f}{\partial t} &+ \boldsymbol{u}\cdot\boldsymbol{\nabla}f - \boldsymbol{n}\cdot\boldsymbol{\nabla}\boldsymbol{u}\cdot\boldsymbol{n}f \\ &= D_f\left(\boldsymbol{\nabla}^2 f - \boldsymbol{n}\cdot\boldsymbol{\nabla}\boldsymbol{\nabla}\cdot\boldsymbol{n}f + \kappa(\boldsymbol{n}\cdot\boldsymbol{\nabla}f)\right),\end{aligned} \tag{21}$$

where D_f is the surfactant diffusion coefficient. We employ the Langmuir equation of state to relate the interfacial tension and surfactant concentration,

$$\gamma(f) = \gamma_0\left[1 + \beta\ln\left(1 - \frac{f}{f_\infty}\right)\right]. \tag{22}$$

Here, $\beta = \bar{R}Tf_\infty/\gamma_0$ is the surface elasticity number, and f_∞ is the maximum surfactant packing. $\bar{R}$ is the universal gas constant, T the temperature and γ_0 is the interfacial tension of the clean surface.

Since we assume that the surfactant is insoluble, it is only defined on the interface. In order to solve the evolution equation numerically, we must therefore first extend the surfactant concentration off the interface[30]. We solve an equation similar to Eq. (3) for the extension of the velocities,

$$\frac{\partial f}{\partial\tau} + S(\phi_0)\boldsymbol{n}\cdot\boldsymbol{\nabla}f = 0. \tag{23}$$

C. Non-dimensionalization

We solve the above equations in their dimensional form, but express the results in terms of relevant non-dimensional quantities. To cast the mathematical model in nondimensional form, we introduce the following nondimensional variables, denoted with a $*$,

$$x^* = \frac{x}{R}, \qquad t^* = \sqrt{\frac{\gamma_e}{\rho_2 R^3}}t, \qquad \boldsymbol{u}^* = \boldsymbol{u}\sqrt{\frac{\rho_2 R}{\gamma_e}}, \tag{24}$$

$$p^* = \frac{pR}{\gamma_e}, \qquad \rho^* = \frac{\rho}{\rho_2}, \qquad \mu^* = \frac{\mu}{\mu_2}, \tag{25}$$

$$f^* = \frac{f}{f_\infty}, \qquad \kappa^* = \kappa R, \qquad \varepsilon^* = \frac{\varepsilon}{\varepsilon_2}, \tag{26}$$

$$\sigma^* = \frac{\sigma}{\sigma_2} \qquad \gamma^* = \frac{\gamma}{\gamma_e}, \qquad \boldsymbol{E}^* = \frac{\boldsymbol{E}}{E_\infty}. \tag{27}$$

Here, the time scale is based on the frequency of a freely oscillating drop of radius R, and the pressure scale is based on the capillary pressure. Subscript 2 denotes the continuous phase. The electric field scale, E_∞, is found by dividing the potential difference by the domain height. The interfacial tension is scaled by the equilibrium interfacial tension, denoted by subscript e. This means that only the effect of a non-uniform interfacial tension is highlighted, and not the effect of a uniform lowering of the interfacial tension.

The above scalings yield the Navier–Stokes equations as

$$\begin{aligned}\rho^*\left(\frac{\partial\boldsymbol{u}^*}{\partial t^*} + (\boldsymbol{u}^*\cdot\boldsymbol{\nabla})\boldsymbol{u}^*\right) &= -\boldsymbol{\nabla}p^* \\ &\quad + Oh\boldsymbol{\nabla}\cdot[\mu^*(\boldsymbol{\nabla}\boldsymbol{u}^* + \boldsymbol{\nabla}\boldsymbol{u}^{*T})] \\ &\quad + \boldsymbol{f}_c^* + Ca_E\boldsymbol{f}_e^* \\ \boldsymbol{\nabla}\cdot\boldsymbol{u}^* &= 0,\end{aligned} \tag{28}$$

where $\boldsymbol{f}_c^*$ and $\boldsymbol{f}_e^*$ are equivalent to $\boldsymbol{f}_c$ and $\boldsymbol{f}_e$, only with dimensionless quantities. Two dimensionless quantities appear, the Ohnesorge number, $Oh = \mu_2/\sqrt{\rho_2\gamma_e R}$, which indicates the ratio of viscous force to interfacial-tension force, and the electric capillary number, $Ca_E = \varepsilon_2 R(\boldsymbol{E}\cdot\boldsymbol{E})_\infty/\gamma_e$, which is the dimensionless strength of the external electric field.

The equation for the electric potential becomes

$$\boldsymbol{\nabla}\cdot(\sigma^*\boldsymbol{\nabla}\Psi^*) = 0, \tag{29}$$

and the surfactant equation becomes

$$\begin{aligned}\frac{\partial f^*}{\partial t} &+ \boldsymbol{u}^*\cdot\boldsymbol{\nabla}f^* - \boldsymbol{n}\cdot\boldsymbol{\nabla}\boldsymbol{u}^*\cdot\boldsymbol{n}f^* \\ &= \frac{1}{Pe}\left(\boldsymbol{\nabla}^2 f^* - \boldsymbol{n}\cdot\boldsymbol{\nabla}\boldsymbol{\nabla}\cdot\boldsymbol{n}f^* + \kappa^*(\boldsymbol{n}\cdot\boldsymbol{\nabla}f^*)\right),\end{aligned} \tag{30}$$

where $Pe = RU/D_f$ is the surface Peclet number.

Henceforth we will omit the superscript $*$ for the non-dimensional quantities.

D. Numerical method

The equations are spatially discretized on a Cartesian staggered grid, with scalar values stored in cell centers and vector values stored at cell boundaries. The convective terms are discretized using the fifth order Weighted Essentially Non-Oscillatory (WENO) scheme[11], and viscous terms are discretized using standard second-order central differences.

A second-order projection scheme is used to solve the Navier–Stokes equations. First, a temporary vector field, $\boldsymbol{a}$, is calculated:

$$\boldsymbol{a} = -(\boldsymbol{u}\cdot\boldsymbol{\nabla})\boldsymbol{u} + Oh\boldsymbol{\nabla}\cdot[\mu(\boldsymbol{\nabla}\boldsymbol{u}+\boldsymbol{\nabla}\boldsymbol{u}^T)] + \boldsymbol{f}_c + Ca_E\boldsymbol{f}_e. \tag{31}$$

Then the pressure is found by solving

$$\boldsymbol{\nabla}\cdot\left(\frac{\boldsymbol{\nabla}p}{\rho}\right) = \boldsymbol{\nabla}\cdot\boldsymbol{a}. \tag{32}$$

Finally, the velocity field is calculated with

$$\frac{\partial \boldsymbol{u}}{\partial t} = \boldsymbol{a} - \frac{\boldsymbol{\nabla}p}{\rho}. \tag{33}$$

The evolution in time is calculated using a four-step third-order, strong stability-preserving (SSP) Runge-Kutta (RK) method[12,13]. This method is also used for the level-set equation and the surfactant equation, while a four-step second-order SSP-RK method is employed for the reinitialization of the level-set equation and extrapolation of the velocity field and surfactant.

One substep in the main RK solver can be summarized as follows:

1. Solve Eq. (19) for the electric potential and find the electric field.
2. Calculate electric forces using Eq. (20).
3. Find the interfacial tension using Eq. (22) and calculate interfacial-tension forces with Eq. (15).
4. Calculate $\boldsymbol{a}$ using Eq. (31) and solve Eq. (32) for pressure.
5. Extrapolate the velocity from the previous time step by solving Eq. (3).
6. Calculate the rate of change of the level-set function using Eq. (2). Here, the extrapolated velocities are employed.
7. Extrapolate the surfactant concentration from the previous time step by solving Eq (23).
8. Calculate the rate of change of the surfactant concentration using Eq. (21).

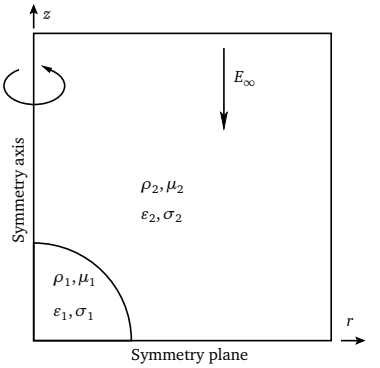

FIG. 1. Illustration of the computational domain.

III. RESULTS AND DISCUSSION

We first present a comparison with theoretical results for the steady-state deformation of a clean drop to validate our implementation and establish a frame of reference for the simulation with surfactants. Then, we present results for the steady-state deformation of a surfactant-covered drop for various electrical properties. Finally, we discuss the influence of surfactants on the transient deformation of a conductive drop when the electric field is so high that no steady-state solution exists.

The computational domain is illustrated in Fig. 1. The simulations are performed in an axisymmetric, cylindrical coordinate system, where the axis of symmetry is aligned with the electric field. Additionally, it is assumed that the fluid mechanics are symmetric about the r-axis, while the electric problem is anti-symmetric. This means that the simulations are only performed in one quadrant of the drop, which reduces the computational complexity. The domain size was $4R \times 4R$, and the grid spacing was $h = R/20$. Since we use a transient numerical method, we stop the simulation when the relative change in deformation from one time step to the next is less than 1×10^{-4}.

An issue with level-set simulations is mass conservation. We ensured that for all the simulations presented here, the change in mass for both fluid and surfactant was less than 1 %.

A. Comparison with small-deformation theory for clean drops

In the limit of small perturbations, an expression for the deformation of a leaky-dielectric drop in a leaky-dielectric medium was derived by Taylor[26] to the first order, and later extended to second order by Ajayi[2]. This

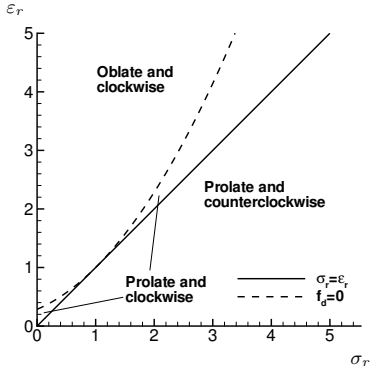

FIG. 2. A map of the different induced flow patterns and deformations for $\mu_r = 1$.

can be written as

$$D = \frac{b-a}{b+a} = k_1 Ca_E + k_2 Ca_E^2, \tag{34}$$

where a and b are the drop extensions along the r-axis and z-axis, respectively. The coefficients k_1 and k_2 are given by

$$\begin{aligned} k_1 &= \frac{9}{16}\frac{\sigma_r^2}{(2+\sigma_r)^2} f_d, \\ k_2 &= \frac{(139\sigma_r - 154)\sigma_r^2 f_d + (\sigma_r^2 + 2\sigma_r - \sigma_r\varepsilon_r - 2\varepsilon_r)80\beta}{80(2+\sigma_r)^3} k_1, \\ f_d &= \frac{\sigma_r^2 - 2\sigma_r + 1 + (\sigma_r - \varepsilon_r)\left[2 + \frac{3}{5}\frac{2+3\mu_r}{1+\mu_r}\right]}{\sigma_r^2}, \\ \beta &= \frac{23}{20} - \frac{139}{210}\frac{1-\mu_r}{1+\mu_r} - \frac{27}{700}\left(\frac{1-\mu_r}{1+\mu_r}\right). \end{aligned} \tag{35}$$

Here, subscript r denotes the ratio between phase 1 and phase 2. The form of deformation is given by f_d. If $f_d > 0$, the drop will have a prolate shape. If $f_d < 0$, the shape will be oblate. If $\varepsilon_r < \sigma_r$, then $f_d > 0$ and the deformation will always be prolate. For $\varepsilon_r > \sigma_r$, however, both kinds of deformation may occur. Additionally, when the deformation is oblate, the induced flow pattern is always clockwise in the first quadrant of the drop. For the prolate shape, the flow can be both clockwise and counterclockwise. A map of these situations is given in Fig. 2.

Simulations of four different configurations were performed at various electric capillary numbers and compared to Eq. (34). The different configurations were chosen to correspond to the different deformation types and flow patterns given in Fig. 2, and are summarized in Table I. The viscosity ratio is set to unity.

The results are shown in Fig. 3. For small Ca_E, the numerical simulations are in good agreement with the first-order theory, while for higher numbers, they start to deviate. This behavior is expected since the theory is only valid for small deformations, and our results are in line with other numerical investigations[8,10,27]. The second-order theory is a better match to the simulations, which was also observed in Lac and Homsy [14].

TABLE I. The parameters used for validation of the electric forces, together with the predicted deformation types and flow patterns. C=Clockwise, CC=Counterclockwise.

Case	σ_r	ε_r	f_d	Deformation	Flow pattern
A	3	1	1.22	Prolate	CC
B	3	3.5	0.25	Prolate	C
C	1	2	-3.50	Oblate	C
D	2	2.2857	0.00	None	C

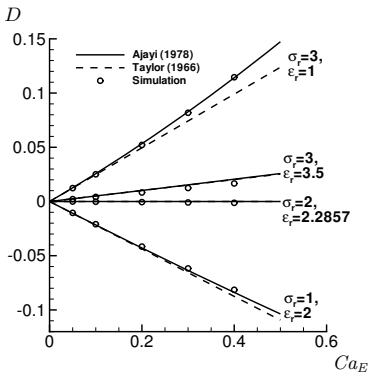

FIG. 3. Comparison of numerical results (circles) and the small deformation theory of Taylor [26] (dashed lines) and Ajayi [2] (solid lines) for the parameters given in Table I.

The drop morphology along with induced flow patterns for $Ca_E = 0.4$ are shown in Fig. 4. We see that for case A, the flow is from pole to equator, for case B, the flow is from equator to pole, and for case C, the flow is from pole to equator. These patterns match those predicted from the theory.

B. Influence of surfactants on steady-state deformation

We now turn our attention to the steady-state deformation of a drop with a surfactant present on the interface.

To limit the parameter space, we will consider the above cases A, B and C, and vary the electric capillary number and surfactant coverage. For the surfactant, we choose an elasticity of $\beta = 0.2$ and a surfactant Peclet number of $Pe = 10$. The Ohnesorge number is set to $Oh = 0.1$ and the viscosity ratio is set to unity unless otherwise noted.

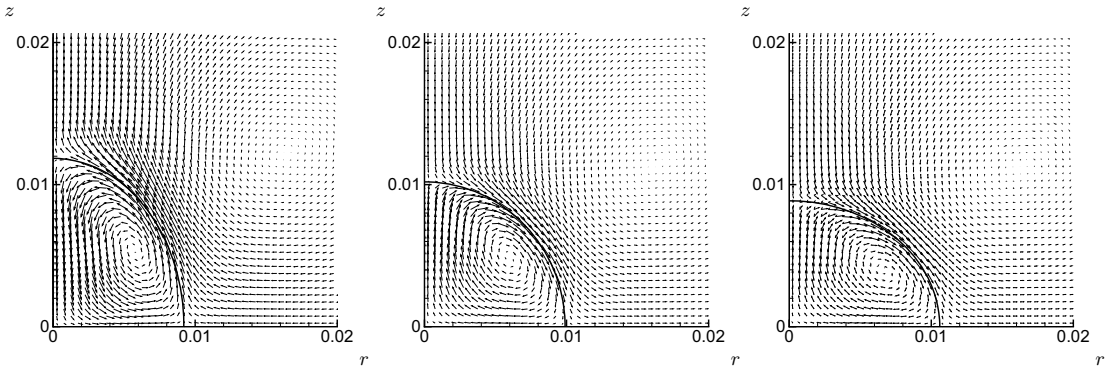

(a) Case A (b) Case B (c) Case C

FIG. 4. Drop deformation and induced flow pattern for $Ca_E = 0.4$ for the three typical cases given in Tab. I. Note that the velocity scale is different in the three figures.

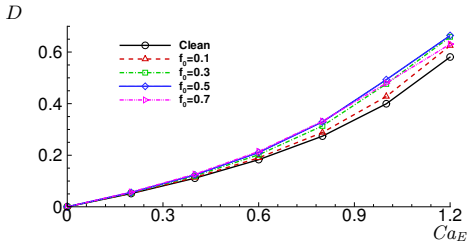

FIG. 5. (Color online) Case A. Deformation as a function of electric capillary number for various surfactant coverages.

1. *Case A*

We first study the effect of surfactants on the system with prolate deformation and counter-clockwise flow. The deformation as a function of electric capillary number for different surfactant coverages is shown in Fig. 5. For low Ca_E, higher surfactant concentrations lead to higher deformation. This is due to the induced flow which for this case is from the equator to the poles (see Fig. 4(a)). This will transport surfactant to the tip of the drop, which reduces interfacial tension at the poles. Since there must be a balance between the normal interfacial-tension forces, the hydrodynamic pressure and the electric pressure, the drop extends more to yield a higher mean curvature. However, as the drop is stretched further, the average interfacial tension increases due to dilution of the surfactant. This will act to reduce deformation, and eventually this effect becomes stronger than the effect of reduced interfacial tension at the tips, leading to less deformation. This is clearly seen for $f_0 = 0.7$ in the figure. At low Ca_E, the deformation is higher than for the lower f_0 numbers, but at high Ca_E, it becomes lower.

In Figure 6 we illustrate the drop shapes and velocity patterns for electric capillary numbers 0.2, 0.8 and 1.2, and for a clean and surfactant-covered drop. We immediately see the reduced velocities for the surfactant-covered drop, which is due to the Marangoni stresses acting in the opposite direction to the electrically induced shear stresses. An important application area of electrically induced flow is enhanced mixing, for instance in heat exchangers. Here, we see that the presence of surfactants may significantly inhibit the internal circulation, and this may be important for industrial applications.

Additionally, we observe that for the higher Ca_E, the velocities are larger near the tip of the drop. This leads to an increase in surfactant convection here. This is further illustrated in Figure 7, which shows the interfacial tension as a function of arc length, s, starting from the tip of the drop and moving in the clockwise direction. For low Ca_E, the interfacial tension follows a smooth S-curve, but for higher Ca_E, there is a sharper gradient near the drop pole and very little change near the equator.

In Figure 8, we plot the actual surfactant concentration for $Ca_E = 1.2$. At low concentrations, the area around the equator is nearly depleted, and then there is a sharp gradient towards the tip. However, since the concentration is low, this only leads to modest gradients in the interfacial tension as shown in Figure 7(c). At higher concentrations, the concentration at the tips approaches the maximum surfactant packing. This leads to larger gradients in the interfacial tension than for the low concentrations, and correspondingly higher Marangoni stresses which lead to more uniform surfactant profiles. The gradient of the interfacial tension, which is the main component of the Marangoni stresses, is shown in Figure 9 for $Ca_E = 1.2$. From this we see that the Marangoni stresses is largest in the area near the tip, where the convection is strongest, and that higher surfactant concentrations lead to higher Marangoni stresses.

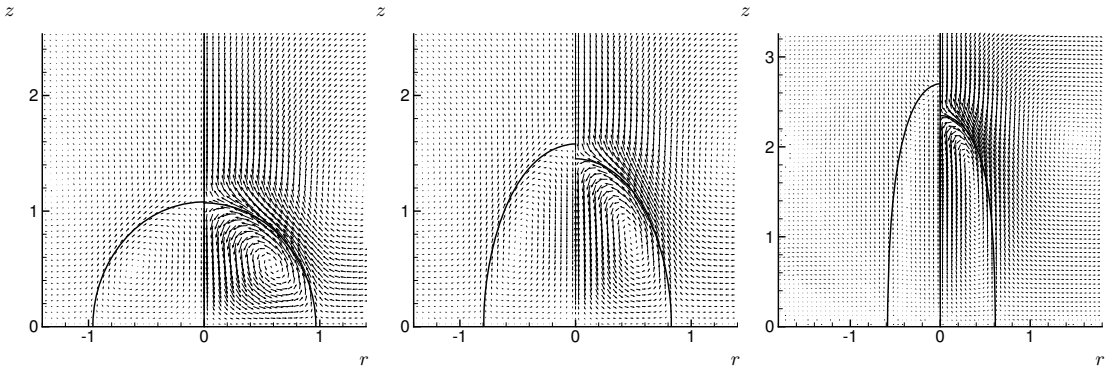

(a) $Ca_E = 0.2$ (b) $Ca_E = 0.8$ (c) $Ca_E = 1.2$

FIG. 6. Case A. Drop deformation and induced flow pattern. The right quadrant shows the clean drop and the left quadrant shows the surfactant-covered drop with $f_0 = 0.7$. The velocity scale is different in the three figures.

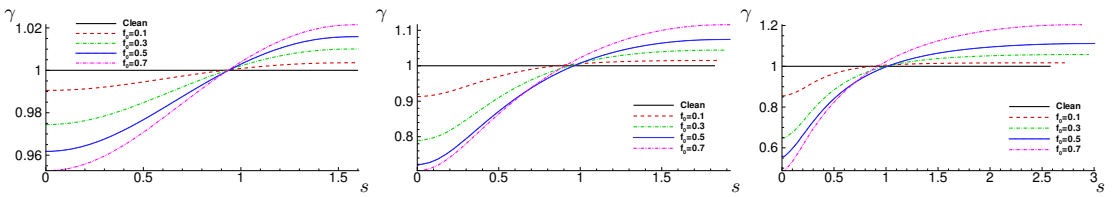

(a) $Ca_E = 0.2$ (b) $Ca_E = 0.8$ (c) $Ca_E = 1.2$

FIG. 7. (Color online) Case A. Interfacial tension along the interface for various surfactant coverages.

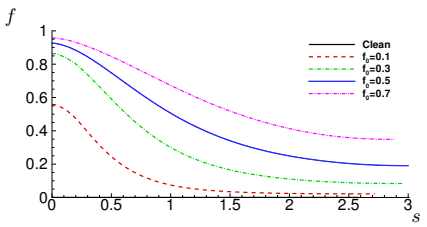

FIG. 8. (Color online) Case A. Deformation as a function of electric capillary number for various surfactant coverages.

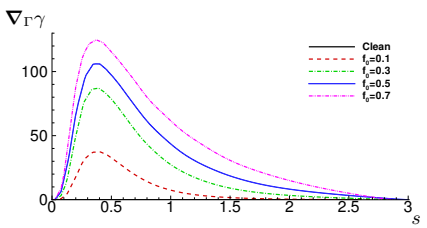

FIG. 9. (Color online) Case A. Deformation as a function of electric capillary number for various surfactant coverages.

2. *Case B*

Here, we consider the case where the drop deforms in a prolate fashion, but the induced flow is from the poles to the equator. The deformation as a function of electric capillary number for different surfactant coverages is shown in Fig. 10. We see that a higher concentration of surfactant consistently gives a lower degree of deformation. The reason for this is that now surfactant is swept towards the equator instead of the poles. The interfacial tension will therefore become higher at the tips, and give a larger resistance against deformation than for a clean drop.

Note that the deformation is relatively low for the Ca_E considered here. We would expect that dilatational effects would occur here as well for higher deformations. However, for this case these effects would only give an even lower deformation, further increasing the difference between the clean and surfactant-covered drops. We would also expect, as we will see in the next section, that the dilatational effects would occur sooner than for case A. This is because when surfactant is swept towards the equator instead of towards the poles, it will be spread over a larger surface area and thereby contribute less to-

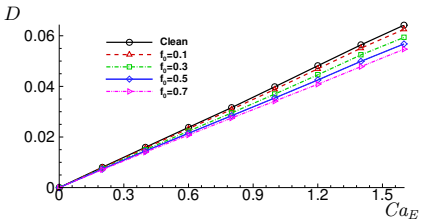

FIG. 10. (Color online) Case B. Deformation as a function of electric capillary number for various surfactant coverages.

wards a change in the balance between capillary forces and electrical forces.

3. Case C

Next, we consider the case of oblate deformation, with induced flow from the poles to the equator. The deformation as a function of electric capillary number for different surfactant coverages is shown in Fig. 11. For the chosen parameter set, we see that the effect of surfactant is very small at low Ca_E. As shown in the closeup in Fig. 11(b), the deformation is slightly larger for increasing surfactant concentrations. This is again because surfactant is swept towards the drop equator by the induced flow, and the resulting low interfacial tension here gives a corresponding lower resistance towards deformation. The change in deformation is lower because the surfactant now is spread across the equator instead of concentrated at the tips.

This also means that the relative effect of dilatation will occur earlier than for case A. This can be seen at higher Ca_E from Fig. 11. For higher Ca_E (but still low D compared to case A), the differences in deformation is completely reversed such that the clean drop has the highest deformation and the surfactant-covered drop with $f_0 = 0.7$ has the lowest deformation.

4. Influence of viscosity ratio

We end by presenting results on the influence of viscosity ratio. This parameter has proved to be an important parameter for the deformation of a drop in extensional flow. In Milliken and Leal [19] it was shown that smaller viscosity ratios gave a larger sensitivity to surfactant. We therefore rerun our previous simulations with a viscosity ratio of $\mu_r = 0.1$. The results for all three cases are presented in Figure 12. It is evident that the difference in deformation due to surfactants here is higher. The reason for this is that for higher viscosity ratios, the internal circulation is already retarded due to viscosity, and the contribution from the additional Marangoni stresses will become relatively smaller than for lower viscosity ratios. Since the circulation is higher here, more surfactant will

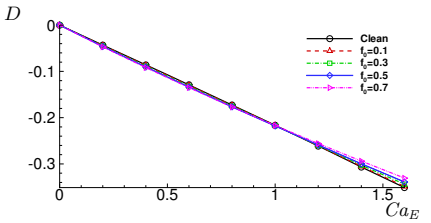

(a) Full view

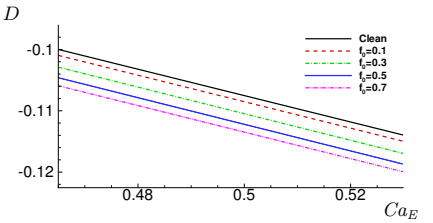

(b) Close up of the curves near $Ca_E = 0.5$.

FIG. 11. (Color online) Case C. Deformation as a function of electric capillary number for various surfactant coverages.

be swept towards the tips and the change in deformation will be higher. The stronger Marangoni stresses at lower viscosity ratios also make the dilatational effects less prominent. For instance, we see that for the oblately deformed drop, Fig 12(c), the deformation is now higher for higher surfactant coverages, even at high Ca_E.

IV. CONCLUSIONS

A level-set model for two-phase flows, coupled with models for electrohydrodynamic forces and surface-active agents was developed to investigate the influence of surfactants on the steady-state deformation of a drop in an electric field.

Leaky-dielectric fluids can deform into both prolate and oblate shapes, depending on the ratio of conductivities and permittivities. Additionally, the direction of the induced circulation can be both clockwise and counter-clockwise for the prolate shapes. It was found that for prolate deformation and counter-clockwise circulation, the presence of surfactant leads to greater deformation at low surfactant concentrations. At high surfactant concentrations and high electric capillary numbers, however, the effect of surfactant dilution becomes stronger than the effect of reduced interfacial tension at the tips, and the deformation decreases. This behavior is similar to that of a drop in extensional flow.

For prolate deformation and clockwise flow, the surfactants are swept in the opposite direction, and cause a reduction in deformation. Although not shown here, it seems clear that dilatational effects will lead to an additional reduction in deformation for the surfactant-

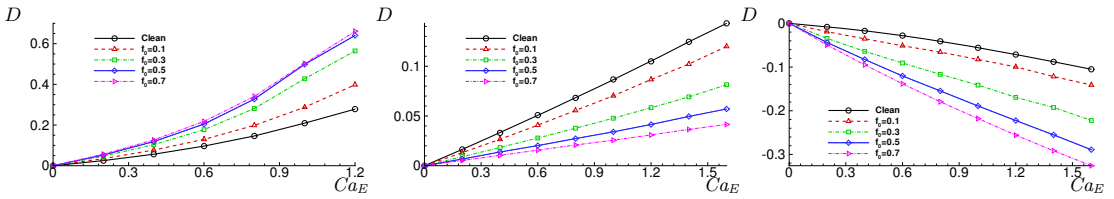

(a) Case A (b) Case B (c) Case C

FIG. 12. (Color online). Deformation as a function of electric capillary number for various surfactant coverages at viscosity ratio $\mu_r = 0.1$.

covered drop, and thereby increase the differences between the clean and surfactant-covered case further.

For oblate deformation, which always gives clockwise flow, the results are similar to that of prolate deformation and counter-clockwise flow, deformation is increased until dilatational effects start to dominate. However, this occurs earlier here, since the surfactant is not concentrated at the tips, but instead spread out over the equator of the drop. Finally, it was shown that for smaller viscosity ratios, the influence of surfactant is stronger, since the relative importance of the Marangoni stresses becomes higher.

In this work, only steady-state deformation was considered. At high electric capillary numbers, no steady state exists and the drop will stretch further and eventually break up. It would be of interest to investigate the influence of surfactants on this breakup behavior. In particular, for a conductive drop in an otherwise dielectric medium, the influence of surfactant may be important even though it has no influence on the steady-state deformation. The presented numerical method is applicable to such a study as well.

ACKNOWLEDGMENTS

This work is funded by the project "Electrocoalescence – Criteria for an efficient process in real crude oil systems"; co-ordinated by SINTEF Energy Research. The project is supported by The Research Council of Norway, under the contract no: 169466/S30, and by the following industrial partners: Aker Solutions AS, BP Exploration Operating Company Ltd, Hamworthy Technology & Products AS, Petrobras, Saudi Aramco, Shell Technology Norway AS and Statoil ASA.

[1] Adalsteinsson, D. and Sethian, J.A., "The fast construction of extension velocities in level set methods," J. Comput. Phys. **148**, 2–22 (1999).
[2] Ajayi, O. O., "A note on Taylor's electrohydrodynamic theory," Proc. R. Soc. Lond. A **364**, 499 – 507 (1978).
[3] De Bruijn, R. A., "Tipstreaming of drops in simple shear flows," Chem. Eng. Sci. **48**, 277–284 (1993).
[4] Eggleton, C. D., Tsai, T., and Stebe, K. J., "Tip streaming from a drop in the presence of surfactants," Phys. Rev. Lett. **87**, 048302 (2001).
[5] Eggleton, Charles D., Pawar, Yashodhara P., and Stebe, Kathleen J., "Insoluble surfactants on a drop in an extensional flow: a generalization of the stagnated surface limit to deforming interfaces," J. of Fluid Mech. **385**, 79–99 (1999).
[6] Eggleton, Charles D. and Stebe, Kathleen J., "An adsorption-desorption-controlled surfactant on a deforming droplet," J. Colloid Interface Sci. **208**, 68 – 80 (1998).
[7] Eow, J. S. and Ghadiri, M., "Electrostatic enhancement of coalescence of water droplets in oil: a review of the technology," Chem. Eng. J. **85**, 357–368 (2002).
[8] Feng, J. Q. and Scott, T. C., "A computational analysis of electrohydrodynamics of a leaky dielectric drop in an electric field," J. Fluid. Mech. **311**, 289 – 326 (1996).
[9] Ha, J. and Yang, S., "Effect of nonionic surfactant on the deformation and breakup of a drop in an electric field," J. Colloid and Interface Sci. **206**, 195 – 204 (1998).
[10] Hua, J., Lim, L. K., and Wang, C., "Numerical simulation of deformation/motion of a drop suspended in viscous liquids under influence of steady electric fields," Phys. Fluids **20**, 113302 (2008).
[11] Jiang, G. S. and Peng, D., "Weighted ENO schemes for Hamilton–Jacobi equations," SIAM J. Sci. Comput. **21**, 2126–2143 (2000).
[12] Ketcheson, D. I. and Robinson, A. C., "On the practical importance of the SSP property for Runge-Kutta time integrators for some common Godunov-type schemes," Int. J. Numer. Meth. Fluids **48**, 271–303 (2005).
[13] Kraaijevanger, J. F. B. M, "Contractivity of Runge-Kutta methods," BIT **31**, 482–528 (1991).
[14] Lac, E. and Homsy, G. M., "Axisymmetric deformation and stability of a viscous drop in a steady electric field," J. Fluid Mech. **590**, 239–264 (2007).
[15] Lai, M.-C., Tseng, Y.-H., and Huang, H., "An immersed boundary method for interfacial flows with insoluble surfactant," J. Comput. Phys. **227**, 7270–7293 (2008).
[16] Laohalertdecha, S., Naphon, P., and Wongwises, S., "A review of electrohydrodynamic enhancement of heat transfer," Renew. Sustain. Energy Rev. **11**, 858 – 876 (2007).
[17] Li, X. and Pozrikidis, C., "The effect of surfactants on drop deformation and on the rheology of dilute emulsions in Stokes flow," J. of Fluid Mech. **341**, 165–194 (1997).
[18] Melcher, J. R. and Taylor, G. I., "Electrohydrodynamics: A review of the role of interfacial shear stresses," Annu. Rev. Fluid Mech. **1**, 111–146 (1969).
[19] Milliken, W. J. and Leal, L. G., "The influence of surfactant on the deformation and breakup of a viscous drop - the effect of surfactant solubility," J. Colloid and Interface Sci. **166**, 275–285 (1994).
[20] Milliken, W. J., Stone, H. A., and Leal, L. G., "The effect of surfactant on transient motion of Newtonian drops," Phys. Fluids A **5**, 69–79 (1993).
[21] Osher, Stanley and Fedkiw, Ronald, *Level set methods and dynamic implicit surfaces* (Springer, 2003).

[22]Pawar, Y. and Stebe, K. J., "Marangoni effects on drop deformation in an extensional flow: The role of surfactant physical chemistry. I. Insoluble surfactants," Phys. Fluids **8**, 1738–1751 (1996).

[23]Renardy, Y. Y., Renardy, M., and Cristini, V., "A new volume-of-fluid formulation for surfactants and simulations of drop deformation under shear at a low viscosity ratio," Eur. J. Mech. B Fluids **21**, 49 – 59 (2002).

[24]Sjöblom, J., Aske, N., Auflem, I. H., Brandal, Ø., Havre, T. E., Sæther, Ø., Westvik, A., Johnsen, E. E., and Kallevik, H., "Our current understanding of water-in-crude oil emulsions.: Recent characterization techniques and high pressure performance," Advances in Colloid and Interface Science **100-102**, 399 – 473 (2003).

[25]Sussman, Mark, Smereka, Peter, and Osher, Stanley, "A level set approach for computing solutions to incompressible two-phase flow," J. Comput. Phys. **114**, 146–159 (1994).

[26]Taylor, G. I., "Studies in electrohydrodynamics I. the cirulation produced in a drop by an electric field," Proc. R. Soc. A **291**, 159–166 (1966).

[27]Tomar, G., Gerlach, D., Biswas, G., Alleborn, N., Sharma, A., Durst, F., Welch, S. W. J., and Delgado, A., "Two-phase electrohydrodynamic simulations using a volume-of-fluid approach," J. Comput. Phys. **227**, 1267–1285 (2007).

[28]Xu, J. J., Li, Z., Lowengrub, J., and Zhao, H., "A level set method for interfacial flows with surfactant," J. Comp. Phys. **212**, 590–616 (2006).

[29]Xu, J. J. and Zhao, H., "An Eulerian formulation for solving partial differential equations along a moving interface," J. Sci. Comp. **19**, 573–594 (2003).

[30]Zhao, H. K., Chan, T., Merriman, B., and Osher, S., "A variational level set approach to multiphase motion," J. Comput. Phys. **127**, 179 – 195 (1996).

E A diffuse-interface approach for modelling transport, diffusion and adsorption/desorption of material quantities on a deformable interface

Teigen, K.E, Li, X., Lowengrub, J., Wang, F., Voigt, A.,
Communications in Mathematical Sciences. Volume 7, Number 4 (2009), 1009-1037

COMMUN. MATH. SCI.
Vol. 7, No. 4, pp. 1009–1037

A DIFFUSE-INTERFACE APPROACH FOR MODELING TRANSPORT, DIFFUSION AND ADSORPTION/DESORPTION OF MATERIAL QUANTITIES ON A DEFORMABLE INTERFACE*

KNUT ERIK TEIGEN†, XIANGRONG LI‡, JOHN LOWENGRUB§, FAN WANG¶, AND AXEL VOIGT‖

Abstract. A method is presented to solve two-phase problems involving a material quantity on an interface. The interface can be advected, stretched, and change topology, and material can be adsorbed to or desorbed from it. The method is based on the use of a diffuse interface framework, which allows a simple implementation using standard finite-difference or finite-element techniques. Here, finite-difference methods on a block-structured adaptive grid are used, and the resulting equations are solved using a non-linear multigrid method. Interfacial flow with soluble surfactants is used as an example of the application of the method, and several test cases are presented demonstrating its accuracy and convergence.

Key words. Partial differential equations, diffuse interface, interfacial dynamics, complex geometry,multigrid, adaptive grid, finite difference, multiphase, adsorption, desorption

AMS subject classifications. 35Q35, 35K05, 35K57, 65Z05, 65M06, 65M50, 65M55, 76Txx, 82C24.

1. Introduction Many problems in the biological, physical and engineering sciences involve systems of equations that need to be solved in evolving domains with complex shapes. In addition, the solutions in the bulk domain may couple with the surface through adsorption of mass from the bulk to the surface and desorption from the surface to the bulk. Furthermore, the evolution of the domain boundary may depend on the distribution of the surface concentration through the modification of interfacial forces. Surfactants are a classic example where the amphiphilic organic compounds may adsorb to and desorb from a liquid/liquid or liquid/gas interface and lower the surface tension on the interface. Thus, inhomogeneous distribution of surfactants produces Marangoni forces — tangential forces along the interface — that affect the dynamics; surfactants play important roles in vortex pair interaction (e.g., [86, 34]), fingering (e.g., [84, 63]) and drop break-up and coalescence (e.g., [35, 36, 48, 32]). Other examples include biomembranes where transmembrane proteins play an important role in intra- and extra-cellular dynamics (e.g., [46, 2, 51, 29]), epitaxially grown thin films where adsorbing/desorbing adatoms affect the dynamics and coarsening of the thin film (e.g., [23, 81, 52]), and electrochemical dissolution of binary alloys where one component is removed selectively and dissolved in an electrolyte solution (e.g., [19, 15]).

*Received: June 4, 2009; accepted (in revised version): August 26, 2009. Communicated by Chun Liu.

†Department of Energy and Process Engineering, Norwegian University of Science and Technology, 7491 Trondheim, Norway (knut.erik.teigen@ntnu.no)

‡Department of Mathematics, University of California, Irvine, Irvine CA-92697, USA (xli@math.uci.edu)

§Department of Mathematics, University of California, Irvine, Irvine CA-92697, USA (lowengrb@math.uci.edu)

¶Department of Mathematics, University of California, Irvine, Irvine CA-92697, USA (wangf@math.uci.edu)

‖Department of Mathematics, Technische Universitt Dresden, 01062 Dresden, Germany (axel.voigt@tu-dresden.de)

From a numerical point of view, solving a coupled bulk/surface system of equations on a moving, complex domain is highly challenging; the domain boundary may stretch, break-up or coalesce with other interfaces. Adsorption of mass to, and desorption of mass from, the interfaces poses another challenge. Furthermore, the surface concentration may only be soluble in either the exterior or interior of the domain (e.g., amphiphilic nature of surfactants). The available numerical methods for solving these problems can roughly be divided into two categories: interface tracking and interface capturing methods. Interface tracking methods use either through a separate grid for the interface, or a set of interconnected points to mark the interface. For example, boundary integral methods use a surface mesh to track the interface. In the context of surfactants, a boundary integral method for studying the effect of insoluble surfactants on drop deformation was developed in [82]. This method was extended to arbitrary viscosity ratios in [67], and to soluble surfactants in [66]. Another tracking method is the front-tracking method, where a fixed grid is used to compute the flow, while a set of connected marker particles is used to track the interface and any interfacial quantities. A front-tracking method for insoluble surfactants was developed in [39], and this method was extended to handle soluble surfactants in [91] and [69]. Lagrangian approaches are typically very accurate, but can be relatively complicated to implement, especially in three dimensions and for problems involving topological changes.

In interface capturing methods, the interface is not tracked explicitly, but instead is implicitly defined through a regularization of the interface. This means that the solution of the problem can be done independently of the underlying grid, which greatly simplifies gridding, discretization, and handling of topological changes. For example, a volume-of-fluid (VOF) method for insoluble surfactants was developed in [75]. A more general method which allows non-linear equations of state for surface tension was then developed in [38]. A level-set method for solving the surfactant equation was presented in [89], and later coupled to an external flow solver in [88]. An alternative approach tracking and approach was developed in [90, 32], using the so-called Arbitrary Lagrangian-Eulerian (ALE) method. An immersed interface boundary method for interfacial flows with insoluble surfactants was recently developed in [47]. In the context of thin films, a level-set method for the simulating the motion of thin films under surface diffusion with free adatoms was developed in [81]. In addition, an immersed interface method was developed to simulate electrodeposition in an evolving complex domain [77]. Level-set methods for solving more general equations on implicitly defined, but stationary, surfaces have also been developed in [5, 30].

Other approaches for solving equations in complex domains include fictitious domain methods (e.g., [27, 28, 65, 31, 70, 12, 74, 72, 56, 33]), immersed interface methods (e.g., [49, 54, 37]), modified finite volume/embedded boundary/cut-cell methods (e.g., [41, 64, 62, 40, 42, 76, 59]) and ghost fluid methods (e.g., [20, 24, 25, 26, 60, 61]). All these methods, however, require non-standard tools typically not available in standard finite element and finite difference software packages.

The diffuse-interface, or phase-field, method represents yet another approach for simulating solutions of equations in complex, evolving domains. In this method, which we follow here, the complex domain is represented implicitly by a a phase-field function, which is an approximation of the characteristic function of the domain. The domain boundary is replaced by a narrow diffuse interface layer such that the phase-field function rapidly transitions from one inside the domain to zero in the exterior of the domain. The boundary of the domain can thus be represented as an isosurface of

the phase-field function. The bulk and surface PDEs are then extended on a larger, regular domain with additional terms that approximate the adsorption-desorption flux boundary conditions and source terms for the bulk and surface equations respectively. Standard finite-difference or finite-element methods may be used. Here, we focus on a finite difference approach.

The diffuse interface method, which has a long history in the theory of phase transitions dating back to van der Waals (e.g., [79, 3]), was used in [46] to study diffusion inside a cell with zero Neumann boundary conditions at the (stationary) cell-boundary (see also [8, 9]), and later was used to simulate electrical waves in the heart [21]. This approach has been extended [51] to simulate coupled bulk diffusion with an ordinary-differential equation description of reaction-kinetics on the bounding surface of a stationary domain to simulate membrane-bound Turing patterns. More recently, general diffuse-interface methods have been developed for solving PDEs on stationary surfaces [73], evolving surfaces [13, 14, 16, 17] and for solving PDEs in complex evolving domains with Dirichlet, Neumann and Robin boundary conditions [53].

As shown in the previous paragraphs, bulk/surface problems are important in a wide range of areas. Here, we combine and refine previous work on diffuse-interface methods to develop a new method for solving coupled bulk/surface problems on general, evolving domains. The method is very simple compared to other methods, and can handle advection, diffusion and adsorption/desorption in a straight-forward manner. Matched asymptotic expansions are used to demonstrate that the diffuse interface system converges to the original sharp interface equations as the interface thickness tends to zero. The use of a non-linear multigrid method and block-structured, adaptive grids also make the method computationally efficient. We present several test cases demonstrating the accuracy and convergence of the proposed method.

The paper is organized as follows. In section 2, the governing equations for the surface concentration and the bulk concentration are introduced, and the interface representation presented. Section 3 presents an asymptotic analysis of the proposed method. Section 4 then details the numerical implementation. In section 5, the performance of the numerical method is evaluated on a set of test cases. Finally, section 6 contains conclusions and discussions of future work.

2. Mathematical formulation

2.1. Governing equations Consider a domain $\Omega \subset \mathbb{R}^{2,3}$, which contains a closed interface, Γ. The interior of the interface is $\Omega_0 \subset \Omega$, and the exterior is $\Omega_1 \subset \Omega$. See figure 2.1 for an illustration. Let f denote a surface concentration defined on Γ. We suppose that f is extended off Γ constant in the normal direction (i.e., $\boldsymbol{\nabla} f \cdot \mathbf{n} = 0$) so that f is defined in a neighborhood of Γ. Then, the sharp interface mass conservation equation is

$$\frac{\partial f}{\partial t} + \mathbf{u} \cdot \boldsymbol{\nabla} f = \boldsymbol{\nabla}_\Gamma \cdot (D_f \boldsymbol{\nabla}_\Gamma f) - f \boldsymbol{\nabla}_\Gamma \cdot \mathbf{u}_\Gamma - f \kappa u_n + j, \tag{2.1}$$

where $\mathbf{u}$ is the velocity, $\boldsymbol{\nabla}_\Gamma = (\mathbf{I} - \mathbf{nn})\boldsymbol{\nabla}$ is the surface gradient, $\mathbf{n}$ is the normal vector to Γ pointing into Ω_0, D_f is the diffusion coefficient, $\mathbf{u}_\Gamma = (\mathbf{I} - \mathbf{nn})\mathbf{u}$, $u_n = \mathbf{u} \cdot \mathbf{n}$, κ is the total curvature of Γ (positive for a sphere), and j is a source term that arises from adsorption to and desorption from Γ

$$j = r_a F - r_d f, \tag{2.2}$$

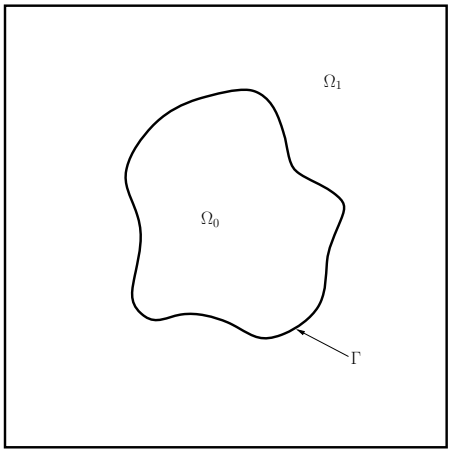

Fig. 2.1: Illustration of the mathematical domain.

where r_a and r_d are adsorption and desorption coefficients, respectively, and F is the bulk concentration (evaluated immediately adjacent to Γ). Note that in the context of surfactants, the interface may become saturated and instead one may use

$$j = r_a F(f_\infty - f) - r_d f, \tag{2.3}$$

where f_∞ is the maximum interface concentration. An equivalent formulation is

$$\frac{\partial f}{\partial t} + \boldsymbol{\nabla}_\Gamma \cdot (\mathbf{u} f) = \boldsymbol{\nabla}_\Gamma \cdot (D_f \boldsymbol{\nabla}_\Gamma f) + j. \tag{2.4}$$

We refer the reader also to [11] for further discussion of formulations involving interfacial transport using constant normal extensions and to [38] for Eulerian formulations of the dynamics of surface concentrations.

Assume that the surface concentration f is soluble in Ω_1, but not in Ω_0. Then, define the bulk concentration in Ω_1 to be F, which evolves according to the bulk mass conservation equation

$$\frac{\partial F}{\partial t} + \boldsymbol{\nabla} \cdot (F\mathbf{u}) = D_F \boldsymbol{\nabla}^2 F \text{ in } \Omega_1, \tag{2.5}$$

with the boundary condition at Γ

$$D_F \boldsymbol{\nabla} F \cdot \mathbf{n} = -j \text{ on } \Gamma. \tag{2.6}$$

Note that if the surface concentration were soluble in Ω_0, then an additional mass conservation equation would need to be posed. Our formulation is sufficiently general to handle this case.

Next, we consider a distribution formulation of equation (2.4) by introducing a surface delta function δ_Γ, such that

$$\int_\Gamma f \, \mathrm{d}\Gamma = \int_\Omega f \delta_\Gamma \, \mathrm{d}\Omega, \tag{2.7}$$

where $\Omega = \Omega_1 \cup \Omega_0$ (actually the above equation holds for any domain Ω that contains Γ). The mass conservation equation may be rewritten accordingly as

$$\frac{\partial}{\partial t}(f\,\delta_\Gamma) + \boldsymbol{\nabla}\cdot(f\,\delta_\Gamma\,\mathbf{u}) = \boldsymbol{\nabla}\cdot(\delta_\Gamma D_f \boldsymbol{\nabla} f) + \delta_\Gamma j. \tag{2.8}$$

This distribution formulation formally holds in Ω.

Analogously, the bulk equation (2.5) may be extended to hold in Ω in distribution form. Introducing the Heaviside function

$$H = \begin{cases} 1 \text{ in } \Omega_1, \\ 0 \text{ in } \Omega_0, \end{cases} \tag{2.9}$$

the bulk concentration equation (2.5) and boundary condition (2.6) may be reformulated as

$$\frac{\partial}{\partial t}(HF) + \boldsymbol{\nabla}\cdot(HF\,\mathbf{u}) = D_F \boldsymbol{\nabla}\cdot(H\boldsymbol{\nabla}F) - \delta_\Gamma j, \tag{2.10}$$

where the boundary condition has been included as a singular source term following [53].

2.2. Interface representation A phase-field function c may be used to approximate the characteristic function of Ω_1. Let

$$c(\mathbf{x},t) = \frac{1}{2}\left[1 + \tanh\left(\frac{r(\mathbf{x},t)}{2\sqrt{2}\epsilon}\right)\right], \tag{2.11}$$

where ϵ is a small parameter related to the interface thickness and $r(\mathbf{x},t)$ is a signed distance function to Γ (positive in Ω_1). The position of the interface may be taken to be $\Gamma(t) = \{\mathbf{x} \in \Omega \,|\, c(\mathbf{x},t) = 1/2\}$. To evolve c, one may evolve r by

$$\frac{\partial r}{\partial t} + \mathbf{v}\cdot\boldsymbol{\nabla} r = 0, \tag{2.12}$$

where $\mathbf{v}$ is an extension of $\mathbf{u}$ off the interface which is constant in the normal direction [1]. Alternatively, an advective Cahn-Hilliard equation can be used,

$$\frac{\partial c}{\partial t} + \mathbf{u}\cdot\boldsymbol{\nabla} c = \boldsymbol{\nabla}\cdot(M(c)\boldsymbol{\nabla}\mu), \tag{2.13}$$

$$\mu = g'(c) - \epsilon^2 \boldsymbol{\nabla}^2 c, \tag{2.14}$$

where μ is a chemical potential. Here, we take $g(c) = \frac{1}{4}c^2(1-c)^2$ as the double well potential. Note that this polynomial energy does not constrain $c \in [0,1]$ but the deviation from this interval is typically $O(\epsilon)$ at most. Alternative choices (e.g., double-obstacle [6, 7] or logarithmic potentials [4]) may be used that do constrain $c \in [0,1]$. The mobility M is localized on the interface and is taken to be $M(c) = \sqrt{4g(c)}$. This equation is fourth-order and nonlinear and thus requires specialized numerical methods to solve in an efficient manner. This is discussed further in section 4.

2.3. Regularized delta and Heaviside functions In order to evaluate equation (2.8) and equation (2.10) numerically, regularizations of the surface delta function and Heaviside function are needed. In the phase-field context, several definitions of

the delta function are available from the literature. In this work, the approximation from [73],

$$\delta_\Gamma \approx \frac{3\sqrt{2}}{\epsilon} B(c), \quad B(c) = c^2(1-c)^2, \tag{2.15}$$

is used for the surface equation. Note that other choices may be used [17]. For the boundary condition in the bulk equation, the approximation

$$\delta_\Gamma \approx |\boldsymbol{\nabla} c| \tag{2.16}$$

is used, which avoids additional scaling issues in the equation [53]. Further, the regularized Heaviside function is simply taken to be [53]

$$H(c) \approx c. \tag{2.17}$$

The final system of equations can now be summarized as

$$\frac{\partial}{\partial t}(B(c) f) + \boldsymbol{\nabla} \cdot (B(c) f \mathbf{u}) = \boldsymbol{\nabla} \cdot (D_f B(c) \boldsymbol{\nabla} f) + B(c) j, \tag{2.18}$$

$$\frac{\partial}{\partial t}(cF) + \boldsymbol{\nabla} \cdot (cF \mathbf{u}) = D_F \boldsymbol{\nabla} \cdot (c \boldsymbol{\nabla} F) - |\boldsymbol{\nabla} c| j. \tag{2.19}$$

3. Asymptotic analysis In this section, the method of matched asymptotic expansions is used to provide a formal justification for the diffuse interface approach. To make the system slightly more general, we may add reaction terms to the bulk and surface equations, i.e., $R_f(f)$ and $R_F(F)$ may be added to equations (2.18) and (2.19) respectively. In this approach, the domain Ω is separated into two regions — the regions far from Γ (outer region, i.e., the portions of Ω_1 and Ω_0 away from Γ) and the region near Γ (inner region). In each region, the variables are expanded in powers of the diffuse interface thickness. In the outer region, the variables are expanded as

$$c(\mathbf{x},t) = c_0(\mathbf{x},t) + \epsilon c_1(\mathbf{x},t) + \ldots, \tag{3.1}$$

and analogously for the other variables. In the region near Γ, we introduce a new coordinate system.

3.1. New Coordinate Introduce the following local normal-tangential coordinate system with respect to the curve Γ. Let $\Gamma = \mathbf{X}(\mathbf{s},t) = (X(\mathbf{s},t), Y(\mathbf{s},t), Z(\mathbf{s},t))$, where $\mathbf{s} = (s_1, s_2)$ is a parametrization of the surface and t is time. Let $r = r(\mathbf{x};\epsilon)$ be the signed distance along the normal from a point $\mathbf{x}$ to Γ, and is positive when outside Γ (i.e. in Ω_1). Then, if Γ is smooth, there exists a neighborhood

$$U_\epsilon := \{\mathbf{x} \in \Omega : |r(\mathbf{x},\epsilon)| < \rho\}$$

of Γ for some $0 < \rho \ll 1$, such that the local coordinate transformation from (x,y,z) to (r,s_1,s_2) is valid, e.g., $\mathbf{x} = \mathbf{X}(\mathbf{s},t) + r\mathbf{n}(\mathbf{s},t)$. Near the interface, we introduced a stretched normal coordinate $z = \frac{r}{\epsilon}$. Note that as $\epsilon \to 0$, the inner region extends from $-\infty < z < \infty$. We then assume that the variables may be expanded in regular power series in ϵ in the stretched coordinate system:

$$c(\mathbf{x},t) = C(z,\mathbf{s},t) = C_0(z,\mathbf{s},t) + \epsilon C_1(z,\mathbf{s},t) + \ldots, \tag{3.2}$$

and analogously for the other variables. Furthermore, in this coordinate system we have

$$\partial_t = -\epsilon^{-1}\hat{V}_0\partial_z + \partial_t + \mathcal{O}(\epsilon), \tag{3.3}$$

$$\boldsymbol{\nabla} = \epsilon^{-1}\mathbf{n}\partial_z + \boldsymbol{\nabla}_\Gamma + \mathcal{O}(\epsilon), \tag{3.4}$$

where $\hat{V}_0$ is the leading term of the normal velocity of Γ.

3.2. Matching Condition Assuming that there is an overlapping region where both the inner and outer expansions are valid, we may write the outer expansion in the local coordinate system as

$$c(\mathbf{x},t) = c(r,\mathbf{s},t) = c_0(r,\mathbf{s},t) + \epsilon c_1(r,\mathbf{s},t) + \ldots, \tag{3.5}$$

and analogously for the other variables. Matching the inner and outer expansions in this region, the following matching conditions hold [10, 71, 22]

$$\lim_{r\to 0^\pm} F_0 = \lim_{z\to\pm\infty} \hat{F}_0, \tag{3.6}$$

$$\lim_{r\to 0^\pm} f_0 = \lim_{z\to\pm\infty} \hat{f}_0, \tag{3.7}$$

$$\lim_{r\to 0\pm} \mathbf{n}\cdot\boldsymbol{\nabla} F_0 = \lim_{z\to\pm\infty} \partial_z \hat{F}_1, \tag{3.8}$$

$$\lim_{z\to\pm\infty} \partial_z \hat{F}_0 = 0. \tag{3.9}$$

Analogous matching conditions hold for the other variables.

3.3. Bulk Equation

3.3.1. Outer expansion The $\mathcal{O}(\epsilon^0)$ term of equation (2.19) gives:

$$\frac{\partial F_0}{\partial t} + \boldsymbol{\nabla}\cdot(F_0\mathbf{u}_0) = \boldsymbol{\nabla}\cdot(D_F\boldsymbol{\nabla}F_0) + R_F(F_0). \tag{3.10}$$

Thus at leading order equation (2.5), with the reaction term, is recovered. To determine the boundary conditions on Γ, we match with the inner expansion.

3.3.2. Inner expansion At $\mathcal{O}(\epsilon^{-2})$, we obtain

$$\partial_z(C_0 D_F \partial_z \hat{F}_0) = 0, \tag{3.11}$$

which implies $\partial_z \hat{F}_0 = 0$. At $\mathcal{O}(\epsilon^{-1})$ we obtain

$$\left(U_{N,0} - \hat{V}_0\right)\partial_z\left(C_0\hat{F}_0\right) = \partial_z(C_0 D_F \partial_z \hat{F}_1) + \left(r_a\hat{F}_0 - r_d\hat{f}_0\right)\partial_z C_0. \tag{3.12}$$

Since $U_{N,0} = \hat{V}_0$ by the asymptotic analysis of the advective Cahn-Hilliard equation [58], $\hat{F}_0$ is independent of z and, as we show below, $\hat{f}_0$ is also independent of z, we may integrate equation (3.12) and use that $\int_{-\infty}^{+\infty} \partial_z C_0 \, dz = 1$, again taken from [58], to obtain

$$D_F \lim_{z\to+\infty} \partial_z \hat{F}_1 = -(r_a\hat{F}_0 - r_d\hat{f}_0). \tag{3.13}$$

Together with equation (3.8), we therefore recover the Neumann boundary condition (2.6) for the outer solution at leading order

$$D_F \lim_{r\to 0+} \mathbf{n}\cdot\boldsymbol{\nabla}F_0 = D_F \lim_{z\to+\infty} \partial_z \hat{F}_1 = -(r_a F_0 - r_d f_0), \tag{3.14}$$

where we have set $\hat{f}_0 = f_0$ since $\hat{f}_0$ is independent of z. Next, we turn to the surface concentration equation.

3.4. Surface Equation Here, we only focus on the inner expansion since the equation is localized around the interface. At $\mathcal{O}(\epsilon^{-2})$, we obtain

$$\partial_z \left(D_f B(C_0) \partial_z \hat{f}_0 \right) = 0, \tag{3.15}$$

which implies $\partial_z \hat{f}_0 = 0$, as claimed above. The $\mathcal{O}(\epsilon^{-1})$ term gives

$$0 = \partial_z (B(C_0) \partial_z \hat{f}_1), \tag{3.16}$$

where we have used that $U_{N,0} = \hat{V}_0$. Equation (3.16) implies that $\partial_z \hat{f}_1 = 0$ also. At $\mathcal{O}(\epsilon^0)$, we obtain

$$\begin{aligned} \partial_t (B(C_0)\hat{f}_0) + \boldsymbol{\nabla}_\Gamma \cdot \left(B(C_0) \hat{f}_0 \mathbf{U}_0 \right) = \partial_z (D_f B(C_0) \partial_z \hat{f}_2) + \boldsymbol{\nabla}_\Gamma \cdot \left(D_f B(C_0) \boldsymbol{\nabla}_\Gamma \hat{f}_0 \right) \\ + B(C_0)(r_a \hat{F}_0 - r_d \hat{f}_0) + B(C_0) R_f(f_0). \end{aligned} \tag{3.17}$$

Since $\hat{f}_0$ is independent of z, we may integrate equation (3.17) in z from $-\infty$ to $+\infty$, and divide by $\int_{-\infty}^{+\infty} B(C_0) \mathrm{d}z > 0$ to obtain

$$\partial_t f_0 + \boldsymbol{\nabla}_\Gamma \cdot (f_0 \mathbf{u}_0) = \boldsymbol{\nabla}_\Gamma \cdot (D_f \boldsymbol{\nabla}_\Gamma f_0) = r_a F_0 - r_d f_0 + R_f(f_0), \tag{3.18}$$

where we taken $\hat{f}_0 = f_0$, $\hat{F}_0 = F_0$ and we also have assumed that $\mathbf{U}_{\Gamma,0}$ is independent of z (which implies there is no jump in velocity across Γ) so that we may write $\mathbf{U}_0 = \mathbf{u}_0$. Thus, equation (2.4), with the reaction term, is recovered at leading order.

4. Numerical methods This section briefly describes the numerical methods used to solve the above equations. The algorithm follows the one developed in [87]. In particular, the equations are discretized using finite differences in space and a semi-implicit time discretization. A block-structured, adaptive grid is used to increase the resolution around the interface in an efficient manner. The nonlinear equations at the implicit time level are solved using a non-linear Adaptive Full Approximation Scheme (AFAS) multigrid algorithm. For a detailed discussion of the adaptive algorithm and the multigrid solver, the reader is referred to [87].

The equations are discretized on a rectangular domain. The surface concentration, the bulk concentration, the phase-field function and the chemical potential are defined at the cell-centers, while the velocity components are defined on cell-edges.

Special care has to be taken for the temporal discretization. The Cahn-Hilliard system is fourth order in space, and requires the use of an implicit method to avoid severe limitations in the time step. Here, Crank-Nicholson type schemes are used [45],

$$\begin{aligned} \frac{c^{k+1} - c^k}{\Delta t} = &- \frac{1}{2} \left[\boldsymbol{\nabla}_d \cdot (\mathbf{u}^{k+1} c^{k+1}) + \boldsymbol{\nabla}_d \cdot (\mathbf{u}^k c^k) \right] \\ &+ \frac{1}{2} \left[\boldsymbol{\nabla}_d \cdot (M^{k+1} \boldsymbol{\nabla}_d \mu^{k+1}) + \boldsymbol{\nabla}_d \cdot (M^k \boldsymbol{\nabla}_d \mu^k) \right], \end{aligned} \tag{4.1}$$

$$\mu^{k+1} = g'(c^{k+1}) - \epsilon^2 \boldsymbol{\nabla}_d^2 c^{k+1}. \tag{4.2}$$

In [45, 87] this approach was shown to be robust and efficient. The equations for

surface concentration and bulk concentration are discretized in a similar fashion,

$$\begin{aligned}\frac{\delta_\Gamma^{k+1}f^{k+1}-\delta_\Gamma^k f^k}{\Delta t} =& -\frac{1}{2}\left[\boldsymbol{\nabla}_d\cdot(\mathbf{u}^{k+1}\delta_\Gamma^{k+1}f^{k+1})+\boldsymbol{\nabla}_d\cdot(\mathbf{u}^k\delta_\Gamma^k f^k)\right]\\ &+\frac{D_f}{2}\left[\boldsymbol{\nabla}_d\cdot(\delta_\Gamma^{k+1}\boldsymbol{\nabla}_d f^{k+1})+\boldsymbol{\nabla}_d\cdot(\delta_\Gamma^k\boldsymbol{\nabla}_d f^k)\right]\\ &+\frac{1}{2}\left[\delta_\Gamma^{k+1}j^{k+1}+\delta_\Gamma^k j^k\right],\end{aligned} \tag{4.3}$$

$$\begin{aligned}\frac{H^{k+1}F^{k+1}-H^kF^k}{\Delta t} =& -\frac{1}{2}\left[\boldsymbol{\nabla}_d\cdot(\mathbf{u}^{k+1}H^{k+1}F^{k+1})+\boldsymbol{\nabla}_d\cdot(\mathbf{u}^kH^kF^k)\right]\\ &+\frac{D_f}{2}\left[\boldsymbol{\nabla}_d\cdot(H^{k+1}\boldsymbol{\nabla}_d F^{k+1})+\boldsymbol{\nabla}_d\cdot(H^k\boldsymbol{\nabla}_d F^k)\right]\\ &+\frac{1}{2}\left[|\boldsymbol{\nabla}_d c^{k+1}|j^{k+1}+|\boldsymbol{\nabla}_d c^k|j^k\right],\end{aligned} \tag{4.4}$$

where, in the above equations, we set $\delta_\Gamma^{k+1}=B(c^{k+1})+\alpha$ and $H^{k+1}=\sqrt{(c^{k+1})^2+\alpha^2}$, with α being a small parameter ($\alpha=10^{-6}$) that is used to ensure that division by zero does not occur; the results are found to be quite insensitive to the precise choice of α provided it is sufficiently small. The operator $\boldsymbol{\nabla}_d$ represents the standard second-order finite-difference discretization. The convective terms of the form $\boldsymbol{\nabla}\cdot(\mathbf{u}\phi)$ are discretized using the third-order WENO reconstruction method [78, 55]. The WENO reconstruction method has the advantage that it handles steep gradients well, which may occur in the type of dynamics described in this work. Additionally, fewer grid points are needed to achieve a high order solution. This is particularly important for the efficiency of the adaptive grid, because fewer ghost cell values have to be calculated at the boundaries of each grid block.

Homogeneous Neumann far-field boundary conditions are prescribed for all variables. This is imposed by introducing a set of ghost cells around the domain. These ghost cells are updated before every smoothing operation.

The AFAS multigrid algorithm is used to solve the discretized equations at every time step. The full description of the AFAS multigrid method will not be given here, the details can be found in [87] and in the reference text [85]. The ideal run-time complexity of this algorithm is optimal, i.e., $\mathcal{O}(N)$ where N is the number of grid points. The present implementation achieves this complexity, which is shown in section 5.6.

5. Code validation

5.1. Surface diffusion on a stationary circle First, a problem without bulk concentration is considered. This tests the validity of the diffuse interface representation of the surface equation, and of the correct implementation of the diffusion term.

Consider a stationary circle of radius R, with an initial surface concentration given by

$$f_0(\theta)=\frac{1}{2}(1-\cos\theta), \tag{5.1}$$

where θ denotes the angle measured in the counter-clockwise direction from the y-axis. The surface concentration equation can now be written in polar coordinates as

$$\frac{\partial f(\theta,t)}{\partial t}=\frac{D_f}{R^2}\frac{\partial^2 f(\theta,t)}{\partial\theta^2}, \tag{5.2}$$

with initial condition f_0 and periodic boundary condition in the θ-direction. This equation can be solved analytically, yielding

$$f(\theta,t)=\frac{1}{2}\left(1-e^{-\frac{D_f}{R^2}t}\cos\theta\right). \tag{5.3}$$

A series of simulations are performed comparing the numerical solution to the analytical solution. The computational domain chosen for the simulations is $[-2,2]\times[-2,2]$ and a circle with radius $R=1$ is placed in the center of the domain. The phase-field function is initialized by

$$c(x,y)=\frac{1}{2}\left[1-\tanh\left(\frac{\sqrt{x^2+y^2}-R}{2\sqrt{2}\epsilon}\right)\right]. \tag{5.4}$$

The initial surface concentration is given by the analytical solution, and the time step is $\Delta t=1\times10^{-2}$.

In the numerical code, the surface concentration is defined at grid points near the interface. To enable a direct comparison with the analytical solution, the concentration at the interface is needed. This is done by using a marching squares algorithm (see e.g. [57]) to generate a set of points at the 0.5 isocontour of the phase-field function. Bilinear interpolation is then used to interpolate the grid values of the surface concentration to these interface points. Note that this will introduce extra uncertainties, so the absolute errors given later may not be exact values. The order of convergence results should not be affected by this.

An example of the adaptive grid is shown in figure 5.1. Clearly, the grid follows the circle shape very well. No significant difference between the solutions on adaptive grids and uniform grids was found for this test case for the same effective resolution. Figure 5.2 shows comparisons between the numerical solution and the analytical solution at various times and surface diffusion coefficients. Good agreement is observed. The error in the infinity norm between the interpolated values and the exact values at the interface is given in Table 5.1. The numerical solution converges towards the exact solution in a first order fashion, as predicted by the asymptotic analysis.

Table 5.1: The error and convergence order for the surface diffusion test case at $t=1$. The interface thickness is defined as $\epsilon=1.6h_{\min}$, where h_{min} the minimum grid size.

Grid spacing	Error ($\times10^{-2}$)	Order
1/8	4.29	-
1/16	2.35	0.87
1/32	1.18	0.99
1/64	0.60	0.98
1/128	0.30	1.00

5.2. Surface diffusion on an advected circle Now, the circle in the above test case is put in a constant velocity field, $\mathbf{u}=(2,0)$. The analytical solution is the same, only translated in the computational domain. The computational domain is extended by two in the x-direction to accomodate the translation.

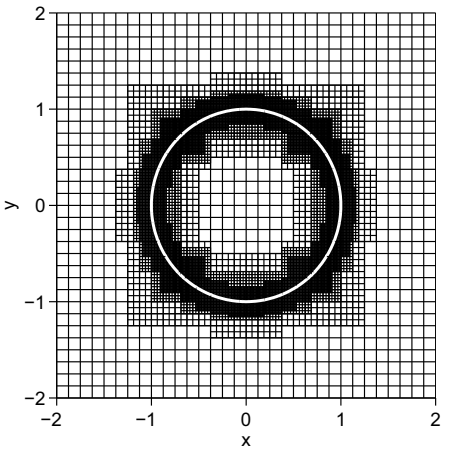

Fig. 5.1: Example of the adaptive grid for the surface diffusion on a fixed circle. The root level has 32×32 grid points and there are three levels of refinement, giving an effective resolution at the interface of 256×256.

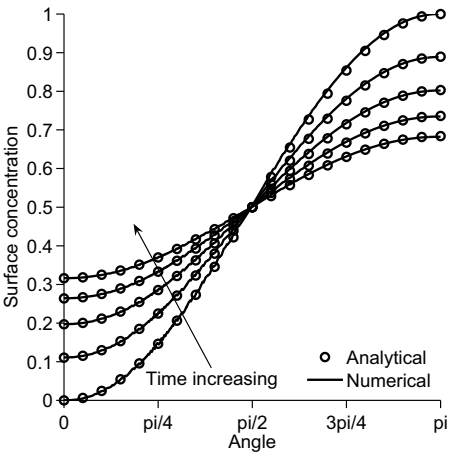

(a) Surface concentration profiles at times $t = 0.0, 0.25, 0.5, 0.75$ and 1 for $D_f = 1$.

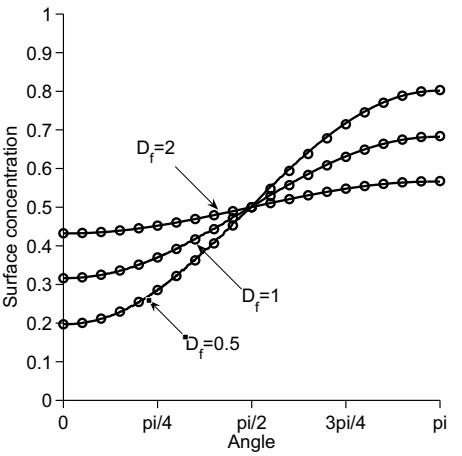

(b) Surface concentration profiles at $t = 1$ for different D_f.

Fig. 5.2: Comparison of the numerical and exact solutions for the surface diffusion test case. Because the solution is symmetric with respect to the y-axis, only one half of the circle is shown here. The grid spacing is $h_{\min} = 1/64$.

The initial and final surface concentration is given in figure 5.3. As shown in Table 5.2, the convergence is first order as in the diffusion only test case. The error is slightly higher due to the additional errors caused by the advection.

Table 5.2: The error and convergence order for the diffusion on a translating circle at $t=1$. The interface thickness is defined as $\epsilon=1.6h_{\min}$.

Grid spacing	Error ($\times 10^{-2}$)	Order
1/8	4.60	-
1/16	2.47	0.90
1/32	1.23	1.01
1/64	0.62	0.99
1/128	0.31	1.01

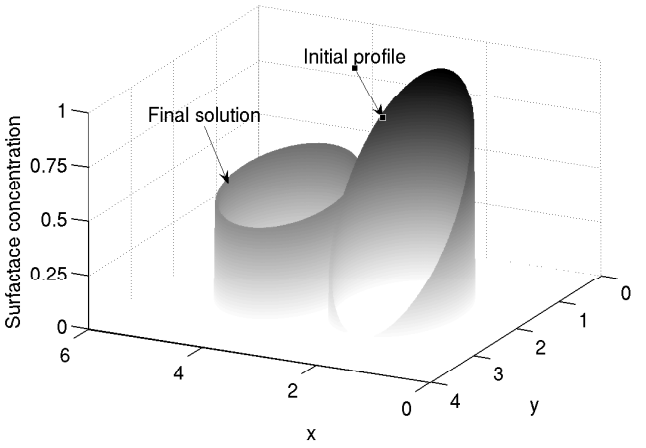

Fig. 5.3: The initial and final surface concentration for the advected circle test case.

5.3. Surface concentration evolution on an expanding circle A circle is placed in the velocity field given by

$$u=\cos\theta, v=\sin\theta, \tag{5.5}$$

which is illustrated in figure 5.4(a). In the absence of diffusion, the surface concentration is just a function of the circle circumference, so the mass conservation equation reduces to

$$f(t)=\frac{C_0}{C(t)}f_0, \tag{5.6}$$

where $C=2\pi R$ is the surface area, and subscript 0 denotes the initial condition.

For this test case, the computational domain was set to $\Omega=[-16,16]\times[-16,16]$ to accomodate the expansion. The initial radius was set to $R_0=1$, and the initial surface concentration was set to $f_0=0.5$. Instead of solving the Cahn-Hilliard system, equations (2.13)–(2.14), the phase-field function is evolved analytically for this test case. No significant difference is observed if the interface is evolved according to the Cahn-Hilliard system, as is done below.

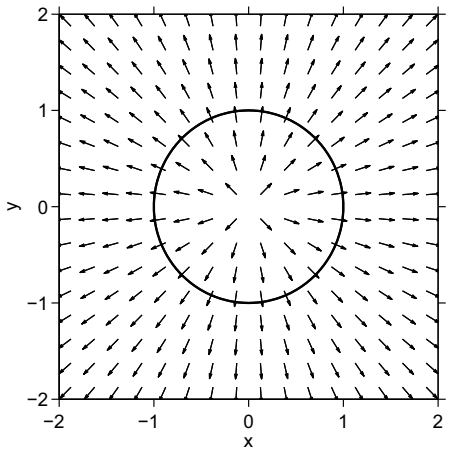

(a) Illustration of the expanding circle test case.

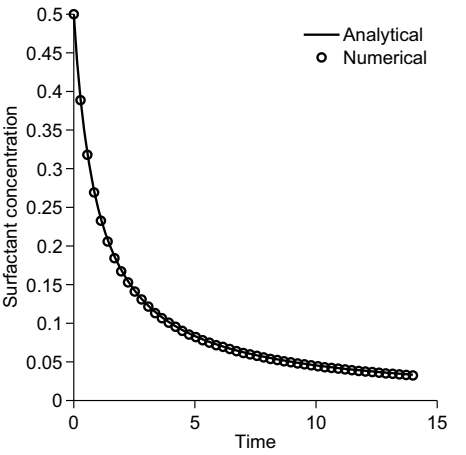

(b) Comparison of the mean value of the computed surface concentration and the analytical value. $h = 1/8$.

Fig. 5.4: Numerical setup and results for the expanding circle test case.

The numerical and analytical solutions are compared in figure 5.4(b), and excellent agreement is observed. The convergence behaviour is given in Table 5.3, and as in previous test cases, the method converges in a first-order fashion.

Table 5.3: The error and convergence order for the expanding circle test case. The error is measured as the maximum deviation of the mean surface concentration to the analytical concentration. The interface thickness $\epsilon = 1.6 h_{\min}$.

Grid spacing	Error ($\times 10^{-2}$)	Order
1	13.6	-
1/2	6.60	1.04
1/4	3.30	1.00
1/8	1.62	1.03

5.4. Bulk diffusion and bulk-surface mass transfer This test case was introduced in [69] in the context of surfactants, to test the coupling between a bulk concentration and a surface concentration. Consider an initially clean circle of radius a in a domain which contains an initial bulk concentration F_∞. A simplified version of the source term is used, where mass moves from the bulk to the interface,

$$j = r_a F. \tag{5.7}$$

Table 5.4: Values used in the bulk diffusion and bulk-surface mass transfer test case.

Quantity	Value
Radius, a	1.0
Adsorption rate, r_a	1.0
Diffusion coefficient, D_F	1.0
Initial bulk concentration, F_∞	1.0

The evolution of the bulk concentration can now be described with the heat equation in an infinite, hollow cylinder,

$$\frac{\partial F}{\partial t} = D_F \left(\frac{\partial^2 F}{\partial r^2} + \frac{1}{r} \frac{\partial F}{\partial r} \right), \tag{5.8}$$

with boundary conditions

$$\left. \frac{\partial F}{\partial r} \right|_{r=a} = r_a F(r=a), \tag{5.9}$$

$$F(r=R) = F_\infty, \tag{5.10}$$

where R is the extent of the domain; R is taken to be 4. In lieu of an analytical solution, a fourth-order accurate finite-difference discretization of the above 1D problem is used for comparison to the diffuse-interface solution. The grid size for this problem was chosen high enough to give a resolution independent solution. The physical properties used in the simulations are given in Table 5.4.

A visual comparison between the 1D solution and the diffuse-interface results for the bulk concentration at various time steps is given in figure 5.5(a). Apart from the small errors close to the interface during the early times due to the sharp gradients, the agreement is excellent.

The amount of mass accumulated on the interface can be found from the 1D solution via mass conservation,

$$M_f(t) = M_F(0) - 2\pi \int_a^R F(t) r \mathrm{d}r. \tag{5.11}$$

Figure 5.5(b) shows that the diffuse-interface solution is in good agreement with the 1D solution.

The error and convergence for both the bulk concentration and the surface concentration is given in Table 5.5. The error decreases in a second-order fashion. The reason for this is that for this test case, the surface concentration is uniform, so there is no surface diffusion.

Next, the effect of varying the surface diffusion coefficient relative to the bulk diffusion coefficient, $D = D_f / D_F$, is investigated. The initial bulk concentration is set to

$$F_0(y) = (y_{\max} - y) \times 10^{-3} \tag{5.12}$$

instead of the previous uniform concentration and we consider both adsorption and desorption. There is a non-uniform adsorption to the interface which gives rise to

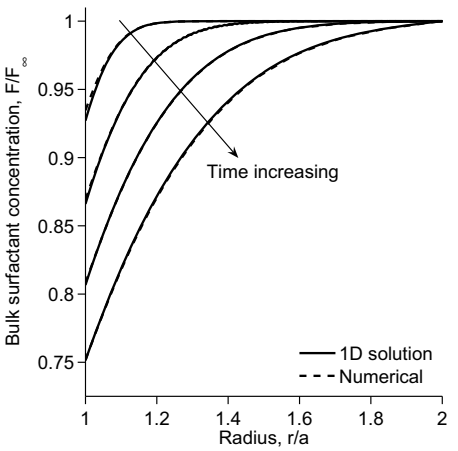

(a) The $y=0$ slice of the bulk concentration distribution at times $t=0.005$, 0.02, 0.05 and 0.1.

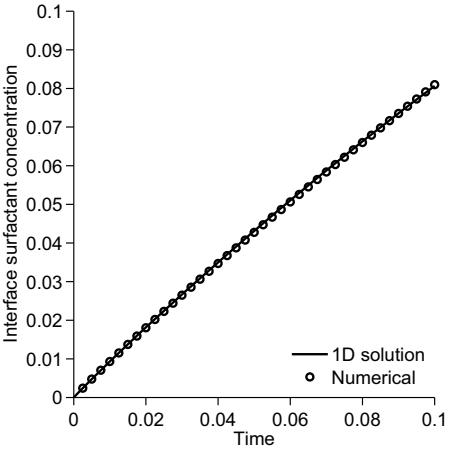

(b) Interface surfactant concentration.

Fig. 5.5: Comparison of the 4th order 1D solution and the phase-field solution for the bulk diffusion and bulk-surface mass transfer test case. $h_{\min}=1/128$, $\epsilon=1/80$.

Table 5.5: The error in the infinity norm and convergence order for the bulk concentration and the accumulated surface mass in the bulk diffusion and bulk-surface mass transfer test case. The interface thickness is $\epsilon=1.6h_{\min}$.

	Bulk concentration		Surface mass	
Grid spacing	Error ($\times 10^{-2}$)	Order	Error ($\times 10^{-3}$)	Order
1/8	11.38	-	9.66	-
1/16	5.21	1.13	4.50	1.10
1/32	1.57	1.73	1.20	1.91
1/64	0.343	2.20	0.22	2.44
1/128	0.0473	2.86	0.036	2.61

diffusion effects on the surface. Additionally, desorption is added to yield more complex dynamics. The radius is set to $r=0.15$ and the drop is centered at (0.5,0.5). The adsorption and desorption rates are $r_a=r_d=100$ and the bulk diffusion coefficient is $D_F=1.0$. Figure 5.6 shows the concentration in the bulk and on the surface at $t=0.08$ for varying diffusion ratios. A grid spacing of $h=1/256$ was employed, along with interface thickness $\epsilon=0.004$. Because of the non-uniform bulk distribution, the adsorption will be higher at the bottom of the circle than at the top. As the surface diffusion coefficient increases, mass is diffused from the bottom to the top of the circle faster, which further reduces the adsorption at the top. This effectively increases the diffusion and leads to a more uniform concentration distribution in the bulk. This is illustrated in figure 5.7, which shows the bulk concentration along $x=0.5$. The larger surface diffusion also leads to lower total interface concentration, since mass is

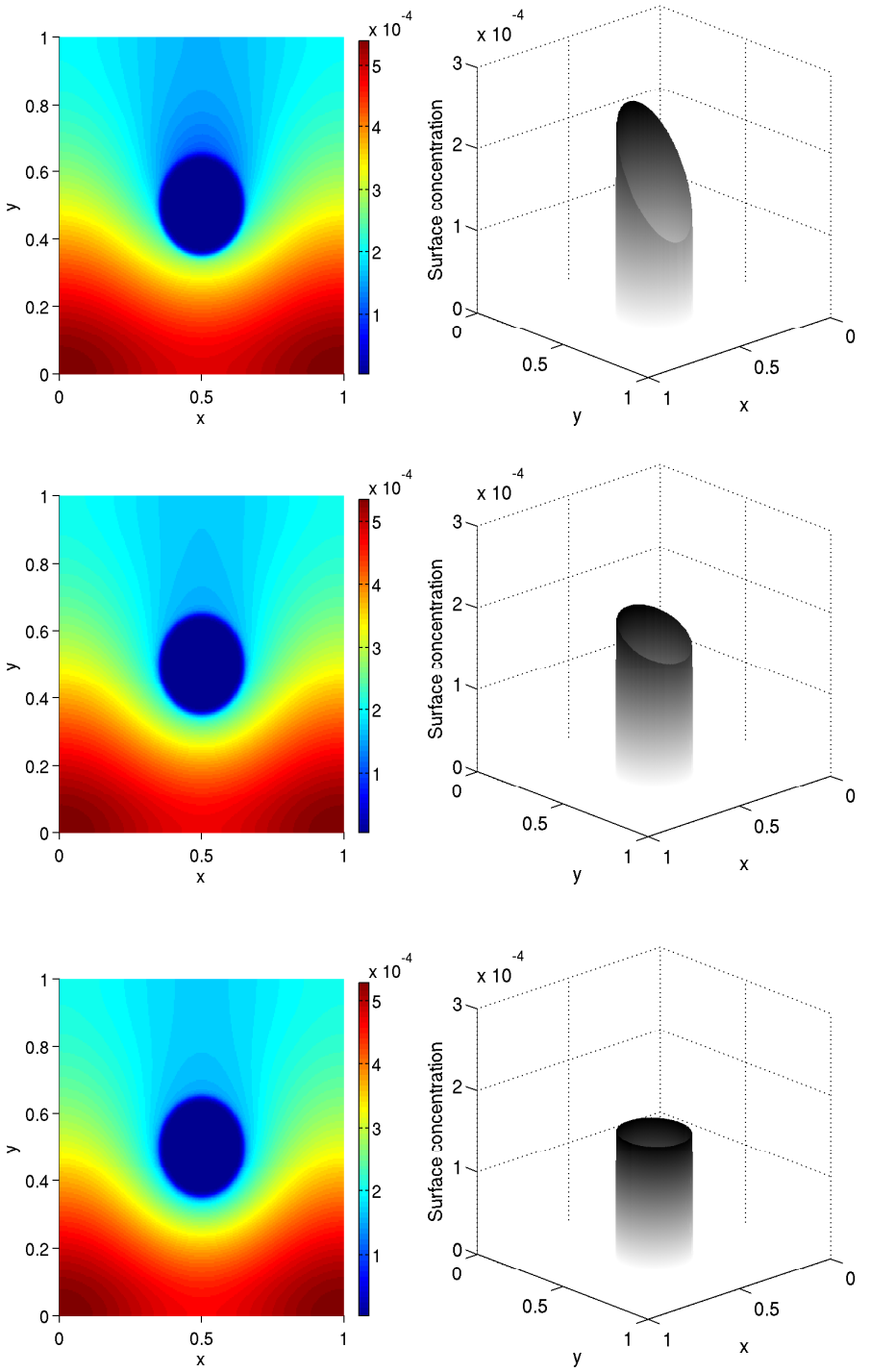

(a) Bulk concentration (b) Surface concentration

Fig. 5.6: Bulk concentration and surface concentration for the mass transfer test case with non-uniform initial bulk concentration at $t = 0.08$. From top to bottom, $D = 0.1$, $D = 1.0$ and $D = 10$.

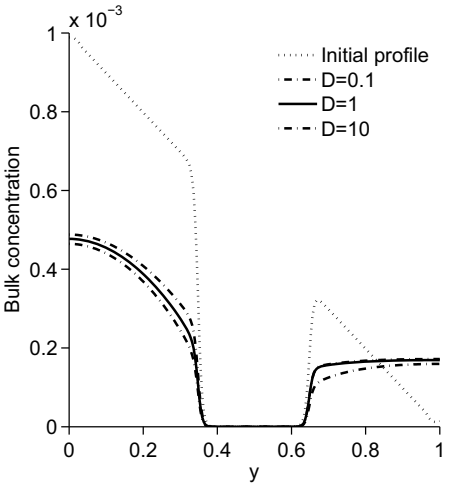

Fig. 5.7: Bulk concentration along $x=0.5$ for three different diffusion coefficient ratios at $t=0.08$. A larger surface diffusion coefficient increases the transport of bulk concentration and gives a more uniform profile.

desorbed back into the bulk.

5.5. Bulk-surface coupling on a perturbed circle In this test case, the surface evolution on, and the bulk evolution inside, a perturbed circle is considered. The circle is given by

$$r(\theta)=1+0.1\cos(3\theta), \tag{5.13}$$

and forcing functions are added to the surface and bulk equations so that the exact solution is known. More specifically,

$$\frac{\partial f}{\partial t}=\boldsymbol{\nabla}_s^2 f-f+F+\zeta_1 \text{ on } \Gamma \tag{5.14}$$

$$\frac{\partial F}{\partial t}=\boldsymbol{\nabla}^2 F-F+\zeta_2 \text{ in } \Omega_0 \tag{5.15}$$

is solved subject to the boundary condition

$$\boldsymbol{\nabla} F\cdot\mathbf{n}=f-F \text{ on } \Gamma. \tag{5.16}$$

The forcing functions are chosen such that the solution in Ω_0 is

$$F=\frac{1}{4}(x^2+y^2)e^{-3t}, \tag{5.17}$$

and the solution on Γ is

$$f=\left(\frac{1}{2}\frac{r(\theta)}{\sqrt{r(\theta)^2+r'(\theta))^2}}+\frac{1}{4}r(\theta)^2\right)e^{-3t}. \tag{5.18}$$

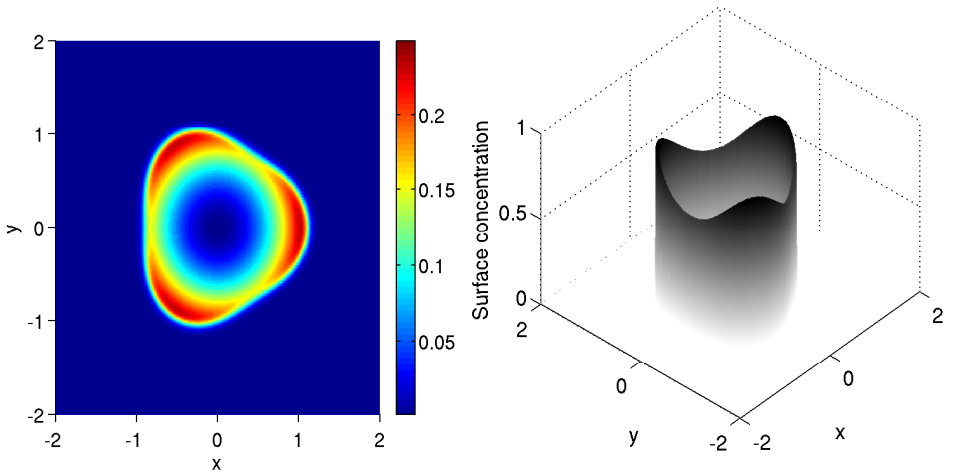

(a) Bulk concentration (b) Surface concentration

Fig. 5.8: The solutions at $t = 2.0 \times 10^{-3}$ for the bulk-surface coupling on a perturbed circle.

The diffuse-interface representation of the above system is

$$\frac{\partial}{\partial t}(f B(c)) = \boldsymbol{\nabla} \cdot (B(c) \boldsymbol{\nabla} f) - B(c)(f + F + \zeta_1) \tag{5.19}$$

$$\frac{\partial}{\partial t}(H F) = \boldsymbol{\nabla} \cdot (H \boldsymbol{\nabla} F) - HF + H\zeta_2 + (f - F)|\boldsymbol{\nabla} c|, \tag{5.20}$$

where the Heaviside function is now given by

$$H(c) = 1 - c, \tag{5.21}$$

instead of equation (2.17) since the bulk concentration is required in Ω_0 (not in Ω_1).

The simulation was run to time $t = 2.0 \times 10^{-3}$, and the interface thickness was scaled as $\epsilon = 1.28 h_{\min}$. Figure 5.8 shows the final solution for the surface concentration and the bulk concentration for a grid spacing of $h_{min} = 1/128$. The analytical solutions given by equations (5.17) and (5.18) are compared to the numerical results in figure 5.9. Excellent agreement is observed. In Table 5.6, the respective errors compared to the analytical solutions are listed together with the convergence order. Again, first order convergence results are obtained.

5.6. Bulk-surface coupling in a 2D vortical flow A circle with radius $r = 0.15$ is placed at $\mathbf{x} = (0.5, 0.75)$ in a domain $\Omega = [0,1] \times [0,1]$. The circle is advected by a prescribed velocity field defined by the stream function

$$\Psi = -\cos(\pi t) \frac{1}{\pi} \sin^2(\pi x) \sin^2(\pi y), \tag{5.22}$$

which gives the individual velocity components as

$$u = -2 \cos(\pi t) \sin^2(\pi x) \sin(\pi y) \cos(\pi y), \tag{5.23}$$

$$v = 2 \cos(\pi t) \sin^2(\pi y) \sin(\pi x) \cos(\pi x). \tag{5.24}$$

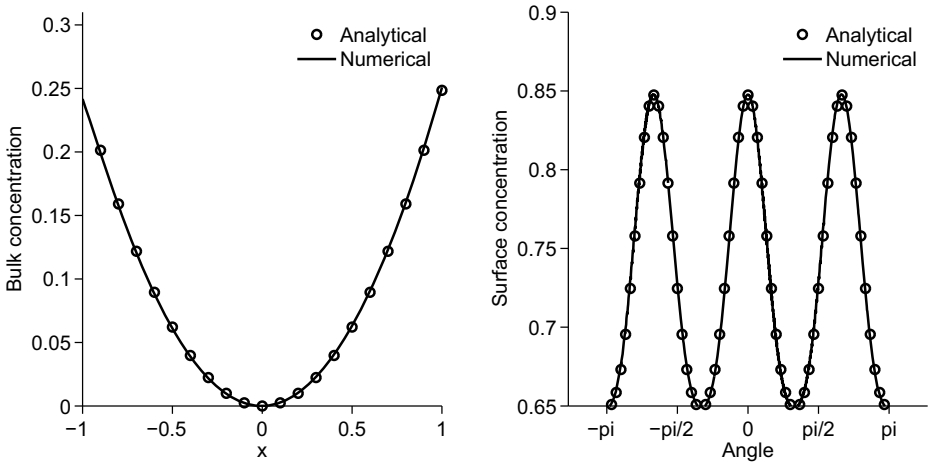

(a) Bulk concentration along $y=0$ (b) Surface concentration

Fig. 5.9: Comparison between the analytical solutions and numerical solutions for $h=1/128$ at $t=2.0\times10^{-3}$s for the perturbed circle test case.

Table 5.6: The error in the infinity norm and convergence order for the bulk concentration and the interface concentration in the perturbed circle test case. The interface thickness is $\epsilon=1.28h$.

Grid spacing	Bulk concentration Error ($\times10^{-3}$)	Order	Surface concentration Error ($\times10^{-2}$)	Order
1/16	17.0	-	11.0	-
1/32	9.5	0.84	4.4	1.32
1/64	5.1	0.90	1.5	1.55
1/128	2.6	0.97	0.74	1.02

The initial condition is illustrated in figure 5.10. This is a demanding test case for both the interface advection and the adaptive grid, because the interface undergoes large deformations. Because of the periodicity of the flow field, it is common to compare the initial solution to the solution after one period. However, with diffusion and adsorption/desorption, the solution is not time-reversible. Here, a comparison with the results from [90] is first considered as a validation case, before simulations with bulk/interface coupling are presented.

For the validation case, the diffusion is set to $D_f=10^{-3}$ for the surface concentration, and the evolution of the bulk concentration is not considered. Hence, there is no coupling between the bulk and surface for this test case. The initial surface concentration is $f_0=1.0$. An effective grid spacing of $h_{min}=1/512$ was used along with an interface thickness $\epsilon=0.002$. Figure 5.11(a) shows the evolution of the interface and the adaptive grid. The grid clearly tracks the interface in an efficient manner, and the

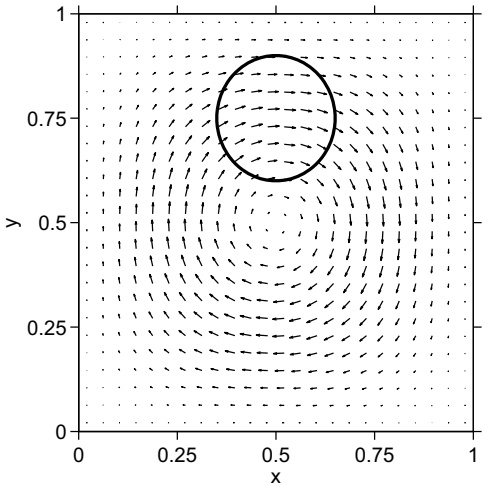

Fig. 5.10: Illustration of the vortical velocity field and initial surface position.

morphology at $t=0.5$ matches that of figure 11(b) in [90]. The surface concentration along the interface is shown in figure 5.11(b). Due to the complex flow field, mass is swept to the lower and upper part of the stretching circle. The concentration is particularly high at the upper part. This profile is in good agreement with the equivalent figure 11(c) in [90].

Next, the effect of varying the surface diffusion coefficient relative to the bulk diffusion coefficient, $D=D_f/D_F$, is investigated. The initial surface concentration is $f_0=10^{-4}$ and the initial bulk concentration is given by the non-uniform profile $F_0=10^{-4}y$. Additionally, the bulk and interface is coupled, with adsorption coefficient $r_a=100$ and desorption coefficient $r_d=200$. The bulk diffusion coefficient is $D_F=0.1$, while the surface diffusion coefficient is varied. An effective grid spacing of $h_{\min}=1/256$ was employed, along with interface thickness $\epsilon=0.004$.

The concentration at $t=0.5$ for the bulk and the interface for three different diffusion coefficient ratios is shown in figure 5.12. When the surface diffusion coefficient is low, the main transport mechanism is the convection. Some mass is adsorbed onto the interface, but the low diffusion coefficient leads to a highly non-uniform profile. As the surface diffusion coefficient increases, more mass is adsorbed from the upper part of the domain, where the bulk concentration is high, then diffused along the interface and finally desorbed in the lower part of the domain. This leads to a more uniform bulk distribution around the advected circle.

Finally, a test of the efficiency of the multigrid algorithm and the adaptive grid was performed on this test case. This was done by comparing the time taken to complete 1000 time steps on several grid sizes on both uniform and adaptive grids. The time step size was kept constant, and low enough so that the number of V-cycles on each time step was equivalent for all grid sizes. The results are shown in figure 5.13. Both the uniform and adaptive run-times increase in a linear fashion, which indicates that the numerical implementation achieves the optimal $\mathcal{O}(N)$ run-time complexity of the multigrid algorithm, where N is the total number of grid points. Additionally, the slope for the adaptive simulations is much lower than the corresponding slope for the

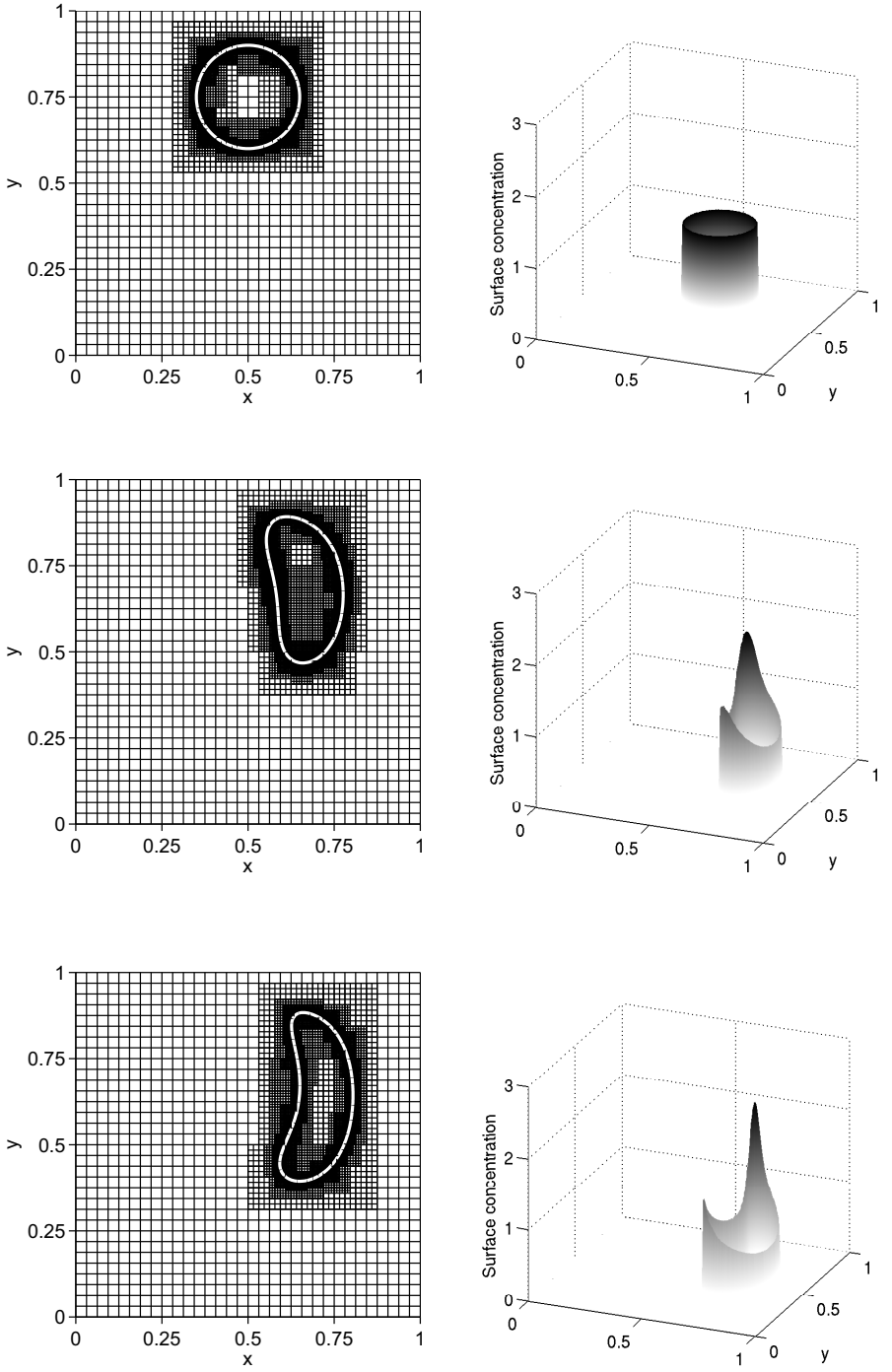

(a) Adaptive grid and interface morphology. (b) Surface concentration along the interface.

Fig. 5.11: Evolution of a circle in a vortex field, depicted at $t=0.0,0.25,0.5$. The parent grid level has spacing $h=1/32$, and there are 4 levels of refinement, giving an effective grid spacing of $h_{\min}=1/512$.

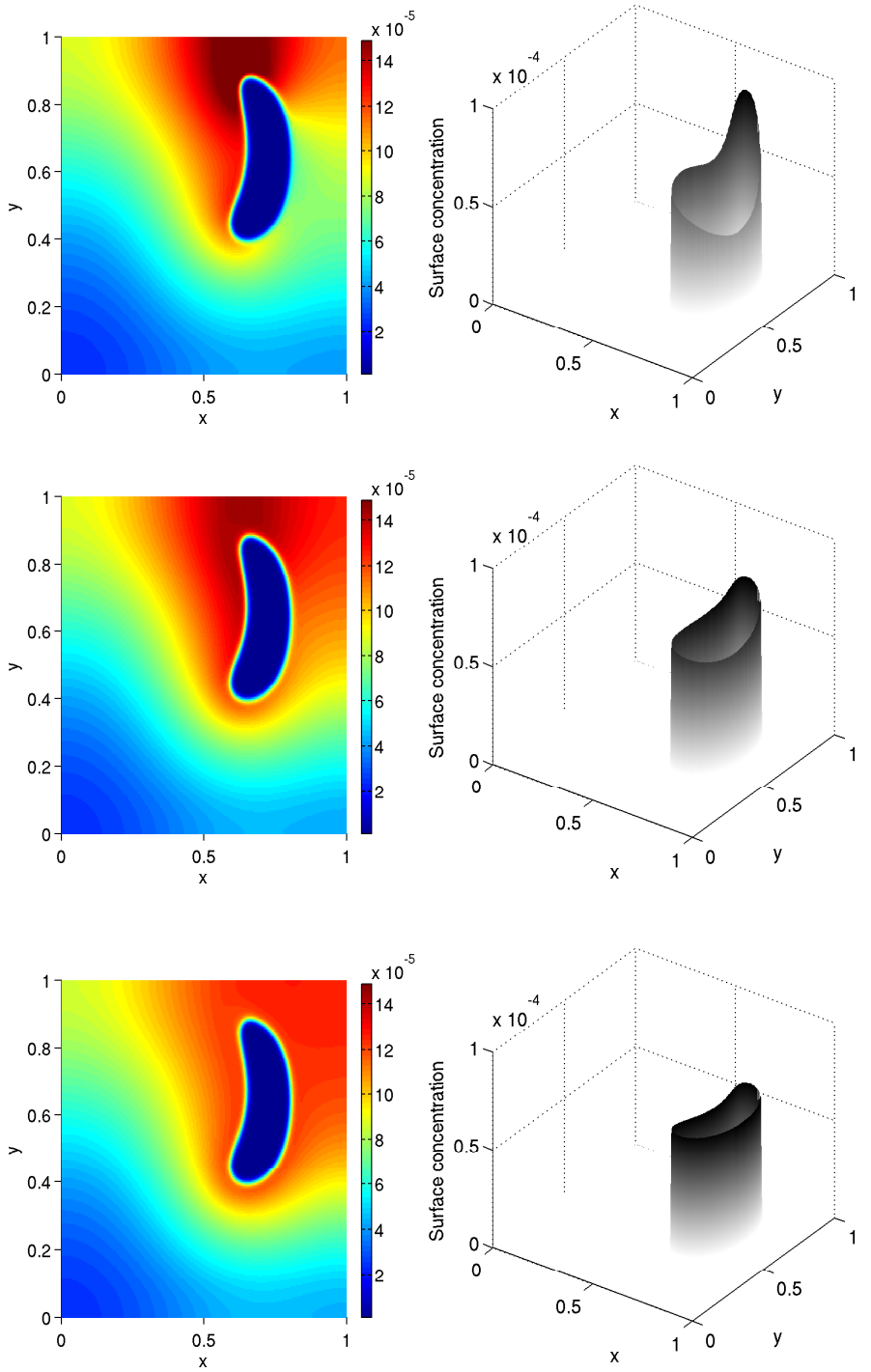

(a) Bulk concentration (b) Surface concentration

Fig. 5.12: Bulk concentration and interface concentration at $t = 0.5$ for the vortex test case with non-uniform initial bulk concentration and bulk/interface coupling. From top to bottom, $D = 0.1$, $D = 1.0$ and $D = 10$.

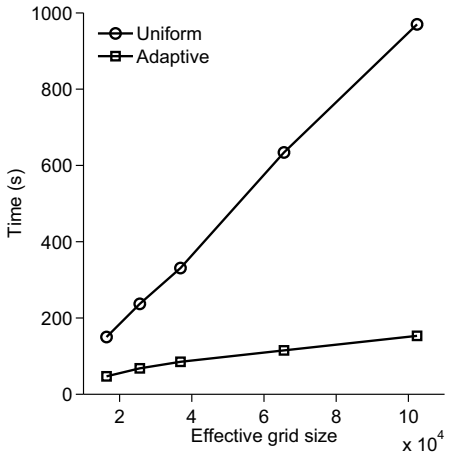

Fig. 5.13: Run-time of the vortex simulation versus grid size for both uniform and adaptive grids.

uniform simulations, which is a demonstration of the efficiency of block-structured, adaptive grids for these types of simulations.

5.7. Bulk-surface coupling in a 3D deformation field Finally, a three-dimensional test problem is considered. The flow field is the one proposed by [50], which combines a deformation in the x-y plane with one in the x-z plane. The velocity components are

$$u = 2\cos\left(\frac{\pi t}{3}\right)\sin^2(\pi x)\sin(2\pi y)\sin(2\pi z), \tag{5.25}$$

$$v = -\cos\left(\frac{\pi t}{3}\right)\sin(2\pi x)\sin^2(\pi y)\sin(2\pi z), \tag{5.26}$$

$$w = -\cos\left(\frac{\pi t}{3}\right)\sin(2\pi x)\sin(2\pi y)\sin^2(\pi z), \tag{5.27}$$

and a sphere of radius 0.15 is placed at (0.35,0.35,0.35) in a unit cube computational domain. The initial surface concentration is $f_0 = 10^{-4}$ and the initial bulk concentration is given by the non-uniform profile $F_0 = 10^{-4}y$. Additionally, the bulk and interface is coupled, with adsorption coefficient $r_a = 100$ and desorption coefficient $r_d = 200$. The bulk and surface diffusion coefficients are matched with $D_F = D_f = 1$. A grid with spacing $h = 1/32$ at the root level and three levels of refinement is used ($h_{\min} = 1/256$), along with the interface thickness $\epsilon = 0.004$.

Figure 5.14(a) shows the evolution of the sphere. The morphology agrees well with figure 29 from [18], where the same problem was solved with the level set method, only without any surface quantities. As the interface stretches, the surface concentration becomes lower. The concentration is higher at the front of the deforming sphere, because of adsorption from the bulk. The bulk concentration increases in the y-direction, and the front of the sphere moves through this part, thereby increasing the local concentration on the front. This can be seen from the slice of the bulk concentration, figure 5.14(b), at time 1.0, where the concentration is lower near the

region that the interface has moved through. The middle of the stretched sphere has a much lower concentration, due to the fact that it has experienced a large deformation and is in a region of low bulk concentration.

Figure 5.15 shows a sequence of the block-structured grids used in the simulation. The boxes denote grid level boundaries, so that inside each box the resolution is doubled. This demonstrates that the adaptive grid algorithm also works well for three-dimensional problems.

6. Conclusion A diffuse-interface method for solving problems involving transport, diffusion, and adsorption/desorption of a material quantity on a deformable interface was presented. The method was shown to perform well on a wide range of test cases. The efficiency of the numerical implementation, using adaptive grids and a multigrid method, was also demonstrated.

The asymptotic analysis suggests, and numerical evidence confirms, that the convergence to the sharp interface system is first order in the interface thickness parameter ϵ. It may be possible to gain second order accuracy in ϵ by explicitly removing the corresponding term in the asymptotic expansion as can be done in the context of solidification to enable simulations with arbitrary kinetic coefficients [43, 44]. This should be explored.

A natural extension of the method is to couple it to an external flow solver. The ability of the diffuse-interface method to handle complex fluids and interfacial dynamics makes this a very attractive combination. We are currently developing such an algorithm to simulate the dynamics of interfacial flows with soluble surfactants. Another interesting extension is to couple the method with models of cellular mechanics to simulate cell-polarization and motility.

Finally, this work used a phase-field function to represent the interface. Alternatively, a level-set function could be used instead. Accurate representations of delta functions and Heaviside functions in the level-set context can be found in for example [80, 83, 68].

Acknowledgment. The authors thank Steven Wise and Fang Jin for assistance with the numerical code and visualization, and the reviewers, whose comments have improved the paper. KET is funded by the project "Electrocoalescence – Criteria for an efficient process in real crude oil systems"; coordinated by SINTEF Energy Research. The project is supported by The Research Council of Norway, under the contract no: 169466/S30, and by the following industrial partners: Aibel AS, Aker Solutions AS, BP Exploration Operating Company Ltd, Saudi Aramco, Shell Technology Norway AS, StatoilHydro ASA and Petrobras. KET also acknowledges support from the Research Council of Norway through grant IS-BILAT 192532 and from the Fulbright Foundation. FW, JL and XL acknowledge support from the National Science Foundation Division of Mathematical Sciences (DMS) and from the National Institutes of Health through grant P50GM76516 for a Centre of Excellence in Systems Biology at the University of California, Irvine. AV acknowledges support from the German Science Foundation through grants Vo899/6-1 and SFB 609.

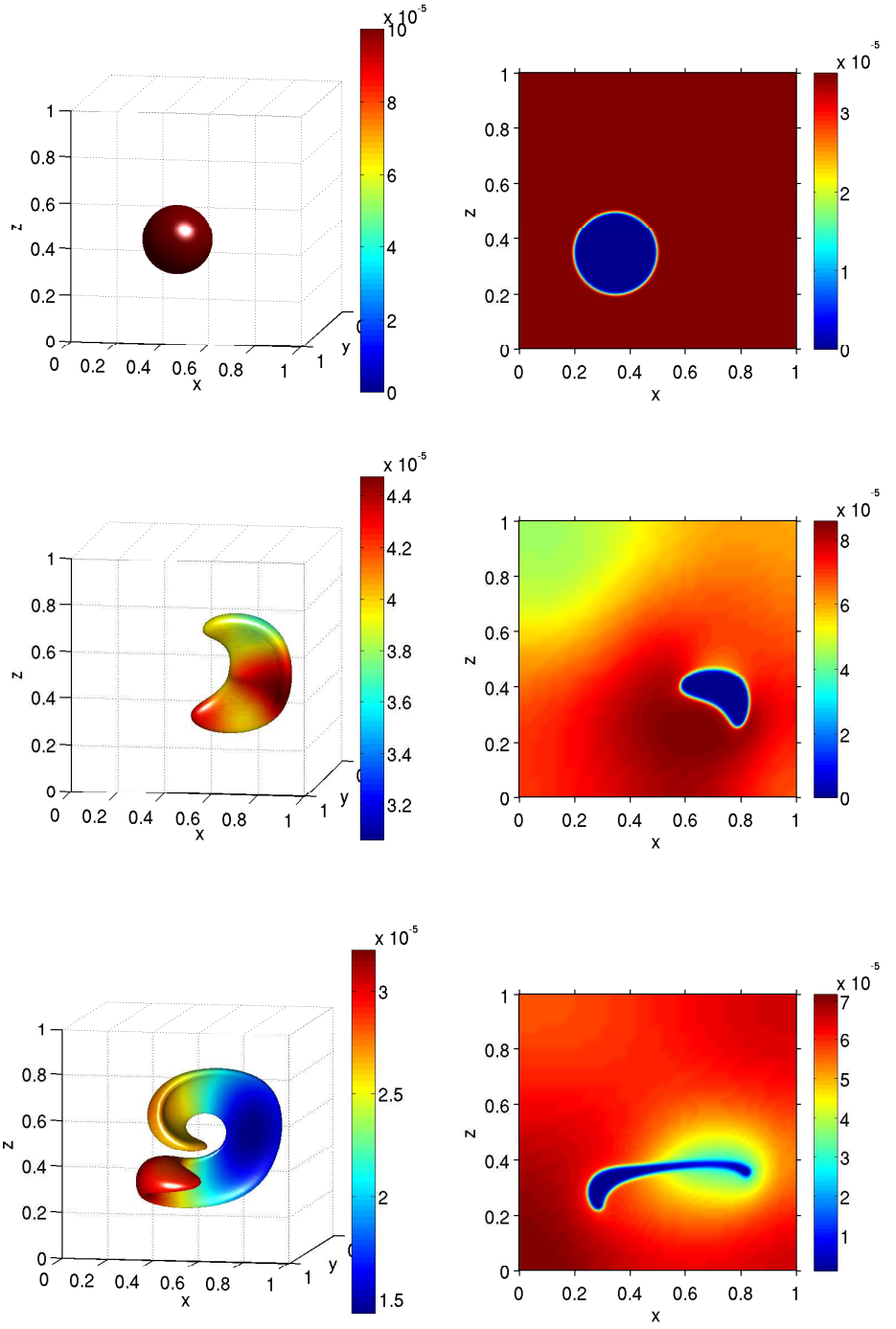

(a) Surface concentration (b) Slice of bulk concentration

Fig. 5.14: Sphere in 3D deformation field. The left column shows the interface and the surface concentration at times 0, 0.5 and 1.0. The right column shows slices of the bulk concentration at the same times and y-positions 0.35, 0.5 and 0.6, respectively.

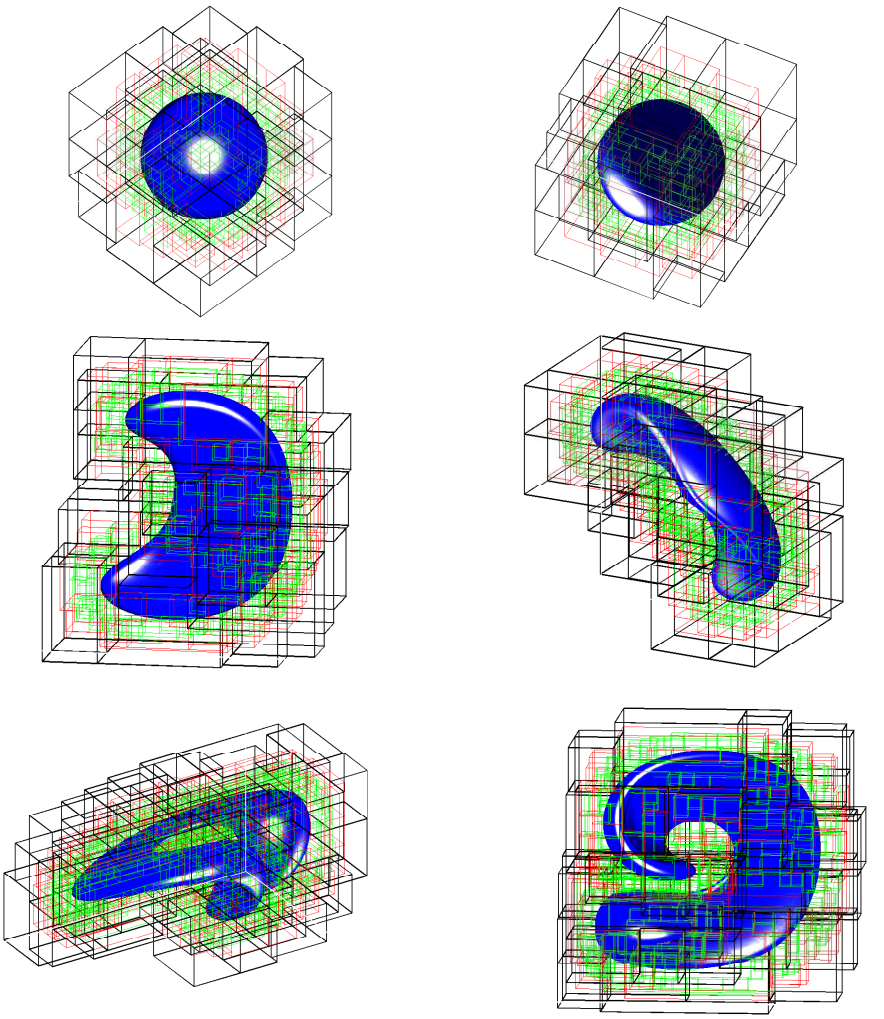

Fig. 5.15: Sphere in 3D deformation field. Illustration of the adaptive grids at times (from top to bottom) 0, 0.5 and 1.0. Two different angles are shown for each time step. Inside the black boxes, the grid spacing is $h = 1/64$, inside the red boxes $h = 1/128$ and inside the green boxes $h = h_{\min} = 1/256$.

REFERENCES

[1] D. Adalsteinsson and J. A. Sethian, *The fast construction of extension velocities in level set methods*, J. Comput. Phys., 148, 2–22, 1999.

[2] J.-M. Allain and M. B. Amar, *Biphasic vesicle: instability induced by adsorption of proteins*, Physica A, 337, 531–545, 2008.

[3] D. M. Anderson, G. B. McFadden, and A. A. Wheeler, *Diffuse-interface methods in fluid mechanics*, Ann. Rev. Fluid Mech., 30, 139–165, 1998.

[4] J. Barrett, J. Blowey, and H. Garcke, *Finite element approximation of the Cahn-Hilliard equation with degenerate mobility*, SIAM J. Numer. Anal., 37, 286–318, 1999.

[5] M. Bertalmio, L. Cheng, S. Osher, and G. Sapiro, *Variational problems and partial differential*

equations on implicit surfaces, J. Comput. Phys., 174, 759–780, 2001.
[6] J. Blowey and C. Elliott, *The Cahn-Hilliard gradient theory for phase separation with non-smooth free energy part 1: mathematical analysis*, Eur. J. Appl. Math., 2, 233–280, 1991.
[7] J. Blowey and C. Elliott, *The Cahn-Hilliard gradient theory for phase separation with non-smooth free energy part 2: Numerical analysis*, Eur. J. Appl. Math., 3, 147–179, 1992.
[8] A. Bueno-Orovio and V. Perez-Garcia, *Spectral methods for partial differential equations on irregular domains: the spectral smoothed boundary method*, SIAM J. Sci. Comput., 28, 886–900, 2006.
[9] A. Bueno-Orovio and V. Perez-Garcia, *Spectral smoothed boundary methods: the role of external boundary conditions*, Numer. Meth. Partial Diff. Eqns., 22, 435–448, 2006.
[10] G. Caginalp and P. Fife, *Dynamics of layered interfaces arising from phase boundaries*, SIAM J. Appl. Math., 48, 506–518, 1988.
[11] P. Cermelli, E. Fried, and M. Gurtin, *Transport relations for surface integrals arising in the formulation of balance laws for evolving fluid interfaces*, J. Fluid Mech., 544, 339–351, 2005.
[12] C. Duarte, I. Babuska, and J. Oden, *Generalized finite element methods for three-dimensional structural mechanics problems*, Comp. Struct., 77, 215–232, 2000.
[13] G. Dziuk and C. Elliott, *Eulerian finite element method for parabolic PDEs on complex surfaces*, Int. Free Bound., 10, 119–138, 2008.
[14] G. Dziuk and C. Elliott, *An Eulerian approach to transport and diffusion on evolving implicit surfaces*, Comput. Visualization Sci., in press, 2009.
[15] C. Eilks and C. Elliott, *Numerical simulation of dealloying by surface dissolution by the evolving surface finite element method*, J. Comput. Phys., 227, 9727–9741, 2008.
[16] C. Elliott and B. Stinner, *Analysis of a diffuse interface approach to an advection diffusion equation on a moving surface*, Math. Mod. Meth. Appl. Sci., in press, 2009.
[17] C. Elliott, B. Stinner, V. Styles, and R. Welford, *Numerical computation of advection and diffusion on evolving diffuse interfaces*, preprint, 2009.
[18] D. Enright, R. Fedkiw, J. Ferziger, and I. Mitchell, *A hybrid particle level set method for improved interface capturing*, J. Comput. Phys., 183, 83–116, 2002.
[19] J. Erlebacher, M. Aziz, A. Karma, N. Dimitrov, and K. Sieradzki, *Evolution of nanoporosity in dealloying*, Nature, 410, 450–453, 2001.
[20] R. Fedkiw, T. Aslam, B. Merriman, and S. Osher, *A non-oscillatory Eulerian approach to interfaces in multimaterial flows (the ghost fluid method)*, J. Comput. Phys, 152, 457–492, 1999.
[21] F. Fenton, E. Cherry, A. Karma, and W.-J. Rappel, *Modeling wave propagation in realistic heart geometries using the phase-field method*, Chaos, 15, 103502, 2005.
[22] P. Fife and O. Penrose, *Interfacial dynamics for thermodynamically consistent phase-field models with nonconserved order parameter*, Elect. J. Diff. Eqs., 16, 1–49, 1995.
[23] E. Fried and M. Gurtin, *A unified treatment of evolving interfaces accounting for small deformations and atomic transport with emphasis on grain-boundaries and epitaxy*, Adv. Appl. Mech., 40, 1–177, 2004.
[24] F. Gibou and R. Fedkiw, *A fourth order accurate discretization for the Laplace and heat equations on arbitrary domains with applications to the Stefan problem*, J. Comput. Phys, 202, 577–601, 2005.
[25] F. Gibou, R. Fedkiw, L. Cheng, and M. Kang, *A second order accurate symetric discretization of the Poisson equation on irregular domains*, J. Comput. Phys, 176, 205–227, 2002.
[26] J. Glimm, D. Marchesin, and O. McBryan, *A numerical method for 2 phase flow with an unstable interface*, J. Comput. Phys, 39, 179–200, 1981.
[27] R. Glowinski, T. Pan, and J. Periaux, *A fictitious domain method for external incompressible viscous-flow modeled by Navier-Stokes equations*, Comput. Meth. Appl. Mech. Engin., 112, 133–148, 1994.
[28] R. Glowinski, T. Pan, R. Wells, and X. Zhou, *Wavelet and finite element solutions for the Neumann problem using fictitious domains*, J. Comput. Phys., 126, 40–51, 1996.
[29] A. Gomez-Marin, J. Garcia-Ojalvo, and J. Sancho, *Self-sustained spatiotemporal oscillations induced by membrane-bulk coupling*, Phys. Rev. Lett., 98, 168303, 2007.
[30] J. Greer, A. Bertozzi, and G. Sapiro, *Fourth order partial differential equations on general geometries*, J. Comput. Phys., 216, 216–246, 2006.
[31] W. Hackbusch and S. Sauter, *Composite finite elements for the approximation of PDEs on domains with complicated micro-structures*, Num. Math., 75, 447–472, 1997.
[32] M. Hameed, M. Siegel, Y.-N. Young, J. Li, M. R. Booty, and D. T. Papageorgiou, *Influence of insoluble surfactant on the deformation and breakup of a bubble or thread in a viscous fluid*, J. of Fluid Mech., 594, 307–340, 2008.
[33] J. Hao, T. Pan, R. Glowinski, and D. Joseph, *A fictitious domain/distributed lagrange multiplier*

method for the particulate flow of Oldroyd-B fluids: a positive definiteness preserving approach, J. Non-Newtonian Fluid Mech., 156, 95–111, 2009.

[34] A. Hirsa and W. W. Willmarth, *Measurements of vortex pair interaction with a clean or contaminated free surface*, J. Fluid Mech., 259, 25–45, 1994.

[35] Y. T. Hu, D. J. Pine, and L. G. Leal, *Drop deformation, breakup, and coalescence with compatibilizer*, Phys. Fluids, 12, 484–489, 2000.

[36] S. D. Hudson, A. M. Jamieson, and B. E. Burkhart, *The effect of surfactant on the efficiency of shear-induced drop coalescence*, J. Colloid and Interface Science, 265, 409–421, 2003.

[37] K. Ito, M.-C. Lai, and Z. Li, *A well-conditioned augmented system for solving Navier-Stokes in irregular domains*, J. Comput. Phys., 228, 2616–2628, 2009.

[38] A. J. James and J. Lowengrub, *A surfactant-conserving volume-of-fluid method for interfacial flows with insoluble surfactant*, J. Comput. Phys., 201, 685–722, 2004.

[39] Y. J. Jan, *Computational Studies of Bubble Dynamics*, PhD thesis, University of Michigan, 1994.

[40] H. Ji, F.-S. Lien, and E. Yee, *An efficient second-order accurate cut-cell method for solving the variable coefficient Poisson equation with jump conditions on irregular domains*, Int. J. Num. Meth. Fluids, 52, 723–748, 2006.

[41] H. Johansen and P. Colella, *A Cartesian grid embedded boundary method for Poisson's equation on irregular domains*, J. Comput. Phys, 147, 60–85, 1998.

[42] H. Johansen and P. Colella, *Embedded boundary algorithms and software for partial differential equations*, J. Phys., 125, 012084, 2008.

[43] A. Karma and W.-J. Rappel, *Phase-field method for computationally efficient modeling of solidification with arbitrary interface kinetics*, Phys. Rev. E, 53, R3017–R3020, 1996.

[44] A. Karma and W.-J. Rappel, *Quantitative phase-field modeling of dendritic growth in two and three dimensions*, Phys. Rev. E, 57, 4323–4349, 1998.

[45] J.-S. Kim, K. Kang, and J. Lowengrub, *Conservative multigrid methods for Cahn-Hilliard fluids*, J. Comput. Phys., 193, 511–543, 2004.

[46] J. Kockelkoren, H. Levine, and W.-J. Rappel, *Computational approach for modeling intra- and extracellular dynamics*, Phys. Rev. E, 68, 037702, 2003.

[47] M.-C. Lai, Y.-H. Tseng, and H. Huang, *An immersed boundary method for interfacial flows with insoluble surfactant*, J. Comput. Phys., 227, 7270–7293, 2008.

[48] L. G. Leal, *Flow induced coalescence of drops in a viscous fluid*, Phys. of Fluids, 16, 1833–1851, 2004.

[49] R. LeVeque and Z. Li, *The immersed interface method for elliptic equations with discontinuous coefficients and singular sources*, SIAM J. Num. Anal., 31, 1019–1044, 1997.

[50] R. J. Leveque, *High-resolution conservative algorithms for advection in incompressible flow*, SIAM J Numer. Anal., 33, 627–665, 1996.

[51] H. Levine and W.-J. Rappel, *Membrane-bound Turing patterns*, Phys. Rev. E, 72, 061912, 2005.

[52] B. Li, J. Lowengrub, A. Ratz, and A. Voigt, *Geometric evolution laws for thin crystalline films: modeling and numerics*, Commun. Comput. Phys., 6, 433–482, 2009.

[53] X. Li, J. Lowengrub, A. Ratz, and A. Voigt, *Solving PDEs in complex geometries: a diffuse domain approach*, Comm. Math. Sci., 7, 81–107, 2009.

[54] Z. Li and K. Ito, *The immersed interface method: Numerical solutions of PDEs involving interfaces and irregular domains*, SIAM Front. Appl. Math., 33, 2006.

[55] S. Liu and T. Chan, *Weighted essentially non-oscillatory schemes*, J. Comput. Phys., 115, 200–212, 1994.

[56] R. Lohner, J. Cebral, F. Camelli, J. Baum, E. Mestreau, and O. Soto, *Adaptive embedded/immersed unstructured grid techniques*, Arch. Comput. Meth. Eng., 14, 279–301, 2007.

[57] W. E. Lorensen and H. E. Cline, *Marching cubes: a high resolution 3d surface construction algorithm*, Computer Graphics, 21, 163–169, 1987.

[58] J. Lowengrub and L. Truskinovsky, *Quasi-incompressible Cahn-Hilliard fluids and topological transitions*, R. Soc. Lond. Proc. Ser. A Math. Phys. Eng. Sci., 454, 2617–2654, 1998.

[59] S. Lui, *Spectral domain embedding for elliptic PDEs in complex domains*, J. Comput. Appl. Math., 225, 541–557, 2009.

[60] P. Macklin and J. Lowengrub, *Evolving interfaces via gradients of geometry-dependent interior poisson problems: application to tumor growth*, J. Comput. Phys, 203, 191–220, 2005.

[61] P. Macklin and J. Lowengrub, *A new ghost cell/level set method for moving boundary problems: Application to tumor growth*, J. Sci. Comput., 35, 266–299, 2008.

[62] S. Marella, S. Krishnan, and H. Udaykumar, *Sharp interface Cartesian grid method I: an easily implemented technique for 3D moving boundary computations*, J. Comput. Phys, 210, 1–31, 2005.

[63] O. K. Matar and S. M. Troian, *The development of transient fingering patterns during the*

spreading of surfactant coated films, Phys. Fluids, 11, 3232–3246, 1999.
[64] P. McCorquodale, P. Colella, and H. Johansen, *A Cartesian grid embedded boundary method for the heat equation on irregular domains*, J. Comput. Phys, 173, 620–635, 2001.
[65] J. Melenk and I. Babuska, *The partition of unity finite element method: basic theory and applications*, Comp. Meth. Appl. Mech. Eng., 139, 289–314, 1996.
[66] W. J. Milliken and L. G. Leal, *The influence of surfactant on the deformation and breakup of a viscous drop - the effect of surfactant solubility*, J. Colloid and Interface Sci., 166, 275–285, 1994.
[67] W. J. Milliken, H. A. Stone, and L. G. Leal, *The effect of surfactant on transient motion of Newtonian drops*, Phys. Fluids A, 5, 69–79, 1993.
[68] C. Min and F. Gibou, *Robust second-order accurate discretizations of the multi-dimensional Heaviside and Dirac delta functions*, J. Comput. Phys., 227, 9686–9695, 2008.
[69] M. Muradoglu and G. Tryggvason, *A front-tracking method for computation of interfacial flows with soluble surfactants*, J. Comput. Phys., 227, 2238–2262, 2008.
[70] J. Oden, C. Duarte, and O. Zienkiewicz, *A new cloud-based hp finite element method*, Comp. Meth. Appl. Mech. Eng., 153, 117–126, 1998.
[71] R. Pego, *Front migration in the nonlinear Cahn-Hilliard equation*, Proc. Roy. Soc. London A, 422, 261–278, 1989.
[72] I. Ramiere, P. Angot, and M. Belliard, *A general fictitious domain method with immersed jumps and multilevel nested structured meshes*, J. Comput. Phys., 225, 1347–1387, 2007.
[73] A. Ratz and A. Voigt, *PDEs on surfaces—a diffuse interface approach*, Commun. Math. Sci., 4, 575–590, 2006.
[74] M. Rech, S. Sauter, and A. Smolianski, *Two-scale composite finite element method for Dirichlet problems on complicated domains*, Num. Math., 102, 681–708, 2006.
[75] Y. Y. Renardy, M. Renardy, and V. Cristini, *A new volume-of-fluid formulation for surfactants and simulations of drop deformation under shear at a low viscosity ratio*, European Journal of Mechanics - B/Fluids, 21, 49–59, 2002.
[76] P. Schwartz, M. Barad, P. Colella, and T. Ligocki, *A Cartesian grid embedded boundary method for the heat equation and Poisson's equation in three dimensions*, J. Comput. Phys, 211, 531–550, 2006.
[77] J. Sethian and Y. Shan, *Solving partial differential equations on irregular domains with moving interfaces, with applications to superconformal electrodeposition in semiconductor manufacturing*, J. Comput. Phys, 227, 6411–6447, 2008.
[78] C. W. Shu and S. Osher, *Efficient implementation of essentially non-oscillatory shock-capturing schemes*, J. Comput. Phys., 77, 439–471, 1988.
[79] I. Singer-Loginova and H. Singer, *The phase field technique for modeling multiphase materials*, Rep. Prog. Phys., 71, 106501, 2008.
[80] P. Smereka, *The numerical approximation of a delta function with application to level set methods*, J. Comput. Phys., 211, 77–90, 2006.
[81] C. Stocker and A. Voigt, *A level set approach to anisotropic surface evolution with free adatoms*, SIAM J. Appl. Math, 69, 64–80, 2008.
[82] H. A. Stone and L. G. Leal, *The effect of surfactants on drop deformation and breakup*, J. Fluid. Mech., 220, 161–186, 1990.
[83] J. D. Towers, *Two methods for discretizing a delta function supported on a level set*, J. Comput. Phys, 220, 915–931, 2007.
[84] S. M. Troian, E. Herbolzheimer, and S. A. Safran, *Model for the fingering instability of spreading surfactant drops*, Phys. Rev. Lett., 65, 333–336, 1990.
[85] U. Trottenberg, C. Oosterlee, and A. Schller, *Multigrid*, London, UK: Academic Press, 2000.
[86] G. Tryggvason, J. Abdollahi-Alibeik, W. W. Willmarth, and A. Hirsa, *Collision of a vortex pair with a contaminated free surface*, Phys. Fluids A, 4, 1215–1229, 1992.
[87] S. Wise, J.-S. Kim, and J. Lowengrub, *Solving the regularized, strongly anisotropic Cahn-Hilliard equation by an adaptive nonlinear multigrid method*, J. Comput. Phys., 226, 414–446, 2007.
[88] J. J. Xu, Z. Li, J. Lowengrub, and H. Zhao, *A level set method for interfacial flows with surfactant*, J. Comput. Phys, 212, 590–616, 2006.
[89] J. J. Xu and H. Zhao, *An Eulerian formulation for solving partial differential equations along a moving interface*, J. Sci. Comp., 19, 573–594, 2003.
[90] X. Yang and A. J. James, *An arbitrary Lagrangian-Eulerian (ALE) method for interfacial flows with insoluble surfactants*, FDMP, 3, 65–96, 2007.
[91] J. Zhang, D. Eckmann, and P. Ayyaswamy, *A front tracking method for a deformable intravascular bubble in a tube with soluble surfactant transport*, J. Comput. Phys., 214, 366–396, 2006.

F A diffuse-interface method for two-phase flows with soluble surfactants

Teigen, K.E., Song, P., Lowengrub, J., Voigt, A.,
Submitted to Journal of Computational Physics, 2010

A diffuse-interface method for two-phase flows with soluble surfactants

Knut Erik Teigen[a], Peng Song[c], John Lowengrub[*,b], Axel Voigt[d]

[a]*Department of Energy and Process Engineering, Norwegian University of Science and Technology, NO-7491 Trondheim, Norway*

[b]*Department of Mathematics, University of California, Irvine, Irvine CA-92697, USA*

[c]*Department of Mathematics, University of California, Irvine, Irvine CA-92697, USA*

[d]*Department of Mathematics, Technische Universität Dresden, 01062 Dresden, Germany*

Abstract

A method is presented to solve two-phase problems involving soluble surfactants. The incompressible Navier–Stokes equations are solved along with equations for the bulk and interfacial surfactant concentrations. A non-linear equation of state is used to relate the surface tension to the interfacial surfactant concentration. The method is based on the use of a diffuse interface, which allows a simple implementation using standard finite difference or finite element techniques. Here, finite difference methods on a block-structured adaptive grid are used, and the resulting equations are solved using a non-linear multigrid method. Results are presented for a drop in shear flow in both 2D and 3D, and the effect of solubility is discussed.

Key words: Multiphase flows, interfacial dynamics, surfactant, soluble surfactant, surface phase, bulk phase, adsorption, desorption, complex geometry, diffuse interface, phase field, multigrid, adaptive grid, finite difference
2000 MSC: 35Q30, 35K57, 65Z05, 65M06, 65M50, 65M55, 76Txx, 82C24

1. Introduction

The presence of surface active agents (surfactants) at fluid interfaces can have a considerable effect on flow dynamics. Surfactants are amphiphilic organic compounds, which can be adsorbed at liquid/gas or liquid/liquid interfaces. The presence of surfactant typically alters the interface dynamics by a reduction in the surface tension of the

[*]Corresponding author.
Email addresses: knut.erik.teigen@ntnu.no, knutert@gmail.com (Knut Erik Teigen), kevinsongpeng@yahoo.com.cn (Peng Song), lowengrb@math.uci.edu (John Lowengrub), axel.voigt@tu-dresden.de (Axel Voigt)

interface. An inhomogeneous distribution of surfactants produces gradients in surface tension, which again gives rise to tangential forces along the interface. Through this so-called Marangoni effect, surfactants can play an important role in several physical phenomena such as vortex pair interaction (e.g., [1]), fingering (e.g., [2]), drop break-up and coalescence (e.g., [3, 4, 5]) and tip-streaming (e.g., [6, 4]).

From a numerical point of view, solving the problem of soluble surfactants is highly challenging. A coupled bulk/surface system of equations must be solved on a moving, complex domain, where the domain boundary may stretch, break-up or coalesce with other interfaces. Adsorption of mass to, and desorption of mass from, the interfaces poses another challenge. Further, the surface concentration may only be soluble in either the exterior or interior of the domain (e.g., amphiphilic nature of surfactants). The available numerical methods for solving these problems can roughly be divided into two categories: interface tracking and interface capturing methods. Interface tracking methods use either a separate grid for the interface, or a set of interconnected points to mark the interface. For example, boundary integral methods use a surface mesh to track the interface. In the context of surfactants, a boundary integral method for studying the effect of insoluble surfactants on drop deformation was developed in [7]. This method was extended to arbitrary viscosity ratios in [8], to 3D in [9, 4] and to soluble surfactants in [10]. See the review [11]. Another tracking method is the front-tracking method (see the review [12]), where a fixed grid is used to compute the flow, while a set of connected marker particles is used to track the interface and any interfacial quantities. A front-tracking method for insoluble surfactants was developed in [13], and this method was extended to handle soluble surfactants in [14] and [15]. A related front tracking method is the immersed boundary method (see the review [16]), which was recently used to simulate interfacial flows with insoluble surfactants using a surfactant-conserving algorithm [17]. A ghost-cell immersed boundary method was introduced in [18], and was used to study the effects of a diffusion controlled surfactant on a viscous drop injected into a viscous medium [19]. A hybrid level-set/front-tracking approach was used to study the dynamics of capillary waves with insoluble surfactant [20]. Another front-tracking method which combines a finite element methodology with adaptive body-fitted meshes was used to simulate the deformation and break-up of axisymmetric liquid bridges [21] and thin filaments [22] with insoluble surfactants. Very recently, Booty & Siegel [80] developed a hybrid numerical method to simulate bubbles in Stokes flow by combining a boundary integral method with a fixed grid solution of the bulk surfactant equation (using a mapped domain) that incorporates a singular perturbation analysis to account for the rapid variation of the bulk surfactant concentration near the interface when the bulk Peclet number is large. In general, interface tracking methods can be made very accurate but can be relatively complicated to implement, especially in three dimensions and for problems involving topological changes.

In interface capturing methods, the interface is not tracked explicitly, but instead is implicitly defined through an auxilliary function (e.g. level-set, color or phase-field function). This means that the solution of the problem can be done independently of the underlying grid, which greatly simplifies gridding, discretization and handling of topological changes. For example, a volume-of-fluid (VOF) method (see the review [23]) for insoluble surfactants was developed in [24]. A more general method which

allows non-linear equations of state for surface tension was later developed in [25]. Very recently, a VOF method was developed for soluble surfactants in the limit of large sorption rates where there is an analytic relationship between the surface and bulk concentrations at the interface [26]. A level-set method [27] for solving the surfactant equation was presented in [28], and later coupled to an immersed-interface external flow solver in [29]. See the review [30] for fluid dynamics applications. An alternative approach for simulating fluid interfaces with insoluble or soluble surfactant was developed in [31, 5, 32], using the so-called Arbitrary Lagrangian-Eulerian (ALE) method (see the review [33]) together with a coupled level-set and volume of fluid method. Very recently, surfactant dynamics was simulated using a conservative smoothed particle hydrodynamics algorithm [34].

The diffuse-interface, or phase-field, method represents yet another approach for simulating solutions of equations in complex, evolving domains (see the reviews [35, 36]). In this method, which we follow here, the complex domain is represented implicitly by a phase-field function, which is an approximation of the characteristic function of the drop or matrix fluid domain. The domain boundary is replaced by a narrow diffuse interface layer such that the phase-field function rapidly transits from one inside the domain to zero in the exterior of the domain. The boundary of the domain can thus be represented as an isosurface of the phase-field function. The bulk and surface PDEs are then extended on a larger, regular domain with additional terms that approximate the adsorption-desorption flux boundary conditions and source terms for the bulk and surface equations respectively. Standard finite-difference or finite-element methods may be used. Here, we focus on a finite difference approach.

The diffuse interface method, which has a long history in the theory of phase transitions dating back to van der Waals (e.g., [37, 35, 36]), has been used to simulate multiphase flows in simple geometries including drop coalescence and break-up, electrowetting, and viscoelasticity (e.g., [38, 39, 40, 41, 42, 43, 44, 45]). In [46], a diffuse interface model is implemented using a lattice Boltzmann scheme to simulate the effect of surfactant adsorption on droplet dynamics; preliminary simulations were performed. The interaction of multiphase flows with complex boundaries has also been investigated using the diffuse interface method including contact line dynamics and the effect of wetting (e.g., [47, 48, 49]). More generally, diffuse interface methods have been developed for solving PDEs on stationary surfaces [50], evolving surfaces [51, 52, 53, 54] and for solving PDEs in complex stationary [55, 56, 57] and evolving domains with Dirichlet, Neumann and Robin boundary conditions [58]. Extending previous work [56], in [59] it was shown how to solve the coupled bulk/surface problem on general, evolving domains with the diffuse interface method.

Here, we couple the diffuse interface approach from [59] with the solution of the Navier–Stokes equations, and use the method to simulate a drop in shear flow in the presence of a soluble surfactant. The method is very simple compared to previous methods, and can handle advection, diffusion and adsorption/desorption in a straightforward manner. The use of a non-linear multigrid method and block-structured, adaptive grids also make the method computationally efficient. Results are presented for a drop in shear flow in both 2D and 3D, and the effect of surfactant solubility is discussed. As observed

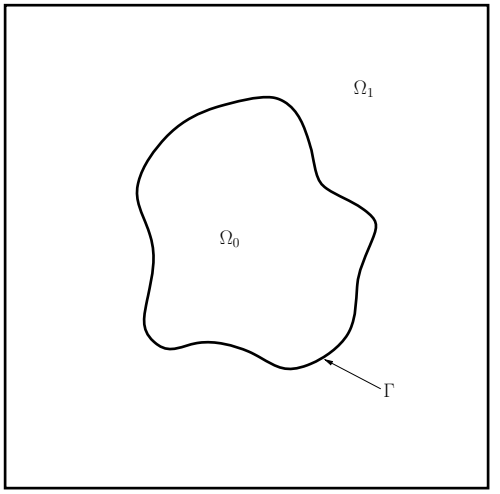

Figure 1: Illustration of the mathematical domain.

by Milliken and Leal [10] in the context of drop deformation in extensional flows, solubility mitigates many of the surfactant effects by making the surface concentration more uniform. In particular, while an insoluble surfactant can immobilize a surface, solubility may remobilize the surface due to surfactant exchange with the bulk.

The paper is organized as follows. In Section 2, the mathematical formulaton of the problem is stated. The governing equations for the interfacial surfactant and the bulk surfactant are introduced, and the interface representation is presented. Section 3 then details the numerical implementation of the mathematical formulation and Section 4 presents some validation test cases of the method. In Section 5, a drop in shear flow is studied in detail and the effect of solubility discussed. Finally, Section 6 provides conclusions and discusses future work.

2. Mathematical formulation

2.1. Governing equations

Consider a domain $\Omega \subset \mathbb{R}^{2,3}$, which contains a closed interface, Γ. The interior of the interface is $\Omega_0 \subset \Omega$, and the exterior is $\Omega_1 \subset \Omega$. See Figure 1 for an illustration.

We assume that the flow inside the domain Ω is governed by the incompressible Navier–Stokes equations, which in dimensional form are

$$\begin{aligned} \rho^* \left(\frac{\partial \boldsymbol{u}^*}{\partial t} + (\boldsymbol{u}^* \cdot \boldsymbol{\nabla}) \boldsymbol{u}^* \right) &= -\boldsymbol{\nabla} p^* + \boldsymbol{\nabla} \cdot \left(\mu^* (\boldsymbol{\nabla} \boldsymbol{u}^* + \boldsymbol{\nabla} (\boldsymbol{u}^*)^T) \right) + \boldsymbol{F}^*, \\ \boldsymbol{\nabla} \cdot \boldsymbol{u}^* &= 0. \end{aligned} \tag{1}$$

where ρ is the density, $\boldsymbol{u}^*$ is the velocity, p^* is the pressure, μ is the dynamic viscosity, and $\boldsymbol{F}^*$ is the interfacial force, given below in Eq. (5). The density and viscosity can be

discontinuous across the interface. We will only consider cases where the densities and viscosities are equal in the two phases in this work, but the discontinuity can in general be handled by interpolating their values using an indicator or characteristic function χ that varies from 0 to 1 across the interface (characteristing function of Ω_1), such that

$$\mu^* = \mu_0(1-\chi) + \mu_1\chi \tag{2}$$
$$\rho^* = \rho_0(1-\chi) + \rho_1\chi. \tag{3}$$

In practice, χ may be smoothed so that the transition from 0 to 1 is steep but finite. An example of a smoothed characteristic function is given in Section 2.3.

We consider the deformation of an initially circular drop of radius a, placed in a shear flow of shear rate $\dot{\gamma}$. Choosing $\mathcal{L} = a$ as the length scale and $\mathcal{T} = \dot{\gamma}^{-1}$ as the time scale, and $\mathcal{U} = \dot{\gamma}a$ as the velocity scale, the nondimensional Navier–Stokes equations can be written as

$$\begin{aligned} \frac{\partial \boldsymbol{u}}{\partial t} + (\boldsymbol{u}\cdot\boldsymbol{\nabla})\boldsymbol{u} &= -\boldsymbol{\nabla}p + \frac{1}{\mathrm{Re}}\boldsymbol{\nabla}^2\boldsymbol{u} + \frac{1}{\mathrm{ReCa}}\boldsymbol{F}, \\ \boldsymbol{\nabla}\cdot\boldsymbol{u} &= 0, \end{aligned} \tag{4}$$

where $Re = \rho_1\dot{\gamma}a^2/\mu_1$ is the Reynolds number, which measures the relative strength of the inertial and viscous forces, and $Ca = \mu_1\dot{\gamma}/\sigma_0$ is the Capillary number which measures the relative strength of the viscous and surface tension forces, where σ_0 is the surface tension of a clean drop. The influence of these parameters on a clean interface has been extensively studied in the literature (e.g., [60, 61, 62, 63]). For example, as the capillary number is increased, the drop will become increasingly elongated. There exists a critical capillary number, above which the drop will no longer attain a steady shape, but continue to stretch until it breaks into smaller droplets. The value of the critical capillary number increases with increasing Reynolds numbers and viscosity ratios $\lambda = \mu_0/\mu_1$. Larger viscosity ratios serve to reduce the deformation, and for creeping flow there exists a limit where there is no critical capillary number. However, for flows with higher Reynolds numbers, break-up may still occur, due to inertial forces. In this work, we will only consider flows with moderate Reynolds numbers and viscosity ratios.

The interface force $\boldsymbol{F}^*$ is given by

$$\boldsymbol{F}^* = \boldsymbol{\nabla}\cdot\left((\mathbf{I} - \boldsymbol{n}\otimes\boldsymbol{n})\sigma^*\delta_\Gamma\right). \tag{5}$$

Here, σ^* is the interfacial tension, $\mathbf{I}$ is the identity tensor and $\boldsymbol{n}$ is the outward pointing unit normal vector. δ_Γ is a regularized delta function, to be defined in Section 2.3. Alternately, one may write

$$\boldsymbol{F}^* = -\sigma^*\kappa\delta_\Gamma\boldsymbol{n} + (\boldsymbol{\nabla}_s\sigma^*)\delta_\Gamma, \tag{6}$$

where κ is the total curvature and $\boldsymbol{\nabla}_s = (\mathbf{I} - \boldsymbol{n}\otimes\boldsymbol{n})\boldsymbol{\nabla}$ is the surface gradient operator. The first term on the right hand side is the normal surface tension force, while the second is the tangential (Marangoni) force, which appears due to non-uniform surface tension.

Next, we assume that the interface is covered by surfactants, and we let f^* denote the dimensional surfactant concentration defined on Γ. The presence of a surfactant will

decrease the surface tension of the interface. We assume that the dependence of the surface tension is governed by the Langmuir equation of state,

$$\sigma^*(f^*) = \sigma_0 \left[1 + \frac{\mathcal{R}T f_\infty}{\sigma_0} \ln\left(1 - \frac{f^*}{f_\infty}\right) \right], \tag{7}$$

where $\mathcal{R}$ is the ideal gas constant, T is the absolute temperature, σ_0 is the surface tension of a clean interface and f_∞ is the maximum interfacial surfactant concentration. Let f_e denote the average of f^* at time $t = 0$. We define $f = f^*/f_e$ to be the dimensionless surfactant concentration, which gives the dimensionless surface tension

$$\sigma(f) = 1 + \beta \ln(1 - xf), \tag{8}$$

where $\beta = \mathcal{R}T f_\infty/\sigma_0$ is the elasticity number and $x = f_e/f_\infty$ is the dimensionless surfactant coverage. The elasticity number is a measure of the sensitivity of the surface tension to the surfactant concentration, and thus a larger elasticity number increases the deformation. In this definition, β is independent of x, see [64].

For low surfactant concentrations, Eq. (8) can be simplified to

$$\sigma(f) = 1 - \beta x f, \tag{9}$$

which is known as the linear equation of state. These two expressions are compared in Figure 2. We see that the expressions are similar for low surfactant concentrations, but deviate significantly for higher concentrations. Also note that for large elasticity numbers and surfactant concentrations close to $1/x$, the non-linear equation of state may give unphysical (negative) values of surface tension. In [15], a minimum surface tension was introduced to alleviate this problem. However, in [65], it was argued that high elasticity numbers rarely occur in real systems. We use Eq. (8) directly for all the simulations in this work and do not encounter negative surface tension.

In [66], the sharp-interface representation of the surfactant mass balance equation is

$$\frac{df^*}{dt} - \boldsymbol{u}^* \cdot \boldsymbol{\nabla}_s f^* + f^*(\boldsymbol{u}^* \cdot \boldsymbol{n})(\boldsymbol{\nabla}_s \cdot \boldsymbol{n}) = -\boldsymbol{\nabla}_s \cdot (f^* \boldsymbol{u}_s^*) + D_f \boldsymbol{\nabla}_s^2 f^* \tag{10}$$

where $\frac{d}{dt}$ is the material derivative, $\boldsymbol{u}_s^* = (\mathbf{I} - \boldsymbol{n} \otimes \boldsymbol{n})\boldsymbol{u}^*$ is the tangential velocity, D_f is the diffusion coefficient, and j^* is the source term. Assuming that f^* may be extended off Γ, the time derivative term can be changed to

$$\frac{df^*}{dt} = \frac{\partial f^*}{\partial t} + \boldsymbol{u}^* \cdot \boldsymbol{\nabla} f^* \tag{11}$$

Since

$$\begin{aligned}
-\boldsymbol{u}^* \cdot \boldsymbol{\nabla}_s f^* &= -\boldsymbol{u}^* \cdot \boldsymbol{\nabla} f^* + (\boldsymbol{u}^* \cdot \boldsymbol{n}) \boldsymbol{n} \cdot \boldsymbol{\nabla} f^*, && (12)\\
f^*(\boldsymbol{u}^* \cdot \boldsymbol{n})(\boldsymbol{\nabla}_s \cdot \boldsymbol{n}) &= \kappa f^* \boldsymbol{u}^* \cdot \boldsymbol{n}, && (13)\\
\boldsymbol{\nabla}_s \cdot (f^* \boldsymbol{u}_s^*) &= \boldsymbol{u}^* \cdot \boldsymbol{\nabla} f^* - (\boldsymbol{u}^* \cdot \boldsymbol{n}) \boldsymbol{u}^* \cdot \boldsymbol{\nabla} f^* - \kappa f^* \boldsymbol{u}^* \cdot \boldsymbol{n} - f^* \boldsymbol{n} \cdot \boldsymbol{\nabla} \boldsymbol{u}^* \cdot \boldsymbol{n}, && (14)\\
\boldsymbol{\nabla}_s^2 f^* &= (\mathbf{I} - \boldsymbol{n} \otimes \boldsymbol{n}) \boldsymbol{\nabla} \cdot (\mathbf{I} - \boldsymbol{n} \otimes \boldsymbol{n}) \boldsymbol{\nabla} f^* \\
&= \boldsymbol{\nabla}^2 f^* - \boldsymbol{n} \cdot \boldsymbol{\nabla} \boldsymbol{\nabla} f^* \cdot \boldsymbol{n} - \kappa \boldsymbol{n} \cdot \boldsymbol{\nabla} f^*, && (15)
\end{aligned}$$

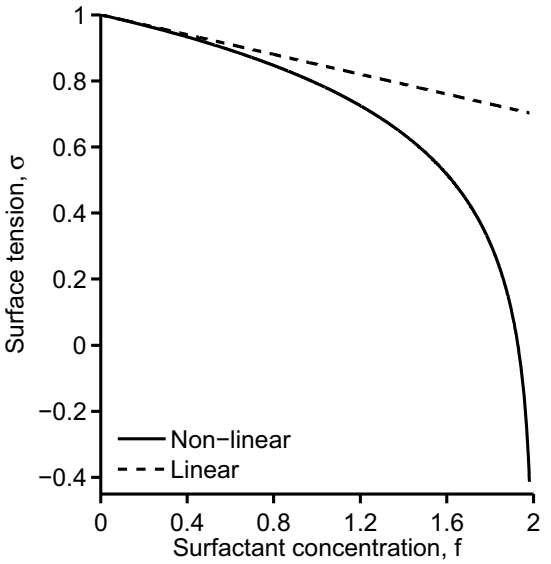

Figure 2: Dependence of surface tension on surfactant concentration. Comparison of a linear and non-linear equation of state. $\beta = 0.3$, $x = 0.5$.

Eq. (10) is equivalent to

$$\frac{\partial f^*}{\partial t} + \boldsymbol{u}^* \cdot \boldsymbol{\nabla} f^* - f^* \left(\boldsymbol{n} \cdot \boldsymbol{\nabla} \boldsymbol{u}^* \cdot \boldsymbol{n}\right) = D_f (\boldsymbol{\nabla}^2 f^* - \boldsymbol{n} \cdot \boldsymbol{\nabla}\boldsymbol{\nabla} f^* \cdot \boldsymbol{n} - \kappa \boldsymbol{n} \cdot \boldsymbol{\nabla} f^*) + j^*, \quad (16)$$

The source term, j^*, is given by

$$j^*(f^*, F^*) = r_a F_s^* \left(f_\infty - f^*\right) - r_d f^*, \quad (17)$$

where r_a and r_d are adsorption and desorption coefficients, respectively, and F_s^* is the bulk surfactant concentration immediately adjacent to the surface. For dilute concentrations, this can be simplified to

$$j^*(f^*, F^*) = r_a f_\infty F_s^* - r_d f^*. \quad (18)$$

In this work, we use the full nonlinear form in Eq. (17).

Now, assume that f^* is soluble in Ω_1, but not in Ω_0. The bulk concentration, F^*, in Ω_1, evolves according to

$$\frac{\partial F^*}{\partial t} + \boldsymbol{\nabla} \cdot (F^* \boldsymbol{u}^*) = D_F \boldsymbol{\nabla}^2 F^* \text{ in } \Omega_1, \quad (19)$$

with the boundary condition at Γ

$$D_F \boldsymbol{\nabla} F^* \cdot \boldsymbol{n} = -j^* \text{ on } \Gamma. \quad (20)$$

The equation for the surface surfactant concentration, Eq. (16), can be extended to the general domain Ω by introducing a surface delta function, δ_Γ, such that

$$\int_\Gamma f^* \, \mathrm{d}\Gamma = \int_\Omega f^* \delta_\Gamma \, \mathrm{d}\Omega. \quad (21)$$

Following [59], Eq. (16) can be rewritten in distribution form as

$$\frac{\partial}{\partial t}(f^*\,\delta_\Gamma) + \boldsymbol{\nabla}\cdot(f^*\,\delta_\Gamma\,\boldsymbol{u}^*) = D_f\boldsymbol{\nabla}\cdot(\delta_\Gamma\boldsymbol{\nabla}f^*) + \delta_\Gamma j^*, \tag{22}$$

The formulation given by Eq. (22) is considerably simpler than the sharp-interface formulation.

Similarly, the bulk concentration equation (19) can be extended to Ω by using the characteristic function χ

$$\chi = \begin{cases} 1 & \text{in} \quad \Omega_1, \\ 0 & \text{in} \quad \Omega_0. \end{cases} \tag{23}$$

In distribution form, Eq. (19) becomes

$$\frac{\partial}{\partial t}(\chi F^*) + \boldsymbol{\nabla}\cdot(\chi F^*\,\boldsymbol{u}^*) = D_F\boldsymbol{\nabla}\cdot(\chi\boldsymbol{\nabla}F^*) - \delta_\Gamma j^*, \tag{24}$$

where the boundary condition has been included using the approach from [58, 59].

Let $F = F^*/F_e$ be the dimensionless surfactant concentration in the bulk fluid, where F_e average of the initial bulk concentration. Then, Eqs. (22) and (24) can be written in dimensionless form as

$$\frac{\partial}{\partial t}(f\,\delta_\Gamma) + \boldsymbol{\nabla}\cdot(f\,\delta_\Gamma\,\boldsymbol{u}) = \frac{1}{\mathrm{Pe}_f}\boldsymbol{\nabla}\cdot(\delta_\Gamma\boldsymbol{\nabla}f) + \delta_\Gamma j, \tag{25}$$

$$\frac{\partial}{\partial t}(\chi F) + \boldsymbol{\nabla}\cdot(\chi F\,\boldsymbol{u}) = \frac{1}{\mathrm{Pe}_F}\boldsymbol{\nabla}\cdot(\chi\boldsymbol{\nabla}F) - h\delta_\Gamma j, \tag{26}$$

where $\mathrm{Pe}_f = \dot{\gamma}a^2/D_f$ is the surface Peclet number, $\mathrm{Pe}_F = \dot{\gamma}a^2/D_F$ is the bulk Peclet number and $h = f_e/(aF_e)$ is the adsorption depth. The dimensionless source term, j, is given by

$$j(F,f) = \mathrm{Bi}\left[kF_s\left(\frac{1}{x} - f\right) - f\right] \tag{27}$$

The dimensionless parameters are $\mathrm{Bi} = r_d/\dot{\gamma}$ (Biot number) and $k = r_a F_e/r_d$ (adsorption number). In our simulations, we assume that f_e and F_e are in equilibrium such that $j^*(f_e,F_e) = 0$. Consequently, the following relations hold:

$$k = \frac{x}{1-x}, \tag{28}$$

$$h = \frac{r_a f_\infty}{r_d a}(1-x). \tag{29}$$

An insoluble surfactant may be characterized by $\mathrm{Bi} = 0$. The Biot number is the ratio of the desorption rate to the interfacial surfactant convection due to shear. For large Biot numbers, there is strong coupling between the surface and the bulk.

2.2. Interface representation

To represent the interface implicitly, we may either use a level-set function or a phase-field function. For example, taking $r(\boldsymbol{x},t)$ to be a signed distance function from Γ to $\boldsymbol{x}$, the interface Γ is the $r=0$ isosurface. Alternatively, using a phase field function c, which is 1 in Ω_0 and 0 in Ω_1, we may define $\Gamma(t) = \{\boldsymbol{x} \in \Omega \mid c(\boldsymbol{x},t) = \frac{1}{2}\}$. We follow the latter here and evolve the phase field function using an advective Cahn-Hilliard equation

$$\frac{\partial c}{\partial t} + \boldsymbol{\nabla} \cdot (c\boldsymbol{u}) = \boldsymbol{\nabla} \cdot (M(c)\boldsymbol{\nabla}\mu_c), \tag{30}$$

$$\mu_c = g'(c) - \varepsilon^2 \boldsymbol{\nabla}^2 c, \tag{31}$$

where $M = \sqrt{c^2(1-c)^2}$ is a mobility function, and $g = c^2(1-c)^2/4$ is a double well potential. The function μ_c is called the chemical potential and ε is a small parameter related to the interface thickness. Note that the above equation system is fourth-order and non-linear, which requires specialized numerical methods to solve in an efficient manner. Note that for small ε, the following relation holds near Γ

$$c(\boldsymbol{x},t) \approx \frac{1}{2}\left[1 - \tanh\left(\frac{r(\boldsymbol{x},t)}{2\sqrt{2}\varepsilon}\right)\right]. \tag{32}$$

2.3. Regularized delta and characteristic functions

To be able to evaluate Eqs. (3), (25) and (26) numerically, regularizations of the surface delta function and characteristic function are needed. In the phase-field context, several definitions of the delta function are available from the literature. In this work, the approximation from [50],

$$\delta_\Gamma \approx B(c) = \frac{3\sqrt{2}}{\varepsilon} c^2(1-c)^2, \tag{33}$$

is used for the surface equation. For the surface tension term and the boundary condition in the bulk equation, the approximation

$$\delta_\Gamma \approx |\boldsymbol{\nabla} c| \tag{34}$$

is used. This is to avoid any scaling of the equations. Note that in the surface equation (25), the constants in Eq. (33) cancel out in the discretized equations.

The regularized characteristic function, is simply taken as [58]

$$\chi \approx 1 - c. \tag{35}$$

In [59], it was shown that the regularized equations for the interfacial surfactant and the bulk surfactant converge to the sharp interface equations in the sharp interface limit.

3. Numerical methods

This section briefly describes the numerical methods used to solve the above equations. The algorithm follows that developed in [67]. In particular, the equations are discretized using finite differences in space and a semi-implicit time discretization. A block-structured, adaptive grid is used to increase the resolution around the interface in an efficient manner. The nonlinear equations at the implicit time level are solved using a non-linear Adaptive Full Approximation Scheme (AFAS) multigrid algorithm.

Special care has to be taken for the temporal discretization. The Cahn-Hilliard system is fourth order in space, and requires the use of an implicit method to avoid severe limitations in the time step. Here, we employ a combination of explicit Adam-Basforth schemes for the convective terms and implicit Crank-Nicholson schemes for other terms.

First, the Cahn-Hilliard system is solved to find the phase-field function at the new time step. This is solved using

$$\frac{c^{k+1}-c^{k}}{\Delta t} = -\boldsymbol{\nabla}\cdot(\boldsymbol{u}c)^{k+\frac{1}{2}} + \frac{1}{2}\left(\boldsymbol{\nabla}_d\cdot(M^{k+1}\boldsymbol{\nabla}_d\mu_c^{k+1}) + \boldsymbol{\nabla}_d\cdot(M^{k}\boldsymbol{\nabla}_d\mu_c^{k})\right), \tag{36}$$

$$\mu_c^{k+1} = g'(c^{k+1}) - \varepsilon^2\boldsymbol{\nabla}_d^2 c^{k+1}. \tag{37}$$

The operator $\boldsymbol{\nabla}_d$ represents the standard, second-order, finite-difference discretization. The convective terms of the form, $\boldsymbol{\nabla}\cdot(\boldsymbol{u}\phi)$, are discretized using the third-order WENO reconstruction method [68, 69]. The WENO reconstruction method has the advantage that it handles steep gradients well, which may occur in the type of dynamics described in this work. Additionally, fewer grid points are needed to achieve a high order solution. This is particularly important for the efficiency of the adaptive grid, because fewer ghost cell values have to be calculated at the boundaries of each grid block.

The velocities and concentration at the half-step are found by extrapolation, $\boldsymbol{u}^{k+\frac{1}{2}} = \frac{1}{2}(3\boldsymbol{u}^{k}-\boldsymbol{u}^{k-1})$ and $c^{k+\frac{1}{2}} = \frac{1}{2}(3c^{k}-c^{k-1})$. The velocities at the cell-edges are needed to construct the convective term. These are found by

$$u_{i+\frac{1}{2},j} = \frac{u_{i,j}+u_{i+1,j}}{2} - \frac{\Psi_{i+1,j}-\Psi_{i,j}}{h} \tag{38}$$

$$v_{i,j+\frac{1}{2}} = \frac{v_{i,j}+v_{i,j+1}}{2} - \frac{\Psi_{i,j+1}-\Psi_{i,j}}{h}, \tag{39}$$

where Ψ is the MAC projection found by solving

$$\boldsymbol{\nabla}_d^2\Psi = \boldsymbol{\nabla}_d^c\cdot\boldsymbol{u}^{k+\frac{1}{2}}, \tag{40}$$

with $\nabla\Psi\cdot\mathbf{n}=0$ on $\partial\Omega$ (assumed to be along Cartesian directions). In the AFAS nonlinear multigrid method used to solve Eqs. (36)-(37), the non-linear term in the chemical potential equation, $g'(c^{k+1})$, is linearized in the smoother (local linearization) by

$$g'(c^{m}) \approx g'\left(c^{m-1}\right) + g''\left(c^{m-1}\right)\left(c^{m}-c^{m-1}\right), \tag{41}$$

where m is the V-cycle iteration index. See [67] for details.

Next, the surfactant concentration on the surface and in the bulk at the new time step is found. Because of the regularized delta functions and characteristic functions, no special treatment of these equations are needed. We use the method from [59], and solve

$$\begin{aligned}\frac{(Bf)^{k+1}-(Bf)^{k}}{\Delta t} =& -\boldsymbol{\nabla}\cdot(\boldsymbol{u}Bf)^{k+\frac{1}{2}} \\ &+\frac{1}{2\mathrm{Pe}_f}\left(\boldsymbol{\nabla}_d\cdot(B^{k+1}\boldsymbol{\nabla}_d f^{k+1})+\boldsymbol{\nabla}_d\cdot(B^{k}\boldsymbol{\nabla}_d f^{k})\right) \\ &+\frac{1}{2}\left((Bj)^{k+1}+(Bj)^{k}\right).\end{aligned} \tag{42}$$

$$\begin{aligned}\frac{(\chi F)^{k+1}-(\chi F)^{k}}{\Delta t} =& -\boldsymbol{\nabla}\cdot(\boldsymbol{u}\chi F)^{k+\frac{1}{2}} \\ &+\frac{1}{2\mathrm{Pe}_F}\left(\boldsymbol{\nabla}_d\cdot(\chi^{k+1}\boldsymbol{\nabla}_d F^{k+1})+\boldsymbol{\nabla}_d\cdot(\chi^{k}\boldsymbol{\nabla}_d F^{k})\right) \\ &-\frac{1}{2}\left(|\boldsymbol{\nabla}_d c^{k+1}|(hj)^{k+1}+|\boldsymbol{\nabla}_d c^{k}|(hj)^{k}\right)\end{aligned} \tag{43}$$

as a coupled system, where we use $\chi = 1-c$. The source terms at the new time step are lagged in the V-cycle of the multigrid algorithm [59], i.e. $j^{k+1} \approx j^{k+1,m-1}$ where m is the V-cycle iteration index. This did not degrade the multigrid performance, the residual is typically reduced by an order of magnitude for each iteration.

The Navier–Stokes equations are solved using a second-order projection method. The details can be found in [70, 71, 44].

3.1. Mesh adaptivity

We use block-structured, adaptive mesh refinement to increase the resolution around the interface in an efficient manner. Near the interface, patches of overlapping, uniform, Cartesian grids are applied.

At every time step, we check grid cells for refinement using a simple undivided gradient test. Since it is essential for our problem to have a fine resolution in the diffuse interface region, this test marks grid cells where the finite difference of the phase-field function is large. In particular, we mark a cell for refinement if

$$\sqrt{(c_{i+1,j}-c_{i-1,j})^2+(c_{i,j+1}-c_{i,j-1})^2)} > C_k, \tag{44}$$

where C_k is the tolerance for level k. We note that more sophisticated refinement criteria could also be applied. For instance, [72] used a criteria based on curvature and vorticity with a level-set method. It may also be important to refine where finite differences of f and F are large; in particular this is needed when Pe_f and/or Pe_F are large. After the cells are marked for refinement, they are grouped together into rectangular patches, and populated with data from the old grid. For a detailed discussion of all the aspects of the adaptive algorithm, the reader is referred to [67].

4. Code validation

In this section, three test cases are presented to validate the proposed numerical method. Because the bulk/surface coupling was thoroughly tested in [59], we will here focus on validating the flow solver and the coupling between the flow solver and the surfactant concentration.

In the numerical implementation, surface quantities are defined at grid points near the interface. To find values on the interface, we use a marching squares algorithm (see e.g. [73]) to generate a set of points on the 0.5 isocontour of the phase-field function. Bilinear interpolation is then used to interpolate the grid values of the surface concentration to these interface points.

4.1. Oscillations of a capillary wave

First a two-phase system without surfactants is considered to test the Navier–Stokes solver and the adaptive grid algorithm. The test problem is the damping of a sinusoidal, capillary wave. For the case of small amplitudes and matched viscosities, an analytical solution for the amplitude was found in [74].

The frequency of a wave with wavenumber $k = 2\pi/\lambda$, where λ is the wave length, is given by

$$\omega_0^2 = \frac{\sigma k^3}{\rho_0 + \rho_1}. \tag{45}$$

Assuming the amplitude is small, the analytical solution for the amplitude $a(t)$ is given in dimensional form by

$$\begin{aligned} a(t) = {} & \frac{4(1-4b)k^4\nu^2}{8(1-4b)k^4\nu^2 + \omega_0^2} a_0 \mathrm{erfc}\left(\nu k^2 t\right)^{1/2} \\ & + \sum_{i=4}^{4} \frac{z_i}{Z_i} \left(\frac{\omega_0^2 a_0}{z_i^2 - \nu k^2} - \dot{a}_0 \right) \exp[(z_i^2 - \nu k^2)t] \mathrm{erfc}\left(z_i t^{1/2}\right), \end{aligned} \tag{46}$$

where the z_i's are the four roots of the algebraic equation

$$\begin{aligned} & z^4 - 4b(k^2\nu)^{1/2} z^3 \\ & \quad + 2(1-6b)k^2\nu z^2 + 4(1-3b)(k^2\nu)^{3/2} z + (1-4b)k^4\nu^2 + \omega_0^2 = 0 \end{aligned} \tag{47}$$

and $Z_i = (z_2 - z_1)(z_3 - z_1)(z_4 - z_1)$ with Z_2, Z_3, Z_4 obtained by circular permutation of the indices. Further, b is given by

$$b = \frac{\rho_0 \rho_1}{(\rho_0 + \rho_1)^2}. \tag{48}$$

Here, we will consider a computational domain given by a unit square box, with an interface given by

$$y = 0.5 - 0.01\cos(2\pi x). \tag{49}$$

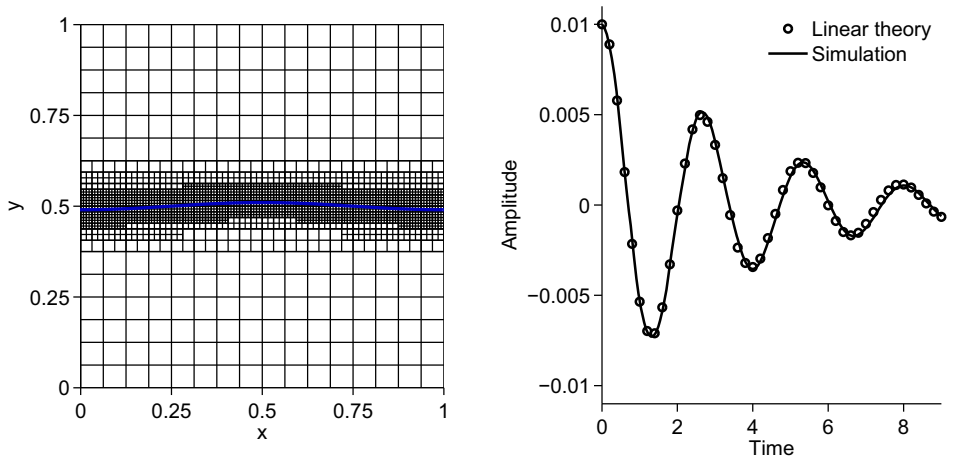

Figure 3: Capillary wave test case. An adaptive grid with root level 16×16 and three levels of refinement are used. $\varepsilon = 5 \times 10^{-3}$. Left: Computational domain with intial interface position and adaptive grid; Right: Amplitude of capillary wave, simulation versus linear theory.

We choose dimensional variables $\rho_0 = \rho_1 = 18.3$, $\mu_0 = \mu_1 = 0.078$ and $\sigma = 1.0$, giving $\omega_0^2 = 6.778$. Periodic boundary conditions are used in the horizontal direction, no-slip boundary conditions are imposed on the upper and lower boundaries, and an interface thickness parameter of $\varepsilon = 5 \times 10^{-3}$ is used along with a time step of $\Delta t = 5 \times 10^{-3}$.

The initial condition is shown in Figure 3 (left). An adaptive grid with 16×16 grid points at the root level and three levels of mesh refinement are used ($h_{\max} = 6.25 \times 10^{-2}$ and $h_{\min} = 7.8125 \times 10^{-3}$). There are 8-10 grid points across the interface layer. Figure 3 (right) shows the evolution of the amplitude compared to the analytical solution. The numerical method is clearly capable of accurately simulating the oscillatory behavior.

4.2. Rising drop in a linear surfactant gradient

In [75], an approximation for the rise velocity of a viscous drop in a linear temperature gradient was found. This approximation is used here to test the implementation of the Marangoni stresses. Instead of a temperature gradient, the interfacial surfactant concentration is assumed to vary linearly in the vertical direction.

In dimensional variables, consider an axisymmetric drop of radius R in a channel of radius $5R$ and height $L = 15R$. Let the interfacial surface concentration be given by

$$\frac{f(z)}{f_\infty} = \frac{z}{L}, \tag{50}$$

and the relationship between surfactant and surface tension as

$$\sigma(z) = \sigma_s \left(1 - \beta \frac{f(z)}{f_\infty}\right), \tag{51}$$

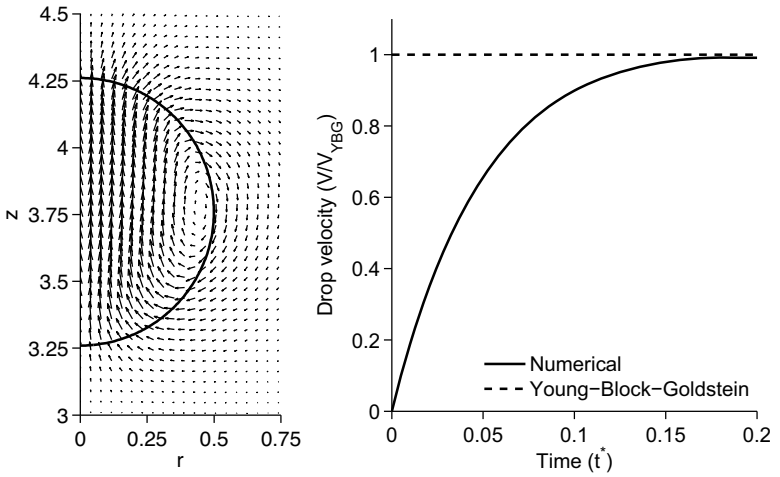

Figure 4: Velocity field at steady state shown every fourth grid point (left) and rise velocity versus time (right), compared to the theoretical result, for the linear surfactant gradient test case.

then an approximation for the terminal rise velocity is [75]

$$V_{YBG} = \frac{2(\sigma_s \beta_s R/L - \Delta\rho g R^2(\mu_0+\mu_1)/\mu_1}{(6\mu_0+9\mu_1)}. \tag{52}$$

We choose dimensional parameters $\rho_0 = \rho_1 = 0.2$, $\mu_0 = \mu_1 = 0.1$, $R = 0.5$, $\sigma_s = 1.0$ and $\beta_s = 1.0$. According to Eq. (52), this should give a Reynolds number of $\mathrm{Re} = 0.0889$, which is well within the creeping flow regime for which the equation is valid.

Because of the relatively large domain needed to keep the boundary conditions from interfering with the solution, this test case lends itself very well to an adaptive grid. Here, a root level grid spacing of $h_{\max} = 5/64 = 7.8125 \times 10^{-2}$ is chosen with three levels of refinement $h_{\min} = 5/512 = 9.76 \times 10^{-3}$. The number of nodes is approximately 9000 throughout the simulation, compared to the 196608 nodes needed for a uniform grid. An interface thickness parameter of $\varepsilon = 6.0 \times 10^{-3}$ is used (8-10 grid points across the interface), and the time step is $\Delta t = 5.0 \times 10^{-4}$. The rise velocity is calculated by

$$V = \frac{\int_\Omega c(\boldsymbol{x},t)\boldsymbol{u}(\boldsymbol{x},t)\cdot \boldsymbol{e}_z \mathrm{d}\Omega}{\int_\Omega c(\boldsymbol{x},t)\mathrm{d}\Omega}, \tag{53}$$

where $\boldsymbol{e}_z$ is the unit vector in the z-direction. This integral was evaluated using the midpoint rule.

The velocity field around the drop at steady state is shown in Figure 4 (left). The figure is in good agreement with the corresponding Figure 10a in [15]. Figure 4 (right) shows the normalized rise velocity. After an initial acceleration phase, the velocity approaches the theoretical prediction asymptotically.

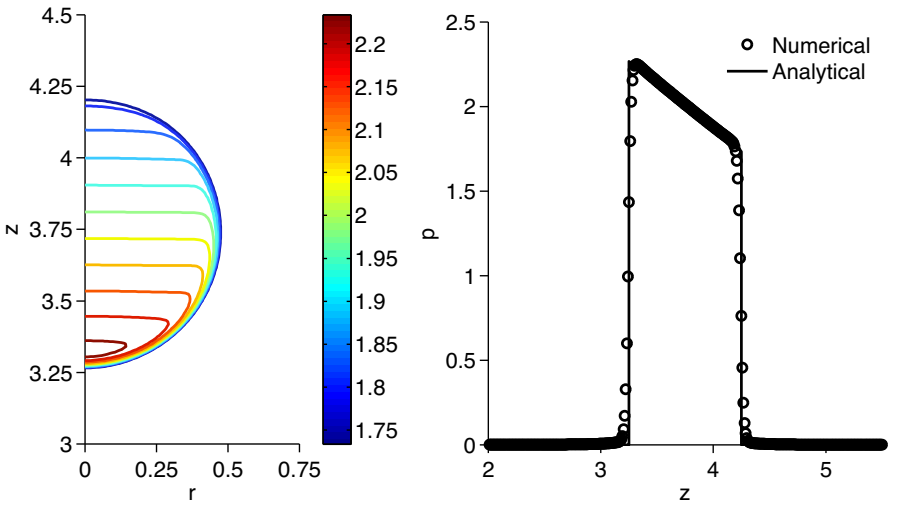

Figure 5: Pressure after one time step for a drop rising in a linear surfactant gradient. Left: Pressure contours (color online), Right: Pressure along vertical centerline compared to analytical result, Eq. (54).

Assuming the pressure in the surrounding fluid is zero, the pressure inside the drop is given by

$$p(z) = \frac{2\sigma(z)}{R}. \tag{54}$$

Figure 5 shows a closeup of pressure contours inside the drop (left), and the pressure along the vertical center line compared to the analytical result (right). Good agreement is observed.

4.3. Drop stretching in linear flow

In [7], an expression was presented for the deformation of a surfactant-covered drop in the creeping flow limit under the assumptions $\mathrm{Ca} \ll 1$, $\mathrm{Pe}_f \ll 1$ and $\lambda = O(1)$. This can be written as

$$D = \frac{L-B}{L+B} \approx \frac{3\mathrm{Ca}\cdot b_r}{4+\mathrm{Ca}\cdot b_r}, \tag{55}$$

where L and B denote the drop extension along the z and x axes, respectively, and the coefficient b_r is given by

$$b_r = \frac{(80+95\lambda) + \frac{4\beta\mathrm{Pe}_f}{\mathrm{Ca}(1-\beta)}}{40(1+\lambda) + \frac{2\beta\mathrm{Pe}_f}{\mathrm{Ca}(1-\beta)}}. \tag{56}$$

Here, we simulate a 3D drop in a velocity field given by $\boldsymbol{u} = (-x, -y, 2z)$, with varying Ca. The viscosity ratio is set to $\lambda = 1$ and the surfactant parameters are $\mathrm{Pe} = 0.1$ and $\beta = 0.5$. Due to symmetry, we only simulate one octant of the drop, and the domain

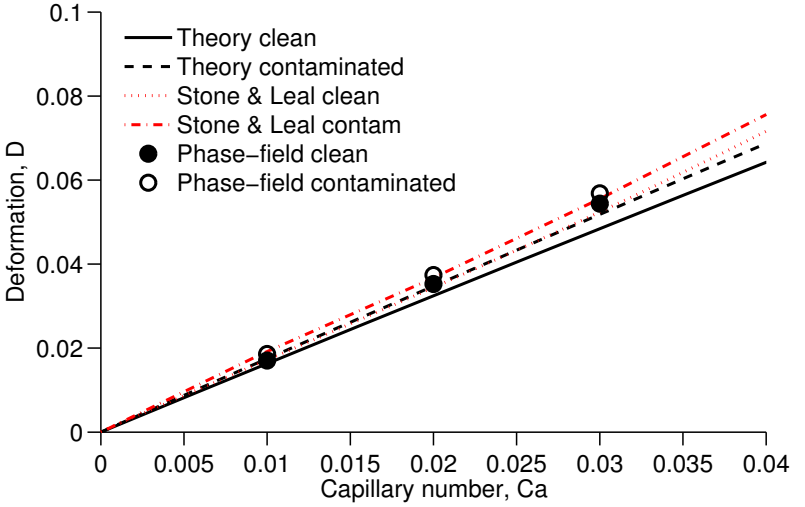

Figure 6: Comparison of small deformation theory and numerical simulations for a drop stretching in linear flow.

size is $4R \times 4R \times 4R$. We use an adaptive mesh with three levels of adaptivity, where the finest level has grid spacing $h = 1/64$. The interface thickness parameter is $\varepsilon = 0.025$.

Figure 6 shows the simulated results together with small deformation theory and results from [7]. We see that there is good agreement with the theory at low Ca and then the discrepancy gets larger at higher Ca. Our results are also in good agreement with the boundary-integral simulations of [7].

5. Influence of soluble surfactant on drop deformation and break up in shear flow

In this section, we consider the deformation of an initially circular drop placed in a shear flow. We begin by presenting 2D results. The (nondimensional) computational domain chosen for the simulations is a rectangular domain of size 12×4. The nondimensional velocity, $u = y$ is imposed on the upper and lower boundaries, and periodicity is assumed in the horizontal direction. In effect, we are simulating an infinite array of drops placed 8 units (in drop radii) apart. The root level grid spacing is $h_{\max} = 1/16$, and three levels of refinement are used ($h_{\min} = 1/128$), unless otherwise specified. The interface thickness parameter is $\varepsilon = 1/160$, and we choose a time step of 1×10^{-3}. There are approximately 8-10 grid points across the interface layer. We use $\mathrm{Ca} = 0.5$, $\mathrm{Re} = 1.0$, viscosity ratio $\lambda = 1.0$, and $\mathrm{Pe}_f = 10$ for all simulations unless otherwise noted.

5.1. Insoluble surfactant

First, we compare the evolution of a clean drop with a drop covered with insoluble surfactant using $\mathrm{Bi} = 0$. We take $\beta = 0.3$, $x = 0.5$ and the initial surfactant distribution to be uniform: $f|_{t=0} = 1.0$.

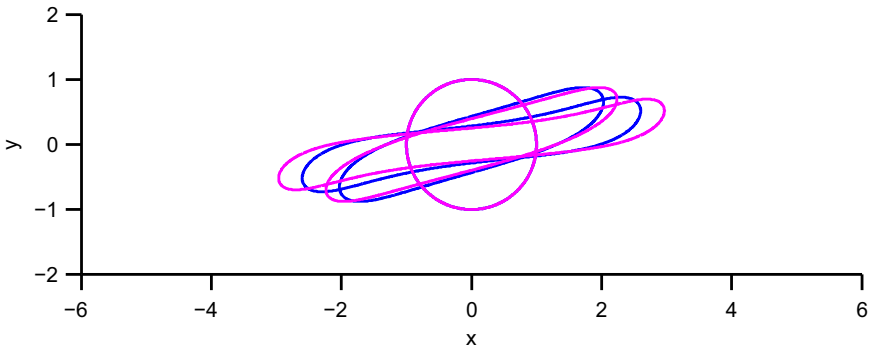

Figure 7: Comparison of drop shapes for clean and insoluble surfactant-covered drops in a shear flow at times $t = 0, 4, 8$. Blue: Clean, Magenta: Insoluble-surfactant-covered. Color online.

Figure 7 shows the morphology of a clean drop and an insoluble surfactant-covered drop at times 0, 4 and 8. As expected, the surfactant-covered drop exhibits a larger deformation and rotates faster due to the lower surface tension. Figure 8 shows the surface quantities surfactant concentration, surface tension, capillary force and Marangoni force as a function of arc length s at times 0, 4 and 8. The point $s = 0$ corresponds to the point $y = 0$ on the right side of the drop and s increases counterclockwise along the drop. The capillary forces are calculated as $-\frac{1}{\mathrm{Ca}}\sigma\kappa$, while the Marangoni forces are calculated as $\frac{1}{\mathrm{Ca}}\nabla_s\sigma\cdot\boldsymbol{t}$, where $\boldsymbol{t}$ is the unit tangential vector. Surfactant is swept to the drop tips, which lowers the surface tension. This reduces the drop the resistance to stretching. Correspondingly, the drop thins, elongates and rotates. The capillary forces reach a maximum at the tips due to the high curvature. The presence of surfactant does not alter the capillary forces significantly, but does lower the forces near the tips (not shown). Due to symmetry, the Marangoni forces are zero at the drop tips. Near the tips, the Marangoni force has local maxima and minima. The maxima occur on the upper part of the drop interface near the right tip and on the lower part of th interface near the left tip. The minima occur on the lower region near the right tip and the upper region near the left tip. The velocity near the maxima is larger, which leads to increased surfactant convection and thereby larger surface tension gradients.

A common problem with interface capturing methods is that they do not exactly conserve mass. In the above simulation, there is about a 0.3 % loss of surfactant mass throughout the simulation. The mass is measured by evaluating $m_f = \int_\Omega B f \mathrm{d}\Omega$ using the midpoint rule. In [29], a simple mass correction scheme was used where the surfactant is multiplied by a constant to preserve mass. This scheme could also be easily adapted to our approach. The mass loss for the phase-field concentration was only $5.6 \times 10^{-5}\%$ (measured by the total integral $\int_\Omega c \, \mathrm{d}\Omega$ using the midpoint rule).

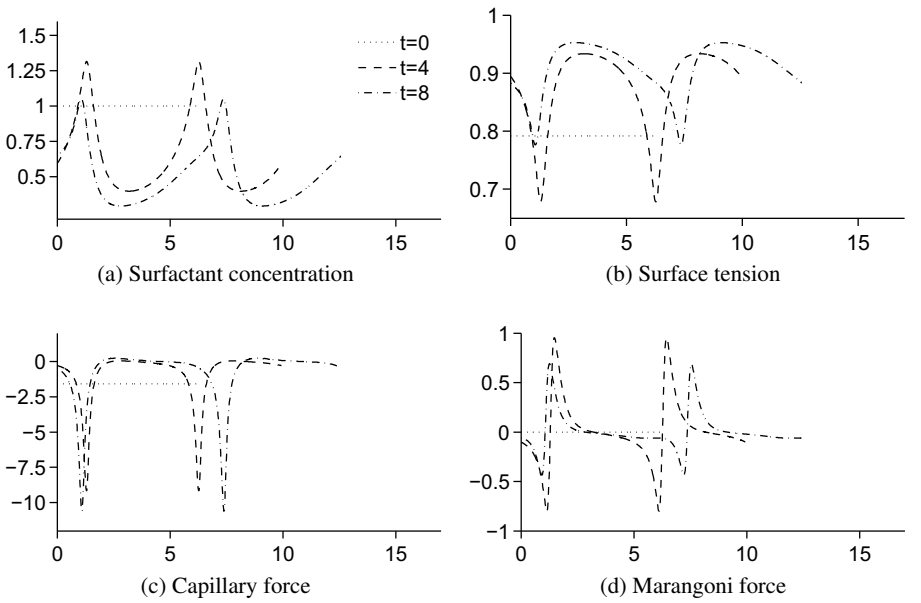

Figure 8: Surface quantities as a function of arclength for a insoluble surfactant-covered drop in shear flow.

5.2. Soluble surfactant

We next investigate the effect of surfactant solubility. We again take $\beta = 0.3$, $x = 0.5$, and the initial surface surfactant distribution to be uniform: $f|_{t=0} = 1.0$. The adsorption number is $k = 1.0$ and the adsorption depth is $h = 0.5$. We take the drop to be in equilibrium with the bulk at the start of the simulation, i.e. $j|_{t=0} = 0$, which gives the initial bulk concentration $F|_{t=0} = 1.0$. We vary the Biot number and the bulk Peclet number.

5.2.1. Influence of Biot number

We first set the bulk Peclet number $Pe_F = 1$, and vary the Biot number. The morphology of the drops for varying Biot numbers is shown in Figure 9. The inner (magenta) drop corresponds to $\mathrm{Bi} = 0$ and the outer drop (black) corresponds to $\mathrm{Bi} = \infty$, simulated by enforcing $f = 1$ throughout the simulation. The drop deformation is an increasing function of Bi. The reason for this is that surfactant adsorption/desorption decreases the surface tension gradients and hence Marangoni forces. If the Biot number tends to infinity, the surface surfactant should be uniform and the Marangoni force vanishes.

This is further elucidated in Figure 10. The left column of Figure 10 shows the surfactant concentration, the surface tension, the capillary force and the Marangoni force at $t = 4$. We see that by increasing the Biot numbers, the surfactant concentration becomes more uniform. This leads to lower surface tension gradients and thereby lower Marangoni forces, which enables the drop to deform more. The capillary force is dominated by the curvature, and remains largely unaffected by the variation in surface tension.

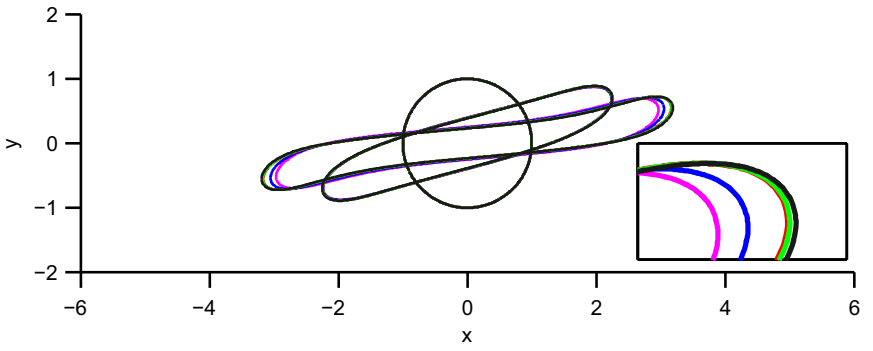

Figure 9: Comparison of drop shapes for various Biot numbers. The times shown are $t = 0, 4, 8$. Magenta: $\mathrm{Bi} = 0$ (insoluble), blue: $\mathrm{Bi} = 0.1$, red: $\mathrm{Bi} = 1$, green: $\mathrm{Bi} = 10$, and black: uniform ($\mathrm{Bi} = \infty$). The inset shows a close-up of the drop tip for $t = 8$. Color online.

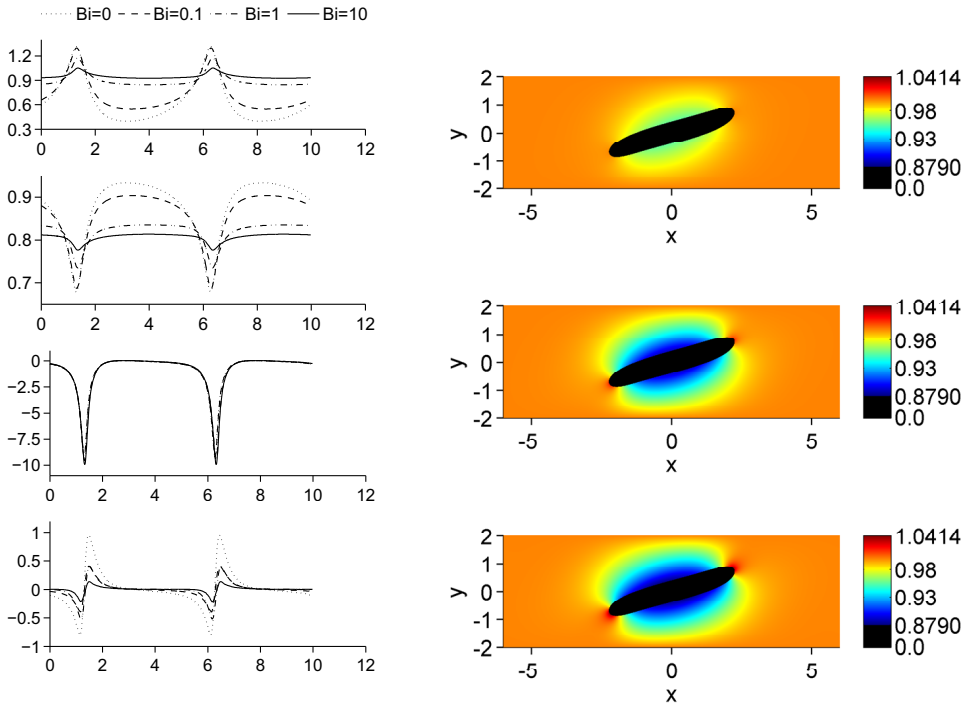

Figure 10: Influence of the Biot number on a drop in shear flow at $t = 4$. Left column shows from top to bottom: Surfactant concentration, surface tension, capillary force and Marangoni force. The right column shows the bulk surfactant concentration, from top to bottom: $\mathrm{Bi} = 0.1, \mathrm{Bi} = 1$ and $\mathrm{Bi} = 10$.

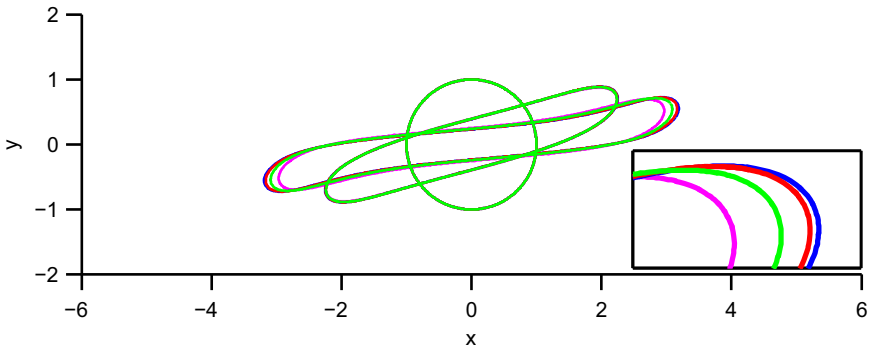

Figure 11: Comparison of drop shapes for various Peclet numbers. The times shown are $t = 0, 4, 8$. Magenta: Insoluble, blue: $\mathrm{Pe}_F = 0.1$, red: $\mathrm{Pe}_F = 1$ and green: $\mathrm{Pe}_F = 10$. The inset shows a close-up of the drop tip for $t = 8$. Color online.

The right column of Figure 10 shows the bulk concentration at $t = 4$. It is evident that a larger Biot number leads to a faster depletion of bulk surfactant due to the higher adsorption at the interface. At the drop tips, there is desorption of surfactant off the interface leading to increased surfactant concentration in the bulk. Also note that the change in dynamics from $\mathrm{Bi} = 1$ to $\mathrm{Bi} = 10$ is not as significant as the change from $\mathrm{Bi} = 0.1$ to $\mathrm{Bi} = 1$. This is because the bulk diffusion is not large enough to maintain a high adsorption/desorption rate. The process has become *diffusion-limited*.

5.2.2. Influence of Peclet number

Next, we examine the effect of the bulk Peclet number Pe_F. The Biot number is Bi=1. Figure 11 shows the morphology of the drops for varying Peclet numbers. The deformation is larger for smaller Peclet numbers since stronger diffusion in the bulk enables the redistribution of bulk surfactant to maintain a more uniform bulk distribution. This in turn supports a larger rate of surfactant adsorption along the drop sides that keeps the surface surfactant concentration more uniform and thus decreases the Marangoni force.

The left column of Figure 12 shows the surfactant concentration, the surface tension, the capillary force and the Marangoni force at $t = 4$. Again, we see that the surface surfactant concentration becomes more uniform due to the mass transfer process when the Peclet number is smaller, thereby decreasing the Marangoni forces. However, the effect is most pronounced away from the drop tips. At the drop tips, the surfactant concentration (surface tension and Capillary force) are somewhat insensitive to Pe_F because convection is relatively more important here than on the sides. In particular, at the sides surfactant is adsorbed to the interface, then swept by convection towards the tips, leaving room for more adsorption along the sides. This depletes the bulk concentration near the sides but at the tips, there is increased bulk concentration above $F_\infty = 1$ because surfactant desorbs to the bulk. A small Peclet number is needed to redistribute bulk surfactant to maintain a more uniform bulk distribution and thus a

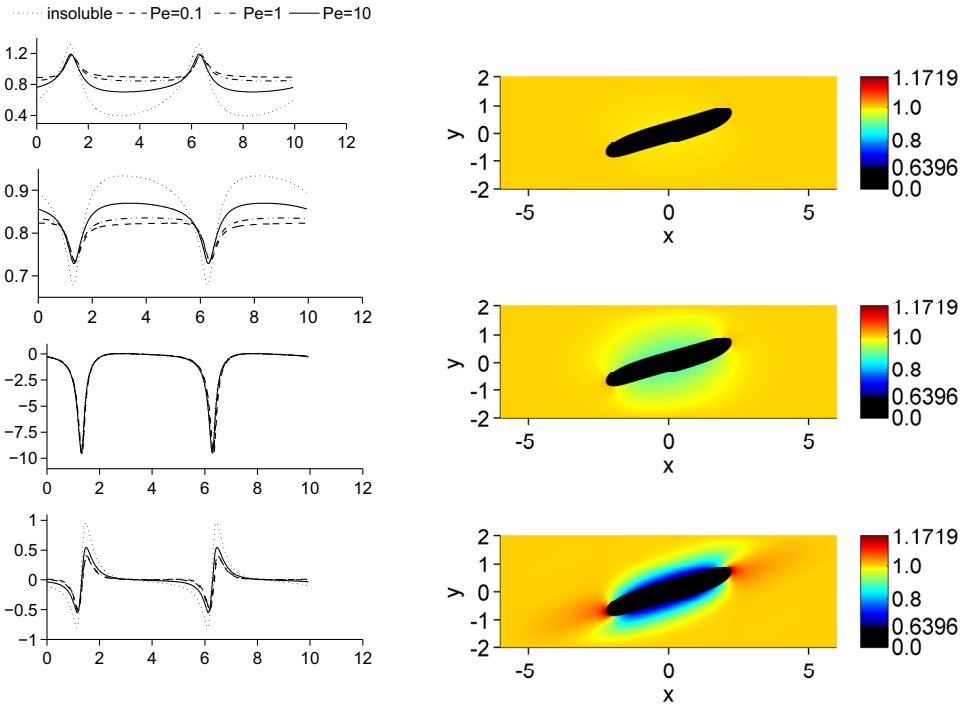

Figure 12: Influence of bulk Peclet number on drop in shear flow at $t = 4$. Left column shows from top to bottom: Surfactant concentration, surface tension, capillary force and Marangoni force. The right column shows the bulk surfactant concentration, from top to bottom: $\mathrm{Pe}_F = 0.1, \mathrm{Pe}_F = 1$ and $\mathrm{Pe}_F = 10$. Color online.

high adsorption rate along the drop sides. In fact, when the Peclet number is small, the adsorption rate is not large enough to adsorb all the available bulk surfactant. Thus the differences between the results from $\mathrm{Pe}_F = 0.1$ to $\mathrm{Pe}_F = 1$ are less pronounced than the differences from $\mathrm{Pe}_F = 1$ to $\mathrm{Pe}_F = 10$. This is because the process becomes *adsorption-limited* for small Peclet numbers.

This is further illustrated in Figure 14, which shows the source term j for the three Peclet numbers. Away from the drop tips, j is positive, which means that surfactant is transported from the bulk to the interface. At the tips, the transportation is reversed due to the accumulation of surfactant here. For a high Peclet number, the mass transfer is lower, because the bulk diffusion is not large enough to transport desorbed surfactant away from the interface or to replenish surfactant adsorbed to the interface. This effect is even more pronounced when the Peclet number is significantly increased to $\mathrm{Pe}_F = 1000$ as seen in Figure 13. At this large Peclet number, a narrow boundary layer of depleted bulk surfactant is observed along the drop sides while the bulk concentration is significantly increased near the drop tips. In order to simulate this case, another level of refinement is required such that $h_{\min} = 1/256$ and in addition the mesh is refined where the undivided gradient of F is sufficiently large; the finest mesh covers the surfactant boundary layer. The thickness of the surfactant boundary layer along the drop sides is approximately 0.14 while at the drop tips the boundary layer thickness is approximately 0.69. For reference, the thickness, $O(\varepsilon)$, of the diffuse interface describing the drop boundary is approximately 0.06.

5.2.3. Convergence study

A convergence study was carried out for the fluid velocity, the interface surfactant and the bulk surfactant for the case where $\mathrm{Pe}_F = 1$ and $\mathrm{Bi} = 1$. Since the analytical solution is not available, we use the solution for a fine mesh as a reference solution and measure the deviation from this solution in the L_2 norm. The L_2 norm is calculated as

$$||\boldsymbol{f}||_2 = \sqrt{\sum \boldsymbol{f}^2}, \tag{57}$$

and the rate of convergence as

$$\text{rate} = \frac{\ln(e_{2h}/e_h)}{\ln 2}, \tag{58}$$

where h denotes grid spacing. All simulations here are carried out on a uniform mesh. Since the variables are collocated, they do not coincide when the mesh is refined. Linear interpolation is used to interpolate the values.

The results are summarized in Table 1. The rate of convergence is around two for the velocities and one for the surfactant concentrations. The result for the surfactant concentrations are in line with what was found in [59].

5.3. Three-dimensional results

Finally, we present some results from three-dimensional simulations. In particular, we investigate drop break up in a shear flow. The grid spacing at the root level is $h_{\max} = 1/4$,

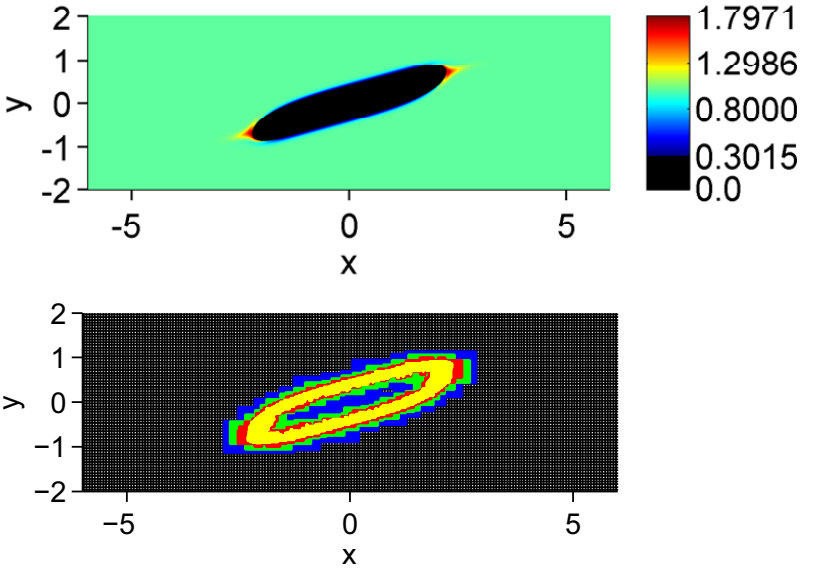

Figure 13: Influence of large bulk Peclet number $\mathrm{Pe}_F = 1000$ on a drop in shear flow at $t = 4$. Top: Bulk surfactant distribution, Bottom: Adaptive mesh. Four levels of refinement are used (black: level 0, blue: level 1, green: level 2, red: level 3, yellow: level 4). Color online.

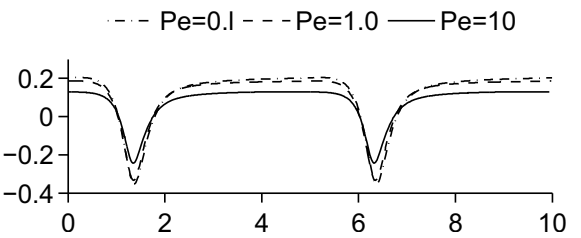

Figure 14: Comparison of the source term j along the interface for different Peclet numbers.

Table 1: Error in L_2 norm and convergence rate for the fluid velocities and the surfactant concentrations.

Grid	$\|\|u-u_{\text{ref}}\|\|_2$ $(\times 10^{-2})$	Rate	$\|\|v-v_{\text{ref}}\|\|_2$ $(\times 10^{-1})$	Rate
1/16	4.03	-	8.49	-
1/32	1.84	1.13	5.20	0.71
1/64	0.503	1.87	1.57	1.73
1/128	0.0754	2.74	0.203	2.95
	$\|\|f-f_{\text{ref}}\|\|_2$ $(\times 10^{-1})$	Rate	$\|\|F-F_{\text{ref}}\|\|_2$ $(\times 10^{-1})$	Rate
1/16	2.93	-	5.96	-
1/32	2.23	0.39	3.64	0.71
1/64	1.58	0.50	1.19	0.92
1/128	0.686	1.20	0.834	1.20

three levels of refinement are used such that $h_{\min} = 1/32$. To elucidate the effects of the interface thickness parameter ε, we simulated two different cases: $\varepsilon = 1/80$ and $1/40$. There are approximately 5-6 grid points across the interface for smaller ε. These simulations took approximately 3 days to complete on one core of an Intel i7 processor.

We take $\text{Ca} = 0.42$ and $\text{Re} = 0.4$, which while smaller than used in 2D are still above the critical threshold for the existence of steady state solutions. This allows us to run the simulation until the drop breaks up to demonstrate the ability of our method to handle topological changes. A similar simulation was presented in [62], although their simulation used $\text{Re} = 0$. For the surfactant, we assume a dilute concentration of $x = 0.1$ and a relatively strong coupling between surfactant and surface tension with $\beta = 0.2$. For the parameters associated with solubility, we again choose initial conditions at equilibrium, $k = 1/9$ and $h = 0.9$. The bulk Peclet number is set to $\text{Pe}_F = 10$.

The results for a clean drop and a drop covered by an insoluble surfactant are shown in Figure 15 (left and right columns respectively). After an initial regime of stretching, necks form near the two drop tips. These become thinner until the drop breaks up. In each case, two tiny satellite drops can be observed after the necks pinch off. In the surfactant case, the satellite drops are very small and are covered with nearly uniform surfactant. We see that the surfactant-covered drop breaks up at an earlier time. There are two principal reasons for this behavior. First, the non-uniform distribution of surfactant leads to larger deformation, as shown in the previous sections, which thins the drop more than the clean case. Second, in the necks, the surfactant concentration is low, which gives a larger surface tension (similar to the surface tension of a clean drop). Since the necks are thinner in the surfactant-laden drop this leads to faster breakup.

In Figure 16, the break-up of a clean drop is shown for a larger value of interface thickness ε ($\varepsilon = 1/40$ compared to $\varepsilon = 1/80$ in Figure 15). For the larger value of ε, the drops break up at an earlier time and satellites are not observed. A similar behavior is

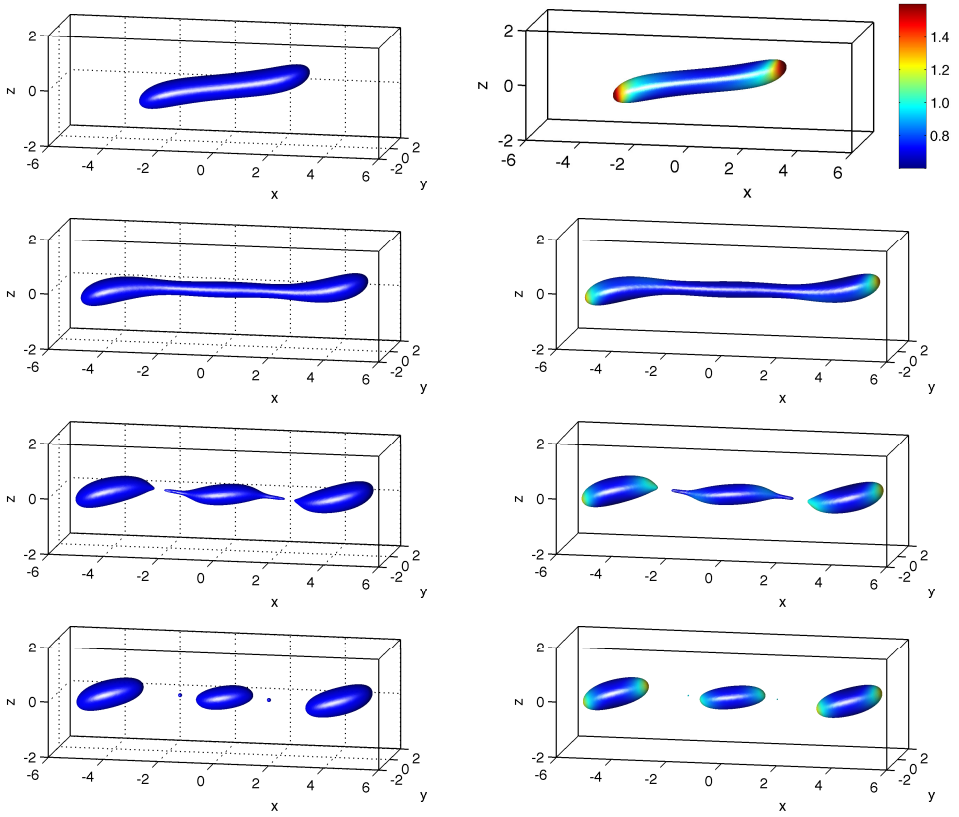

Figure 15: Three-dimensional simulation of a drop in shear flow with interface thickness $\varepsilon = 1/80$. The left column shows a drop with no surfactant. The right column shows a drop with insoluble surfactant. The times shown are from top to bottom: 10, 25, 34, and 35.16.

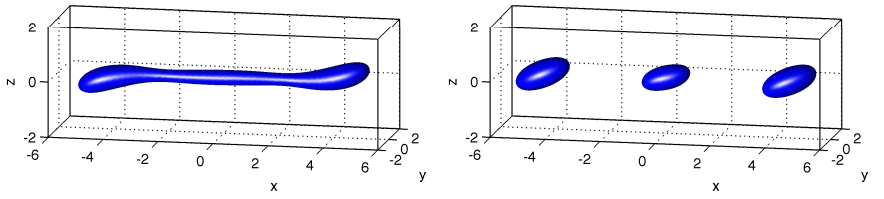

Figure 16: Drop evolution in shear flow without surfactant at times $t = 25$ (left) and 35.16 (right) with $\varepsilon = 1/40$. All other parameters are the same as in Figure 15.

observed in the presence of surfactant.

The results for soluble surfactant are shown in Figure 17, using $\varepsilon = 1/80$. The right column, which shows a slice of the bulk concentration, indicates that surfactant is adsorbed to the surface at the middle of the drop, and desorbed at the tips. This leads to a more uniformly distributed surfactant concentration. Comparing Figure 17 with Figure 15 we can see the soluble-surfactant-covered drop breaks up at a later time than the clean drop. The principle reason is the adsorption and desorption of surfactant. Since adsorption occurs over a larger surface area than desorption, which just occurs at the drop tips, the interfacial surfactant concentration becomes larger across the entire drop. This means that the deformation becomes larger and that there is significant concentration of surfactant near the drop necks. This slows the thinning of the necks since the surface tension is smaller. Thus, the drop breaks up at a *later* time than for the clean drop. This shows that the influence of solubility can have an important influence on drop dynamics.

6. Conclusions and future work

A diffuse-interface method to simulate two-phase flows with soluble surfactants was presented. The method handles advection, diffusion and adsorption/desorption of surfactant, and is easy to implement using standard numerical techniques.

As an example of the applicability of the method, results were presented on the influence of solubility on a drop in shear flow. It was shown that solublity could have a considerable influence on the flow dynamics. Simulations in 3D were also performed, which showed that the influence of soluble surfactants is important for the breakup behavior of the drop.

Although not presented here, asymptotic and numerical evidence suggests that the convergence to the sharp interface system is first order in the interface thickness parameter ε [59]. It may be possible to gain second order accuracy in ε by explicitly removing the corresponding term in the asymptotic expansion as can be done in the context of solidification to enable simulations with arbitrary kinetic coefficients [76, 77]. Also, more consistent projection methods for collocated grids were recently presented in [78]. These two improvements to the proposed method should be explored. In addition, as we have seen, when the bulk Peclet number is large, thin boundary layers develop near the deforming drop. Adaptive meshes can enable accurate simulations for a range of Peclet numbers but in some applications, the bulk Peclet number can reach 10^5-10^6 (e.g., [79]) at which point it is infeasible to use adaptive meshes. Instead, following the approach recently developed by Booty & Siegel [80], a singular perturbation analysis should be incorporated in the numerical algorithm.

Acknowledgment

The authors thank Steven Wise and Fang Jin for assistance with the numerical code and visualization. KET is funded by the project “Electrocoalescence – Criteria for an efficient

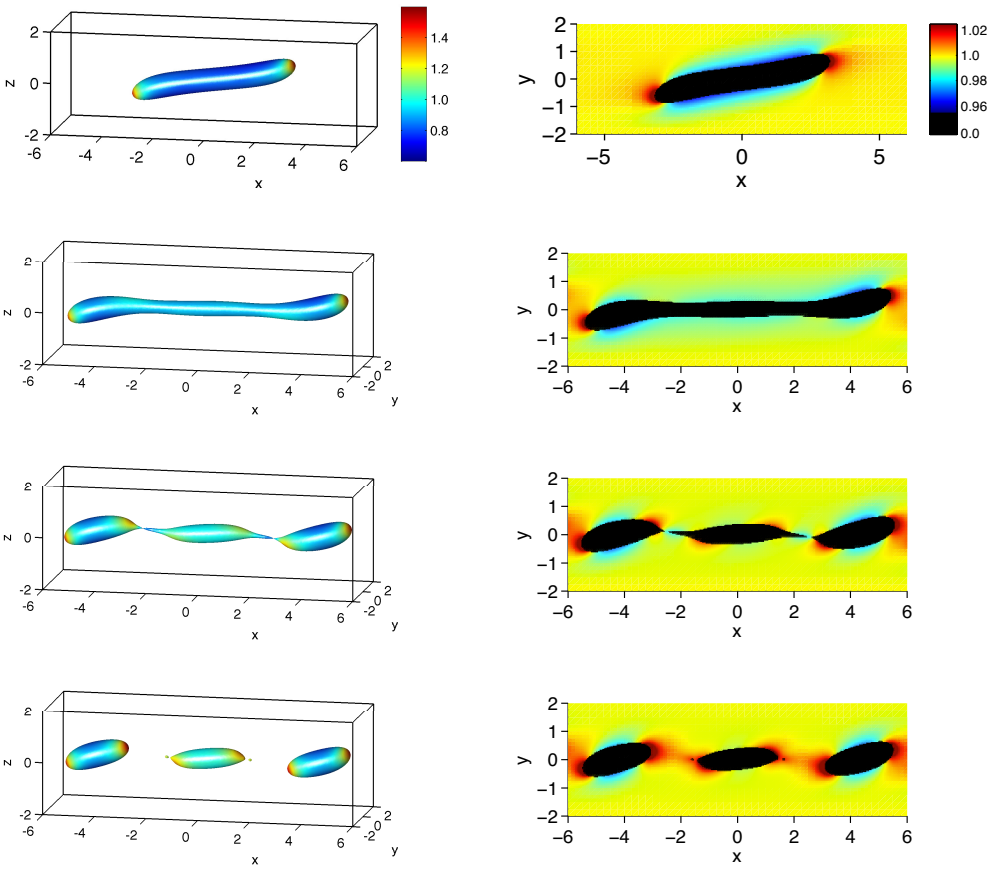

Figure 17: Three-dimensional simulation of a drop in shear flow with soluble surfactant, $\varepsilon = 1/80$. The left column shows the drop shape with the surface colored according to the interface surfactant concentration. The right column shows a slice of the bulk surfactant concentration along the x-axis. The times shown are from top to bottom: 10, 25, 34 and 35.16.

process in real crude oil systems"; coordinated by SINTEF Energy Research. The project is supported by The Research Council of Norway, under the contract no: 169466/S30, and by the following industrial partners: Aker Solutions AS, BP Exploration Operating Company Ltd, Hamworthy Technology & Products AS, Petrobras, Saudi Aramco, Shell Technology Norway AS and Statoil ASA. KET also acknowledges support from the Research Council of Norway through grant IS-BILAT 192532 and from the Fulbright Foundation. JL acknowledges support from the National Science Foundation Division of Mathematical Sciences (DMS) and from the National Institutes of Health through grant P50GM76516 for a Centre of Excellence in Systems Biology at the University of California, Irvine. AV acknowledges support from the German Science Foundation through grants Vo899/6-1 and SFB 609.

References

[1] G. Tryggvason, J. Abdollahi-Alibeik, W. W. Willmarth, A. Hirsa, Collision of a vortex pair with a contaminated free surface, Phys. Fluids A 4 (1992) 1215–1229.

[2] O. K. Matar, S. M. Troian, The development of transient fingering patterns during the spreading of surfactant coated films, Phys. Fluids 11 (1999) 3232–3246.

[3] L. G. Leal, Flow induced coalescence of drops in a viscous fluid, Phys. of Fluids 16 (6) (2004) 1833–1851.

[4] I. Bazhlekov, P. Anderson, H. Meijer, Numerical investigation of the effect of insoluble surfactants on drop deformation and breakup in simple shear flow, J. Coll. Int. Sci. 298 (2006) 369–394.

[5] M. Hameed, M. Siegel, Y.-N. Young, J. Li, M. R. Booty, D. T. Papageorgiou, Influence of insoluble surfactant on the deformation and breakup of a bubble or thread in a viscous fluid, J. of Fluid Mech. 594 (2008) 307–340.

[6] R. D. Bruijn, Tip sreaming of drops in simple shear flows, Chem. Engng. Sci. 48 (1993) 277–284.

[7] H. A. Stone, L. G. Leal, The effect of surfactants on drop deformation and breakup, J. Fluid. Mech 220 (1990) 161–186.

[8] W. J. Milliken, H. A. Stone, L. G. Leal, The effect of surfactant on transient motion of Newtonian drops, Phys. Fluids A 5 (1993) 69–79.

[9] X. Li, C. Pozrikidis, The effect of surfactants on drop deformation and on the rheology of dilute emulsions in Stokes flow, J. Fluid Mech. 341 (1997) 165–194.

[10] W. J. Milliken, L. G. Leal, The influence of surfactant on the deformation and breakup of a viscous drop - the effect of surfactant solubility, J. Colloid and Interface Sci. 166 (1994) 275–285.

[11] C. Pozrikidis, Interfacial dynamics for Stokes flow, J. Comput. Phys. 169 (2001) 250–301.

[12] G. Tryggvason, B. Bunner, A. Esmaeeli, D. Juric, N. Al-Rawahi, W. Tauber, J. Han, S. Nas, Y.-J. Jan, Front tracking method for the computation of multiphase flow, J. Comput. Phys. 169 (2001) 708–759.

[13] Y. J. Jan, Computational studies of bubble dynamics, Ph.D. thesis, University of Michigan (1994).

[14] J. Zhang, D. Eckmann, P. Ayyaswamy, A front tracking method for a deformable intravascular bubble in a tube with soluble surfactant transport, Journal of Computational Physics 214 (2006) 366 – 396.

[15] M. Muradoglu, G. Tryggvason, A front-tracking method for computation of interfacial flows with soluble surfactants, J. Comput. Phys. 227 (2008) 2238–2262.

[16] R. Mittal, G. Iaccarino, Immersed boundary methods, Ann. Rev. Fluid Mech. 37 (2005) 239–361.

[17] M.-C. Lai, Y.-H. Tseng, H. Huang, An immersed boundary method for interfacial flows with insoluble surfactant, J. Comput. Phys. 227 (2008) 7270–7293.

[18] Y. H. Tseng, J. H. Ferziger, A ghost-cell immersed boundary method for flow in complex geometry, J. Comput. Phys. 192 (2003) 593–623.

[19] F. Jin, K. J. Stebe, The effects of a diffusion controlled surfactant on a viscous drop injected into a viscous medium, Phys. Fluids 19 (2007) 112103.

[20] H. Ceniceros, The effects of surfactants on the formation and evolution of capillary waves, Phys. Fluids 15 (2003) 245–256.

[21] Y.-C. Liao, E. Franses, O. Basaran, Deformation and breakup of a stretching liquid bridge covered with an insoluble surfactant monolayer, Phys. Fluids 18 (2006) 022101.

[22] Q. Xu, Y.-C. Liao, O. Basaran, Can surfactant be present at pinch-off of a liquid filament, Phys. Rev. Lett. 98 (2007) 054503.

[23] R. Scardovelli, S. Zaleski, Direct numerical simulation of free surface and interfacial flows, Ann. Rev. Fluid Mech. 31 (1999) 567–603.

[24] Y. Y. Renardy, M. Renardy, V. Cristini, A new volume-of-fluid formulation for surfactants and simulations of drop deformation under shear at a low viscosity ratio, European Journal of Mechanics - B/Fluids 21 (2002) 49 – 59.

[25] A. J. James, J. Lowengrub, A surfactant-conserving volume-of-fluid method for interfacial flows with insoluble surfactant, Journal of Computational Physics 201 (2004) 685 – 722.

[26] A. Alke, D. Bothe, 3d numerical modelling of soluble surfactant at fluidic interfaces based on the volume-of-fluid method, FDMP 1 (2009) 1–29.

[27] S. Osher, J. Sethian, Fronts propagating with curvature-dependent speed– algorithms based on Hamilton-Jacobi formulations, J. Comput. Phys. 79 (1988) 12–49.

[28] J. J. Xu, H. Zhao, An Eulerian formulation for solving partial differential equations along a moving interface, J. Sci. Comp. 19 (2003) 573–594.

[29] J. J. Xu, Z. Li, J. Lowengrub, H. Zhao, A level set method for interfacial flows with surfactant, J. Comp. Phys. 212 (2006) 590–616.

[30] J. Sethian, P. Smereka, Level-set methods for fluid interfaces, Ann. Rev. Fluid Mech. 35 (2003) 341–372.

[31] X. Yang, A. J. James, An arbitrary Lagrangian-Eulerian (ALE) method for interfacial flows with insoluble surfactants, FDMP 3 (2007) 65–96.

[32] Y.-N. Young, M. R. Booty, M. Siegel, J. Li, Influence of surfactant solubility on the deformation and breakup of a bubble or capillary jet in a viscous fluid, Phys. Fluids 21 (2009) 072105.

[33] E. Uzgoren, J. Sim, W. Shyy, Marker-based, 3d adaptive Cartesian grid method for multiphase flow around irregular geometries, Comm. Comput. Phys. 5 (2009) 1–41.

[34] S. Adami, X. Hu, N. Adams, A conservative SPH method for surfactant dynamics, J. Comput. Phys.

[35] D. M. Anderson, G. B. McFadden, A. A. Wheeler, Diffuse interface methods in fluid mechanics, Ann. Rev. Fluid Mech. 30 (1) (1998) 139–165.

[36] H. Emmerich, Advances of and by phase-field modeling in condensed-matter physics, Adv. Phys. 57 (2008) 1–87.

[37] J. Lowengrub, L. Truskinovsky, Quasi-incompressible Cahn-Hilliard fluids and topological transitions, R. Soc. Lond. Proc. Ser. A Math. Phys. Eng. Sci. 454 (1998) 2617–2654.

[38] D. Jacqmin, Calculation of two-phase Navier-Stokes flows using phase-field modeling, J. Comput. Phys. 155 (1999) 96–127.

[39] H. Lee, J. Lowengrub, J. Goodman, Modeling pinchoff and reconnection in a Hele–Shaw cell i. the models and their calibration, Phys. Fluids 14 (2002) 492–513.

[40] H. Lee, J. Lowengrub, J. Goodman, Modeling pinchoff and reconnection in a hele-shaw cell ii. analysis and simulation in the nonlinear regime, Phys. Fluids 14 (2002) 514–545.

[41] V. Baldalassi, H. Ceniceros, S. Banerjee, Computation of multiphase systems with phase field models, J. Comput. Phys. 190 (2004) 371–397.

[42] F. Boyer, L. Chupin, B. Franck, Numerical study of viscoelastic mixtures through a Cahn–Hilliard model, Eur. J. Mech. B-Fluids 23 (2004) 759–780.

[43] P. Yue, J. J. Feng, C. Liu, J. Shen, A diffuse interface method for simulating two phase flows of complex fluids, J. Fluid Mech. 515 (2004) 293–317.

[44] J. Kim, A continuous surface tension force formulation for diffuse-interface models, Journal of Computational Physics 204 (2) (2005) 784 – 804.

[45] H.-W. Lu, K. Glasner, A. Bertozzi, C.-J. Kim, A diffuse interface model for electrowetting droplets in a Hele-Shaw cell, J. Fluid Mech. 590 (2007) 411–435.

[46] R. van der Sman, S. van der Graaf, Diffuse interface model of surfactant adsorption onto flat and droplet interfaces, Rheol. Acta 46 (2006) 3–11.

[47] D. Jacqmin, Contact-line dynamics of a diffuse interface, J. Fluid Mech. 402 (2000) 57–88.

[48] M. Do-Quang, G. Amberg, The splash of a solid sphere impacting on a liquid surface: Numerical simulation of the influence of wetting, Phys. Fluids 21 (2009) 022102.

[49] S. Aland, J. Lowengrub, A. Voigt, Two-phase flow in complex geometries: A diffuse domain approach, in preparation (2009).

[50] A. Rätz, A. Voigt, PDEs on surfaces—a diffuse interface approach, Commun. Math. Sci. 4 (2006) 575–590.

[51] A. R. tz, A. Voigt, A diffuse-interface approximation for surface diffusion including adatoms, Nonlinearity 20 (2007) 177–192.

[52] G. Dziuk, C. Elliott, Eulerian finite element method for parabolic PDEs on complex surfaces, Int. Free Bound. 10 (2008) 119–138.

[53] J. Lowengrub, A. Rätz, A. Voigt, Phase-field modeling of the dynamics of multicomponent vesicles: Spinodal decomposition, coarsening, budding and fission, Phys. Rev. E 79 (2008) 031926.

[54] C. Elliott, B. Stinner, Analysis of a diffuse interface approach to an advection diffusion equation on a moving surface, Math. Mod. Meth. Appl. Sci. (2009) in press.

[55] J. Kockelkoren, H. Levine, W.-J. Rappel, Computational approach for modeling intra- and extracellular dynamics, Phys. Rev. E 68 (3) (2003) 037702. doi:10.1103/PhysRevE.68.037702.

[56] H. Levine, W.-J. Rappel, Membrane-bound Turing patterns, Phys. Rev. E 72 (6) (2005) 061912. doi:10.1103/PhysRevE.72.061912.

[57] F. Fenton, E. Cherry, A. Karma, W.-J. Rappel, Modeling wave propagation in realistic heart geometries using the phase-field method, Chaos 15 (2005) 103502.

[58] X. Li, J. Lowengrub, A. R. tz, A. Voigt, Solving PDEs in complex geometries: A diffuse domain approach, Commun. Math. Sci. 7 (2009) 81–107.

[59] K. E. Teigen, F. Wang, X. Li, J. Lowengrub, A. Voigt, A diffuse-interface approach for modelling transport, diffusion and adsorption/desorption of material quantities on a deformable interface, Commun. Math. Sci. 7 (2009) 1009–1037.

[60] H. A. Stone, The dynamics of drop deformation and breakup in viscous fluids, Ann. Rev. Fluid Mech. 26 (1994) 65–102.

[61] K. S. Sheth, C. Pozrikidis, Effects of inertia on the deformation of liquid drops in simple shear flow, Comput. & Fluids 24 (2) (1995) 101 – 119.

[62] J. Li, Y. Y. Renardy, M. Renardy, Numerical simulation of breakup of a viscous drop in simple shear flow through a volume-of-fluid method, Phys. Fluids 12 (2000) 269 – 282.

[63] V. Cristini, J. Blawzdziewicz, M. Loewenberg, An adaptive mesh algorithm for evolving surfaces: Simulation of breakup and coalescence, J. Comput. Phys. 168 (2001) 445–463.

[64] S. Velankar, H. Zhou, H. Jeon, C. Macosko, CFD evaluation of drop retraction methods for the measurement of interfacial tension of surfactant-laden drops, J. Colloid Interface Sci. 272 (1) (2004) 172–185.

[65] C. D. Eggleton, Y. P. Pawar, K. J. Stebe, Insoluble surfactants on a drop in an extensional flow: a generalization of the stagnated surface limit to deforming interfaces, J. of Fluid Mech. 385 (1999) 79–99.

[66] H. Wong, D. Rumschitzki, C. Maldarelli, On the surfactant mass balance at a deforming fluid interface, Phys. Fluids 8 (1996) 3203–3204.

[67] S. Wise, J. Kim, J. Lowengrub, Solving the regularized, strongly anisotropic Cahn-Hilliard equation by an adaptive nonlinear multigrid method, J. Comput. Phys. 226 (2007) 414–446.

[68] C. W. Shu, S. Osher, Efficient implementation of essentially non-oscillatory shock-capturing schemes, J. Comput. Phys. 77 (2) (1988) 439–471.

[69] S. Liu, T. Chan, Weighted essentially non-oscillatory schemes, J. Comput. Phys. 115 (1994) 200–212.

[70] J. B. Bell, P. Colella, H. M. Glaz, A second-order projection method for the incompressible navier-stokes equations, J. Comput. Phys. 85 (2) (1989) 257 – 283.

[71] J. Kim, K. Kand, J. Lowengrub, Conservative multigrid methods for ternary Cahn-Hilliard fluids, J. Comput. Phys. 193 (2004) 511–543.

[72] M. Sussman, A. S. Almgren, J. B. Bell, P. Colella, L. H. Howell, M. L. Welcome, An adaptive level set approach for incompressible two-phase flows, Journal of Computational Physics 148 (1) (1999) 81 – 124.

[73] W. E. Lorensen, H. E. Cline, Marching cubes: A high resolution 3D surface construction algorithm, Computer Graphics 21 (1987) 163–169.

[74] A. Prosperetti, Motion of two superposed viscous fluids, Phys. Fluids 24 (1981) 1217–1223.

[75] N. O. Young, J. S. Goldstein, M. J. Block, The motion of bubbles in a vertical temperature gradient, J. of Fluid Mech. 6 (03) (1959) 350–356.

[76] A. Karma, W.-J. Rappel, Phase-field method for computationally efficient modeling of solidification with arbitrary interface kinetics, Phys. Rev. E 53 (4) (1996) R3017–R3020.

[77] A. Karma, W.-J. Rappel, Quantitative phase-field modeling of dendritic growth in two and three dimensions, Phys. Rev. E 57 (4) (1998) 4323–4349. doi:10.1103/PhysRevE.57.4323.

[78] M.-J. Ni, Consistent projection methods for variable density incompressible Navier-Stokes equations with continuous surface forces on a rectangular collocated mesh, J. Comput. Phys.Accepted.

[79] C. Chang, E. Franses, Adsorption dynamics of surfactants at the air/water interface: A critical review of mathematical models, data, and mechanisms, Colloids Surfaces A 100 (1995) 1–45.

[80] M. Booty, M. Siegel, A hybrid numerical method for interfacial fluid flow with soluble surfactant, J. Comput. Phys. 229 (2010) 3864–3883.